Characterization of very high energy gamma-radiation from active galactic nuclei observed by the magic telescopes

Tomislav, Terzić

Doctoral thesis / Disertacija

2015

Degree Grantor / Ustanova koja je dodijelila akademski / stručni stupanj: **University of Zagreb, Faculty of Science / Sveučilište u Zagrebu, Prirodoslovno-matematički fakultet**

Permanent link / Trajna poveznica: https://urn.nsk.hr/urn:nbn:hr:217:608616

Rights / Prava: In copyright/Zaštićeno autorskim pravom.

Download date / Datum preuzimanja: **2024-04-19**

University of Zagreb

University of Zagreb
Faculty of Science
Department of Physics

Tomislav Terzić

CHARACTERIZATION OF VERY HIGH ENERGY GAMMA-RADIATION FROM ACTIVE GALACTIC NUCLEI OBSERVED BY THE MAGIC TELESCOPES

DOCTORAL THESIS

Zagreb, 2015

University of Zagreb

University of Zagreb
Faculty of Science
Department of Physics

Tomislav Terzić

CHARACTERIZATION OF VERY HIGH ENERGY GAMMA-RADIATION FROM ACTIVE GALACTIC NUCLEI OBSERVED BY THE MAGIC TELESCOPES

DOCTORAL THESIS

Supervisor:
Dijana Dominis Prester

Zagreb, 2015

Sveučilište u Zagrebu
Prirodoslovno-matematički fakultet
Fizički odsjek

Tomislav Terzić

SVOJSTVA VISOKOENERGIJSKOGA GAMA-ZRAČENJA IZ AKTIVNIH GALAKTIČKIH JEZGRI OPAŽANIH TELESKOPIMA MAGIC

DOKTORSKI RAD

Mentor:
Dijana Dominis Prester

Zagreb, 2015.

Mami i tati

Acknowledgements

Information about the supervisor

Name: dr. sc. Dijana Dominis Prester

Position: Associate professor at the University of Rijeka – Department of Physics

Responsibility in the MAGIC collaboration: Main Observation Scheduler

Project management:

1. 2010, Hunt for the time delay in very high energy gamma rays from (AGN); International project; DAAD, MZOŠ

2. 2013 –, Istraživanje strukture svemira optičkim i Čerenkovljevim teleskopima; University of Rijeka science research support project nr. 13.12.1.3.02

3. 2014 –, Ravnopravno sudjelovanje Sveučilišta u Rijeci u astročestičnim eksperimentima; University of Rijeka project

Conference organisation:

1. 13. – 20.9.1994, Perspectives in Particle Physics '94; Brijuni, Croatia; Conference secretary

2. 9. 2010, MAGIC collaboration Meeting; Split, Croatia; Member of the organisation committee

3. 10. 2009, 6th scientific meeting of the Croatian physical society; Primošten, Croatia; Member of the organisation committee

4. 20. – 30.9.2009, "NOVICOSMO 2009", international school in astrophysics for PhD students; Rabac, Croatia; Member of the organisation committee

Review panels:

1. 2011 – 2013, Member of the international Review Panel of European Science Foundation (ESF) for EUROGENESIS projects

   http://www.esf.org/coordinating-research/eurocores/running-programmes/eurogenesis/committees.html

2. Member of the review panel of Croatian Science Foundation (HRZZ)

Dijana Dominis Prester supervised 9 student theses (master/batchelor/diploma), and published 107 refereed articles in journals (Current Contents). She is the coordinator for the module "Astrophyiscs and particle physics" of the physics master program at the University of Rijeka.

Selected articles (in last 5 years):

1. Cassan, A.; ...; Dominis Prester, D.; ... One or more bound planets per Milky Way star from microlensing observations. // Nature. 481 (2012) , 7380; 167-169

2. Aleksić, Jelena; ...; Dominis Prester, Dijana; ...; Ferenc, Daniel; ...; Godinović, Nikola; ...; Hrupec, Dario; ...; Lelas, Damir; ...; Puljak, Ivica; ...; Surić, Tihomir; ...; Šnidarić, Iva; ...; Terzić, Tomislav; ...; Zanin, R. Performance of the MAGIC stereo system obtained with Crab Nebula data. // Astroparticle physics. 35 (2012)

3. Aleksić, Jelena; ...; Dominis Prester, Dijana; ...; Ferenc, Daniel; ...; Godinović, Nikola; ...; Hrupec, Dario; ...; Lelas, Damir; ...; Puljak, Ivica; ...; Surić, Tihomir; ...; Šnidarić, Iva; ...; Terzić, Tomislav; ...; Ghisellini, G. MAGIC observations of the giant radio galaxy M 87 in a low-emission state between 2005 and 2007. // Astronomy and astrophysics. 544 (2012) ; A96-1-A96-8

4. Aleksić, Jelena; ...; Dominis Prester, Dijana; ...; Ferenc, Daniel; ...; Godinović, Nikola; ...; Hrupec, Dario; ...; Lelas, Damir; ...; Puljak, Ivica; ...; Surić, Tihomir; ...; Terzić, Tomislav; ...; Buson, S. MAGIC discovery of VHE Emission from the FSRQ PKS 1222+21. // The Astrophysical journal. 730 (2011) , L8; 1-6

5. Gould, A.; ...; Dominis Prester, D.,... Frequency of Solar-like ystems and of Ice and Gas Giants Beyond the Snow Line from High-magnification Microlensing Events in 2005-2008. // Astrophysical Journal. 720 (2010) , 2; 1073-1089

Abstract

Active galactic nuclei (AGN) are bright compact regions in the centres of galaxies, that emit radiation across the entire electromagnetic spectrum. They are believed to be powered by supermassive black holes (SMBH), which actively accrete matter. Some of that matter is ejected in the form of collimated jets of ultrarelativistic particles. Jets are sources of electromagnetic radiation of all wavelengths. A significant portion of energy radiated by AGN is emitted in the form of γ-rays. In addition, γ-rays are produced through physical processes different from the ones responsible for lower energy radiation. Therefore, in order to understand how jets are formed and how particles are accelerated to ultrarelativistic energies, it is important to understand the mechanisms and locations of γ-ray production within AGN.

To reach closer to this goal here we study the very high energy (VHE) γ-radiation from three sources belonging to different classes of AGN: M87 (radio galaxy), PKS 1222+21 (flat spectrum radio quasar) and H1722+119 (BL Lac object). For these sources we obtained VHE γ-ray spectra and light curves using the MAGIC ground-based Cherenkov telescopes. We used long term monitoring of M87 to evaluate the level of low emission state. We propose a structured jet "spine-layer" scenario to explain the emission from M87. It places the VHE γ-ray emission region in the vicinity of the SMBH, and suggests that, if viewed head on, the emission from M87 would resemble that from a typical BL Lac. PKS 1222+21 was first detected by the MAGIC telescopes. Very short variability timescale and absence of a cut-off in the VHE spectrum sets constraints on VHE γ-ray emission region, and on emission models. We performed a multiwavelength study using contemporaneous data, concluding that the γ-ray emission region is most probably located outside of the broad line region, and that it is possible to explain the emission using a simple one-zone emission scenario. H1722+119 is a source with unknown redshift, first detected by the MAGIC telescopes. We performed a multiwavelength study using contemporaneous data, and estimated the redshift of the source using γ-rays to $z = 0.4$.

As expected, different types of emission models are required to explain emission from different types of sources. However, we also find that the VHE γ-radiation originates in different locations in the sources we studied.

Key words: active galactic nuclei, blazars, gamma-rays, imaging atmospheric Cherenkov telescopes, M87, PKS 1222+21, 4C +21.35, H1722+119

Sažetak

Aktivne galaktičke jezgre (AGN) su sjajna i zbijena područja u središtima galaksija, koja zrače preko cijelog spektra elektromagnetskog zračenja. Smatra se da ih napajaju supermasivne crne rupe (SMBH) koje aktivno prikupljaju materiju. Dio te materije izbacuju u obliku kolimiranog mlaza ultrarelativističkih čestica. Mlazovi su izvori elektromagnetskog zračenja svih frekvencija. Značajan udio energije koju zrače AGN odnose γ-zrake. Uz to, γ-zrake nastaju u procesima različitima od onih u kojima nastaje zračenje nižih energija. Stoga, da bismo razumjeli mehanizam nastanka mlazova i ubrzavanja čestica do ultrarelativističkih energija, važno je da razumijemo način i područje nastanka γ-zraka.

Da bismo se primakli tom cilju, u ovom radu smo proučili γ-zračenje vrlo visokih energija (VHE) iz tri izvora, od kojih svaki spada u drugi razred AGN: M87 (radio galaksija), PKS 1222+21 (radio kvazar ravnog spektra) te H1722+119 (objekt tipa BL Lac). Spektre i svjetlosne krivulje ovih izvora dobili smo promatrajući ih zemaljskim Čerenkovljevim teleskopima MAGIC. Opažanjem M87 tijekom tri godine, odredili smo osnovnu razinu zračenja. Predložili smo strukturirani "kičma-plašt" model za opis zračenja, čime smo pokazali da je moguće objasniti emisiju iz područja u blizini SMBH u M87. VHE γ-zračenje iz PKS 1222+21 je otkriveno teleskopima MAGIC. Opažena promjenjivost toka zračenja na kratkim vremenskim skalama postavlja granicu na veličinu područja zračenja, te na modele emisije. Koristeći istovremene podatke, napravili smo studiju zračenja na različitim valnim duljinama i zaključili da se područje zračenja γ-zraka najvjerojatnije nalazi izvan područja širokih linija (BLR) te da se emisija može objasniti jednostavnim modelom zračenja iz jednog područja. H1722+119 je izvor nepoznatog crvenog pomaka. VHE γ-zračenje otkriveno je teleskopima MAGIC. Koristeći istovremene podatke, napravili smo studiju zračenja na različitim valnim duljinama te procijenili crveni pomak izvora na $z = 0,4$. Prema očekivanjima, potrebno je primijeniti različite teorijske modele da bismo opisali zračenje iz različitih vrsta izvora. Međutim, vidjeli smo i da VHE γ-zrake nastaju na različitim mjestima u proučavanim izvorima.

Ključne riječi: aktivne galaktičke jezgre, blazari, gama-zrake, atmosferski Čerenkovljevi teleskopi, M87, PKS 1222+21, 4C +21.35, H1722+119

Contents

List of figures

List of tables

Chapter 1

Introduction

Very high energy (VHE, $100\,\mathrm{GeV}$ – $10\,\mathrm{TeV}$) γ-ray astronomy is a relatively new field of research. Technological means to observe the most energetic processes in the universe have been accessible only in the past few decades. γ-rays only partially penetrate atmosphere, creating cascades of particles and depositing their energy. Ground based γ-ray observatories use atmosphere as a calorimeter, detecting faint flashes of light known as Cherenkov radiation. This methodology is very similar to the one used in elementary particle and nuclear experiments.

Active galactic nuclei (AGN) are bright compact regions in the centres of galaxies emit radiation across the entire electromagnetic spectrum. They are believed to be powered by accretion of matter by supermassive black holes (SMBH), that exist in centre of every massive galaxy. Some AGN form collimated jets through which accreted matter is ejected at ultrarelativistic speeds. AGN may, thus, also be considered giant natural particle accelerators[1].

For these reasons the study of AGN in γ-ray energy band is considered a hybrid between astrophysics and elementary particle physics. This new field is known as astroparticle physics.

---

[1]There are indications of protons and heavier atomic nuclei being accelerated to energies above $5 \times 10^{19}\,\mathrm{eV}$ in jets of AGN (see e.g. [1] and references therein).

The most widely accepted description of AGN structure and physical mechanisms is usually referred to as the AGN paradigm [2]. According to this description, SMBH in galactic centres actively accrete matter, which forms a thin accretion disc. Clouds of gas at approximately $(1.6 - 6.7) \times 10^{14}$ m from the SMBH have to orbit the black hole very rapidly in order to maintain their distance, while the clouds of gas further away, at $10^{17} - 10^{19}$ m from the SMBH rotate at lower rate [3]. Nucleus is surrounded by a torus of dust. Approximately 10% of AGN form collimated jets of matter at their poles [4]. The accreted material is propelled through the jets at relativistic speeds. The matter in the accretion disc is ionised, so it is a source of optical and UV continuous thermal radiation. Clouds of gas, that rotate around the nucleus, absorb and reprocess radiation coming from the accretion disk and emit it in the optical and the UV band. The emission lines visible in the spectrum are broadened because of the Doppler effect. The effect is larger for the faster rotating gas clouds, so they are called broad (emission) line region (BLR), while the clouds further away from the nucleus are called the narrow (emission) line region (NLR). Torus is opaque and it obscures the view of the nucleus, if observed under higher angles. It itself is a source of continuous thermal radiation in IR band. Jets are sources of continuous non-thermal radiation of all wavelengths, from radio to VHE γ-rays.

The AGN paradigm will be presented in more details in Section 1.1.2. Although accepted as a broad description of AGN, there are many open questions that we need to answer in order to fully understand the nature of AGN. The most fundamental question is how is the gravitational and rotational energy of SMBH transferred to particles to form jets? To put it more specifically, through which mechanisms are particles accelerated to ultrarelativistic energies, and how are they collimated to form narrow jets? Studying γ-ray emission from AGN carries the potential to shed light on these questions. γ-rays constitute a significant part of the electromagnetic radiation from AGN. Even more important is the fact that γ-rays are produced through inverse Compton scattering, particle-antiparticle annihilation, or particle decay, which are fundamentally different physical processes compared to synchrotron or thermal emission, which is responsible

for electromagnetic radiation in lower energy bands. Therefore, through observations of AGN in γ-ray energy band we access information that is not available in electromagnetic radiation of lower energies. The most important questions regarding the production of γ-rays in AGN are discussed in Section 1.1.5.

All of the AGN that emit VHE γ-rays have jets, and as we shall see in Section 1.1.3 the majority of them are blazars, meaning that the angles between the axes of their jets and our line of sight is up to only a few degrees. To-date only four non-blazar AGN were detected in the VHE γ-ray band (M87 [5], Centaurus A [6], NGC 1275 [7], and IC 310 [8]), and they are classified as radio galaxies. Blazars are subdivided according to the characteristics of their spectra into two classes: BL Lacs and flat spectrum radio quasars (FSRQ). We will see in Section 1.1.3 that members of these two classes are not equally distributed according to the distance to the Earth, FSRQs being more common at larger distances. As a result only three FSRQs have been detected in the VHE γ-ray band so far[2].

The first relativistic jet was discovered by H. D. Curtis [9] in 1918. It is propelled by the AGN in a radio galaxy Messier 87 (M87). However, the first AGN detected in the VHE γ-ray band was a blazar Markarian 421, detected by the Whipple telescope in 1992 [10]. The VHE γ-ray emission from M87 was first detected by the HEGRA collaboration in 2003 [5]. The discovery was confirmed by the H.E.S.S. collaboration in 2006 [11]. It was the first detection of VHE γ-rays from a non-blazar AGN.

In this study, we analyse the VHE γ-ray emission from three sources observed with MAGIC telescopes. The main purpose was to understand the similarities and differences between VHE γ-ray emission in different classes of AGN. Therefore, we have chosen one source from each of the AGN classes mentioned above: a radio galaxy M87, a FSRQ PKS 1222+21, and a BL Lac H1722+119, described in more detail below. We study characteristics of their VHE γ-ray emission, and include also observations performed at lower energy bands.

---

[2]This is a consequence of attenuation of VHE γ-ray flux by the extragalactic background light as explained in Section 1.2.6

Messier 87 (M87) is a giant radio galaxy, and the closest AGN to the Earth at a distance of 16.7 ± 0.2 Mpc [12]. It is the centre of the Virgo cluster, and of our local universe. Due to its proximity, M87 offers an opportunity to study the jet structure in details. Other studies of M87 in the VHE γ-ray band ([11, 13, 14, 15, 16], etc.) are focused on studying variability of the source. Given the sparsity of γ-rays, episodes of pronounced variability and enhanced emission are very practical because a large amount of data can be collected in a shorter observation time. Even more interesting is the fact that variability can be used to set constraints on the size of the emission region (see Section 1.1.4), or to identify γ-ray emission regions by comparing γ-ray light curves with emission in lower energy bands[3]. Nevertheless, we have chosen to study the source in a stable quiescent state. Our goal was to understand whether there is a base line emission that is stable over a long period of time. M87 was a good candidate for this kind of study, because it was (and still is) regularly observed during several years. A study based on contemporaneous observations by all three currently active Cherenkov telescopes (H.E.S.S., MAGIC and VERITAS) and VLBA at 43 GHz in 2007 and 2008 [14] suggested that the VHE γ-ray emitting region is located in the nucleus of M87[4]. Therfore, in our study, we tried to find a scenario that would explain the observed radiation with the emission region located within the nucleus. We suggest a structured jet model that was developed by Tavecchio and Ghisellini [17].

PKS 1222+21 is a FSRQ at a redshift of $z = 0.432$ [18], and only third object of this class detected in the VHE γ-ray band so far. At the time of discovery, it was the second most distant source of the VHE γ-radiation with a well known redshift. MAGIC measured flux variability on the order of 10 minutes, which indicates a very compact emission region (see expression 1.13). In addition, the VHE γ-ray spectrum shows no sign of a cut-off at least up to 130 GeV, which suggests that the emission region is outside of the BLR. This result is quite different from the case of M87. We also collected data from observations in lower frequency bands and divided them in three separate subsamples

---

[3]As we shall see in Sections 1.2.4 and 2.1.3 the angular resolutions of γ-ray detectors are too small to determine the position of the γ-ray emitting region by direct observation.

[4]in this case a region within 170 Schwarzschild radii from the SMBH

according to the source activity. We propose an emission scenario that explains the fast variability and lack of cut-off in the VHE γ-ray band with the γ-ray emission region located outside of the BLR.

H1722+119 is classified as a BL Lac object [19, 20]. Very little is known about this source. Linford et al. [21] (source name: F17250+1151) described it as a compact source with a short jet. The redshift is not determined. In the most recent study Farina et al. (priv. comm.) were unable to detect the host galaxy in the optical band. They set a lower limit on redshift at 0.4. The VHE γ-ray emission was first detected by the MAGIC telescopes in 2013 [22]. We combined results from the observations performed with the MAGIC telescopes with data from quasi simultaneous observations in lower frequency bands to study multiwavelength characteristics of the source. We used MAGIC and *Fermi*-LAT data to estimate the most likely redshift of the source, pointing out another application for observations in γ-rays.

It should be noted that these three campaigns were rather different considering the observation strategy. While M87 was monitored over a period of three years, the other two campaigns were significantly shorter. Also M87 was already a confirmed source of VHE γ-rays at the time the analysis was performed, while no VHE γ-ray signal was detected from PKS 1222+21 or H1722+119 before. Therefore, the PKS 1222+21 and H1722+119 data had to be analysed promptly after each observation. Still, these two sources required somewhat different approaches. In case of H1722+119, the flux was quite constant, so each observation contributed until the statistical significance was high enough to claim the discovery. PKS 1222+21, on the other hand, had a very unstable γ-ray flux during the campaign. After first several observations it was apparent that the signal was below the telescope sensitivity, unless it was in a strong flaring state. Although the data analyses for these sources were the same in principal, the differences we just mentioned required the analyser to adapt to specific tasks. Even more so considering there were time lapses of few years between campaigns, during which the instrument was significantly upgraded (see Table 2.1), requiring modifications of software analysis.

In the rest of this chapter we will cover our present understanding of AGN and introduce the field of γ-ray astronomy. The VHE γ-ray observations used in this study were performed using the MAGIC telescopes. The experiment, observation techniques, and data analysis are described in Chapter 2. Characterisation of VHE γ-radiation from M87, PKS 1222+21 and H1722+119 is presented in Chapters 3, 4 and 5, respectively. Our conclusions are summarised in Chapter 6.

1.1 Active galactic nuclei

Active galactic nuclei are accreting supermassive black holes (SMBH) in the centres of galaxies that emit radiation across the entire electromagnetic spectrum. Although some of the radiation can be explained as thermal radiation, there is an obvious non-thermal component in the spectrum. The origin of the non-thermal radiation is still not unambiguously explained. Several different groups of theoretical models offer possible explanations to the emission mechanisms. In this section we will cover our present understanding of AGN, and state some open problems.

1.1.1 Supermassive black holes

Some AGN are so bright that they outshine the entire galaxy in which they reside. Considering also that the emission region is quite compact, we believe that the observed radiation is a consequence of accretion of matter by SMBH. The geometry of empty spacetime around a spherical mass is described by the Schwarzschild metric [23]

$$\mathrm{d}s^2 = \left(1 - \frac{r_\mathrm{S}}{r}\right)c^2\mathrm{d}t^2 - \left(1 - \frac{r_\mathrm{S}}{r}\right)^{-1}\mathrm{d}r^2 - r^2\left(\mathrm{d}\theta^2 + \sin^2\theta\mathrm{d}\phi^2\right), \qquad (1.1)$$

where c is the speed of light in vacuum, and r_S is the Schwarzschild radius given as

$$r_\mathrm{S} = \frac{2GM}{c^2}. \qquad (1.2)$$

Here G is the gravitational constant and M is the mass with the centre of gravity at $r = 0$. We see that the Schwarzschild metric has singularities at $r = 0$ and $r = r_{\mathrm{S}}$. Unlike $r = 0$, which is a true singularity, $r = r_{\mathrm{S}}$ is a consequence of our choice of coordinate system. Nevertheless, a spherical surface located at r_{S} from the centre of gravity of the mass M has some interesting properties. If r_{S} is reachable, that is if the physical radius in which the mass M is contained is smaller than r_{S}, a black hole (BH) will form. A space-time curvature at region bounded by r_{S} is such that a photon from that region will never cross the $r = r_{\mathrm{S}}$ surface in a finite time, and events occurring within that region will not affect the region outside of the $r = r_{\mathrm{S}}$ surface. For that reason the $r = r_{\mathrm{S}}$ surface is called an *event horizon.*

BHs can be divided in several classes according to their mass: micro black holes, stellar mass black holes, intermediate mass black holes and SMBHs.

It is a commonly accepted belief that a centre of every massive galaxy harbours a SMBH. The smallest SMBH known so far is the one in the centre of late-type bulgeless disc galaxy NGC 4178 [24] with the estimated mass of $M = 2.0^{+8.2}_{-1.6} \times 10^5 \, M_\odot$ (obtained from X-ray and radio luminosity; the possible range of mass is $\sim 10^4 - 10^5 \, M_\odot$), where $M_\odot$ denotes the solar mass i.e. $(1.98855 \pm 0.00025) \times 10^{30} \, \mathrm{kg}$. The largest SMBH found so far is located in a giant elliptical galaxy NGC 4889. The mass is estimated to $(0.55 - 3.7) \times 10^{10} \, M_\odot$, with the best fit of $2.1 \times 10^{10} \, M_\odot$ [25]. From equation (1.2), we can easily calculate that the Schwarzschild radius for this SMBH is $6.2 \times 10^{13} \, \mathrm{m}$, which is over 400 astronomical units. Detections of binary systems of two SMBHs in the centres of galaxies have also been reported. The elliptical radio galaxy 4C +37.11 (Galaxy 0402+379) [26] is the most interesting case because the two SMBHs are of comparable masses with the shortest projected separation between them detected so far of only $7.3 \, \mathrm{pc}$ ($24 \, \mathrm{ly}$). The system has a combined mass of $\sim 1.5 \times 10^8 \, M_\odot$, with the orbital period of $\sim 1.5 \times 10^5 \, \mathrm{yr}$. It is believed that systems like this one resulted from a collision of two massive galaxies, each of which hosted a SMBH in the centre.

A SMBH in the centre of Milky Way galaxy is positionally consistent with a radio source Sagittarius A* [27], and has a mass of $(4.31 \pm 0.36) \times 10^6 \, M_\odot$ (assuming the Earth's

distance to the galactic centre to be $R_0 = 8.33 \, \text{kpc}$). The largest SMBH in the Milky Way's neighbourhood appears to be that of giant elliptical galaxy Messier 87 (M87), with the mass of $(6.4 \pm 0.5) \times 10^9 \, M_\odot$ [28]. SMBHs exhibit a correlation between their masses and properties of the host galaxy bulge component [29], e.g. the mass of the SMBH is typically 0.1% of the stellar mass of the host galaxy's bulge [30, 31]. This leads to a conclusion that the evolutions of SMBHs and their host galaxies are interconnected.

However, there are examples of large deviations from this behaviour. Some recent discoveries may demand modifications of galaxy — SMBH co-evolution models [32, 33]. The most prominent example is a compact, lenticular galaxy NGC 1277. The entire galaxy has a mass of $1.2 \times 10^{11} \, M_\odot$, while the SMBH in its centre has a mass of $1.7 \times 10^{10} \, M_\odot$, which constitutes incredible 59% of the galaxy's bulge mass [34]. A SMBH has also been discovered in the centre of a dwarf galaxy. A peculiar case of an irregular starburst galaxy Henize 2-10 [35] shows that even galaxies without a bulge can host a SMBH. Moreover, this example could imply that the SMBH formed prior to the galactic bulges. Similar to NGC 1277, the mass of the SMBH in Henize 2-10 ($\sim 2 \times 10^6 \, M_\odot$) is quite large compared to the mass of the host galaxy ($3.7 \times 10^9 \, M_\odot$). Interesting as the case of Henize 2-10 my be, it is still too early to extend the conjecture of every galaxy harbouring a SMBH to dwarf galaxies, e.g. as far as we know there is no SMBH in a satellite galaxy of the Milky Way, the Large Magellanic Cloud.

Using equation (1.2), we can see that the average density inside of a BH decreases as the mass of the BH increases

$$\rho = \frac{M}{\frac{4\pi}{3} r_{\text{S}}^3} = \frac{3c^6}{32\pi G^3 M^2}, \tag{1.3}$$

so larger BHs will have lower average density. It is interesting to note that the average density inside of a BH of mass greater than $1.36 \times 10^8 \, M_\odot$ will be less than the density of water ($10^3 \, \text{kg/m}^3$).

The Schwarzschild metric is a solution to the Einstein field equations, obtained assuming that the mass is stationary and electrically neutral. Although numerical simulations

show that stationary black holes can form jets, the outflow is stronger for rotating black holes [36]. The gravitational field outside of a rotating uncharged axially-symmetric black hole is described by the Kerr metric [37, 38]

$$\mathrm{d}s^2 = \left(1 - \frac{r_\mathrm{S}r}{\rho^2}\right)c^2\mathrm{d}t^2 - \frac{\rho^2}{\Delta}\mathrm{d}r^2 - \rho^2\mathrm{d}\theta^2 -$$
$$- \left(r^2 + \alpha^2 + \frac{r_\mathrm{S}r\alpha^2}{\rho^2}\sin^2\theta\right)\sin^2\theta\mathrm{d}\phi^2 + \frac{2r_\mathrm{S}r\alpha\sin^2\theta}{\rho^2}c\mathrm{d}t\mathrm{d}\phi, \tag{1.4}$$

with substitutes

$$\alpha \equiv \frac{J}{Mc}, \tag{1.5}$$

$$\rho^2 \equiv r^2 + \alpha^2\cos^2\theta, \tag{1.6}$$

$$\Delta \equiv r^2 - r_\mathrm{S}r + \alpha^2. \tag{1.7}$$

r_S is the Schwarzschild radius given in expression (1.2), and J denotes the angular momentum of a black hole. The amount of angular momentum of a black hole is usually expressed in a convenient dimensionless parameter

$$a = \frac{cJ}{GM^2}. \tag{1.8}$$

For a stationary BH $a = 0$, and the Kerr metric becomes Schwarzschild metric. A maximally rotating BH has $a = 1$. The radius of the event horizon will now include a factor dependant on the spin of the BH

$$r_\mathrm{in} = \frac{1}{2}r_\mathrm{S}\left(1 + \sqrt{1 - a^2}\right). \tag{1.9}$$

Another physically important surface is determined by the sign change of the purely temporal component of the metric

$$r_\mathrm{out} = \frac{1}{2}r_\mathrm{S}\left(1 + \sqrt{1 - a^2\cos^2\theta}\right). \tag{1.10}$$

The space between surfaces determined by r_{in} and r_{out} is called the *ergosphere*. A particle within the ergosphere can cross the event horizon and fall into the BH, but it can also leave the ergosphere by crossing the surface defined by r_{out}. But, due to relativistic effects, while inside the ergosphere, it has to rotate in the same direction of the central mass.

Using radio interferometry observations at 1.3 mm wavelength, the spin of the SMBH in giant elliptical galaxy Messier 87 (M87) was set to $a > 0.2$ [39]. In the most general case, a BH has some net electric charge, but it is unlikely for an astrophysical BH to have enough charge to be dynamically important.

1.1.2   AGN paradigm

Around 1% of SMBHs actively accrete matter. According to the most widely accepted description of AGN, the so-called AGN paradigm [2], actively accreting SMBH are engines that power AGN. Matter falling into the black hole usually forms a thin disc, called an accretion disc. An accretion disc is defined by its inner (r_{in}) and outer radii (r_{out}). r_{in} is the innermost stable orbit, and it depends on the rotation of the BH. For non-rotating BHs $r_{\text{in}} = 6r_{\text{g}}$, where r_{g} is the gravitational radius, equal to the 1/2 of the Schwarzschild radius. r_{g} is obtained by equating the centrifugal force of a particle rotating at the speed of light around a BH, with the gravitational force. For maximally rotating Kerr BHs $r_{\text{in}} = (1 - 1.2)r_{\text{g}}$. r_{out} is less strictly determined. Once the self gravity of the disc in the vertical direction becomes greater than the vertical component of the central gravitational filed, the matter will start to form small clumps, and will no longer keep the form of a thin disc. Due to the intense gravitational gradient within the disc, a strong friction occurs between its layers, resulting in high temperatures and ionisation of matter. Accretion disc is a source of thermal electromagnetic radiation. Most of the radiation is emitted from the region around $10r_{\text{g}}$ (see [40] for a review). The peak of the spectral energy distribution is usually in the optical/UV energy band, and is called the *big blue bump*. The accretion disc is enclosed in a spherical shell of

HE electrons, the so-called *corona*. Electrons upscatter the radiation from the accretion disc through inverse Compton to produce X-rays [41]. The nucleus is surrounded by gas clouds distributed in a spherical shell at distance of around $(1.6 - 6.7) \times 10^{14}$ m. Atoms in those clouds absorb radiation from the accretion disc and emit lines in the optical and the UV band. Because of the vicinity of the clouds to the black hole, they revolve around it at velocities of $(1 - 25) \times 10^3$ km/s. As a consequence their emission is Doppler shifted in a wide range, hence Broad (emission) Line Region (BLR). The number density of the gas in the BLR is $> 10^9$ cm^{-3}, with the total mass estimated to $10^3 - 10^4 \, M_\odot$ (see [3] for a review). The gas clouds at distances of few parsec to few hundred parsec $(10^{17} - 10^{19})$ m from the black hole orbit at lower velocities (< 500) km/s so their emission lines are much narrower, hence Narrow Line Region (NLR). The gas in the NLR has lower density ($\approx 10^3$ cm^{-3}). The black hole, accretion disc and BLR are wrapped in a large thick torus of dust, located at around 1 parsec from the black hole, and can extend to up to hundreds of parsecs [42]. The torus is opaque to any form of electromagnetic radiation except radio, and it obscures the nucleus if viewed from a large angle. It itself is a source of IR thermal radiation. Approximately 10% of AGN eject matter through relativistic jets [4].

The torus is thick and dense enough to prevent any electromagnetic radiation passing through it. Therefore what the observer sees depends on the angle under which the AGN is being observed. Since the AGN are classified according to the emission we observe, how we classify each AGN depends in great respect on the angle its central axis spans with the direction to Earth. AGN structure is schematically illustrated in Figure 1.1, and the classification of AGN is summarised in Figure 1.2.

1.1.3   Relativistic jet

As already mentioned, approximately 10% of AGN propel matter away from the nucleus forming a conical collimated jet of relativistic matter in the direction of the AGN's axis. Jets are sources of electromagnetic radiation of all wavelengths from radio to γ-rays.
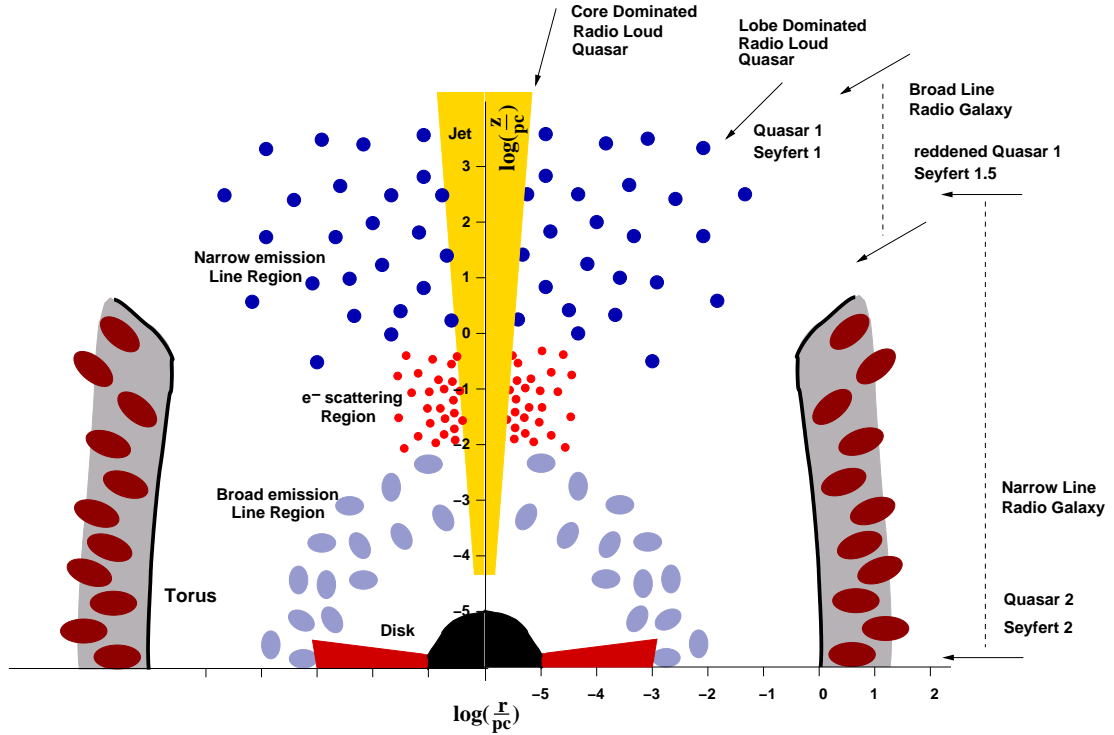
Figure 1.1 Schematic illustration of AGN. The usual components are indicated, as well as the classes of AGN depending on the viewing angle. The scale is logarithmic. However, some shapes are inconsistent with the scale in order to make them visually more comprehensible (e.g. the gas cloud in the BLR should look like a square with round corners, the base corner of conical jet should be closer to 90°). Arrows indicate the direction of the observation. Next to each arrow a respective class of AGN is indicated. Adopted from [43].

The emitted radiation is clearly of non thermal origin. A jet forms in the vicinity of the black hole and extends up to megaparsec distances from the nucleus (e.g. [45]). In some jets, one or several brighter spots are observed, called *knots* (e.g. [46]). These knots are often characterised by apparent superluminal motion, which is the result of the combination of the velocity of the emission region, and the viewing angle. Because of relativistic speeds, knots "chase" the light they emit. If the angle between the jet axis and the line of sight is small, two emitted signals will reach observer in shorter time interval than the interval between emission, and that will make the observed knot
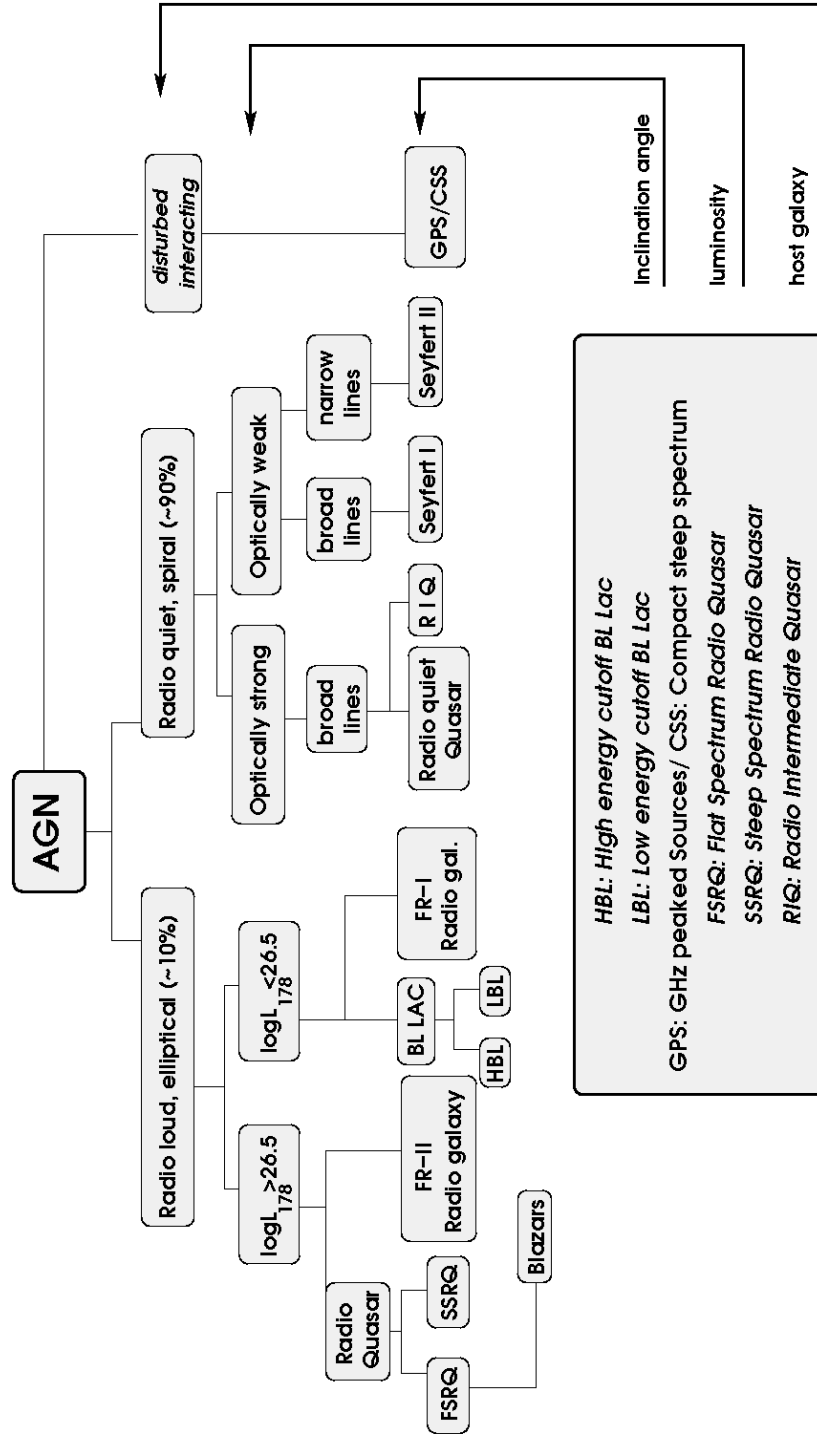
Figure 1.2 AGN classification scheme based on host galaxy (radio loudness), optical luminosity, and inclination. Adopted from [44].

appear to be travelling faster than light. Some jets in the end extend to double, roughly ellipsoidal structures called lobes (e.g. [47]). In AGN whose inclination angle to our line of site is large enough, one can see jets emerging on both sides of the galaxy plane. Although it has not been proven, it is usually assumed that this is the case with all AGN.

We still lack a comprehensive understanding of the physics of relativistic jets, including the process of jet formation. Blandford-Znajek model [48] is the most widely accepted one. It states that the vacuum surrounding the rotating BH will be unstable, which would lead to the electromagnetic field in the vicinity of the event horizon becoming approximately force-free. They find that energy and angular momentum of rotating BH can be extracted by a purely electromagnetic mechanism. According to Blandford-Payne model [49], the angular momentum is magnetically removed from the accretion disc and transferred to the jet. Another puzzling characteristic of relativistic jets is that they stay collimated over huge distances. Possible explanations are that jets are either magnetically or kinetic energy dominated (see e.g. [50]). In the former case the jet is magnetically driven and self-collimated by the toroidal component of the magnetic field. If the jet is kinetic energy dominated, the matter propagates in a ballistic manner and stays grouped as long as it is not perturbed.

The first relativistic jet ever discovered was the one emanating from the centre of the giant radio galaxy M87 [9]. Because of its proximity to Earth, M87 was extensively observed and studied. The details on M87 and the AGN it harbours will be discussed in Chapter 3. For now it is interesting to note that all of the above mentioned properties (knots, lobes, indication of a counter-jet) have been discovered in its jet, making M87 one of the favourite laboratories for studying AGN.

So far γ-radiation has only been observed from AGN with jets, so we will restrict our study on that category of AGN.

Most of the AGN that are confirmed sources of VHE γ-rays are *blazars* (see Table 6.1), which means their jet's axes close an angle of up to few degrees with the line of sight.
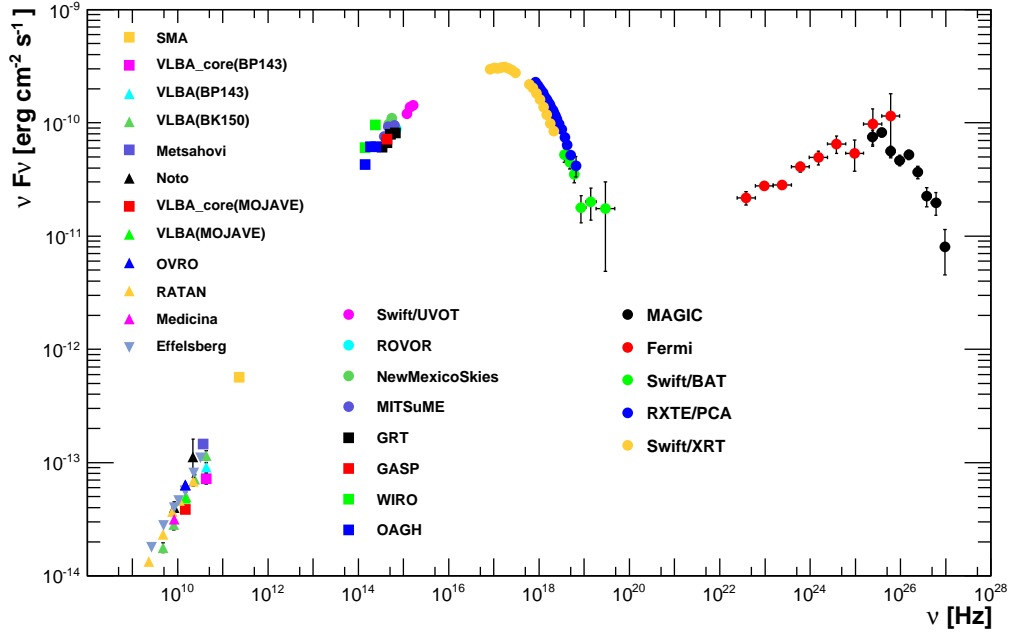
Figure 1.3 SED of Markarian 421, a typical and one of the brightest blazars [51].

The spectral energy distribution (SED) of these sources is characterised by two peaks: a lower-energy peak in optical to X-ray region and a higher-energy peak in γ-ray region. This can be seen in Figure 1.3, which shows the SED of a typical blazar Markarian 421. Blazars are divided in two classes according to the characteristics of their emission: flat spectrum radio quasars (FSRQ) and BL Lacertae objects (BL Lac). FSRQs are known to have prominent broad and narrow emission lines, in addition to strong optical and X-ray continuum emission. Quite common feature is high and wide peak in the optical-UV region associated with thermal emission from the accretion disc. BL Lacs, on the other hand show very narrow line emission if any at all. They are characterised by a strong linear polarisation in optical and radio range. With respect to the position of the first peak in the SED, Nieppola et al. [52] subdivide BL Lacs in low-energy-peaked BL Lacs (LBL; $\log \nu_s < 14.5$), intermediate-energy-peaked BL Lacs (IBL; $14.5 < \log \nu_s < 16.5$), and high-energy-peaked BL Lacs (HBL; $\log \nu_s > 16.5$). In Figure 1.4 we can see that FSRQs active in HE γ-rays are more common at redshifts 1 and higher, while BL Lacs are grouped around $z = 0.2$. For a further discussion on differences and similarities
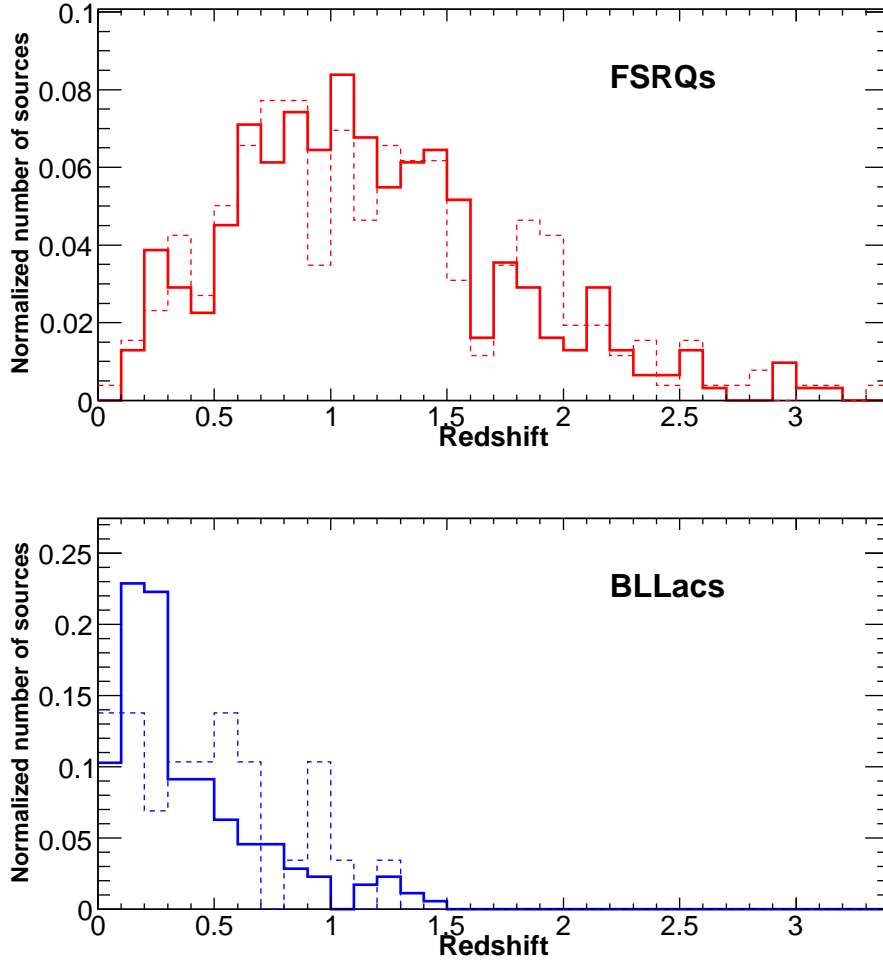
Figure 1.4 Distribution of FSRQs (top) and BL Lacs (bottom) according to the redshift. Solid lines represent blazars in the second *Fermi*-LAT catalog of AGN, and dashed the complete 5 year sample of *WMAP*. Adopted from [55].

between FSRQs and BL Lacs see e.g. [53, 54].

Only four non-blazar AGN have been detected in VHE γ-ray band so far: M87 [5], Centaurus A [6], NGC 1275 [7], and IC 310 [8]. They are all classified as radio galaxies (RG), the type of AGN very luminous in radio band with huge input of energy to intergalactic medium ($10^{60} - 10^{61}$ erg [56]). Their axes are declined from our line of sight, so jets on both sides of galaxy are often visible.

1.1.4   Electromagnetic radiation from AGN

What is the origin of the observed radiation? In the simplest approach, emission region is modelled as a spherical blob of plasma propagating down the jet with bulk Lorentz factor $\Gamma = (1 - \beta^2)^{-1/2}$, where β is the velocity of the blob in units of the speed of light ($\beta = v/c$). These models are usually referred to as single zone models (see e.g. [57]). If the jet closes angle θ with our line of sight, we can define the Doppler factor

$$\delta = [\Gamma(1 - \beta \cos \theta)]^{-1}. \tag{1.11}$$

Due to relativistic effects, energies of observed photons will be blueshifted by a factor of δ and the variability time scales shortened by the same factor, while the observed bolometric flux will be δ^4 times higher [58]. The blob is also filled with magnetic fields, so the moving charges within it will emit synchrotron radiation. There is a general consensus that the lower-energy peak in the SED is a result of ultrarelativistic electrons emitting synchrotron radiation. In case of FSRQs, the synchrotron component will be present, but dominated by the thermal radiation from the accretion disc and the dust torus. A debate on the origin of the emission in X-ray through γ-ray bands, on the other hand, is still not settled. The two fundamentally different approaches are usually referred to as *leptonic* and *hadronic* emission models. The main difference comes from the question whether protons in AGN jets are accelerated to high enough energies to contribute significantly to observed emission.

Leptonic emission models

According to leptonic models, X-rays and γ-rays are the result of inverse Compton scattering of low energy *seed* photons up to TeV energies, by ultrarelativistic electrons. If the seed photons originate from synchrotron radiation of these same electrons (as is the case with BL Lacs), we talk about synchrotron self Compton (SSC) models (see e.g. [57, 59]). External Compton (EC) models (see e.g. [60]), on the other hand, are more

suited to the description of FSRQs, because seed photons are mostly thermally radiated from the BLR, the dust torus and the accretion disc, with some contribution from synchrotron radiation. The spectral distribution of electrons in the blob is described by a broken power-law (PL)

$$N(\gamma) = \begin{cases} n_0 \gamma^{-p_1}, & \gamma < \gamma_{\mathrm{br}} \\ n_0 \gamma_{\mathrm{br}}^{p_2 - p_1} \gamma^{-p_2}, & \gamma > \gamma_{\mathrm{br}}, \end{cases} \tag{1.12}$$

where n_0 is the normalisation factor of the number density of electrons, and γ_{br} the Lorentz factor at the spectral break. p_1 and p_2 are spectral slopes below and above the break, respectively. The break in the power-law comes from the fact that above certain energy electrons start to rapidly lose energy (cool off) through synchrotron radiation. The slope of the spectrum after the break is a balance between acceleration of electrons in the jet and cooling. The motivation for choosing the power-law in the first place comes from observations. A power-law distribution of ultrarelativistic electrons will produce a power-law distributed synchrotron radiation (see Section 1.2.2), and that is what we measure in the data. The size of the blob is usually estimated to $\sim 10^{16}$ cm, and can be constrained by the duration of any observed variability of the flux. Because of the causality, the radius of the blob has to be less than the distance the light can travel for the duration of the variability (t_{var})

$$R \leq c t_{\mathrm{var}} \frac{\delta}{1 + z}. \tag{1.13}$$

Seed photons are inverse Compton scattered on the same population of electrons to produce γ-rays. Because of the power-law spectral distribution of electrons, the scattered photons will also be power-law distributed (see Section 1.2.1). In SSC models there will be electrons with energies below and above the break, and the same will hold for synchrotron emitted photons. So there will be four combinations contributing to the inverse Compton spectrum. A cut-off in the γ-ray spectrum is possible in case inverse Compton scattering enters the Klein-Nishina regime (see Section 1.2.1). EC models

usually have additional parameters that describe the source of thermal radiation, such as the accretion disc, or dust torus luminosity, as well as the position of the γ-ray emission region. If the emission region is located inside the BLR, the photons from the accretion disc will be reflected from the gas particles in the BLR and towards the emission region. In that case, a cut-off in the VHE band is expected. VHE γ-rays annihilate with photons emitted from the gas clouds of the BLR to create electron-positron pairs, which attenuates the flux and manifests as a cut-off in the VHE part of the spectrum. In case the emission region is located outside the BLR, the source of seed photons is the dust torus, and we expect no cut-off in the VHE part of the spectrum.

The total jet power in the host galaxy reference frame is

$$P_{\text{j}} = 2\pi R^2 \beta \Gamma^2 U_{\text{tot}} = P_{\text{j,par}} + P_{\text{j,B}}, \tag{1.14}$$

where U_{tot} is the total energy density in the jet [61, 62, 59]. Total jet power is the sum of particle ($P_{\text{j,par}}$) and the magnetic field contribution ($P_{\text{j,B}}$). The factor 2 accounts for two-sided jet. The energy density of electrons is

$$U_{\text{e}} = \int_{\gamma_{\text{min}}}^{\gamma_{\text{max}}} \text{d}\gamma \gamma N(\gamma), \tag{1.15}$$

where $N(\gamma)$ is given in relation (1.12) while the energy density of the magnetic field is $U_{\text{B}} = B^2/8\pi$. If only synchrotron emission is present, the jet power will be minimised under the assumption of equipartition of energy in the jet, $P_{\text{j,par}} \approx P_{\text{j,B}}$. However, a contribution from the inverse Compton scattering will in general imply a different energy density in electrons compared to the magnetic field energy density [60].

For some sources, the simplest one-zone models do not provide a satisfactory fit to the observation data, so more complex models are being devised, such as two zone models (e.g. [63]), spine-layer model [64], jets within jets model [65], decelerating jet model [66] etc.

Hadronic emission models

Hadronic models have similar configuration to leptonic, that is the emission region is imagined as a spherical blob of ultrarelativistic particles. Here, however, electrons mostly contribute to emission at lower energies with synchrotron radiation, while the higher-energy peak is a result of several processes. Protons that have energies above the threshold for photo-pion production will interact with soft photons and produce pions through

$$\gamma + p \rightarrow n + \pi^+,$$
$$\gamma + p \rightarrow p + \pi^0.$$

Charged pions will decay to muons, electrons and corresponding neutrinos

$$\pi^+ \rightarrow \nu_\mu + \mu^+ \rightarrow \nu_\mu + \nu_\mu + \nu_e + e^+,$$

while neutral pions will decay to two γ-rays. Neutrons will decay through β^- decay to protons, electrons, and electron anti-neutrinos. Further, protons and secondary charged particles ($\pi^\pm$, $\mu^\pm$) will synchrotron radiate γ-rays. Additional γ-rays will come from inverse Compton scattering of soft photons on secondary charged particles. Photo-pion production becomes important if protons are accelerated to energies $\gtrsim 10^{19}$ eV.

A nice overview of emission models can be found in [67] and references therein.

Hadronic models require very strong magnetic fields of few tens of Gauss (~ 2 orders of magnitude higher than in leptonic models) in order to maintain ultrarelativistic protons within the emitting region (blob). Apart from that, hadronic models imply a high flux of neutrinos. It is expected then that a higher flux of neutrinos would be observed simultaneously to observations of higher flux of γ-rays. This has not been observed so far. According to cooperation agreement between collaborations MAGIC and IceCube South Pole neutrino observatory[5], MAGIC receives alerts from IceCube about enhanced neutrino fluxes, believed to originate in AGN. On two occasions, MAGIC observed given

---

[5]icecube.wisc.edu

AGN after such alerts, but no enhanced γ-ray signal was measured. Leptonic models do not suffer from these problems, and in general seem to be more successful in modelling observation data.

Explaining the emission from AGN

How do we go about finding physical interpretation for the observed emission from a given source? As explained in the previous two sections, particular models are used for different types of sources. The simplest class of models are one-zone SSC models. They have two peaks in the SED. The higher energy peak in γ-ray band is associated with inverse Compton scattering of seed photons on ultrarelativistic electrons. The seed photons are the result of synchrotron radiation of the same ultrarelativistic electrons, and they account for the lower energy peak in optical through X-ray band. These models are usually applied to BL Lacs, because BL Lacs show no indication of any other kind of emission. Unlike BL Lacs, spectral energy distributions of FSRQs show additional contribution in optical and UV band other than synchrotron. This contribution is consistent with being due to the thermal radiation from the accretion disc. Additionally, thermal contribution from the dust torus might be prominent in the IR band. Obviously, one-zone SSC models are not appropriate for explaining radiation from FSRQs. The physical interpretation of SSC models is not in agreement with the interpretation of observed emission, and the discrepancy between a theoretical model and the observed data would be obvious and large. When it comes to FSRQs, EC models are usually applied, because we expect that a significant part of seed photons come from the accretion disc, the BLR, or the dust torus.

When choosing a model, the tendency is to use model with the least number of components. For example, we cannot justify using an EC model or a two-zone SSC model if there are no additional peaks in the SED that would suggest a contribution either from thermal radiation, or another IC scattering zone. Additionally, the simpler the model is, the less parameters it has. One-zone SSC models are usually described by nine free

parameters (see e.g. [57, 68]). In addition to n_0 (the electron number density normalisation factor), γ_{br} (the Lorentz factor at the spectral break), p_1 and p_2 (spectral slopes below and above the break) mentioned above, minimal and maximal Lorentz factor of the electron population γ_{min} and γ_{max} are defined to fully specify the electron energy distribution. The other three parameters are the radius of the emission region R, the Doppler factor δ and the magnetic field intensity B.

Once we have selected a model that is physically compatible with the observations, we choose a set of model parameters that best fit the data. Fitting is usually done by eye. It is important to realise that out goal is to propose a physical interpretation for the observed emission. This in no way excludes other possible scenarios, but shows that a particular explanation is possible. Since we are not performing any minimisation method, we cannot quantify the goodness of the fit, so our choice of applied model and parameter values is justified by the physical scenario that we choose to describe the processes in the observed source. There are several reasons we face when trying to describe the observed emission with a theoretical model. First, these models are still somewhat unrefined and there is room for fine tuning. For example, the emission region, although usually referred to as a blob, is in fact described as a perfect sphere defined only by its radius. This means that there is an abrupt boundary on the region where all of the γ-rays are produced. A sphere with a fuzzy boundary, or a gradual transition from γ-loud to γ-quiet region would probably be a more realistic description. Also, the electron energy distribution could be more precisely modelled by introducing additional breaks in the spectrum or smoothing the distribution. However, each of these corrections inevitably introduces additional free parameters into the model. There is a real danger of the parameter set outgrowing data samples. Furthermore, it is possible that we simply do not fully understand all physical processes in AGN.

From the observational point of view the problem is collecting an adequate data sample. Since models predict emission across the whole electromagnetic spectrum, we want to have as many frequency bands covered as possible. But in order to be able to constrain model parameters using observations, the data have to be strictly contemporaneous.

Simultaneous multi-instrument and multiwavelength observation campaigns are sometimes organised, but only for a few sources (see e.g. [51, 69]). In all the other cases, we collect data from other observatories that were by chance taken at the same time with our observations. Overlapping is, of course, rarely perfect in these cases. If the observations do not overlap perfectly, quasi-simultaneous observations can be used, if the flux in all bands was stable during observations. However, some sources are only detectable in the VHE γ-ray band during enhanced emission states (e.g. PKS 1222+21 [70]), and in such cases the emission can be quite variable. Separating data in very short time bins and selecting strictly simultaneous observations would ensure that we are not mixing emission from different states of the source, but in this case we would be limited by the sparsity of γ-rays. Again we can use PKS 1222+21 as a good example. MAGIC telescopes detected VHE γ-radiation from PKS 1222+21 on 2010 June 17, during what was considered a quite violent flare. Nevertheless, in 30 minutes of observations, only 190 VHE γ-rays were detected [71]. So if we construct an SED in short time intervals, we will not have to consider variability having different shape across the spectrum, but tightening time intervals will result in high measurement uncertainty in the γ-ray band.

Furthermore, we face a problem of identifying the emission region. As we shall see in the dedicated sections, the angular resolution of γ-ray telescopes is $0.1°$ or lower, which means that AGN are considered to be point like sources. Therefore, resolving the γ-ray emission region, determining its size and pinpointing the exact location by direct observation is not feasible. We saw in previous section that emission models predict that γ-ray emission regions are also sources of radiation of lower frequencies. Telescopes observing in lower frequencies have better resolution than γ-ray telescopes. This is especially true for radio telescopes, whose angular resolution can be as high a few tens of a milliseconds of arc. So by combining γ-ray observations with observations in lower frequencies we can try to identify the emission region responsible for the radiation across the entire electromagnetic spectrum. However, this is only possible if there is a similar pattern in the emission at different frequencies. That means that we need simultaneous observations to compare the light curves. It is important to note that if a

single emission zone is a source of radiation of all frequencies, and if there is a prominent emission variation, identifying it as a distinct source of radiation in different frequencies is very difficult. First of all, some of the radiation might be absorbed within the region and reprocessed. This might cause the variation pattern to disappear in some parts of the spectrum or to appear at a later time. But even if this does not happen, we have to remember that γ-rays are emitted at much lower rates than photons in lower frequencies. Therefore, if there was a disturbance in the emission region that left its signature in the emission variation, the patterns at different frequencies will not be identical. In addition, there could be regions that are sources of e.g. radio waves, but not of γ-rays. γ-ray emission regions might also be only a part of radio emission region. In fact, from the example of PKS 1222+21, we can see that there is more than one component of radio emission, and that radio emission regions are much larger than the dimension of γ-ray emission region obtained from the causality condition (equation 1.13). Of course, there might be more than one γ-ray emission region too, but we would not be able to resolve them with current instruments.

Last, but certainly not the least problem is the difference between the instruments. Observation of electromagnetic radiation across the whole spectrum requires different observation techniques. Not just because of technical, but also fundamental reasons. This causes further dissimilarities between patterns in the signal at different frequencies, but it also means that different instruments and the analysis of data acquired with them have different methods of error assessment.

In some cases (see e.g. [72, 73]) a minimisation method is used, but these cases are exceptions rather than a rule. Mankuzhiyil et al. [72] model emission from Markarian 421, which is a very bright and very well sampled source, and the data are carefully separated in nine different contemporaneous samples. A one-zone SSC model is used, which is considered to be appropriate for Markarian 421, since it is a BL Lac type of source. A numerical minimisation method is applied to all of the samples separately and independently. There are obvious differences between parameters obtained for different samples, while the χ^2 value is of the same order. So no single set of parameters can be

adopted as the characteristic one for this particular source. One could define an interval of values for each parameter, but that does not mean that modelling on some future observations data would not result in parameters having values outside those intervals. However, the real value behind this work is that the authors are able to compare parameters for different states of the source, and check for possible correlation between them. Although, the objections raised above hold in this case too, they equally apply to all subsamples. Therefore, these problems should not affect the parameter comparison. Cutini et al. [73] study a FSRQ 4C+49.22 (alternative designation S4 1150+49). As expected for a FSRQ, the archival data show prominent thermal radiation from the accretion disc. Those observations were performed during a quiescent state. However, recent observations performed during a flare episode and in a post-flare state show that the non-thermal synchrotron radiation is dominant over the thermal emission from the accretion disc. The authors modelled the emission using two different models: a two-zone SSC, and a combination of a SSC and an EC model. They use a χ^2 based test in order to find out which of these models fits the data best, but the results of the χ^2 test are rather similar. For the flaring episode the results for the two-zone SSC and SSC+EC models are 0.29 and 0.44, respectively. For the post-flare state, the difference is even smaller, 0.23 and 0.20, respectively. The authors conclude that both of the adopted models are appropriate to describe the observations in these two states.

Emission from two out of three sources covered in this work is explained using leptonic models. Specifically, for the emission from M87 we chose a structured jet SSC emission model, since there is a feature in the SED that cannot be explained by a one-zone SSC model. We used a combination of SSC and EC for PKS 1222+21, which is a FSRQ with obvious thermal contribution from the accretion disc and dust torus. As we shall see in the dedicated chapters, no numerical minimisation procedure is used. In case of M87 we intended to show that it is possible to explain the observations with emission region situated close to the nucleus. We will also see that PKS 1222+21 is a very peculiar source. A combination of its very fast variability and VHE γ-ray spectrum without an apparent cut-off, was very puzzling at the moment of the discovery. It was our goal

to show that it is possible to explain the observed emission using simple one-zone SSC model in combination with EC, while other authors proposed emission scenarios with two emission zones [63], or with exotic means of transport of VHE γ-rays through the BLR [74, 75]. Particularities of the specific scenarios are explained in the dedicated chapters.

1.1.5 Open questions on AGN

There are many aspects of AGN that have not been confirmed, and many questions that remain open for discussion. Probably the most important one is the method of particle acceleration in AGN. Considering the enormous amount of energy emitted by AGN, we are convinced that this energy has to come from conversion of gravitational energy of accreted matter into kinetic by the presence of a SMBH. What exactly happens between accretion and ejection of matter through jets, and how exactly is the gravitational energy converted to kinetic energy is not yet clear. We have already mentioned Blandford-Znajek and Blandford-Payne models of particle acceleration, but for now we have not managed to confirm, or reject any of them. But in order to understand how the particles are accelerated to ultrarelativistic energies, we should first understand the electromagnetic radiation they produce. γ-rays are the most energetic form of the electromagnetic radiation and we expect them to be created in the most extreme conditions. Since γ-radiation accounts for a significant part of energy emitted from AGN (Figure 1.3) and since γ-ray emission regions are also sources of radiation at lower frequencies, as we shall see when we discuss the emission models from AGN (Section 1.1.4), we believe that understanding the γ-ray emission would be a great step in that direction. Understanding the γ-ray emission means answering following questions: What is the correct model of γ-ray production? Where are the γ-rays produced, and what is the structure of the emission region? What is the cause of the emission variability, and is there an underlying emission that is stable between emission outburst episodes? It is also important to understand the universality of answers to these questions. Is any

conclusion we reach applicable to all AGN, or only to the given class of AGN? Or is it perhaps valid only for the specific object?

Results presented in this thesis shed some light on these questions. But before presenting them, we have to explain some concepts introduced in this section.

1.2 γ-ray astronomy

γ-radiation is the most energetic form of electromagnetic radiation. In astrophysics, electromagnetic radiation with energies higher that $100\,\mathrm{keV}$ ($\nu > 10^{19}\,\mathrm{Hz}$) is considered γ-radiation. There are several processes through which γ-rays can be produced in AGN. We already mentioned the Compton scattering and the synchrotron radiation as processes that have a crucial role. Here we discuss them in detail. Later we present astronomical sources of γ-rays and means of observing them.

1.2.1 Inverse Compton scattering

Compton scattering is a well known particle process first described by Arthur H. Compton in 1923 [76]. It is an inelastic scattering of a photon by a charged particle. The process is illustrated in Figure 1.5. The change of the photon frequency is given by the following expression:

$$\nu' = \frac{\nu}{1 + \frac{h\nu}{m_{\mathrm{e}}c^2}(1 - \cos\theta)},\tag{1.16}$$

where ν and ν' are frequencies of the photon before and after the scattering respectively, m_{e} is the electron mass, θ is the scattering angle of the photon with respect to its initial momentum, h is the Planck constant, and c is the speed of light in vacuum. In order to calculate the cross section for the Compton scattering, we need to employ quantum electrodynamics. Feynman diagrams contributing to the cross section for Compton scattering are shown in Figure 1.6. The Klein-Nishina (KN) formula, named after its
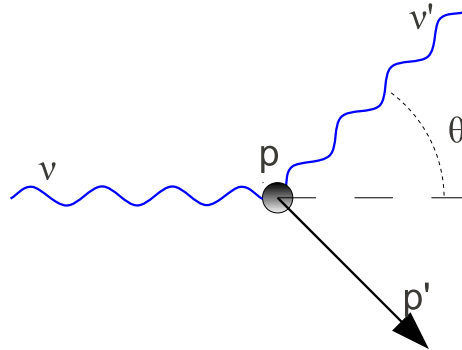
Figure 1.5 Geometry of Compton scattering with an electron initially at rest. ν represents the photon, and p the electron. Primed letters represent particles after the scattering. θ is the scattering angle of the photon.
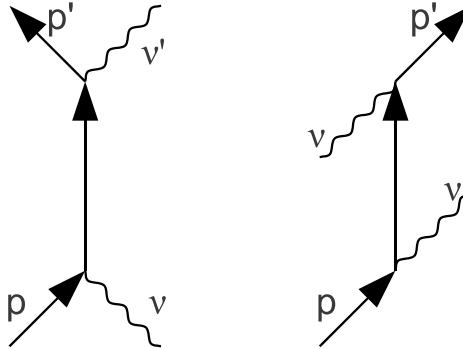
Figure 1.6 Feynman diagrams for Compton scattering. The notation is the same as in Figure 1.5.

authors, who derived it in 1929 [77], states:

$$\frac{d\sigma_{\mathrm{KN}}}{d\cos\theta} = \frac{3}{16\pi}\sigma_{\mathrm{T}}\left(\frac{\nu'}{\nu}\right)^2\left[\frac{\nu'}{\nu} + \frac{\nu}{\nu'} - \sin^2\theta\right]. \tag{1.17}$$

Here σ_{T} denotes the cross section for the Thomson scattering given with

$$\frac{\mathrm{d}\sigma_{\mathrm{T}}}{\mathrm{d}\cos\theta} = \frac{3}{16\pi}\sigma_{\mathrm{T}}\left(1 + \cos^2\theta\right), \quad \sigma_{\mathrm{T}} = \frac{8\pi}{3}\left(\frac{e^2}{m_{\mathrm{e}}c^2}\right)^2, \tag{1.18}$$

where e is the electron charge. Thomson scattering is the same phenomenon as Compton scattering, only these results were derived using classical electrodynamics. Including (1.16) in (1.17) and integrating over $\cos\theta$, we obtain total cross section for Compton scattering

$$\sigma_{\mathrm{KN}} = \sigma_{\mathrm{T}}\frac{3}{4}\left\{\frac{1+x}{x^3}\left[\frac{2x(1+x)}{1+2x} - \ln(1+2x)\right] + \frac{1}{2x}\ln(1+2x) - \frac{1+3x}{(1+2x)^2}\right\}, \tag{1.19}$$

where we used contraction $x = h\nu/m_{\mathrm{e}}c^2$ (the ratio of the initial photon energy to the electron rest energy). The nonrelativistic ($x \ll 1$) and ultrarelativistic ($x \gg 1$) limits for this expression are:

$$\sigma \simeq \begin{cases} \sigma_{\mathrm{T}}\left(1 - 2x + \frac{26x^2}{5} + \cdots\right) & \text{for } x \ll 1 \text{ (Thomson regime)}, \\ \frac{3}{8}\sigma_{\mathrm{T}}x^{-1}\left(\ln 2x + \frac{1}{2}\right) & \text{for } x \gg 1 \text{ (Klein-Nishina regime)}. \end{cases} \tag{1.20}$$

This result can be generalised for photon scattering on any charged particle. It is important to notice here that the cross section remains constant (in the first order approximation) as long as we are in the Thomson regime, while in Klein-Nishina regime it decreases as the initial photon's energy increases.

Compton derived his result for the electron initially at rest. Therefore, the photon could only lose energy in such a process. However, if the electron's kinetic energy is high compared to the photon's, the photon can also gain energy. This is known as inverse Compton scattering, and it is believed to be one of the most important channels

for production of γ-rays in astrophysical sources. In order to calculate the amount of energy a photon can receive if scattered on a relativistic particle, we have to transfer the photon into the rest frame of the electron

$$\epsilon' = \epsilon\gamma(1 - \beta\cos\theta), \tag{1.21}$$

calculate the energy transfer there using (1.16), and then transfer the photon back to the observers frame

$$\epsilon_1 = \epsilon'_1\gamma(1 + \beta\cos\theta'_1). \tag{1.22}$$

Here γ is the Lorentz factor ($\gamma = (1 - \beta^2)^{-1/2}$, $\beta = v/c$). Primed notation is used for calculation in the rest frame of the electron, and the outgoing values have subscript 1. Putting these equations together we can see that the ratio of the resulting photon's energy to the incoming one is approximately $\gamma^2 : 1$, provided the Thomson regime condition is satisfied.

If an isotropic distribution of photons is scattered by an electron, the average transferred power through inverse Compton scattering will be

$$P = \frac{4}{3}\sigma_{\mathrm{T}}c\beta^2\gamma^2 U_{\mathrm{ph}}, \tag{1.23}$$

where U_{ph} is the energy density of initial photons. The spectral emissivity, that is the total power emitted from a unit volume to a unit solid angle per unit frequency, for the inverse Compton scattering of isotropic monochromatic photon field on a power-law distributed population of electrons $N(\gamma) = n_0\gamma^{-p}$ is

$$J(\nu) = \frac{1}{4\pi}\frac{(4/3)^{(p-1)/2}}{2}\sigma_{\mathrm{T}}cn_0\frac{U_{\mathrm{ph}}}{\nu_0}\left(\frac{\nu}{\nu_0}\right)^{-(p-1)/2}, \tag{1.24}$$

where ν_0 is the frequency of incident photons. For detailed calculations of inverse Compton scattering spectrum see e.g. [78, 79, 80].

γ-rays can also be produced in nuclear reactions, through particle-antiparticle annihila-

tion (e.g. $e^- + e^+ \rightarrow \gamma + \gamma$), or unstable particle decay (e.g. $\pi^0 \rightarrow \gamma + \gamma$).

1.2.2 Synchrotron radiation

Synchrotron radiation is another very important phenomenon in astrophysics. A charged particle moving in a magnetic field will interact with the magnetic field, and move in a helical motion along magnetic field line with the gyration frequency

$$\omega_{\mathrm{B}} = \frac{qB}{\gamma mc}, \tag{1.25}$$

and with radius

$$r_{\mathrm{g}} = \frac{c\beta \sin \alpha}{\omega_{\mathrm{B}}}. \tag{1.26}$$

Here B is the strength of the magnetic field, and γ, m and q are the particle's Lorentz factor, mass and charge, respectively. α is the pitch angle, that is the angle between the particle's velocity and the magnetic field. While a nonrelativistic charge will emit isotropic radiation of frequency equal to the gyration frequency, radiation of a relativistic particle moving in a magnetic field will be beamed due to relativistic effects and all radiation will be emitted within a small angle $\theta = 1/\gamma$, as shown in Figure 1.7. It will not radiate at a single frequency, but it will rather have a continuous emission (Figure 1.8). Most of the energy will be radiated below some critical frequency, ω_{C}, defined as

$$\omega_{\mathrm{C}} = \frac{3\gamma^2 qB \sin \alpha}{2mc} = \frac{3}{2}\gamma^3 \omega_{\mathrm{B}} \sin \alpha \tag{1.27}$$

The emitted power is given by the Larmor formula:

$$P = \frac{2q^2}{3c^3}\gamma^4 \left(\frac{v_\perp}{\omega_{\mathrm{B}}}\right)^2, \tag{1.28}$$

where $v_\perp$ is the particle's velocity component perpendicular to the magnetic field. For an isotropic distribution of velocities, the total emitted power is obtained by averaging
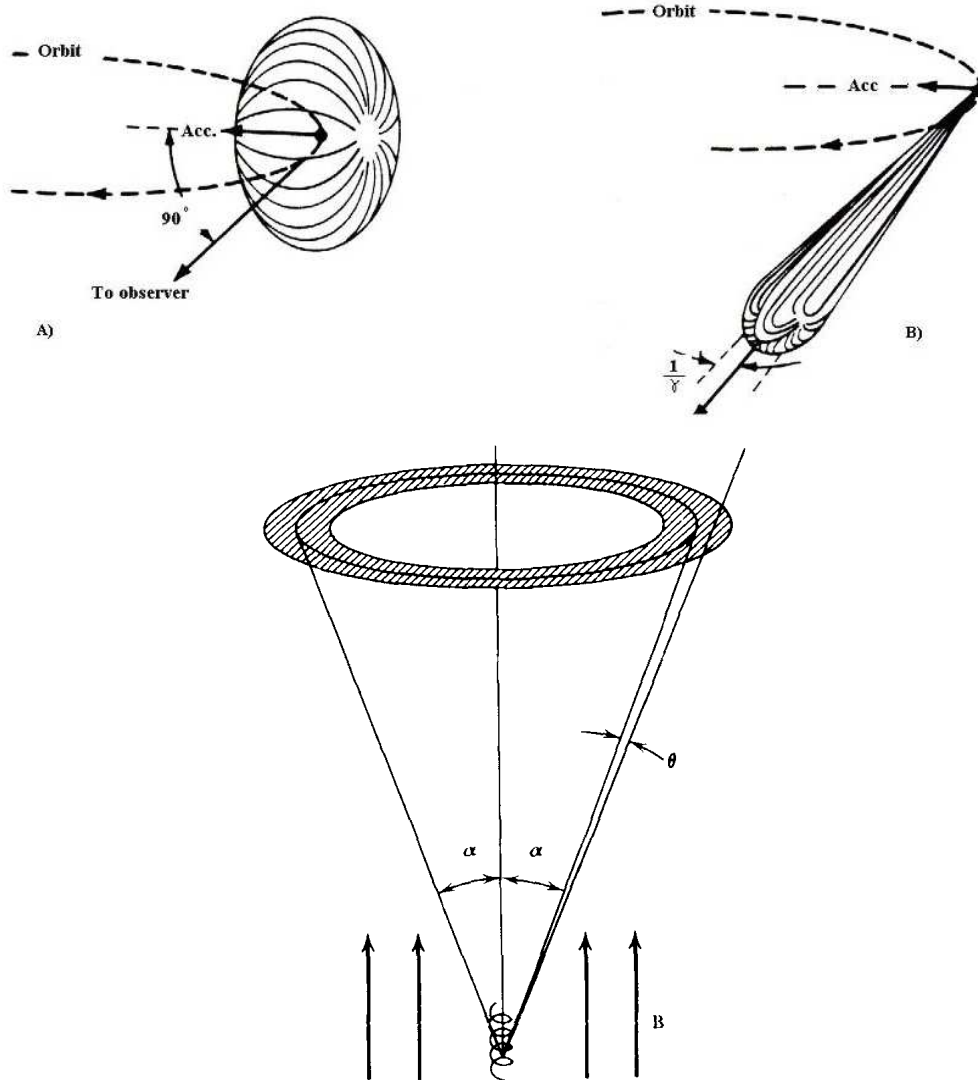
Figure 1.7 Above: Cyclotron (A) and synchrotron (B) radiation energy flux. Image credit: R. Bartolini – John Adams Institute. Below: The geometry of the synchrotron radiation. α is the pitch angle, and θ angle within all radiation is emitted. Adopted from [80].

over α

$$P = \frac{4}{3}\sigma_{\mathrm{T}}c\beta^2\gamma^2 U_{\mathrm{B}}. \tag{1.29}$$

U_{B} is the magnetic energy density ($U_{\mathrm{B}} = B^2/8\pi$), and σ_{T} is the Thomson cross section (equation 1.18). If we compare this result to the radiation from inverse Compton
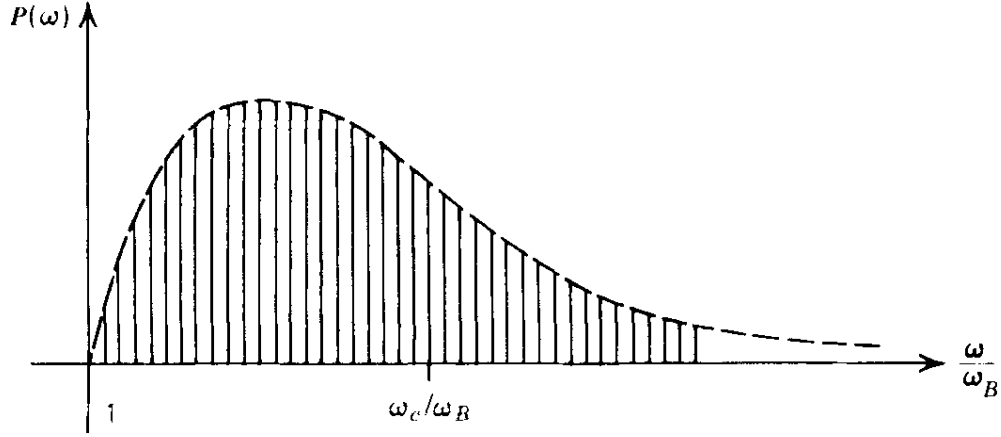
Figure 1.8 The synchrotron radiation power spectrum. Adopted from [80].

scattering (equation 1.23), we get

$$\frac{P_{\mathrm{IC}}}{P_{\mathrm{synch}}} = \frac{U_{\mathrm{ph}}}{U_{\mathrm{B}}}. \tag{1.30}$$

The spectrum is described as

$$P(\omega) = \frac{\sqrt{3}q^3 B \sin\alpha}{2\pi mc^2} F(\omega/\omega_{\mathrm{C}}), \quad F(x) \equiv x \int_x^\infty K_{5/3}(\xi)\mathrm{d}\xi, \tag{1.31}$$

where $K_\alpha(x)$ is the modified Bessel function of the second kind. Asymptotic forms for $F(x)$ are

$$F(x) \simeq \begin{cases} \frac{4\pi}{\sqrt{3}\Gamma(1/3)}\left(\frac{x}{2}\right)^{1/3} & \text{for } x \ll 1, \\ \left(\frac{\pi}{2}\right)^{1/2}\mathrm{e}^{-x}x^{1/2} & \text{for } x \gg 1, \end{cases} \tag{1.32}$$

where $\Gamma(t)$ is the gamma function. If we assume a power-law distribution of particles $(N(\gamma) = n_0\gamma^{-p})$, the total emitted power per unit volume and frequency will also be a power-law

$$P(\omega) = \frac{\sqrt{3}q^3 n_0 B \sin\alpha}{2\pi mc^2(p+1)}\Gamma\left(\frac{p}{4}+\frac{19}{12}\right)\Gamma\left(\frac{p}{4}-\frac{1}{12}\right)\left(\frac{mc\omega}{3qB\sin\alpha}\right)^{-(p-1)/2}. \tag{1.33}$$

Synchrotron radiation of a single particle is elliptically polarised. However, for a population of particles smoothly distributed according to the pitch angle, the elliptical component cancels out, and the total radiation is partially linearly polarised. For a power-law distributed particles as above, the degree of polarisation is

$$\Pi = \frac{p+1}{p+7/3}.\tag{1.34}$$

These results are deduced in greater detail in [80].

Probability of an electron emitting a γ-ray as a synchrotron radiation is negligibly small. A proton ($m_{\mathrm{p}} \approx 2000 m_{\mathrm{e}}$), on the other hand, loses energy through synchrotron radiation much slower (than an electron of the same energy), so, in astrophysical accelerators, it is quite possible for it to reach energies high enough to radiate synchrotron γ-rays.

1.2.3 Astrophysical sources of γ-rays

Astrophysical sources of γ-rays (Figure 1.9) can be divided to galactic and extragalactic sources, based on whether they are situated in the Milky Way galaxy or not. We will shortly describe each type of sources, except AGN, which were already described in details in Section 1.1.

Binary systems are systems of a compact object (neutron star or a black hole) and a companion star. If the accompanying star is large enough (e.g. a red giant star), its material will fall to the compact object and form an accretion disc, and some of the matter will be ejected in a form of a relativistic jet.

Supernova remnants (SNR) are expanding structures of material coming from the supernova explosions. The expansion front is a shock wave, in which particles are accelerated.

Pulsars are fast spinning neutron stars, with strong magnetic fields. Electrons are accelerated in the pulsars' magnetosphere to relativistic energies. Pulsars emit radiation across the entire electromagnetic spectrum including γ-rays. They also power pulsar
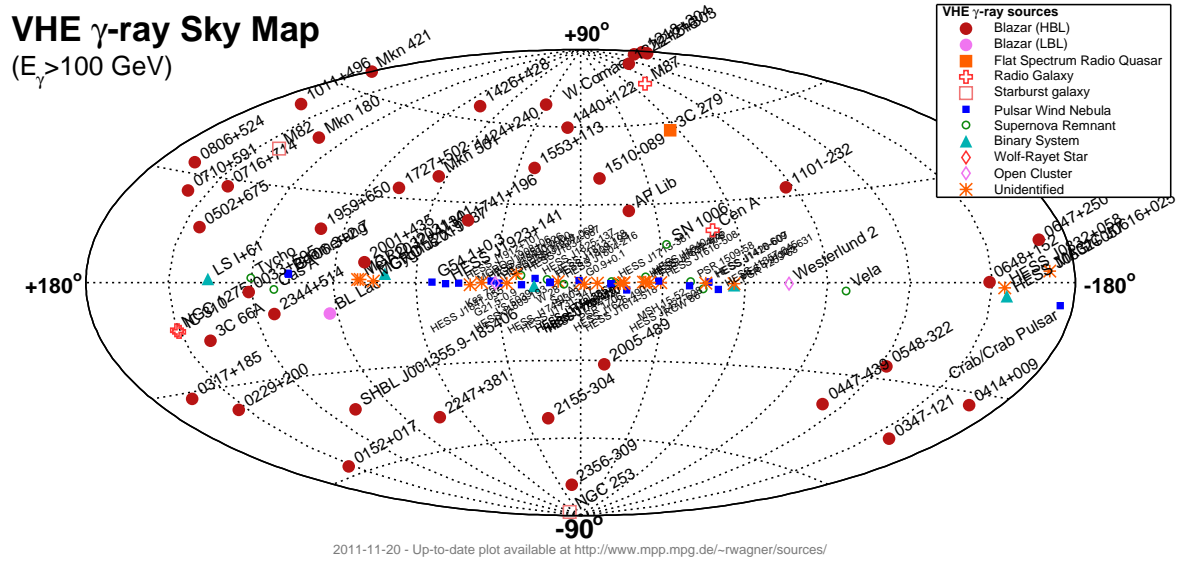
Figure 1.9 Position of known VHE γ-ray sources. Adopted from [81]

wind nebulae.

Pulsar wind nebulae are special types of SNRs with pulsars in their centres. The most important one for the VHE γ-ray astronomy is the Crab Nebula. It is the brightest steady source of VHE γ-rays, so it is used as a standard candle by the ground based γ-ray telescopes. Often integral VHE γ-ray flux from other sources is expressed in Crab Nebula units (C.U.). The spectrum of the Crab Nebula between 65 GeV and 13.5 TeV can be described by a curved power-law $\frac{\mathrm{d}N}{\mathrm{d}E} = N_0(E/E_0)^{a+b\log(E/E_0)}$, with the following parameters: $N_0 = (3.39 \pm 0.09) \times 10^{11}\,\mathrm{TeV}^{-1}\,\mathrm{cm}^{-2}\,\mathrm{s}^{-1}$, $E_0 = 1\,\mathrm{TeV}$, $a = -2.51 \pm 0.02$, and $b = -0.21 \pm 0.03$ [82].

Starburst galaxies are irregular galaxies with enhanced star formation and supernova rates. They are richer in SNR, which on their own are not bright enough sources to be visible from another galaxy. Collectively, however, they produce higher flux of VHE γ-rays. So far VHE γ-rays were detected from only two starburst galaxies: M82 [83] and NGC 253 [84].

Gamma-ray bursts (GRB) are the most violent and the most energetic events in the universe since the Big bang. They are short-lived bursts of γ-rays, which can last between few milliseconds up to few minutes. GRBs can be divided in two groups: short

duration GRBs lasting less than $2\,s$, and long duration GRBs lasting longer that $2\,s$. Short GRBs are associated with merging of compact objects such as neutron stars or black holes [85, 86, 87]. Long GRBs are results of implosions of large supernovae at cosmological distances [88].

Dark matter (DM) is non luminous matter that makes up for almost 27% of total mass–energy content of the universe[6] [89]. The nature of DM is still unclear, but the widely accepted explanation is that it is formed of weakly interacting massive particles (WIMP), whose annihilation products might be γ-rays. Although the existence of DM is inferred based on the gravitational influence of DM on visible matter (see e.g. [90]), a direct detection of DM particles, or their decay products is still lacking.

1.2.4 Satellite borne observations

The atmosphere is opaque to γ-rays, so in order to observe γ-rays from astrophysical sources, the atmosphere has to be avoided by mounting detectors on satellites. Another possibility concerning VHE radiation, as we shall see, is to use the atmosphere as part of a detector.

γ-ray observations became possible in 1960s with the development of space programs and artificial satellites. The first γ-ray telescope was mounted on NASA's Explorer XI satellite and launched in April 1961. It was designed to detect γ-rays above $50\,MeV$. During 23 days, it collected 9 hours of data from "pointing into space". 22 of recorded events were classified as γ-rays, while 22000 events were attributed to charged cosmic rays. This is considered the beginning of the γ-ray astronomy. The launch was announced in [91], and the mission results were published in [92] and [93].

Fermi Gamma-ray Space Telescope

Since Explorer XI, there were many satellite borne γ-ray telescopes in Earth's orbit. The latest and the most sensitive one is the *Fermi Gamma-ray Space Telescope* (hence-

---

[6]Around 68% is mysterious dark energy, while visible matter constitutes less than 5% [89].

forth *Fermi*) shown in Figure 1.10. Because our research is in part based on its data, we will briefly review the instrument. *Fermi* is an international multi-agency space mission launched in June 2008. It caries two γ-ray detectors: the Gamma-ray Burst Monitor (GBM) and the Large Area Telescope (LAT). The GBM's main purpose is early detection and observations of GRBs. It consists of two types of scintillation detectors. 12 Sodium Iodide (NaI) and 2 Bismuth Germanate (BGO) detectors are located on the sides of the spacecraft, so together with LAT they provide almost full sky coverage. The NaI detectors are sensitive from a few keV to about 1 MeV. They provide GRB triggers and locations. The BGO detectors cover the energy range of 150 keV to 30 MeV.
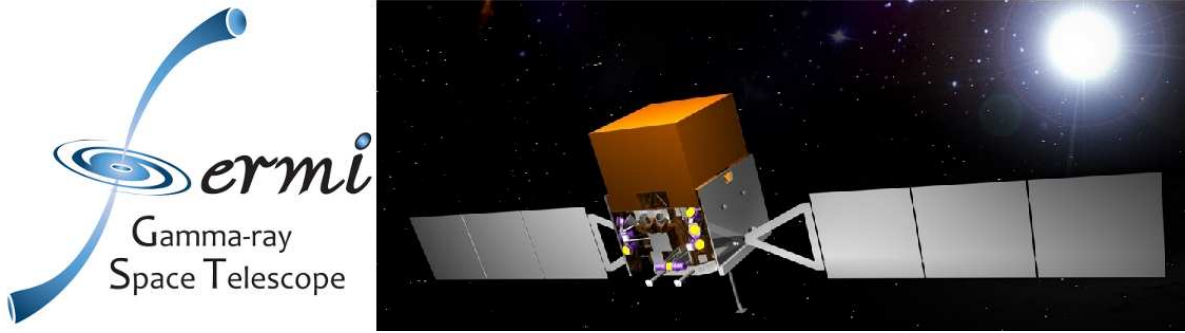
Figure 1.10 Logo and the image of the *Fermi Gamma-ray Space Telescope.*

Fermi-LAT is the main instrument on board the satellite. It uses technology similar to the one used in particle accelerators. It is a cubic detector with 1.8 m side that consists of several components. When a γ-ray hits the detector, it first hits layers of tungsten metal where it interacts with atomic nuclei and it is converted to an electron-positron pair. The layers of tungsten are interlayered with silicon-strip sensors. Electron and positrons ionise silicon, which emits electrical pulses. Using computer algorithms, these signals are later reconstructed to calculate the direction and time of the incoming γ-ray. The last component of the detector is caesium iodide imaging calorimeter, which is used to measure the γ-ray's energy. *Fermi*-LAT is sensitive in the energy range from 20 MeV to 300 GeV, with angular resolution changing with energy from $\sim 3°$ at 100 MeV to $\sim 0.1°$ at 300 GeV. The effective area is $\sim 0.8\,\mathrm{m}^2$, and the field of view (FoV) of 2.4 sr. It primarily operates in an all-sky-survey mode, scanning one hemisphere of the sky for

one orbit, then rocking to scan the other hemisphere for the next orbit. Doing so it covers the entire sky in 3 hours, while any point in sky is observed continuously for 30 minutes. Pointed observations are also possible, however data that we present here were collected in the sky-survey mode. A detailed description of the *Fermi*-LAT is given in [94]. More information on the performance of the instrument can be found in [95].

1.2.5 Ground based observations

All satellite borne telescopes have one obvious restriction — size, i.e. a collection area. An increase in size and mass of instrument greatly increases the complexity and financial cost of the mission. The fact that LAT stands for Large Area Telescope, although the effective area of the detector is less than $1\,\mathrm{m}^2$ illustrates this obstacle perfectly. Since γ-rays are sparse, the collective area of a detector is extremely important. Additional disadvantage of satellite observatories is access to instruments. In case of malfunction repairs are difficult and expensive, and not immediately possible.

Ground based telescopes can have significantly greater collection area than satellite borne detectors without a huge increase in the cost of the experiment. However, the atmosphere is non transparent to γ-rays. Imaging atmospheric Cherenkov telescopes (IACT) rely on that fact to use the atmosphere as a part of the detector of VHE γ-rays.

Extensive air showers (EAS)

When a γ-ray enters the atmosphere, it interacts electromagnetically with atomic nuclei of air. It is absorbed, and an electron-positron pair is created. Each of them emits VHE photons by *bremsstrahlung*, which again create an electron-positron pair. This cascade process forms the so-called extensive air showers (EAS). Since the only particles forming the shower are photons, electrons and positrons, and they only interact electromagnetically, this kind of shower is usually referred to as an electromagnetic shower (Figure 1.11). It has a form of a narrow cone with a front in a shape of a disk. A shower develops as long as the average energy of the newly created electrons and positrons is above

some critical energy E_C. Below this energy, electron and positrons mostly lose energy through ionisation of the surrounding medium, rather than through bremsstrahlung. At that point the multiplication stops and shower particles gradually lose their energy until the shower is extinguished. The value of E_C depends on the characteristics of the medium. For the Earth's atmosphere it is $\approx 85\,\mathrm{MeV}$ [96]. Number of particles created is approximately equal to the fraction of the energy of the γ-ray that induced the shower and E_C. The position at which the shower reaches its maximum also depends on the medium. In the Earth's atmosphere it happens at $\approx 10\,\mathrm{km}$ a.s.l. The theory of electromagnetic showers was first proposed in 1937 by Bhabha and Heitler [97], and Carlson and Oppenheimer [98], but the details and precise calculations were worked out a year later by Landau and Rumer [99].

A high energy cosmic ray entering the atmosphere will also induce a particle shower. However, physics of a cosmic ray induced shower is quite different. Interactions will be governed not only by electromagnetic, but also by strong and weak nuclear force. Unlike γ-ray, a hadron will remain after scattering, only giving a part of its kinetic energy to the scattering products. These are usually mesons (π^0, $\pi^\pm$, $\mathrm{K}^\pm$ etc.), which undergo further decays. An incoming hadron will keep on scattering and creating new particles as long as its energy per nucleon is greater than the pion production threshold, which is $\approx 1\,\mathrm{GeV}$. Differences in the shower development will leave their footprint in the shower morphology. γ-ray induced showers are rather homogeneous and axially symmetric about the direction of the primary γ-ray. The pair production and bremsstrahlung both have small opening angles, so an electromagnetic showers are rather narrow around their axes. Hadron induced showers are less homogeneous and usually have several distinctive subshowers. Furthermore, in hadronic showers, there is a typical transverse momentum in each scattering of $0.3 - 0.4\,\mathrm{GeV/c}$ [100], which will force the shower to spread. Figure 1.12 illustrates differences in the structure of γ-ray and hadron induced atmospheric showers.
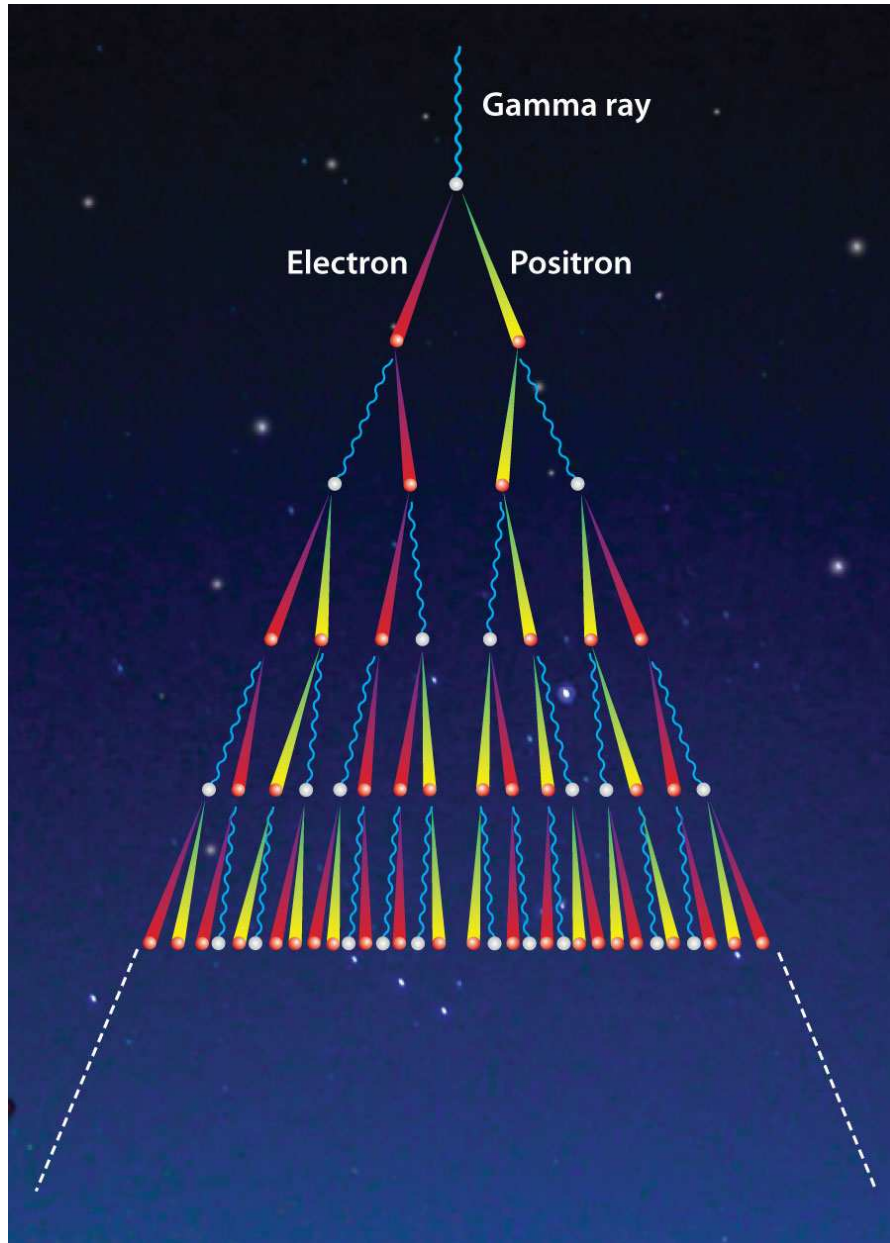
Figure 1.11 A sketch of a development of an electromagnetic EAS induced by a γ-ray. Image credit: Milagro ground based water Cherenkov radiation telescope.
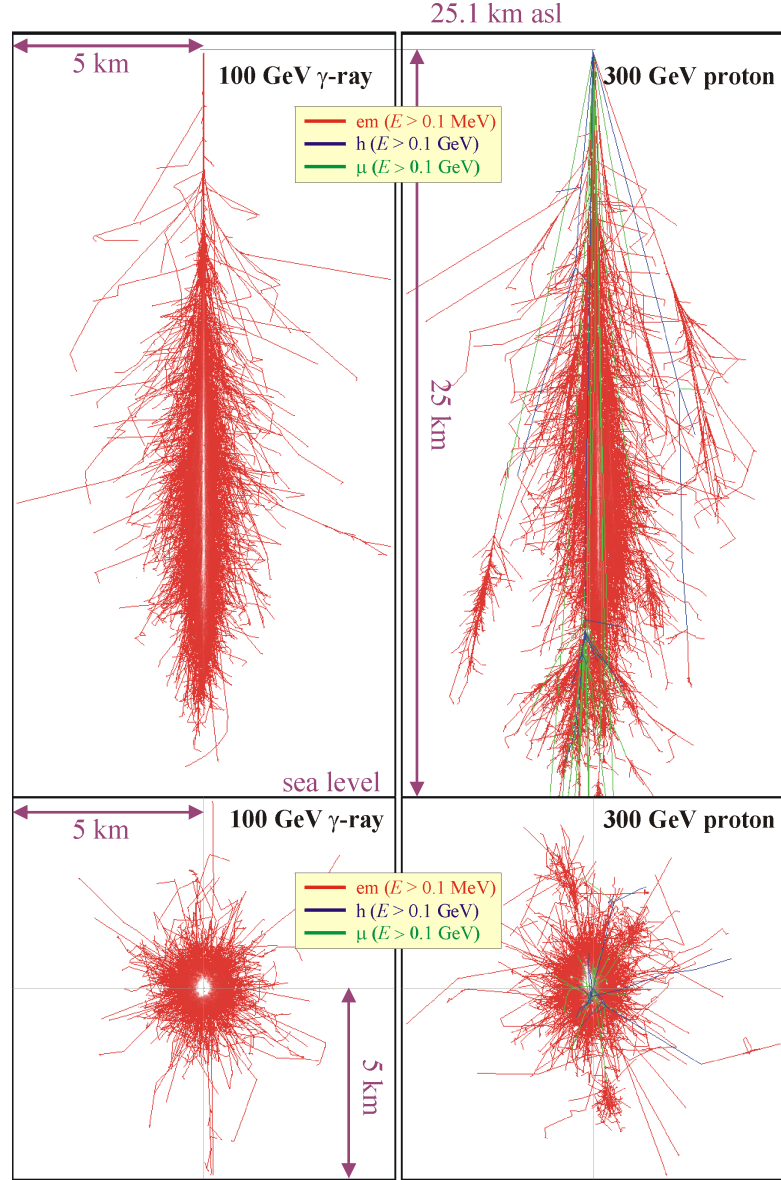
Figure 1.12 Vertical (top panel) and horizontal (bottom panel) projection of a Monte Carlo simulation of an EAS initiated by a 100 GeV γ-ray (left) and a 300 TeV proton (right). The incident angle of the primary particle is 0° and the first interaction occurs at 25 km a.s.l. Tracks of electromagnetic components (electrons, positrons and secondary γ-rays) are red, muons are green, and hadrons are blue. Lighter colour represents higher density of tracks. For that reason centres of showers are white. Only tracks of particles with kinetic energy above the cut are plotted. The energy cuts for electromagnetic components, and for muons and hadrons are 0.1 MeV and 0.1 GeV respectively. Adopted from [101].

Cherenkov radiation

Whenever a charged particle passes through a dielectric medium, it polarises the nearby electric dipoles. After the particle has passed, dipoles return to their equilibrium positions emitting faint blue to ultraviolet light. If the particle's speed is greater then the phase velocity of light in that medium, the disturbance will be left in the wake of the particle, and dipoles will reorientate coherently. Photons from different points along the trajectory will be emitted in phase in the direction of the particle and form a narrow pulse of light. This form of radiation was experimentally detected by Pavel Alekseyevich Cherenkov in 1934 and named after its discoverer. In 1958 he shared the Nobel Prize in physics with Il'ja Mikhailovich Frank and Igor Yevgenyevich Tamm, who explained the origin of Cherenkov radiation.

The minimal energy for an electron to cause Cherenkov radiation of wavelength λ can be easily calculated from the condition that the particles speed is greater than the speed of light in the medium:

$$v(\lambda) > \frac{c}{n(\lambda)} \Rightarrow \beta(\lambda) > \frac{1}{n(\lambda)} \Rightarrow E_{th}(\lambda) = \frac{mc^2}{\sqrt{1 - \frac{1}{n^2(\lambda)}}}, \qquad (1.35)$$

Where n is the refractive index of the medium, m the mass of the particle, and E_{th} the energy threshold for the Cherenkov radiation. The refractive index of air is ≈ 1.0003 at sea level, so $E_{th} \approx 21\,\text{MeV}$. The angle between the emitted flash and the particle is related in the following way

$$\cos\theta = \frac{\frac{c}{n}t}{vt} = \frac{1}{n\beta}, \qquad (1.36)$$

which means that at sea level $\theta \approx 0.1°$. A single electron in EAS emits around 45 Cherenkov photons per metre near the ground. A primary γ-ray of $1\,\text{TeV}$ will result in ≈ 100 Cherenkov photons per m^2 on the ground. The relative difference between the speed of a particle in an EAS and a Cherenkov photon it emits is only about 10^{-4}, so Cherenkov flashes will last only around few nanosecond. An illustration of an electromagnetic EAS with the Cherenkov light pool it creates is shown in Figure 1.13.

Only a small fraction (10^{-4}) of the primary particle's energy will be transformed to Cherenkov radiation.

Imaging atmospheric Cherenkov telescopes

Ground based γ-ray observations are performed with Imaging atmospheric Cherenkov telescopes (IACT). Since γ-rays do not reach the ground, IACTs record Cherenkov radiation in the atmosphere caused by EAS. Strictly speaking IACTs are optical telescopes. Cameras consist of photosensitive electronic elements, usually photomultiplier tubes (PMTs). In 2011 the First G-APD Cherenkov Telescope (FACT) was commissioned, which uses a camera with Geiger-mode avalanche photodiodes (G-APDs) instead of PMTs. One of the goals of FACT is demonstrating the advantages of using G-APDs [102]. Typical sensitivity of camera pixels is to light of wavelength between 300 and 700 nm, because Cherenkov radiation is strongly absorbed by ozone below 300 nm, and dominated by the night sky background light (NSB) above 700 nm [103].

However, IACTs use the atmosphere as part of the detector, thus the atmosphere is in fact a calorimeter, and IACT a counter. From that perspective, the ground based γ-ray observation technique is similar to the ones employed in particle and nuclear experiments.

The first IACT was a 10 m Whipple telescope commissioned in 1968. It discovered TeV emission from Crab Nebula in 1989 [104], and Markarian 421 in 1992, the first AGN ever to be discovered in the VHE γ-ray band [10]. Multiple telescope observations were first performed by the HEGRA (High Energy Gamma-Ray Astronomy) collaboration between 1987 and 2002. Amongst other achievements HEGRA discovered VHE γ-rays from M87 [5]. Currently there are three scientific collaborations that are performing observations with IACTs: H.E.S.S.[7] (High Energy Stereoscopic System), MAGIC[8] (Major Atmospheric Gamma Imaging Cherenkov) and VERITAS[9] (Very Energetic Radiation

---

[7]www.mpi-hd.mpg.de/hfm/HESS/HESS.shtml

[8]wwwmagic.mpp.mpg.de

[9]veritas.sao.arizona.edu
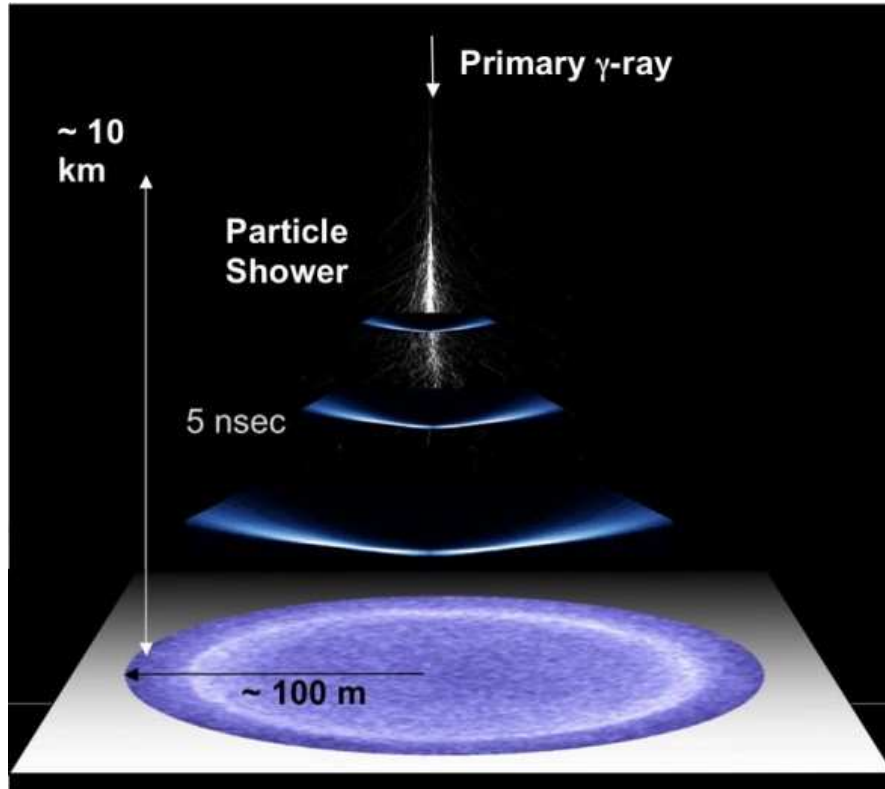
Figure 1.13 A sketch of a γ-ray induced shower and the Cherenkov light pool it creates. Image credit: Cherenkov Telescope Array in Argentina.

Imaging Telescope Array System). Collaborations H.E.S.S. and MAGIC emerged from HEGRA collaboration. MAGIC collaboration built its telescopes in the old HEGRA site at the Observatorio del Roque de los Muchachos in the Canary Island of La Palma, Spain, and H.E.S.S. chose their new site in Namibia. VERITAS is a successor of the Whipple collaboration.

CTA[10] (Cherenkov Telescope Array) is a world-wide project currently being developed. The beginning of construction is expected by the end of 2015, and of operations in 2020. When finished, it will be positioned at one site in each hemisphere, with an array of 19 telescopes in the northern and 99 in the southern hemisphere. It is expected to be sensitive to γ-rays between few tens of GeV to above 100 TeV [105, 106].

Further discussion of IACT methodology is given in Chapter 2, where the MAGIC

---

[10]portal.cta-observatory.org

experiment is described in details.

1.2.6   Extragalactic background light

The universe is filled with diffuse electromagnetic radiation of all wavelengths. The part in the IR–UV band (0.1–1000 μm) is called extragalactic background light (EBL; Figure 1.14). It is believed to be the result of starlight, dust reprocessed starlight, with a contribution from AGN. VHE γ-rays interact with photons of the EBL to create electron-positron pairs, so their flux is attenuated on their way to the Earth. Attenuation is dependant on the energy of γ-rays and the redshift of the source (z). The connection
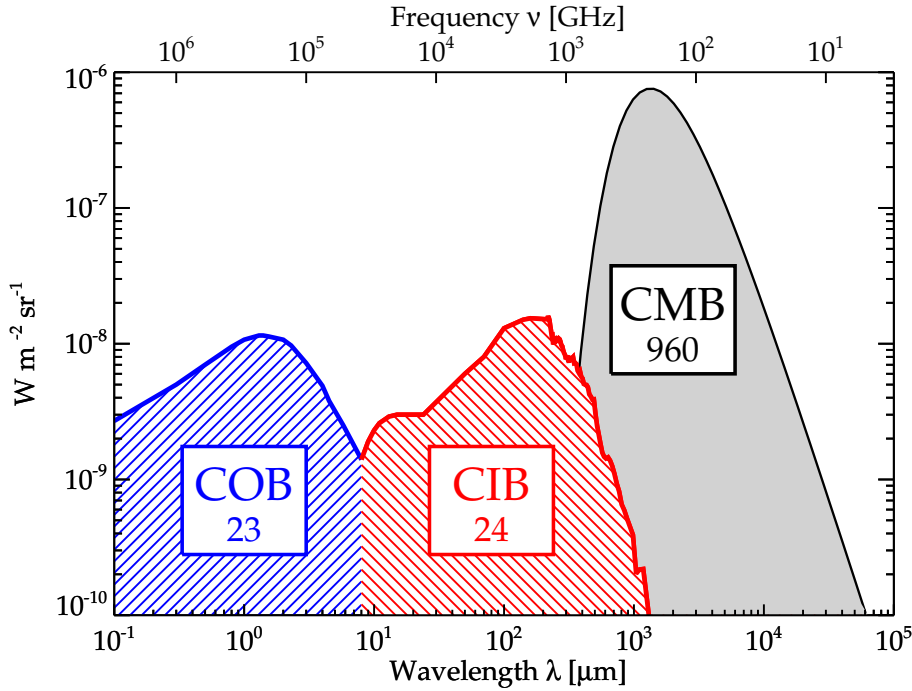
Figure 1.14 Schematic spectral energy distributions of the most important background radiation, with their approximate brightness in nW m^{-2} sr^{-1} written in the boxes. The Cosmic Microwave Background (CMB) is the relic of the Big Bang. The Cosmic Infrared Background (CIB) and the Cosmic Optical Background (COB) together make the EBL. Adopted from [107].

between observed and intrinsic spectra of a given source is given by

$$\frac{dN(E)}{dE}\bigg|_{obs} = \frac{dN(E)}{dE}\bigg|_{int} e^{-\tau(E,z)}, \tag{1.37}$$

where the optical depth (τ) is

$$\tau(E,z) = \int_0^z dz' \frac{dl(z')}{dz'} \frac{1}{2} \int_{-1}^{+1} d\mu(1-\mu) \int_{\epsilon_{th}}^{\infty} d\epsilon' n_{EBL}(\epsilon', z')\sigma_{\gamma\gamma}(E(1+z'), \epsilon', \mu). \tag{1.38}$$

The first integral accounts for the distance covered by γ-ray, the second one integrates over angles in the interaction, where $\mu \equiv \cos\theta$, and the third the probability of the interaction. n_{EBL} is the number density of EBL photons in the comoving frame, and $\sigma_{\gamma\gamma}$ the cross section for pair production. ϵ_{th} is the energy threshold for the interaction, and it depends on the energy of the γ-ray and the angle μ. A good knowledge of the SED of the EBL enables us to reconstruct the intrinsic spectrum of a given source, provided the redshift of that source is well known. That process is called de-absorption. On the other hand, assumption about the intrinsic spectrum of the source (based on spectra of low-redshift sources), combined with well known redshift, can be used to constrain the EBL. A collection of EBL SEDs obtained by different methods is shown in Figure 1.15.

1.2.7 Cosmic rays

γ-ray signal from astrophysical sources sources (see Section 1.2.3) is measured with a background of cosmic rays, charged particles of enormous energies, originating mostly from outside of the Solar system. Cosmic rays are mainly protons (almost 90%) and α particles (around 9%). The rest are electrons and heavier atomic nuclei. For this reasons cosmic rays are often referred to as hadrons. SNRs are sources of large fraction of cosmic rays [109, 110]. AGN are likely also sources of cosmic rays, but this has not been proven. Being charged particles, cosmic rays are subject to Terrestrial, Solar, galactic and extragalactic magnetic fields, therefore the information about their direction is lost.
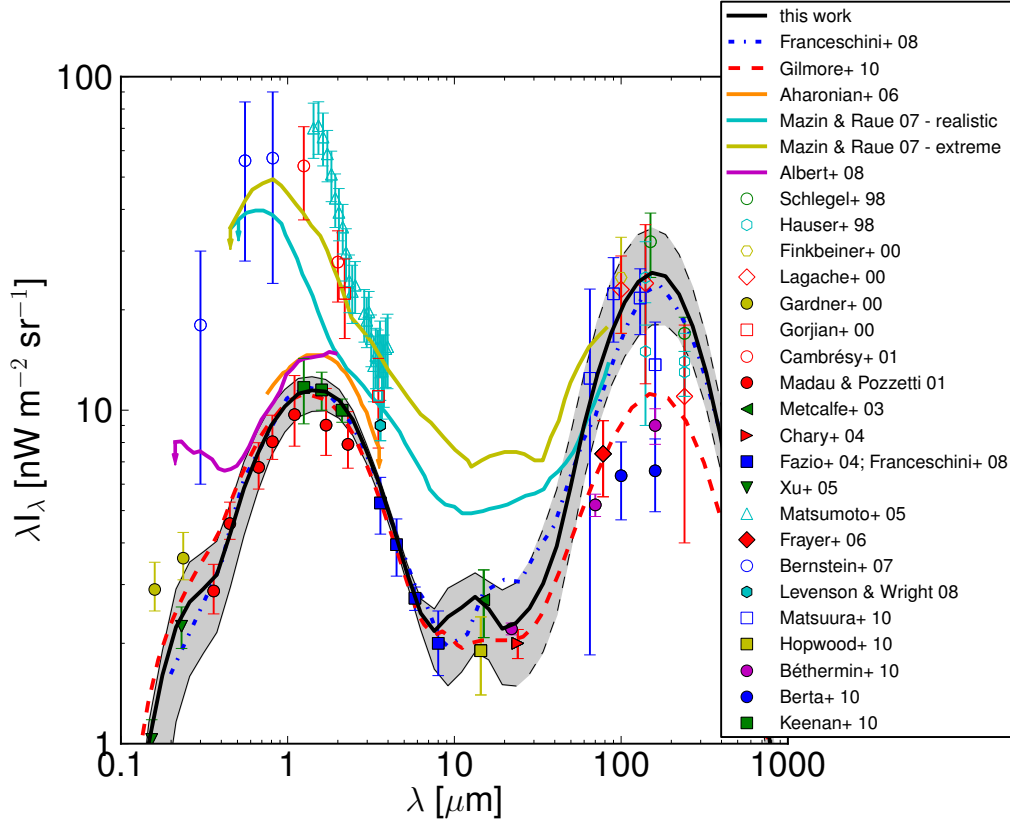
Figure 1.15 A collection of EBL SEDs obtained by different methods. Adopted from [108].

γ-ray observatories study cosmic rays through observations of regions where high density of cosmic rays is expected. However, when entering the Earth's atmosphere they leave trace similar to that produced by VHE γ-rays and represent background (see Section 1.2.5 and Chapter 2). The spectrum of cosmic rays is represented in Figure 1.16. At energies above $10\,\text{GeV/nucleon}$, it can be described by a broken power-law

$$\frac{\mathrm{d}N}{\mathrm{d}E} \propto E^{-\alpha}, \tag{1.39}$$

where

$$\alpha = \begin{cases} 2.7, & E < 10^{16}\,\text{eV}, \\ 3.0, & 10^{16} < E < 10^{18}\,\text{eV}. \end{cases} \tag{1.40}$$

The spectrum appears to become somewhat flatter above 10^{19} eV. The two brakes, at 10^{16} eV and 10^{19} eV, called the knee and the ankle, respectively, are indication of possible energy limits of different cosmic accelerators.
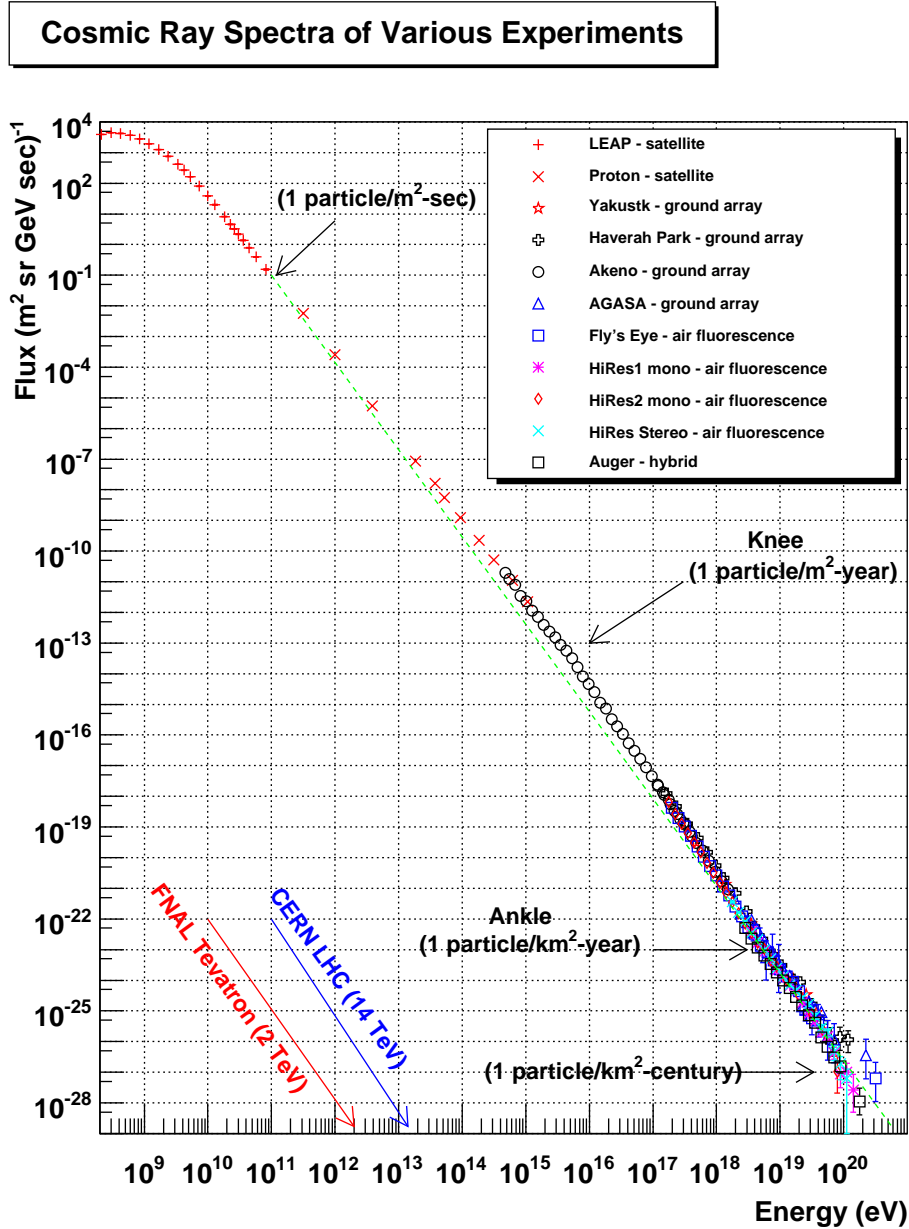
Figure 1.16 Compilation of measurements of the cosmic ray spectrum. Green dashed line represents E^{-3} power-law for comparison. Two characteristic features, the *knee* at $10^{15} - 10^{16}$ eV, and the *ankle* at $10^{18} - 10^{19}$ eV are explained in the text. Adopted from [111].

Chapter 2

The MAGIC telescopes

The MAGIC (Major Atmospheric Gamma Imaging Cherenkov) Florian Goebel[1] telescopes (Figure 2.1) are two 17 m IACTs located at the Observatorio del Roque de los Muchachos in the Canary Island of La Palma, Spain (28°45′ north, 18°54′ west), at 2200 m above sea level. The telescopes are optimised for observations of γ-rays of energies above 50 GeV. Although they can operate as standalone telescopes, the usual operation is in a stereoscopic mode.

The telescopes are operated by an international scientific collaboration of 24 institutes from 10 countries. A group of scientists from Croatia, organised in Croatian MAGIC Consortium, joined the Collaboration in 2008 and was accepted as full members in 2009.

In this chapter a detailed overview of the experiment is given. Section 2.1 is dedicated to the description of the experimental set-up, the way observations are performed is explained in Section 2.2, and the data analysis chain in Section 2.3.

---

[1]Florian Goebel was a distinguished member of the MAGIC collaboration, who strongly contributed to MAGIC and especially to MAGIC-II telescope. He lost his life in a tragic accident at the MAGIC observation site on 2008 September 10, while working on construction of MAGIC-II. To honour his memory, MAGIC telescopes were renamed to MAGIC Florian Goebel telescopes. Since then, every September 10, MAGIC telescopes stay in park position and no operations are performed.

Figure 2.1 MAGIC telescopes at the Observatorio del Roque de los Muchachos. From left to right: MAGIC Counting house (CH), MAGIC-I, MAGIC-II.

2.1 Hardware

The construction of MAGIC-I was completed in 2003 and it is fully operational since 2004. The system was upgraded with the second telescope, MAGIC-II, in 2009. The system has undergone several other major upgrades, each of them enhancing the performance of the system. A summary of characteristics of each period set-up are listed in Table 2.1.

2.1.1 Construction and drive

The reflector dish of each MAGIC telescope has a diameter of 17 m. Until summer of 2012[2] these were the largest IACTs in the world. The total weight of each telescope is 64 t, but the part movable in elevation, including reflector and camera, weights only 20 t. This is due to innovative construction techniques and materials employed. The lower (movable only in azimuth direction) part of the telescope consists of undercarriage and bogeys constructed in steel. The mirror support construction, however, is a space frame of octagonal shape constructed of carbon fibre reinforced plastic tubes. The light

---

[2]The H.E.S.S. collaboration commissioned a 28 m telescope on 2012 July 26.

Figure 2.2 Side view of the MAGIC-I telescope. The construction of carbon fibre reinforced plastic tubes is white, and the lower part constructed of steel bars is grey. On the left, camera is supported on aluminium mast. A web of steel cables is also visible.

weight construction enables reorientation of telescope to any point within 40 seconds on average, with a maximum of 100 seconds. This fast movement mode is used in the case of GRB follow-up observations. A telescope is moved by three electrical servomotors, each of maximally 11 kW. Two motors provide azimuthal, and one elevation movement. Cameras are mounted on aluminium tubular mast and secured against transverse movements by a web of pre-stressed steel cables. The construction can be seen in Figure 2.2.

2.1.2   Reflector

Each MAGIC telescope has a parabolic reflector with total reflective area of $236 \, \mathrm{m}^2$. Both the diameter and the focal distance are 17 m. The reflectors are tessellated of
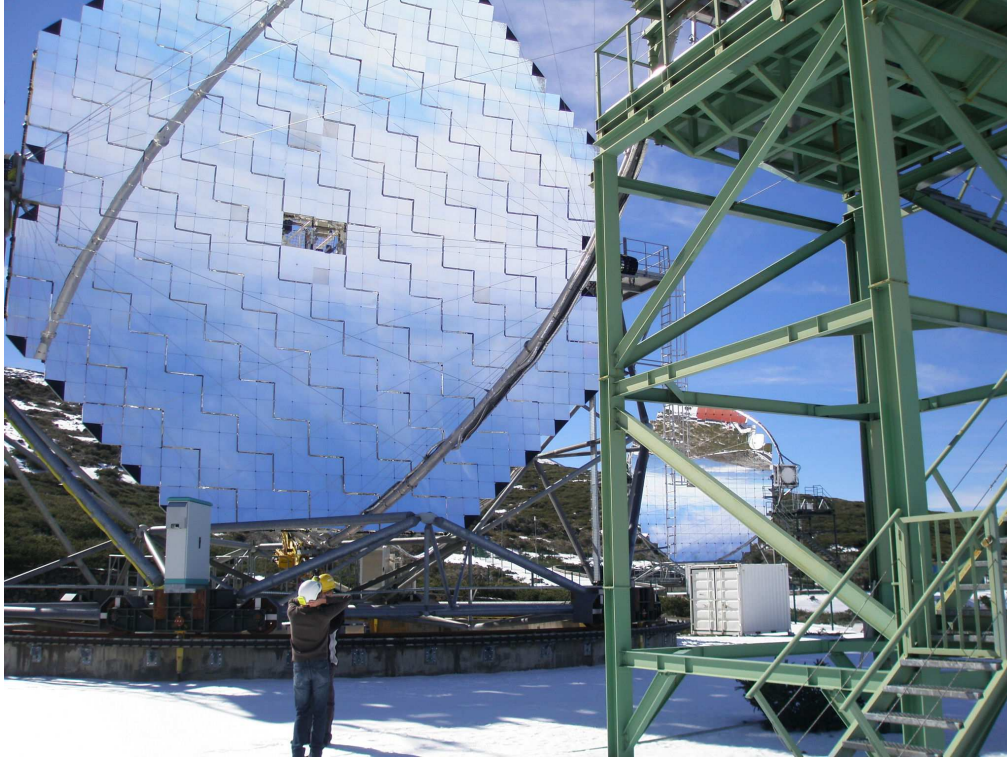
Figure 2.3 Front view of MAGIC-I reflector dish. Each panel has 4 mirrors, except the ones on the edge of the dish, which have three. MAGIC-II is visible in the background.

$1\,m^2$ panels (Figure 2.3). MAGIC-I panels are composed of four $0.5 \times 0.5\,m$ aluminium mirrors on a honeycomb structure. Each panel in MAGIC-II has $1 \times 1\,m$ mirror. 143 of them are aluminium mirrors on a honeycomb structure, while the other 104 of them have a sandwiched glass-honeycomb-glass structure with evaporated aluminium. The mirror surfaces are protected with a quartz layer coating. Average reflectivity of each mirror for wavelengths of 290–650 nm, when focussed on a spot of $2\,cm$ radius is around $80\,\%$. Because of the light telescope structure, the shapes of the reflectors are not fixed. The weight of the camera causes different tension in the structure for different zenith positions, which results in distortion of the reflector shape. To account for this effect, mirror panels are mounted on three points, two of which are computer-controlled actuators. Active Mirror Control (AMC) system automatically adjusts each panel, ensuring optimum focusing for each telescope orientation.
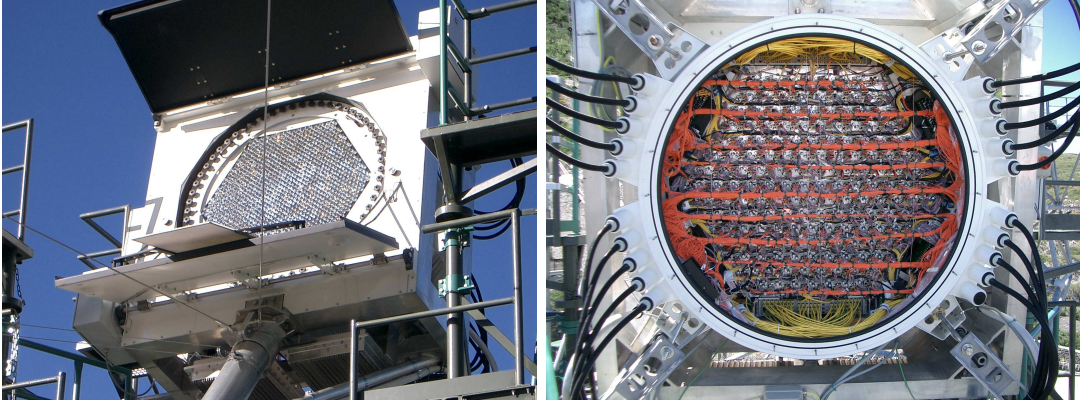
Figure 2.4 Front and back view of the MAGIC-II camera. The new MAGIC-I camera (installed in Summer of 2012) is identical.

2.1.3 Camera

The cameras have a shape of cylindrical boxes 1.46 m in diameter and 0.81 m thick, and each weights $\sim$ 850 kg. From the front side they are protected by movable lids and a plexiglass plate, behind which 1039 pixels are placed in a honeycomb arrangement (Figure 2.4). Power and cooling system, cables, optical fibres and the electronics for signal transmission are placed on the back of the camera. Pixels in cameras of MAGIC telescopes are PMTs equipped with light concentrators (Winston cones), which have hexagonal cross section on the front side. They are $1''$ in diameter, and have a FoV of 0.1°. Each pixel has a single-photon sensitivity and a quantum efficiency of $\approx$ 32%. The FoV of each camera is 3.6°. MAGIC-I camera was first constructed of 577 pixels of two different sizes. 397 inner pixels were the same as described above, while 180 outer, larger pixels, $1.5''$ in diameter, had a FoV of 0.2° (Figure 2.5). The camera weighted around 650 kg. It was exchanged in summer of 2012.

2.1.4 Receiver boards

Data acquisition is performed in a building named Counting house (CH), located next to the telescopes. Analogue signals produced by PMTs are transmitted to the CH via

Figure 2.5 Front and back view of the old MAGIC-I camera, with pixels of two different sizes.

optical fibres. Signal first enters receiver boards, where it is converted from optical to electrical signal, and then split into a digital branch, used by the trigger, and an analogue branch, used by the readout system. The receivers contain trigger for the individual pixel, also called the level zero trigger (LT0). They also measure trigger rate of individual pixels (IPR), which enables controlling the discriminator threshold (DT) for the individual pixels. This feature is used in the case of a bright star in the FoV of the observed source, when the system automatically raises DTs of pixels saturated by the bright star, lowering the rate of accidental triggers. Once the star position in camera changes, the IPRs are restored to normal values.

2.1.5 Trigger

Level one trigger (LT1) is a topological trigger based on temporal coincidence of nearest-neighbour (NN) pixel triggers. Whenever a LT0 is triggered, LT1 checks whether a predetermined number of neighbouring pixels were triggered in a certain time coincidence window. For 3NN and higher, pixels have to be grouped together, rather than in a chain formation. This trigger logic provides the best rejection of events that would otherwise be triggered by the night sky background (NSB). MAGIC can operate in 2 to

5 nearest-neighbour modes, however 3NN is commonly used for stereoscopic and 4NN for monoscopic observations. In old MAGIC-I camera, trigger area was confined to 325 smaller pixels, and had a FoV of 2.1°. In MAGIC-II and new MAGIC-I camera, it is confined to inner circle of 547 pixels with a FoV of 2.5°.

Level three trigger (LT3) is a coincidence trigger between two telescopes, with the gate of 200 ns. Before entering the LT3, a time delay is applied to signal from either of the telescopes. The amount of time delay depends on the pointing of the telescopes. With the distance of 85 m between the telescopes the maximum delay can amount up to 283.5 ns.

2.1.6   Readout

Signal is digitalised by the Domino Ring Sampler (DRS; [112]) chip. The DRS is a ring buffer of 1024 capacitors. Analogue signal charges capacitors with a rate of 2 GHz. The process is looped, so after capacitor 1024, capacitor 1 is recharged. When the LT3 (or LT1 for mono observations) is triggered, the voltage of 60 consecutive capacitors, which corresponds to period of 30 ns (the so called *extraction window*) surrounding the event is digitalised by an Analogue-to-Digital Converters (ADC) and stored to a hard disk. At first DRS2 was used for MAGIC-II, but it proved to be highly nonlinear. During the 2011 upgrade, DRS2 chips were substituted by DRS4. Before 2011, MAGIC-I signal was digitalised by a custom made multiplex (MUX) system with a commercial Flash Analogue-to-Digital Converters (FADC). MUX used fibre optics multiplexers and fibre optics of different length to delay signal from different channels, so 16 channels could be digitalised with a single FADC. In 2006, splitters were added, which split the signal into a low-gain and a high-gain branch to increase the dynamic range of the readout. The sampling rate was 300 MSamples/s until 2007, when it was upgraded to 2 GSamples/s. In 2011, MUX-FADC were substituted by DRS4. Width of the extraction window changed as the experiment evolved as well. During MUX-FADC era it consisted of 50 samples. DRS2 extraction window had 80 samples. It was reduced to 60 with DRS4

instalment in order to save data storage space[3].

2.2   Observations with MAGIC

Observations are planed on yearly bases. Each observation year is called observation cycle. Collaboration members propose objects to be observed and request observations time for the upcoming cycle. Based on those proposals Time Allocation Committee (TAC) decides which objects are to be observed and assigns them priority and observation time. Cycles are subdivided in observation periods, each lasting one lunar cycle. MAGIC telescopes can observe in presence of moonlight up to 75 % of lunar phase, so only 3–4 nights around full moon are not suitable for observations[4]. Based on the decision of TAC, visibility of sources, and moon phase and position, a team of two schedulers plan observation schedule for each period. Activity of known or potential γ-ray sources is constantly monitored; not just in γ-rays, but also in lower energy bands. In case of enhanced activity of a certain source, TAC can decide to activate the so called Target of Opportunity (ToO) program. Then schedule is modified during the observation period. The schedule can also be modified during the given period in case of technical problems.

The telescopes are operated from the CH. An observation shift crew consists of 4–5 Collaboration members. Operators are usually people with less observation experience. They stay at the telescope site for four weeks. The shift leader and the deputy shift leader stay for three weeks, but the shift leader starts the observation period with operators, and the deputy arrives a week later to finish the period. There is another shift leader that finishes one period, stays in the observatory during full moon, and starts the next period with the new shift crew. This way detailed information on current status of the system is transferred from one period shift crew to the next[5]. Telescope operation is almost fully computerised and it can be performed by a single person via *SuperArehucas*, a central

---

[3]MAGIC on average produces around 2 TB of data per night.

[4]An UV Moon filter, designed to allow observations during strong moonlight, is currently in the testing phase.

[5]Additionally, operations logs are recorded on nightly bases, with the most important events and problems compiled for each observation period.

Table 2.1 Periods in the MAGIC experiment history based on hardware upgrades and observation modes. The last column lists references where the system performance for the corresponding period was presented.

Period	Obs. mode	Telescope	Camera	Readout system	Performance Ref.
2004 – 2006	On-Off	MAGIC-I	397 (0.1°) + 180 (0.2°) PMT	FADC 300 MHz	[113]
2006 – 2006	Wobble				
2006 – 2007	Wobble	MAGIC-I	397 (0.1°) + 180 (0.2°) PMT	FADC 300 MHz + Splitters	[114]
2007 – 2009	Wobble	MAGIC-I	397 (0.1°) + 180 (0.2°) PMT	FADC 2 GHz + Splitters	[115]
2009 – 2011	Wobble	MAGIC-I	397 (0.1°) + 180 (0.2°) PMT	FADC 2 GHz + Splitters	[116]
		MAGIC-II	1039 (0.1°) PMT	DRS2 2 GHz	
2011 – 2012	Wobble	MAGIC-I	397 (0.1°) + 180 (0.2°) PMT	DRS4 2 GHz	[117]
		MAGIC-II	1039 (0.1°) PMT		
2012 – pres.	Wobble	MAGIC-I & II	1039 (0.1°) PMT	DRS4 2 GHz	[118, 82]

control software. Only in the beginning and the end of the night, when telescopes have to be secured manually, at least two persons are required. However, for safety reasons, it is required that at any time at least three persons are present. This is especially important in case of technical problems that require entering telescope area during the night. A crew member is never allowed to enter the telescope area alone, it has to be done in pair. Another crew member stays in the CH in contact with other two members via a hand held transceiver (walkie-talkie), ready to provide assistance or call emergency services if necessary.

MAGIC observations can be performed in two different modes: ON-OFF and wobble. In the ON-OFF mode the telescopes point directly at the source during the ON runs. The background is estimated with dedicated OFF runs, which are recorded separately in a FoV of the sky where no γ-ray signal is expected, but the NSB and zenith angles match the ON observations. It is imperative that the telescopes conditions are the same for the ON and the OFF data to avoid additional systematic effects. In the so-called *wobble* (also known as false-source) mode [119] the telescopes are not pointing directly at the source position, but 0.4° away. Accordingly, wobble data do not require dedicated OFF runs since the background can be estimated from points in the camera that are equivalent to the source position. Those positions are equidistant from the camera centre and have sufficient separation from the source location so that the expected γ-ray signal does not spill over into the OFF region.

MAGIC usually observes in stereoscopic mode, with 3NN multiplicity setting of LT1. Individual pixel DTs for dark time are around 5 photoelectrons (phe), which results in IPR of about 0.8 MHz. LT1 rate is then around 15 kHz and LT3 200–250 Hz. Although individual pixels are mostly triggered by the NSB, after LT1 topology and LT3 coincidence triggers are applied, only about 50 events out of those 200 are due to NSB. Additional 25 calibration and 25 pedestal measurement events per second are stored.

2.2.1   *iScream*

In any experiment, and especially one as complex as MAGIC, the state of all subsystems has to be constantly monitored during operations. There are two main reasons for that. First, any parameter having a value outside of a normal operation range can point to a technical problem, which, if not attended promptly, can cause damage to the system, or even endanger the safety of the shift crew. Second reason is that subsystems not operating within the optimal range may result in a low data quality. Each of the MAGIC telescopes is equipped with several subsystems. Additionally there are subsystems not associated to any specific telescope. Although most of the subsystem control programs do have a graphic user interface, it would be impossible to monitor all of them simultaneously.

For that purpose the author wrote a computer code called *iScream* (Interactive Surveillance system for Checking the Report files and Exposing Alerts in MAGIC). It receives reports from the main control code *SuperArehucas* containing current parameter values from all subsystems that are monitored. These values are stored in several databases (DB), plotted and published on an internal MAGIC operations website (Figure 2.6). In case any of the monitored variables reaches a value outside of normal operations range, a visual and auditory warning is issued to alert the shift crew.

iScream is written in programming language Python, using RRDtool[6], an OpenSource tool for logging and plotting time series data in round-robin database (RRD). RRD stores data in a circular buffer. Each value can be stored as a standalone value, or added to a time bin to obtain averaged values. The length of a database is determined by a programer, but after a full circle, old data are overwritten by new entries.

iScream structure and functionality

SuperArehucas and *iScream* are both located in a computer designated as *pc1*. The path to *iScream* program files is: */home/control/SA++/rrd/*. *iScream* consists of the

---

[6]oss.oetiker.ch/rrdtool/

Figure 2.6 Website of the *iScream* monitoring tool.

main program, four subroutines and a configuration file. The main program file is *rrd-scream.py*, and the subroutines are *rrdscreamCreate.py*, *rrdscreamPlot.py*, *rrdscream-Publish.py* and *rrdscreamUpdate.py* (*Create*, *Plot*, *Publish* and *Update* for short).

Subroutine *Create* was used in the beginning of the monitoring to create databases. At the moment there are six databases where values are stored: *hourly*, *daily*, *weekly*, *monthly*, *yearly* and *decadally*, located in *pc1:/home/control/SA++/rrd/db/*. These databases store data for the period suggested by their names. The *hourly* database stores every value reported within the last hour, and its purpose is to make subsystems monitoring easier for the shift crew. The values in other databases are averaged with different time binning, and although they can also be of use to the shift crew as a reference to previous observations, their main purpose is to identify possible trends and their causes in a longer time period. For example a small but constant change in some value over a long period might indicate a deterioration of some piece of equipment. Such trend could not be spotted in *hourly*, *daily*, or even *weakly* or *monthly* plots. However, it might become noticeable in a *yearly* plot. In the future the need for monitoring new variables might rise, or we might find that a different time step in storing data would

pc1:

rrdreport.txt
  • created by SArehucas
    every 20sec

rrdscreamUpdate.py
  • reads rrdreport.txt
  • updates dbases
  • issues an alert to pc32

rrdscreamPlot.py
  • plots graphs

pc32:
  alerts & warnings
  • popups on screen
  • audio with voice

wwwint:
crontab
• copies plots

www:
  webpage
  • reloaded every 30s
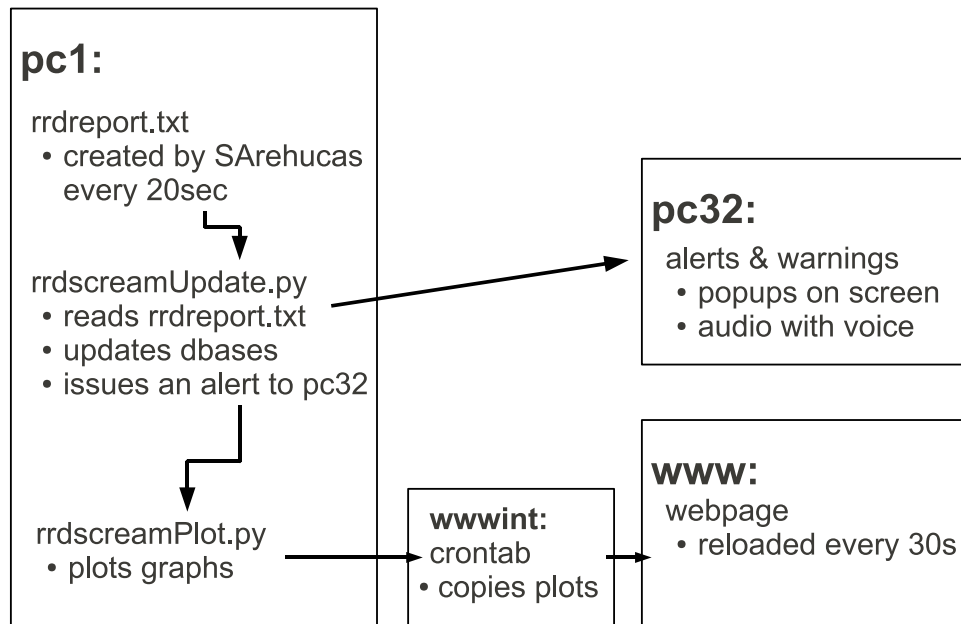
Figure 2.7 Locations and functionalities of different parts of *iScream.*

better meet our needs. Since an existing database cannot be modified, new databases will be created by the subroutine *Create.* For example a new kind of trigger (*Sum-Trigger*) was installed recently, and its subsystem parameters are expected to become part of the *iScream* monitoring program in the near future. When writing the code for *iScream,* we anticipated such upgrades and created databases that store 121 values. With 81 variables currently being monitored, we have 40 spare slots for additional variables. Adding *Sum-Trigger* variables will not fill all those slots, so subroutine *Create* will not be necessary at that point. However a major upgrade (e.g. commissioning of another telescope) would require extending databases.

Subroutine *Publish* is used to create a template for the *iScream* website. Just like *Create,* it is used only when significant modifications to the monitoring program are required. Subroutines *Update* and *Plot,* on the other hand, are constantly called. *iScream* is automatically started by *SuperArehucas,* which also creates a report, a single line textual

file located in *pc1:/home/operator/SA++/trash/rrd/rrdreport.txt*, which contains current values for all variables from all subsystems that are monitored, every 20 s. A Cron job is set up to call *iScream*'s subroutines *Update* and *Plot*. Subroutine *Update* reads *rrdreport.txt*. Since it contains 81 value plus a creation timestamp, and the databases expect 121 values, the report is first extended by blanks up to the full length, and then the databases are updated. Next, the *Update* subroutine checks if any of the monitored variables has a value outside of normal operations range. If so, a warning for the shift crew is prepared and sent to computer *pc32*, which alerts the crew. Next the *Plot* subroutine is called to plot the new values in all the databases except for the *decadally*. Plots typically have three regions, the normal operation region, which is white, and warning and alarm regions, which are yellow and red, respectively. Below each plot, all variables that are shown in it are listed, including their minimal, maximal and last value. In case some value in certain graph reaches a warning or an alarm state, the graph background will turn yellow or red, respectively, and it will remain in that colour until the status changes. The plots are created in *pc1:/home/control/SA++/trash/rrd/graphs/*, and then copied by a Cron job in computer *wwwint* to computer *www*, which hosts the *iScream* web page.

All computers included in this process are located in CH. The *iScream* structure we have just described is shown in Figure 2.7.

Alerts

The shift crew is alerted by a visual message in a form of a pop-up, which appears on the monitoring screen, stating the variable that is either too low or too high and in which plot it is shown. The pop-up remains until acknowledged by clicking it. At the same time an audio message with the same content is read by a speech synthesizer. Additionally, the background of the plot in which the abnormality has appeared changes colour. There are two levels of alert states. The warning state alert is issued while a certain value is still in the normal operation range, but closing to the borderline. If a

borderline is crossed, the subsystem is in an alarm state. While a warning state requires only closer monitoring, an alarm state requires an immediate reaction from the members of the shift crew.

Before creating an alert message, the *Update* subroutine first checks whether the given variable was already in a warning or alarm state in the previous report. If so, the shift crew is considered to have already been warned, and no new warning is issued. In case a variable remains in a warning, or an alarm state for a longer period of time, issuing a new pop-up and sound alert every 10 seconds would distract the crew members, and their attention would be more focused on acknowledging the alerts, than on solving the problem that caused them. The check is performed by creating an auxiliary file */home/control/SA++/trash/rrd/GraphsInAlarm.tmp* after each update. It contains statuses of all variables after the last update. Possible statuses are integers between -2 and 2. Negative values are for lower boundaries, and positive for upper ones. 0 meaning given variable is in normal range. Statuses -1 and 1 denote warning, and -2 and 2 alarm states.

Configuring *iScream*

The configuration file *rrdscream.conf* contains paths to locations of databases, report file and graphs. It configures the databases by defining their name, starting point, time interval between consecutive entries, number of consecutive entries which are averaged, and length. It also contains a bit that determines whether plots for each database are plotted or not.

Plots are also configured by *rrdscream.conf*. For each monitored variable, the name, unit, minimum and maximum value are given. The boundary values for warning and alarm states are defined. Whether a warning or an alarm should be raised is controlled by *WarnEnable* and *AlarmEnable* bits. Bit *Plot* controls whether each plot will be plotted or not.

The origin of *iScream*

The first version of *iScream* was written by Gianluca Giavitto, in programming language
C++. However, C++ is not the best choice of programming language when parsing text
and continuous plot updating is required. For that reason, the graphs were plotted with
a delay of a few minutes. As a consequence, the shift crew was notified of occurring
problems too late. The new *iScream* written in Python shares only the name and
purpose with the version written in C++. The entire code was written anew. The
author participated in a major system upgrade in 2012 (Table 2.1), at which time, he
wrote the code for the new *iScream*. The program is constantly used during observations
as part of the standard observation procedure. It is maintained by the author.

2.3 MAGIC data analysis

MAGIC data are analysed by a set of programs called MARS (MAGIC Analysis and
Reconstruction Software) [120]. It is written in C++ in ROOT[7] data analysis frame-
work [121]. MAGIC data analysis chain can be divided in low, intermediate, and high
level data processing (Figure 2.8). Low level data processing is performed automatically
in the observatory each day after the data taking has finished. This is usually referred
to as On Site Analysis (OSA). Afterwords data are transferred to Port d'Informació
Cientifica (PIC)[8] in Barcelona, where they are stored, and re-analysed in case of major
modifications in analysis chain or bugfixes. Analysers acquire data from PIC and per-
form intermediate and high level analysis. In order for analysis results to be accepted
as valid, at least two independent analysis have to be performed and the results have to
be consistent. In what follows each step is described.

---

[7]ROOT is maintained in CERN. root.cern.ch/drupal
[8]www.pic.es/index.gsp
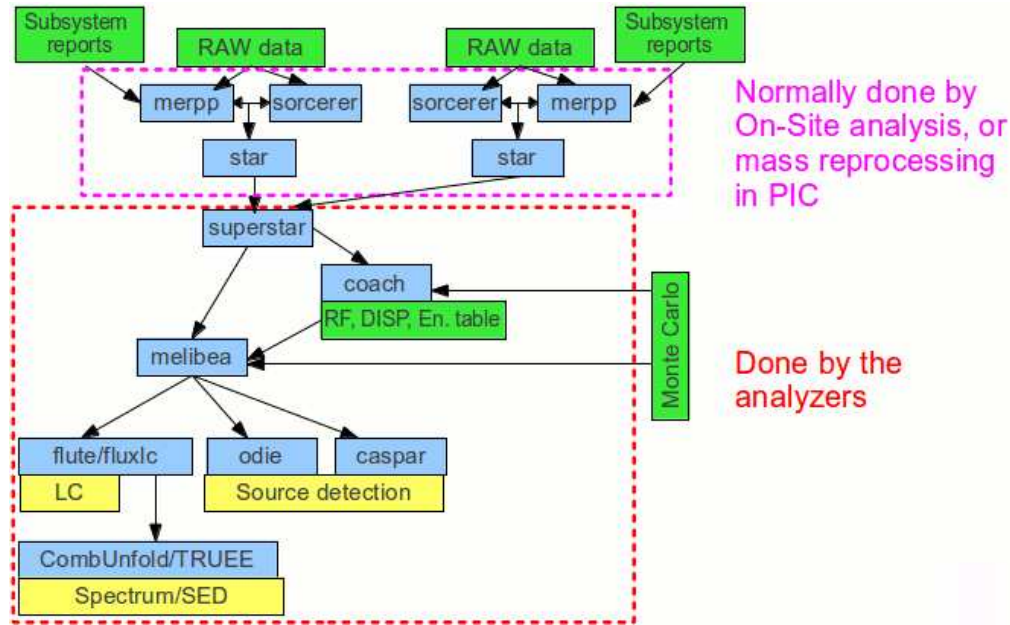
Figure 2.8 Standard MAGIC analysis chain. Image credit: J. Sitarek.

2.3.1 Low level data processing

During observations data are stored in binary format files. In order to be manageable they need to be converted to ROOT format. This is done by a program called *merpp*. Simultaneously with conversion, data are merged with subsystem reports, which contain information on taken observations and condition in which they were performed.

Calibration

Before the start of data taking on each individual source, a pedestal and calibration data run is taken. Additionally pedestal and calibration data are taken during observations with the rate of 25 Hz each. These data are used to measure the bias and background noise level, and response of individual pixels and associated electronics respectively. In case of DRS chips, additional run has to be taken before the observations in order to calibrate the pedestal level, and in case of DRS2 for linearity calibration. Calibration programs subtract pedestal levels and convert the digitalised voltage of each pixel in each sample to a number of phe, and to determine the arrival time of the signal. In the

era of MUC-FADC readout, calibration was performed by a program called *callisto*. It used a simple cubic spline to interpolate samples. The signal intensity was determined by integrating slices around the peak, and the arrival time as the position of the half maximum of the rising edge of the spline. Since the DRS chips were introduced, a program called *sorcerer* is used. It sums the signal of 6 consecutive samples within the extraction window. The highest sum is taken as the signal intensity, while the arrival time is the average position of the chosen 6 samples. This is so called sliding window algorithm.

Image cleaning and parametrisation

In order to estimate the type of primary particle, its energy and direction, the image has to be parametrised. Before calculating parameters, image has to be *cleaned*. When an event is recorded, only a small number of pixels contain Cherenkov light coming from the EAS. Signal in most of the pixels comes from NSB and electronic noise. Cleaning is a process of determining which pixels contain Cherenkov light, and which should be discarded. The algorithm used in MAGIC is called *Absolute Image Cleaning*. It is based on number of phes contained pixels. There are two thresholds: Q_{core} and $Q_{boundary}$ ($Q_{core} > Q_{boundary}$). All the pixels with charge greater than Q_{core} are selected in the first step. Any selected pixel that has at lest one first neighbour that was also selected is marked as core pixel. All pixels which have at least one neighbouring pixel marked as core pixel, and have charge greater than $Q_{boundary}$, are marked as boundary pixels. After upgrading MUX-FADC readout from $300\,\mathrm{MSamples/s}$ to $2\,\mathrm{GSamples/s}$, additional cleaning criteria based on temporal information was used. After choosing core pixels, their arrival times are compared. If the arrival time of a core pixel is not within a window of $4.5\,\mathrm{ns}$ with respect to the mean arrival time of all core pixels, that pixel is discarded. A similar criteria is applied to selection of boundary pixels: the arrival time has to be within $1.5\,\mathrm{ns}$ with respect to its neighbouring core pixel. When only absolute cleaning is used, Q_{core} and $Q_{boundary}$ are set to 10 and 5 respectively. Use of time image cleaning allows relaxing of those criteria to 6 and 3.5 respectively.
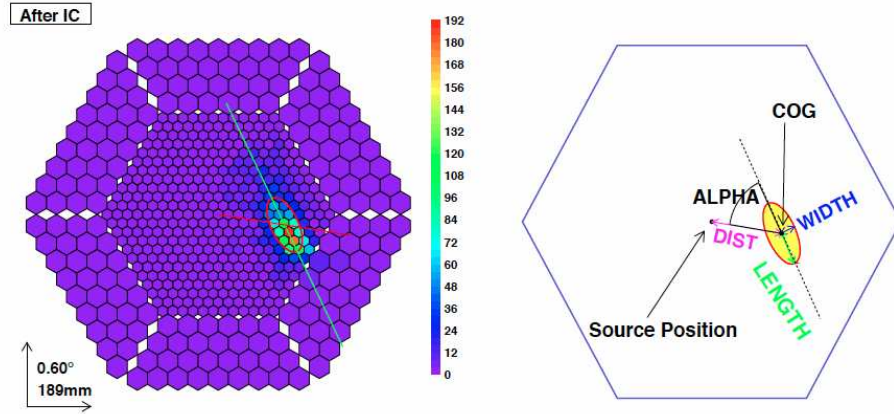
Figure 2.9 Reconstructed image of an EAS in MAGIC-I camera configuration, with some of the main image parameters. Image credit: S. Lombardi.

Once the image has been cleaned, following image parameters are calculated (Figure 2.9):

Size: total number of phes in the shower image. In first approximation it is proportional to the primary particle's energy.

CoG: centre of gravity of image, given as a pair of values that determine the position of weighted mean signal in the camera.

Length: length of a semi-major axis of the shower ellipse. It is correlated to the longitudinal development of the shower.

Width: length of a semi-minor axis of the shower ellipse. It is correlated to the transversal development of the shower.

Conc-n: fraction of phes contained in the n brightest pixels.

M3long: third momentum of the image along the major axis. It is positive if it points towards the camera centre, and negative otherwise. Head of the image is expected to have higher concentration of phes compared to the tail, so it is used to determine the direction of the image.

Leakage: fraction of a signal in the outermost ring of the camera to the total size. Images of EAS with large impact parameters (explained in Section 2.3.2) will record only part of the shower. If the leakage is too high, the image will be impossible to reconstruct.

NoI: number of islands, i.e. distinct groups of pixels that survive image cleaning.

α: the angle between the major axis and the line connecting the CoG with the position of the source in the camera.

Dist : the distance between the CoG and the position of the source in the camera.

Time gradient: the arrival time in pixels along the major axis is fitted with a linear function. The linear coefficient is time gradient or time profile of the image.

Time RMS: the spread of arrival times of pixels included in the image.

Image cleaning and parametrisation is performed by program *star*. Image parameters were first introduced by Hillas in 1985 [122].

2.3.2   Intermediate level data processing

Data quality selection

Data quality selection is done by program *quate*. It calculates average values of parameters explained in the previous section per data file (around 1 min of single telescope data in current configuration). It also calculates average event rate, and other parameters connected to the quality of data (e.g. cloudiness) can be added as criteria. Based on average values, and tolerance range set by the analyser, quate discards data files that do not satisfy set criteria.

Stereo data reconstruction

Program *superstar* matches events in MAGIC-I and MAGIC-II data and geometrically reconstructs showers in 3D. This results in additional parameters (Figure 2.10):

Shower direction: if shower images from both telescopes are superimposed on a single camera, the crossing point of major axes of shower images is the incident direction in the sky of the primary γ-ray.

Impact point: point on the ground where the shower axis points to. Similarly determined as the previous parameter, but with taking the relative position of telescopes in account (no superimposing of shower images).

Impact parameters: shower direction and impact point determine the shower axis. Impact parameter for each telescope is the distance of the telescope to the shower axis in a plane perpendicular to to the shower axis.

Height of the shower maximum (h_{max}): the intersection of the shower axes and the lines going from the telescopes to the position of the CoG in the sky. In reality the three lines will form a triangle and never cross, so maximum height is taken as the height at which the triangle has the smallest perimeter.

Cherenkov radius (r_C): the radius of Cherenkov light pool on the ground resulting from an $86\,\mathrm{MeV}$ electron at the h_{max}.

Cherenkov density: the density of Cherenkov light on the ground produced by a $1\,\mathrm{m}$ track of an electron with the same characteristics as in r_C.

Disp: the distance between the CoG and the impact point. It is actually evaluated for each telescope separately, but it is used in stereo data reconstruction and proved to be a useful criteria for γ/hadron separation. For a single telescope two impact points will be determined, so there will be four pairs of impact points. If the squared angular distance between points in all pairs is greater than $0.05\,\mathrm{deg}^2$, the
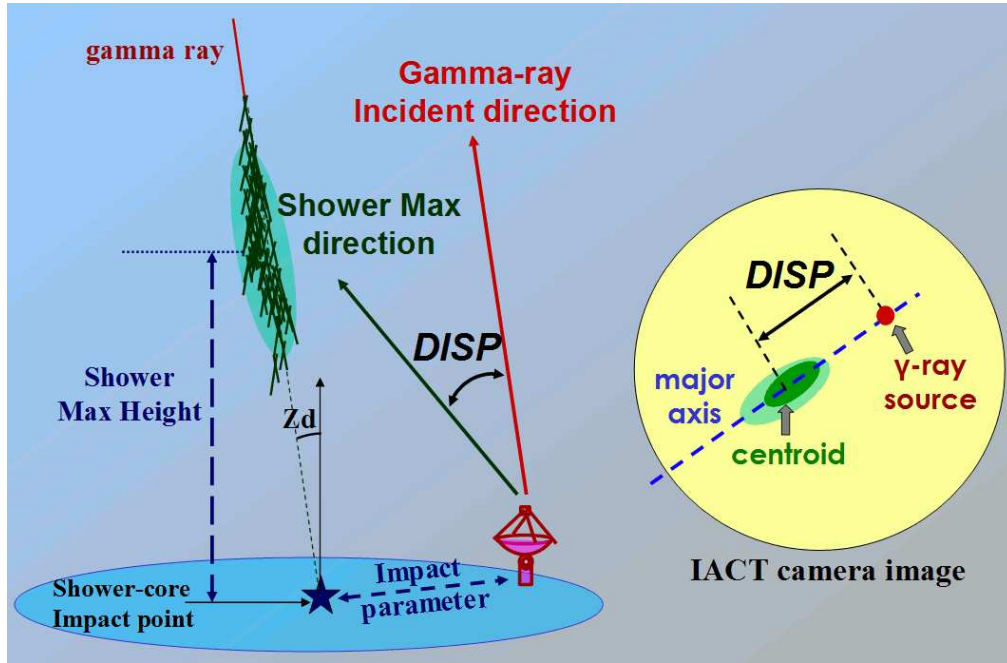
Figure 2.10 Geometry of EAS observation. Image credit: P. Colin.

event is discarded. The impact point is then obtained by averaging disp parameters of both telescopes.

γ/hadron separation

γ/hadron separation is based on a parameter called *hadronness*, which is basically a probability that the given event was not caused by a γ-ray. It is estimated using a Random Forest (RF) algorithm, and can have values between 0 and 1. RF is grown using Monte Carlo (MC) simulations of γ-ray showers and actual data to represent hadrons. It is assumed that the fraction of γ-rays contained in observation data is $\sim 10^{-4} - 10^{-3}$ for monoscopic observations. Stereo trigger is more effective at hadron events rejection, so the sample contamination with γ-rays will be higher by an order of magnitude. In this case, the data in which no excess γ-ray signal was detected will be used. The RF decision trees are grown in the following way[9]: a parameter (size, length,

---

[9]For this purpose MC data will be referred to as gammas, and observation data as hadrons.

width...) is chosen randomly, and the value that most efficiently splits the data sample to gammas and hadrons is determined. The process continues until the whole sample is separated to gammas and hadrons. This is repeated for each tree (usually 100 trees are grown). When RF is applied to real data, each event faces a decision tree. Based on values of parameters it follows a certain path down the tree and it is assigned value 0 or 1, depending on whether it landed with gammas or hadrons. After passing 100 trees, hadronness is the sum of results of all trees divided by 100.

For MAGIC-I data analysis a program called *osteria* was used for growing RF. RF was also used for energy reconstruction. The RF program for stereo data is called *coach*. The disp parameter is estimated on the same principle also using coach, but energy is reconstructed using lookup tables (LUT). LUTs are also created by coach, based on MC data which are divided in bins according to values of parameters considered for energy reconstruction. A multidimensional table contains mean energy for each combination of parameters, which is assigned to real event with given values of parameters. RFs and LUTs are applied to real data with program *melibea*.

2.3.3   High level data processing

On this level, the final analysis results, such as spectrum, light curve etc. are obtained.

γ-ray signal

The squared angular distance between nominal source position in the camera and the reconstructed source position (shower direction) is θ^2. In order to count the number of γ-rays and check for excess signal, we plot the θ^2 distribution of events (Figure 2.11). Prior to that, cuts based on hadronness and size are applied to data to clean the sample from what we believe to be hadrons. In order to estimate the background radiation, a θ^2 distribution is plotted for events in the OFF-source region. For ON-OFF observation mode (see Section 2.2) it is the centre of the camera pointing to OFF region in the sky. In case of wobble observations, the OFF-source position is taken as the point symmetric
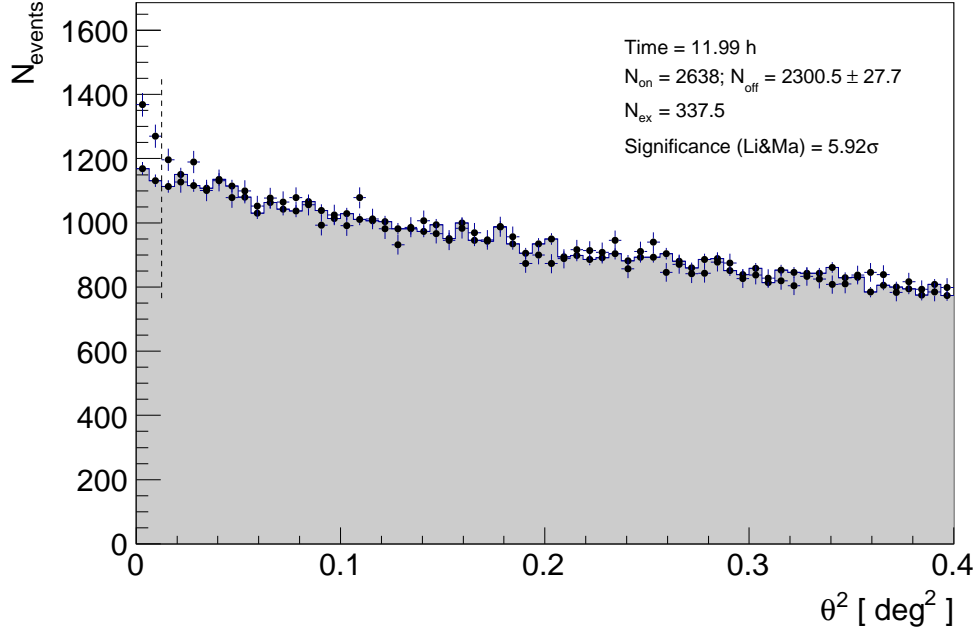
Figure 2.11 An example of a θ^2 plot. ON-source events are represented with black points, and OFF-source ones with grey area. Vertical dashed line represents the cut on θ^2.

to to the source position with respect to the camera. For wobble observations more than one OFF-source position can be used, and the number of events will be normalised by the ratio of number of ON and OFF-source positions (α). However, if the number of OFF-source positions is too high, γ-rays from the source position might spill over into OFF-source position. Usually 3 OFF-source positions are used. After the events are distributed according to θ^2, a cut is applied. All events from ON-source region, that have θ^2 less than a given cut, are counted as $N_{\rm on}$, and the events from OFF-source region that pass the θ^2 cut are counted as $N_{\rm off}$. The significance of the signal is calculated using equation 17 of [123]:

$$\sigma = \sqrt{2 \left\{ N_{\rm on} \ln \left[\frac{1+\alpha}{\alpha} \left(\frac{N_{\rm on}}{N_{\rm on} + N_{\rm off}} \right) \right] + N_{\rm off} \ln \left[(1+\alpha) \left(\frac{N_{\rm off}}{N_{\rm on} + N_{\rm off}} \right) \right] \right\}}. \quad (2.1)$$

Spectrum

The differential energy spectrum is defined as the number of γ-rays of a certain energy that pass through a unit area in a unit of time:

$$\frac{\mathrm{d}\Phi}{\mathrm{d}E} = \frac{\mathrm{d}^3 N_\gamma}{\mathrm{d}E\,\mathrm{d}A_{\mathrm{eff}}\,\mathrm{d}t_{\mathrm{eff}}}, \tag{2.2}$$

where A_{eff} is effective area, t_{eff} effective time, and N_γ is the number of excess events i.e. the difference between N_{on} and N_{off}. In order to evaluate the spectrum, data are divided in bins according to energy, and for each energy bin, effective area and effective time are evaluated as follows. A_{eff} is calculated using MC simulated γ-rays. $N_{\gamma,\mathrm{tot}}$ simulated γ-rays are produced in an area above the telescopes A_{sim}. After the cuts are applied to those events, $N_{\gamma,\mathrm{sel}}$ survive. Effective area is then calculated from

$$\mathrm{d}A_{\mathrm{eff}} = \mathrm{d}A_{\mathrm{sim}} \frac{N_{\gamma,\mathrm{sel}}}{N_{\gamma,\mathrm{tot}}}. \tag{2.3}$$

Effective time is the difference between total observation time and total dead time, which is constrained by the readout. For DRS2 chip it was $0.5\,\mathrm{ms}$, and with DRS4 it improved to $26\,\mu\mathrm{s}$ per event.

Due to finite resolution of the instrument and non-controllable experimental conditions (e.g. weather), the measured spectrum is not necessarily the true spectrum of the source. The two values are connected through the formula

$$g_i = \sum_j M_{ij} \dot{f}_j, \tag{2.4}$$

where g_i are values of measured spectrum in corresponding energy bins, f_j values of real spectrum in corresponding energy bins, and M_{ij} is called migration matrix. In MAGIC, M_{ij} is determined using MC simulated γ-rays. Determining the real spectrum is a matter of matrix inversion. This is called unfolding. Unfortunately, M_{ij} is not a square

matrix, and the minimisation method ($\chi_0^2 = \sum_i (g_i - \sum_j M_{ij} f_j)^2$) gives unstable results. Regularisation is performed by adding a regularisation term $Reg(\vec{f})$ in the following way:

$$\chi^2 = \frac{\omega}{2} \chi_0^2 + Reg(\vec{f}), \tag{2.5}$$

where ω is strength of the regularisation. Different algorithms (Bertero [124], Schmelling [125], Tikhonov [126]) use different regularisation terms. Alternative way is called *forward unfolding*, which assumes a parametric analytical form for the real spectrum and minimises χ_0^2 numerically [127].

As we shall see in Chapter 6 (Figure 6.2), majority of AGN spectra measured with MAGIC telescopes are consistent with having a power-law shape (Figure 2.12)

$$\frac{\mathrm{d}N}{\mathrm{d}E} = N_0 \left(\frac{E}{E_0} \right)^{-\Gamma}, \tag{2.6}$$

where N_0 is the number of photons of energy E_0, that hit a unit area in a unit of time. E_0 is usually referred to as the pivot energy. Its value is typically taken between $100\,\mathrm{GeV}$ and $1\,\mathrm{TeV}$.

Light Curve

Light curve shows temporal evolution of integrated flux, which is calculated simply by counting all the events in a certain time bin with energy higher than some E_{min} (see Figure 2.13). Time bins and E_{min} are determined by the analyser.

In case the relative error of the integral flux is greater than 0.5, an upper limit is calculated for that time bin. Knowing the performance of the system and assuming spectrum of the observed source, the number of expected signal events is

$$g = t_{\mathrm{eff}} \int_0^\infty \mathrm{d}E \frac{\mathrm{d}\Phi}{\mathrm{d}E} A_{\mathrm{eff}}. \tag{2.7}$$
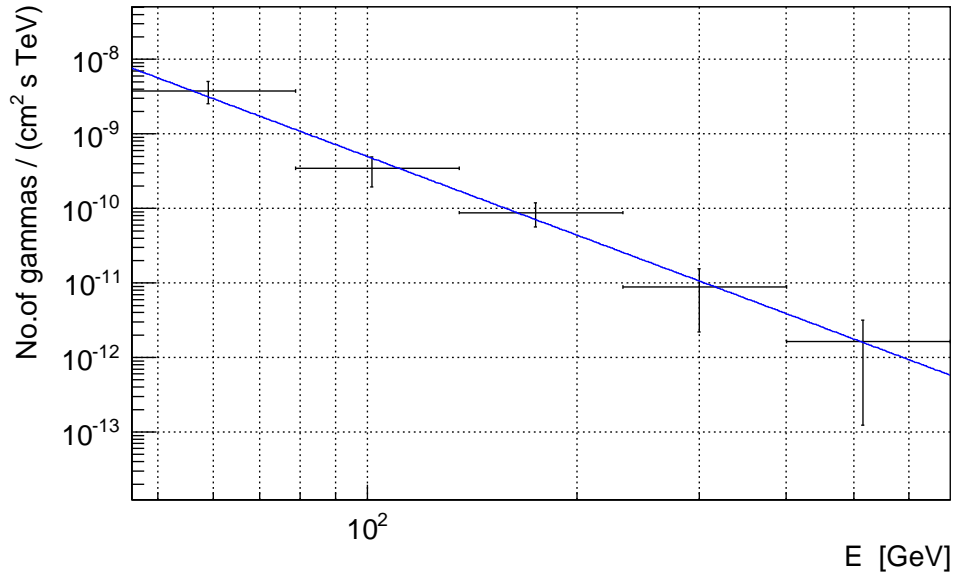
Figure 2.12 An example of a power-law shaped spectrum. Horizontal "error bars" represent widths of energy bins.
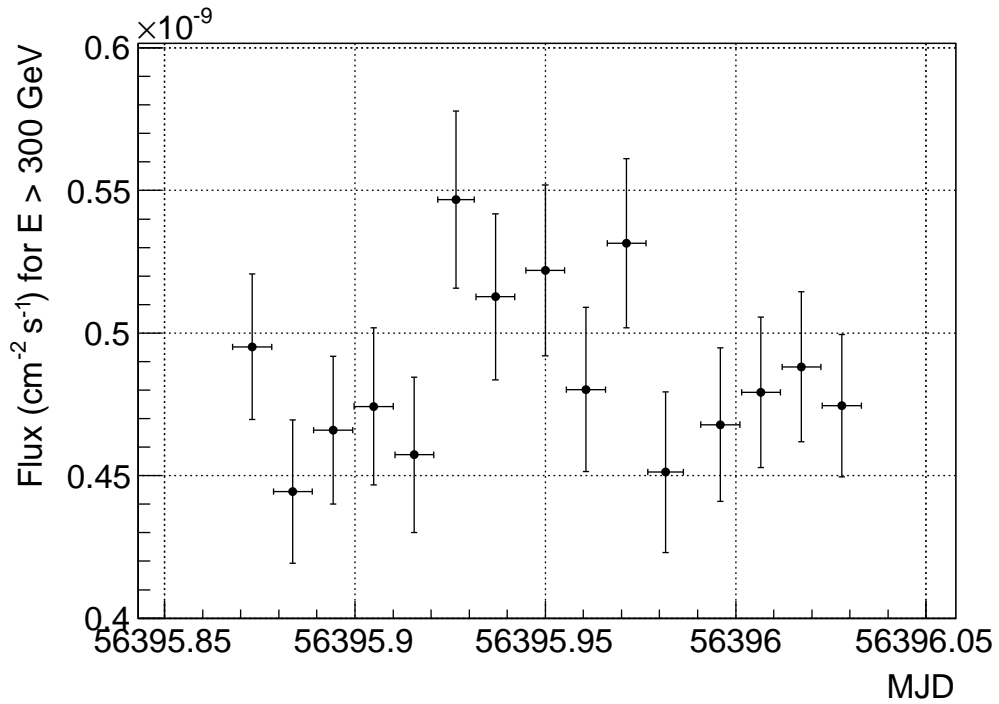
Figure 2.13 An example of a light curve. Horizontal "error bars" represent widths of time bins.

For number of detected events less than g, one can invert (2.7) to determine the spectrum that produced the detected signal. From that we can calculate upper limit on the integral flux. The same procedure is performed to calculate upper limits in certain energy bins of spectrum in case the relative error of that spectral point is greater than 0.5.

High level analysis steps for MAGIC-I data were performed by program *fluxlc*. For stereo data program *odie* plots θ^2 plots and calculates significance of the signal, and spectrum and flux are calculated by *flute*. Spectrum unfolding is performed by *combunfold*.

significance.C macro

As we already saw, each event is characterised by a set of parameters. When performing high level data analysis, a set of cuts on those parameters are applied to the data in order to separate possible signal from the background. Usually cuts are placed on size, hadronness and θ^2, but any of the parameters listed above can be used. By applying cuts, we are in fact selecting a part of the parametric space. Our goal in doing so is to select the part that has the highest ratio of signal to background events. If the chosen cuts are too loose, many background events will be contained in the sample, and the signal to noise ratio will be low. By choosing too strict cuts, we will get much cleaner sample, but also lose a lot of signal events.

For the purpose of cut optimisation, the author devised a ROOT macro called *significance.C*. It uses Crab Nebula data to simulate the expected signal from the source that is being studied, and choose the set of cuts that will result in the highest significance. First the analyser has to analyse the data taken on Crab Nebula. Crab Nebula is very bright and rather stable source, so it is considered a "standard candle" for the VHE γ-ray observations. Because of that reason it is often observed and there is abundance of data taken at different observing conditions. It is very important that the chosen Crab Nebula data were taken in the same observing conditions (zenith angle, weather conditions, moonlight etc.) as the data on which the cuts will be applied.

After analysing Crab Nebula data and calculating the spectrum, the analyser runs *sig-*
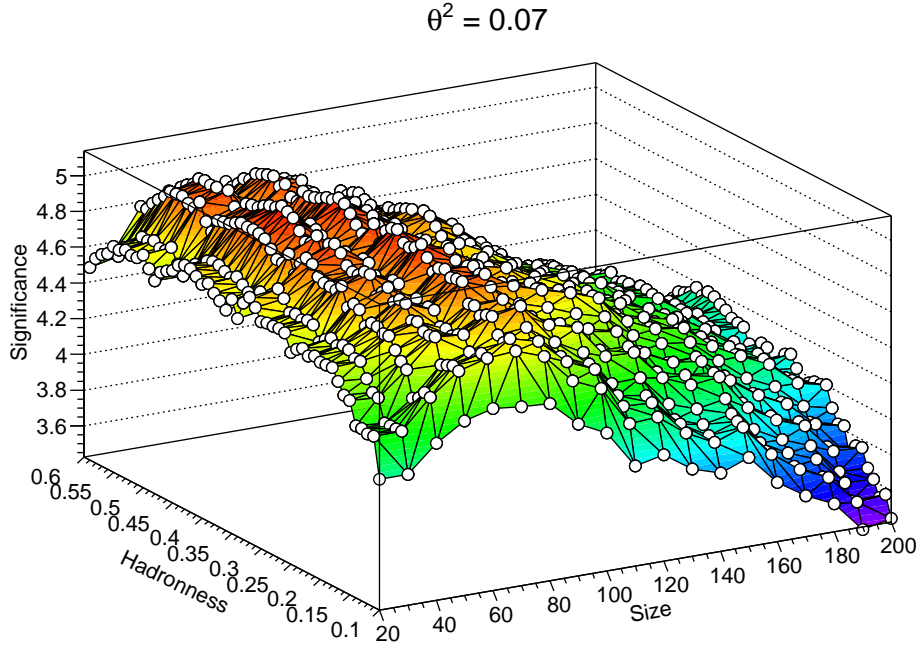
Figure 2.14 An example of a *significance.C* output.

nificance.C on those data. The input parameters are the spectrum of the Crab Nebula data and the expected spectrum of the source that is being studied. In addition, the analyser chooses boundaries on energy and zenith, as well as ranges and step size in the parametric space spanned by θ^2, hadronness and size. *significance.C* then covers the parametric space. For each set of cuts, the number of signal and background events that satisfy the chosen cuts is counted. Those numbers are then scaled based on the ratio of the assumed source spectrum and the calculated Crab Nebula spectrum. The scaled numbers are used as N_{on} and N_{off} in equation (2.1). In this way, significance is calculated for each set of cuts applied on θ^2, hadronness and size. The set that results in the highest significance is considered optimal and is later applied to the data of the source we are interested in. In addition, a histogram of significances obtained for different set of cuts is plotted (Figure 2.14). Checking the histogram, the analyser can make sure that the distribution of significances is smooth and that there are no sudden jumps in the distribution, which would point to a fluctuation.

Macro *significance.C* proved to be quite useful for analysis of MAGIC-I data, and it was used to optimise cuts for M87 data analysis used in the study presented in Chapter 3.

Chapter 3

Messier 87

3.1 Introduction

Messier 87 (M87) is a type-cD (supergiant elliptical) galaxy situated in the centre of the Virgo cluster of galaxies at a distance of 16.7 ± 0.2 Mpc from Earth [12][1]. The redshift is estimated to $z = (4.238 \pm 0.017) \times 10^{-3}$ [129].

It is populated dominantly by old, population II stars, and it is very poor in dust (the total mass of dust in the entire galaxy is less than $7 \times 10^4 M_\odot$ [130]). Orbital motions of the stars in M87 ware believed to be completely randomised [131], and the galaxy appeared to spherical in profile [132]. Recently, however, an evidence of a bulk rotation and of a more complex shape of the galaxy was found [133]. Regardless of this new finding, what we see now in M87 is most probably a result of (possibly many) galactic mergers, which in great respect randomised orbits of stars and "cleaned up" the interstellar dust.

M87 is a dominant galaxy in every respect. Its stellar halo extends up to $\simeq 150$ kpc [134]. The luminous mass is estimated to $(4-5) \times 10^{11} M_\odot$ [135], however, according to Gebhardt and Thomas [28], mass-to-light ratio is 6.3 ± 0.8, so the actual mass of the

---

[1]A more recent research [128] puts M87 at 16.4 ± 0.5 Mpc, however in our research we used the value from [12], and both results are within errors.

galaxy is much higher. Based on the two-component model of Nulsen and Böhringer [136], but using their own measurements, Doherty et al. [134] estimate the galaxy mass within a radius of $\simeq 149\,\text{kpc}$ to be $\simeq 5.4 \times 10^{12} M_{\odot}$ and the mass of the cluster dark matter mass in the same radius $\simeq 1.2 \times 10^{13} M_{\odot}$. There are 12000 ± 800 globular clusters orbiting M87 [137]. Due to its vast mass, M87 is not just in the centre — it in fact is the centre of the Virgo cluster, and of our local universe.

The centre of the galaxy harbours a SMBH with a mass of $(6.4 \pm 0.5) \times 10^{9} M_{\odot}$ [28]. It powers an AGN that emits a relativistic jet of matter, extending over $20''$ [138], which is equivalent to a distance of $2\,\text{kpc}$ from the nucleus. The jet was first discovered by H. D. Curtis [9] in 1918, and since then it has been observed and investigated extensively.

The jet in M87 is inclined from our line of sight. Depending on the reference the inclination values vary between $10°$ [139] and $45°$ [140]. This distinguishing characteristic combined with proximity of M87, gives us opportunity to study different parts of the jet, which is not homogeneous but shows several distinctive regions. Throughout the jet several brighter spots (knots) are visible, often characterized by superluminal motion with apparent speeds reaching $\sim 6\,c$ ([141, 139]). The one closest to the nucleus (60 pc), known as HST-1 [139], contains blobs with superluminal motion, as revealed by radio Very-long-baseline interferometry (VLBI) observations [142], and shows high variability of its optical and X-ray emission (e.g. [143, 144]). A closer inspection also indicates the existence of a counter-jet [139]. Recently, Hada et al. [145] used the core-shift effect detected in Very Long Baseline Array (VLBA) multi-frequency data between 2 and $43\,\text{GHz}$ to estimate that the central engine of M87 lies within a distance of 14–23 Schwarzschild radii of the radio core at $43\,\text{GHz}$. The jet does not end abruptly. Instead matter is spread across 80 kpc forming giant lobes. Figure 3.1 is a collection of images at different wavelengths showing jet structure in great detail.

The discovery of γ-ray emission from M87 (and more generally from radio-galaxies) stimulated an intense theoretical work aimed at clarifying the mechanisms that produce the observed radiation. Early models suggested γ-radiation to be produced in jet at kpc distances from the nucleus, through inverse Compton scattering of stellar and cir-

(A): Comparison of characteristic scales. **(B):** A 90 cm radio image of giant lobes taken with VLA. **(C):** X-ray (Chandra, upper panel), optical (V band, middle) and radio (6 cm, lower panel) images of the jet (2 kpc). Individual knots are exceptionally prominent in the X-ray image, however note that HST-1 appears merged with the nucleus. **(D):** An averaged radio image of the nucleus. The logarithm of the flux density in units of 0.01 mJy/beam is given in the colour scale. A feature to the left of the most luminous region indicates the existence of a counter-jet.

Figure 3.1 Jet of M87 at different frequencies and scales adopted from [14].

Credits: **(B):** F.N. Owen, J.A. Eilek and N.E. Kassim [47], NRAO/AUI/NSF; **(C):** X-ray: NASA/CXC/MIT/H. Marshall et al., radio: F. Zhou, F. Owen (NRAO), J. Biretta (STScI), optical: NASA/STScI/UMBC/E. Perlman et al. [146]; **(D):** [14]

cumstellar dust radiation [147]. However, this was discarded after the flux variability on time scales of day was discovered, which suggested a very compact emission region. Two main classes of models applied to the case of M87 suggest that the emission either originates in electromagnetic mechanisms acting in the magnetosphere of the black hole (e.g. [148, 149, 150]), or from the innermost regions of the jet, through the mechanism usually applied to radiation from blazars. The models from the latter class differ on the geometry of the emission regions and on the emission mechanism (e.g. [66, 65, 17, 151, 152]), but they agree that multiple regions are needed to fully reproduce the observed SED. In particular in the so called "spine-layer" model of [64, 17] the jet is structured as two concentric layers: an inner, faster (bulk Lorentz factor $\Gamma = 10 - 15$) *spine* surrounded by a slower ($\Gamma = 3 - 4$) sheath. The radiative interaction between the two regions leads to an effective enhancement of the inverse Compton emission and the possibility to decelerate the spine through the *Compton drag* effect [153]. This structure may account for the emission properties of both blazars, which are observed at small angles, so the emission is dominated by the spine, and radio-galaxies, which are viewed at larger angles and substantial observed emission originates from the layer. Another possibility is the involvement of electromagnetic cascades from relativistic electrons that propagate along the jet [154, 155]. Finally, there are models that assume that the emission originates from the jet but identify the emission region with the HST-1 knot, invoking extreme re-collimation of the flow to reproduce the fast variability (e.g. [156, 157]).

3.2 Previous observations of M87 in the HE and VHE γ-ray range

The first indication that M87 is a source of VHE γ-radiation was reported by the HEGRA collaboration [5]. During 1998 and 1999 M87 was observed for a total of 83.4 hours. The analysis showed an excess of 4.1 σ at energies above a mean energy threshold of 730 GeV.

The H.E.S.S collaboration reported a discovery with a high statistical significance of $13\,\sigma$ above $730\,\mathrm{GeV}$ [11]. The research was based on 89 hours of data collected between 2003 and 2006. The spectrum between 400 GeV and 10 TeV was compatible with a simple power-law with a spectral index of 2.62±0.35 (2004 data) and 2.22±0.15 (2005 data). Within the errors, the spectra of the two years has the same slope, although the flux normalization in 2005 is five times higher. The same study revealed a variability of the flux on time scales of two days, suggesting that the VHE γ-rays are emitted from a very compact region with a dimension comparable to the Schwarzschild radius of the central black hole.

The VERITAS collaboration detected VHE γ-radiation above 250 GeV from M87 in 2007 [13]. 44 hours of data yielded a signal with statistical significance of $5.9\,\sigma$. The spectral index of 2.31±0.17 is consistent with the H.E.S.S. measurements. No indication of short time variability was reported. The authors claim to see a correlation between the γ-ray and ASM/RXTE count rate over a time scale of several years using all previous VHE observations. It should however be noted that the soft X-ray photons detected by ASM cannot be used to resolve the nucleus or the jet structure of M87.

Fermi-LAT discovered the HE γ-radiation above 100 MeV from M87 with a significance of $10.4\,\sigma$ [158]. The discovery was one of the results of the first 10 months of the mission. No significant variability was found. The spectral index of 2.26±0.13 between 100 MeV and 30 GeV is consistent with the VHE measurements.

M87 was the first radio galaxy that was found to be a source of γ-radiation. Since then γ-rays were detected from other three radio galaxies. Namely Centaurus A [6] discovered by H.E.S.S., and NGC 1275 [7] and IC 310 [8] discovered by MAGIC. 3C 66B is another radio galaxy that might be of such kind. The first detection by the MAGIC collaboration was reported in [159]. However due to its close proximity to 3C 66A, it could not be excluded with high confidence that the VHE γ-ray emission was coming from 3C 66A.

3.3 Observations and studies of M87 by the MAGIC Collaboration

MAGIC started to observe M87 regularly in 2005 and continued to monitor it until present day. As a result several studies were performed.

3.3.1 The 2005 − 2007 low state study

The data taken in the 2005 − 2007 period resulted in a long term monitoring study [160]. A total of 154.1 hours of data was collected, out of which 128.6 hours survived the quality selection cuts. The source was detected with a significance of 7σ. The VHE γ-ray flux appears to be constant during observations. Our intention was to study the characteristics of M87 in the low emission state. Since the observations prior to autumn 2009 were performed by a single telescope, the sensitivity was much lower and a lot of observation time was required in order to obtain enough data to perform this study. For the same reason it was important to confirm that the flux was constant throughout the campaign. Figure 3.2 shows a very steady increase of excess events over observation time, implying a constant emission, and excluding any possibility of a significant flare occurring during our observations. Since the observations are not evenly spaced (often interrupted by hardware changes of the telescope) and the length of each observation run differs greatly, the binning of the light curve is not uniform. Instead, we divided the data into calender months, starting from March 2005 until May 2007. As shown in the light curve of Figure 3.3, the excess over the entire observing campaign is compatible with a fit to a constant integral flux above $100\,\mathrm{GeV}$ of $(5.06 \pm 0.77) \times 10^{-12}\,\mathrm{cm}^{-2}\,\mathrm{s}^{-1}$ with a reduced χ^2 of 0.51 (corresponding to a probability of 90%). We also analysed data for each observing night separately, but none yielded a significant detection on its own.

Since M87 is a nearby source, the absorption of VHE γ-rays due to the extragalactic background light is negligible in our energy range (see e.g. [108]). The MAGIC spectrum
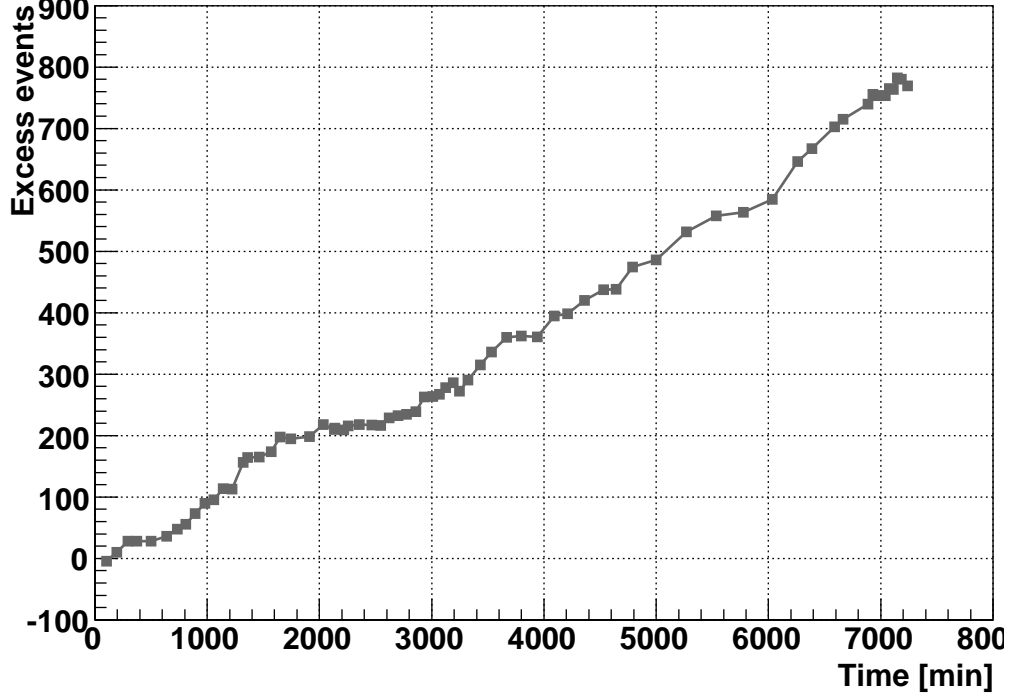
Figure 3.2 Evolution of excess events from M87 over dead-time-corrected observing time. The linear increase is consistent with a constant flux of the source during the entire observing campaign. Only wobble data are shown in this figure in order to reduce systematic uncertainties in the ON-OFF subtraction.

is well described by a single power-law: $dN/dE = N_0\,(E/300\,\mathrm{GeV})^{-\Gamma}$ with a spectral index $\Gamma = 2.21 \pm 0.21$ and a flux normalization $N_0 = (7.7 \pm 1.3) \times 10^{-8}\,\mathrm{TeV}^{-1}\mathrm{m}^{-2}\mathrm{s}^{-1}$. The MAGIC spectral points and fit are shown in blue in Figure 3.4. The spectral index derived from our observations is statistically compatible with previously reported results by H.E.S.S. and VERITAS.

Unfortunately, no contemporaneous observations in the GeV energy band were performed, so, for comparison, we report (red squares, Figure 3.4) the *Fermi*-LAT spectrum obtained integrating over the first 10 months of all-sky survey data (2008 Aug. 4 – 2009 May 31, [158]). Based on contemporaneous X-ray and radio data the authors argue that M87 was most likely in a low emission state during the *Fermi*-LAT observations. To
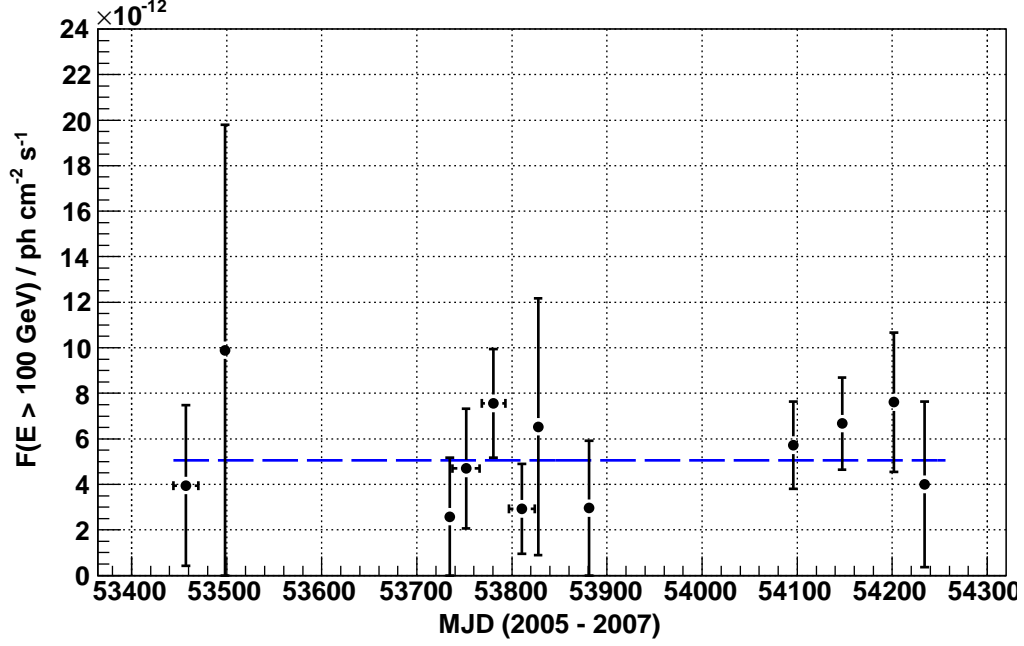
Figure 3.3 Light curve of the integral γ-ray flux above $100\,\text{GeV}$ during the 2005–2007 MAGIC observing period. The dashed blue line corresponds to the fit result of a linear function to the data points, with a reduced $\chi^2/NDF = 5.66/11$ and an average flux of $(5.06 \pm 0.77) \times 10^{-12}\,\text{cm}^{-2}\,\text{s}^{-1}$.

investigate this hypothesis further, we have performed a combined fit to the MAGIC and *Fermi*-LAT results (green line, Figure 3.4). The combined fit yields a spectral index $\Gamma = 2.17 \pm 0.03$ and a flux normalization at $300\,\text{GeV}$ $N_0 = (7.1 \pm 1.0) \times 10^{-8}\,\text{TeV}^{-1}\,\text{m}^{-2}\,\text{s}^{-1}$. The reduced χ^2 changes from 1.14 to 0.86. The fit result is statistically compatible with the standalone fit to the MAGIC data and confirms the low state during the *Fermi*-LAT observations. There is no indication of a break or change in the spectral slope. We therefore include the *Fermi*-LAT data when modelling the spectral energy distribution in Section 3.4. It is worth noting that the peak of the spectral energy distribution appears to lie at particularly low energies, below $100\,\text{MeV}$.
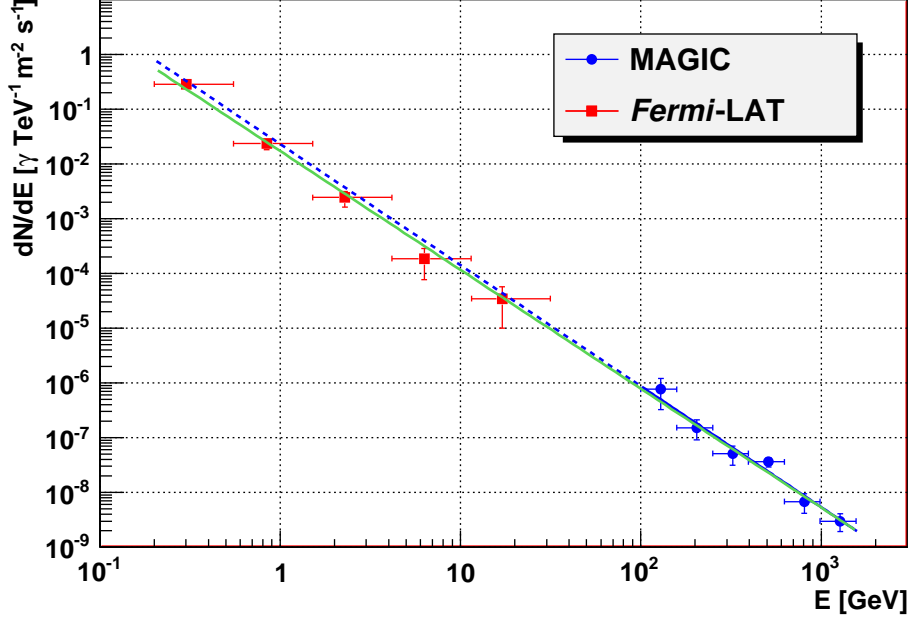
Figure 3.4 The combined *Fermi*-LAT and MAGIC differential energy flux over four orders of magnitude in energy starting from 100 MeV up until 2 TeV. The *Fermi*-LAT spectrum was obtained from [158]. The blue dashed line is an extrapolation of the fit to the MAGIC data points into the *Fermi*-LAT energy range, while the green line represents the combined fit to the MAGIC and *Fermi*-LAT data. No break or change in the spectral slope is apparent and both fits are statistically compatible.

3.3.2 Other studies

Although our study was based on observations performed from 2005 to 2007, due to several significant upgrades during the long observation period the data analysis took a rather long time. As a consequence the results were published much later, so the first significant detection of M87 by MAGIC was based on data from early 2008 [15] when a rapid flare in VHE γ-rays was detected. That study was based on an effective observing time of 22.8 hours collected during 13 consecutive nights. The signal was detected with a significance of $9.9\,\sigma$. The data were divided in two energy ranges ($150 - 350$ GeV and above 350 GeV), and the flux was calculated for both of them. While the flux in the lower energy range was consistent ($\chi^2/NDF = 12.6/8$; NDF stands for the number of degrees of freedom) with the assumption of a constant flux, the flux in the higher energy

range showed variability on a timescale of 1 day. For five nights the flux was calculated in both energy ranges. The assumption of the same flux levels in different energy ranges on these five nights was discarded with a significance of $5.6\,\sigma$. The short timescale variability implies either a compact emission region or a high Doppler boosting. The highest flux (at level of 0.15 C.U.) was observed on 2008 February 1 at a significance of $8.0\,\sigma$. The averaged differential energy spectrum can be described by a power-law with a photon index of $2.30\pm0.11_{stat}\pm0.20_{syst}$, and is consistent with the result of the MAGIC 2005 – 2007 study, as well as previously mentioned H.E.S.S. and VERITAS results.

Observations used in [15] were actually part of a joint monitoring program with H.E.S.S., VERITAS and VLBA. The results of the entire campaign were presented in [14]. The flux of the VHE γ-rays was compared to the radio flux density at $43\,\mathrm{GHz}$, which also showed a significant increase during and after the VHE γ-ray flare (Figure 3.5). The radio signal was divided based on the location of emission. Nucleus is taken as a circular region with radius $r = 1.2\,\mathrm{mas} = 170\,\mathrm{R_s}$, and it is centred on the peak flux. Outer regions of the jet is the section of the jet between 1.2 and 5.3 mas. There is an obvious increase of the flux from the nucleus, while there is very little change in the flux from the outer regions of the jet. The concurrence of flux changes in radio and VHE γ-ray bands implies that the nucleus is also the location of acceleration of charged particles to very high energies, although the radio flux density continues to rise even after the γ-ray flare is gone.

3.4 Characteristics of the M87 emission

We compiled multiwavelength data to study the SED of the quiescent state of M87 (Figure 3.6). The MAGIC spectral points from this study (see Section 3.3.1) are represented by black filled circles. Unfortunately, there were no organised simultaneous multiwavelength observation campaigns, so we use historical data, or data from observations that only partially overlap with our observations. We compare our results to the H.E.S.S. spectra taken in 2004 and 2005 [11], represented by magenta triangles and red open
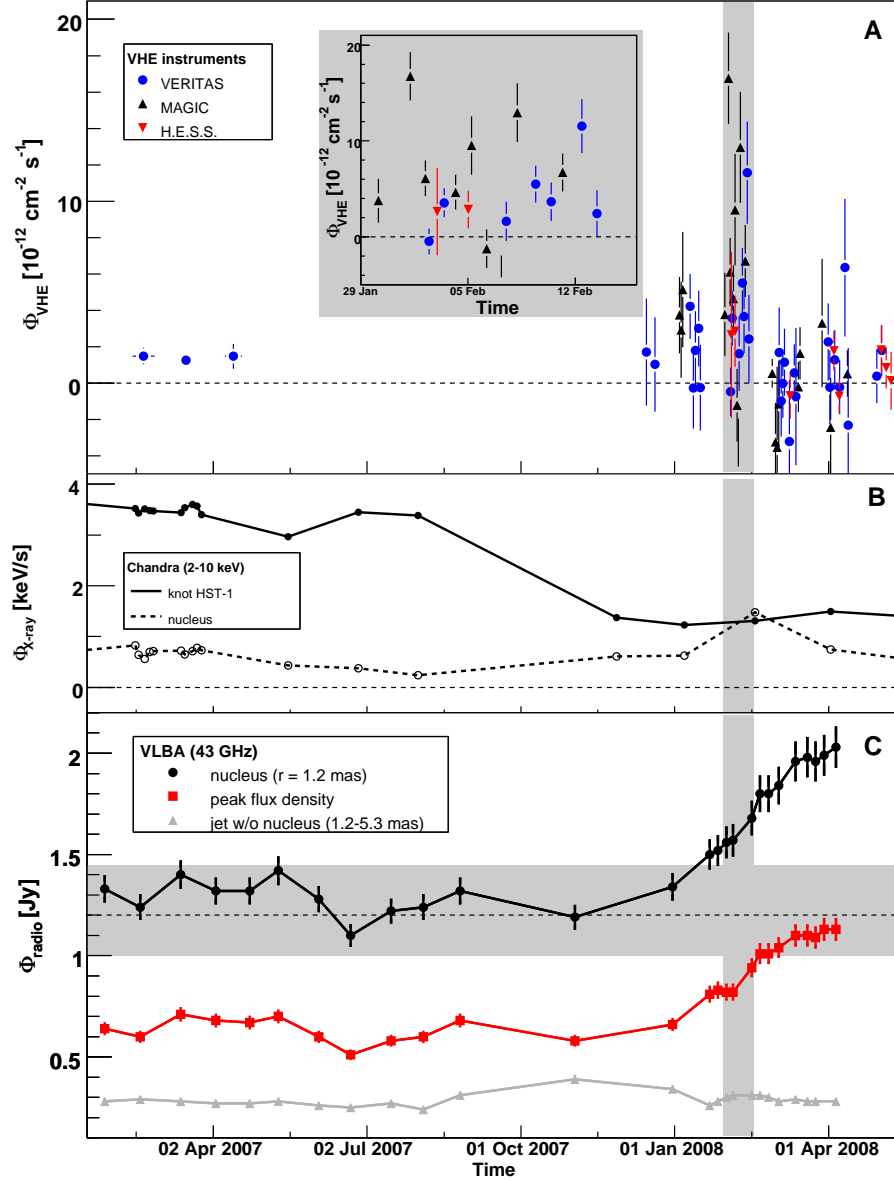
Figure 3.5 Combined M87 light curves for the 2008 multiwavelength campaign adopted from [14]. (**A**): Nightly averaged integral VHE γ-ray fluxes above $350\,\text{GeV}$, taken with the H.E.S.S., MAGIC and VERITAS. The fluxes were calculated assuming a power-law spectral shape of $\text{dN/dE} \propto \text{E}^{-2.3}$. Also shown monthly-binned archival VERITAS data from 2007 [13]. The flaring episode indicated by the grey vertical stripe is shown in the inlay. (**B**): X-ray integral flux in the $2 - 10\,\text{keV}$ energy range of the nucleus and the HST-1 knot measured by Chandra [144]. (**C**): Flux densities at $43\,\text{GHz}$ from the VLBA observations. Red squares indicate the peak flux in the resolution element of the VLBA, black circles represent the nucleus, i.e. a circular region with radius $r = 1.2\,\text{mas} = 170\,\text{R}_\text{s}$ centred on the peak flux, and grey triangles represent the integrated flux from the section of the jet between 1.2 and $5.3\,\text{mas}$. The error bars correspond to 5% of the flux. The grey horizontal stripe indicates the range of fluxes from the nucleus before the 2008 flare.

circles, respectively, and the 2007 VERITAS spectrum [13] represented by cyan squares. Our results are very similar to what H.E.S.S. measured in the "low" 2004 state and VERITAS in 2007. The flux measured by H.E.S.S. in 2005 is around a factor of 5 higher than 2004 and around 4 times the average flux for the 2003 – 2006 period, so we do not consider it the quiescent state. We include the *Fermi*-LAT spectrum (orange open diamonds) obtained by integrating over the first ten months of all-sky survey data [158]. Although observations with *Fermi*-LAT were not contemporaneous to MAGIC observations, we showed in Section 3.3.1 that *Fermi*-LAT and MAGIC spectra can be smoothly connected. So we conclude that they represent the same state of the source. We use the X-ray spectrum measured by *Chandra* in 2000 [161], and represent it with the green "bow tie". Although the observations in the X-ray band were performed during the MAGIC campaign, these observations were not simultaneous to the MAGIC ones, and there was very little overlapping observing time. In addition, a spectrum was not calculated for that period. However, the light curve reported in [144] shows the flux in the period of MAGIC observations four times higher than the one reported in [161]. So we reproduced the contemporaneous X-ray spectrum by keeping the same slope as in [161] and scaling the normalization by a factor of four. The same procedure was performed in [17]. We use historical data for lower energies. The SED shows two pronounced bumps, one peaking in the IR band, one extending from MeV to TeV energies.

We have already discussed in the introductory section of this chapter different possibilities for the location and mechanism of the emission of γ-rays in M87. We have also seen in Section 3.3.2 that the γ-ray light curve has a similar behaviour to radio flux density of the nucleus. So we investigate a possibility that the observed emission is produced in the innermost regions of the jet.

There is no evidence of presence of bright sources of IR-optical radiation in the nucleus of M87, which would emit seed photons for the external Compton mechanism. Therefore we have to assume that the γ-rays are dominantly produced through synchrotron self-Compton process. As discussed by Tavecchio and Ghisellini [17], one-zone models face a severe problem in describing the whole SED of M87. The synchrotron and SSC
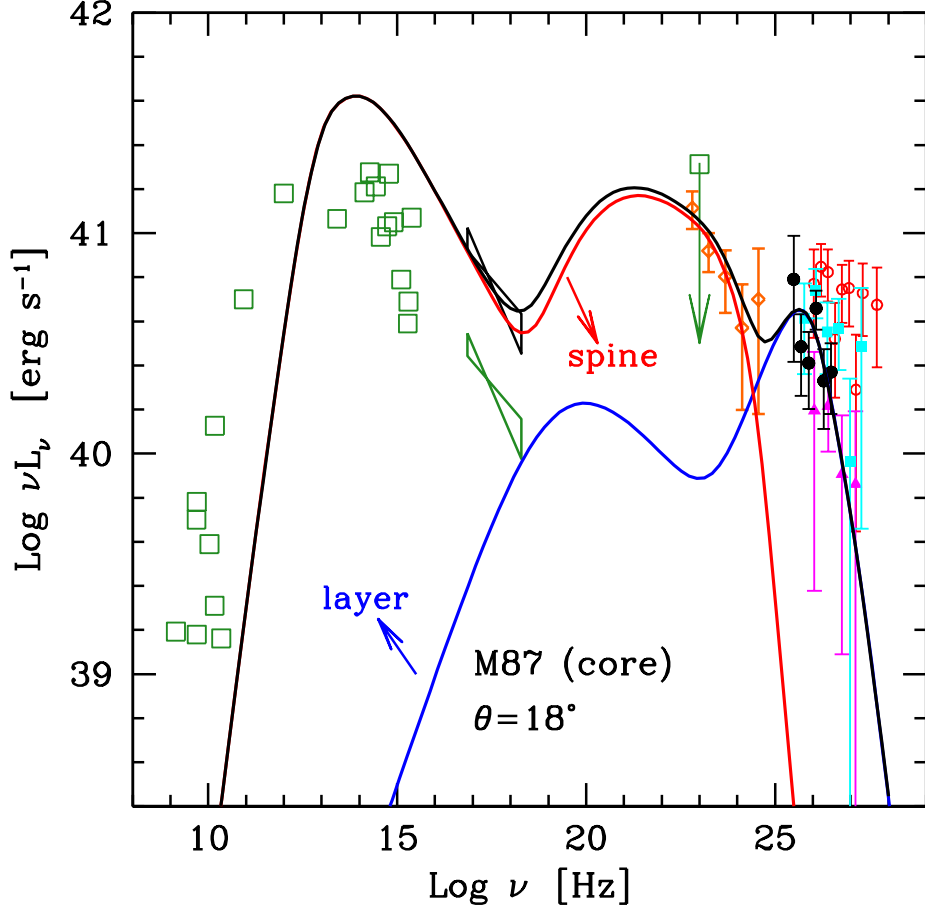
Figure 3.6 SED of M87 in the quiescent state. The MAGIC data points are represented by black filled circles. For comparison we report the H.E.S.S. spectral points from 2004 (magenta triangles) and 2005 (red open circles) [11], and the VERITAS spectrum from 2007 (cyan filled squares) [13]. The *Fermi*-LAT energy spectrum from [158] is represented by orange open diamonds. The green bow tie reports the X-ray spectrum as measured by Chandra in 2000 (from [161]). We reproduced the X-ray emission of the period 2005–2007 assuming the same slope and a higher normalization (black bow-tie, see text). In the high-energy γ-ray range the green open square corresponds to the EGRET upper limit. Other open squares represent historical data for the core of M87. The lines represent the emission from the spine (red) and from the layer (blue), calculated with the parameters reported in Table 3.1, and their sum (black).

components of the M87 SED peak in the IR and TeV band, respectively. The only way a one-zone SSC model can provide peaks at that distance is with very high values for the Doppler factor of $\delta > 100$. This is unacceptably high, especially considering rather high angle between the jet axis and our line of sight.

This problem can be solved by assuming a structured jet emission region, such as the "decelerating jet" model of Georganopoulos, Perlman and Kazanas [66] or in the "spine-layer" model of Ghisellini, Tavecchio and Chiaberge [64]. Other possibilities include multiple regions moving into a wider jet, as expected from the inner regions before the initial collimation [65], or emission by several randomly oriented active regions resulting from reconnection events in the jet (the so-called "jets-in-the-jet" scenario of Giannios, Uzdensky and Begelman [162, 151]). By construction, all these models predict that M87, if observed at smaller angles, would display an SED resembling those commonly observed for blazars.

We propose an interpretation of the SED based on the structured-jet model suggested in [64], and previously applied to M87 by Tavecchio and Ghisellini [17]. Although the conclusion discussed in Section 3.3.2 that the γ-ray emission is coming from the radio core was derived for the high-state emission, we adopt this result, and assume that the low-state γ-ray emission is produced in the same region. As sketched in Figure 3.7, the jet is assumed to have two distinct regions. The layer is assumed to be a hollow cylinder with internal radius R, external radius R_2 and height $H_{\rm L}$, and the spine a cylinder in the hole of the layer of radius R and height $H_{\rm S}$. All of these parameters are measured in their respective frames of references. Each region contains a tangled magnetic field with intensity $B_{\rm L}$ and $B_{\rm S}$ respectively, and is filled by relativistic electrons assumed to follow a purely phenomenological smoothed broken power-law distribution extending from $\gamma_{\rm min}$ to $\gamma_{\rm max}$ with indices p_1, p_2 below and above the break at $\gamma_{\rm b}$. The normalization of this distribution is calculated assuming that the system produces a (bolometric) synchrotron luminosity $L_{\rm syn}$ (as measured in the local frame), which is an input parameter of the model. We assume that $H_{\rm L} > H_{\rm S}$. The bulk motion of the layer is parametrised by the bulk Lorentz factor $\Gamma_{\rm L}$. The spine moves faster with bulk
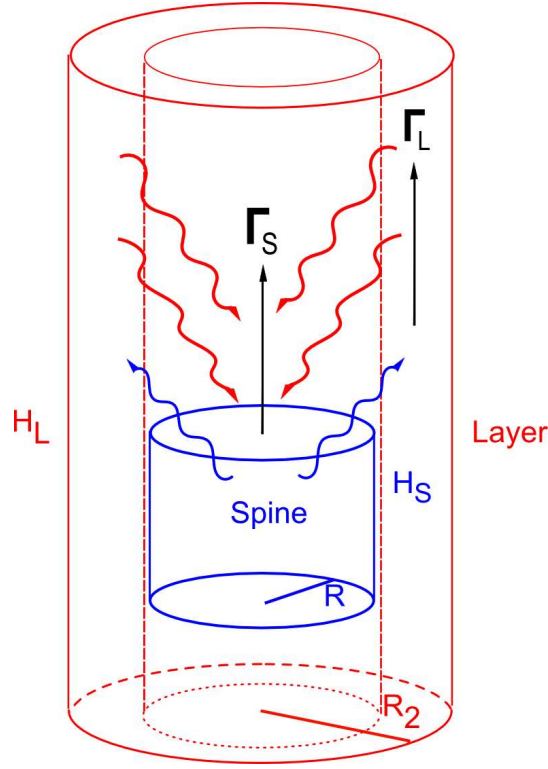
Figure 3.7 A sketch of the "spine-layer" model. Not to scale. Image credit: M. Varašanec.

Lorentz factor Γ_S. In both regions, relativistic electrons emit through synchrotron and inverse Compton mechanisms. The seed photons for the IC scattering are not only those produced locally in the spine, or layer, but we also consider the photons produced in the other part of the jet. So there will be an EC component in the layer coming from the spine, and vice versa. The velocity structure plays an important role in determining the emission properties of the jet. The radiative interaction between the layer and the spine results in the amplification of the inverse Compton emission of both components. In the rest frame of each component the emission of the other is amplified because of the relative speed within the two regions: this "external" radiation contributes to the total energy density, enhancing the emitted inverse Compton radiation. Depending on the parameters, this "external Compton" emission can dominate the internal SSC component that, especially in TeV blazars, is suppressed because scatterings mainly occur in the Klein-Nishina regime. In our scenario the spine is responsible for the MeV–

GeV emission, while the VHE radiation is produced in the layer. Therefore, a strict correlation between these two spectral components although possible, is not required. More details on the model can be found in [64] and [17].

The emission resulting from the scenario we propose is reported in Figure 3.6, where we show the SED of the emission produced by the spine (red) and the layer (blue) and their sum (black). The adopted parameters are reported in Table 3.1. Our result is very similar to that obtained by Tavecchio and Ghisellini for the 2005 high state [17]. In particular, we used the same values of the spine and layer dimensions and Doppler factors. Our result is therefore compatible with our initial assumption that the low- and high-state emissions are originating from the same emission region near the radio core. Unlike the SED considered in [17], here we use the *Fermi*-LAT data, which allow us to constrain the inverse Compton bump of the spine to a luminosity slightly lower than that assumed in [17]. This difference accounts for a stronger magnetic field derived here for the spine. Similarly to [17], since we are forced to reproduce a high X-ray state, the model inevitably over-predicts the non-simultaneous flux in the IR-optical bands. However, as already noted in [17], because the X-ray and optical fluxes are correlated [143], we expect that high X-ray fluxes also corresponds to optical states higher than those presented in the SED.

The "spine-layer" scenario faces several possible problems, none of which are unsolvable. Firstly, the VHE emission from the layer, is partly absorbed through the interaction with the optical-IR photons produced in the spine. This leads to a relatively soft spectrum, compatible with the quiescent state spectrum measured by MAGIC, which extends to $\sim 2\,\mathrm{TeV}$. However, the hard spectrum recorded during the high state by H.E.S.S. is difficult to reproduce. A possible solution of this problem is to enlarge the emission regions, since this would reduce the density of the target photons. However, the increase of the source size is limited by the observed short variability time-scales, $R < 5 \times 10^{15} \delta \,\mathrm{cm}$. In summary, we are able to describe the VHE low-state emission with parameters similar to those adopted in [17] to reproduce the high state. We can therefore conclude that in the framework of the scenario proposed here, both high and quiescent states

Table 3.1 Input parameters for the "spine-layer" scenario. A sketch of the model is shown in Figure 3.7, and the resulting SED in Figure 3.6. All quantities (except the bulk Lorentz factors Γ and the viewing angle θ) are measured in the rest frame of the emitting plasma. The external radius of the layer is fixed to the value $R_2 = 1.2 \times R$.

Parameter	Symbol	Spine	Layer
Emission region radius [cm]	R	7.5×10^{15}	7.5×10^{15}
Emission region height [cm]	H	3×10^{15}	6×10^{16}
Synchrotron luminosity [erg/s]	L_{syn}	4.7×10^{41}	1.6×10^{38}
Magnetic field [G]	B	2.1	0.35
Minimum electron Lorentz factor	γ_{min}	600	1
Break electron Lorentz factor	γ_{b}	2×10^3	2×10^6
Maximum electron Lorentz factor	γ_{max}	1×10^8	1×10^9
Low-energy electron spectral index	p_1	2	2
High-energy electron spectral index	p_2	3.65	3.3
Bulk Lorentz factor	Γ	12	4
Viewing angle [deg]	θ	18	18

can originate from the same emitting region. The opacity of the emitting region to the γ-ray photons is a difficulty that also affects other models, especially those focusing on the acceleration in the BH magnetosphere, where the environment is expected to be extremely rich in IR photons that originate in the accretion flow (e.g. [148, 163]). This problem, instead, could be relaxed in the "mini-jets" model of Giannios, Uzdensky and Begelman [151], due to the high Doppler factor $\delta \simeq 10$ assumed to characterize the emitting regions. Another point concerns the jet power required to reproduce the SED. The parameter values we adopt here suggest that the jet is magnetically dominated, meaning that the Poynting to kinetic power ratio is higher than $\sim$100, with power of $P_{\mathrm{jet}} = 1.5 \times 10^{44}\,\mathrm{erg\,s^{-1}}$. The accretion luminosity in M87, on the other hand, is estimated to be about $L_{\mathrm{accr}} = 10^{40} - 10^{41}\,\mathrm{erg\,s^{-1}}$ (e.g. [164]). For a black hole mass of $M = 6 \times 10^9\,\mathrm{M_\odot}$, this corresponds to Eddington ratios of $L_{\mathrm{accr}}/L_{\mathrm{Edd}} = 10^{-8} - 10^{-7}$. The luminosities as low as this, common among low-power radio galaxies are currently interpreted to be the result of a radiatively inefficient flow, with efficiencies of about $\eta \equiv L_{\mathrm{accr}}/\dot{M}c^2 = 10^{-4} - 10^{-3}$ (e.g. [165]). In that case the power request of the jet can be easily fulfilled by the accretion power, $\dot{M}c^2 = L_{\mathrm{accr}}/\eta \sim 10^{45}\,\mathrm{erg\,s^{-1}}$. We note

that a magnetically dominated jet is postulated to power the "mini-jets" in the [151] model. Finally, we comment on the angle between the plasma velocity and the line of sight. We adopt a value of $\theta = 18°$, which is well within the range confidently derived through radio observations, $\theta = 15° - 25°$ [14]. Figure 3.8 shows the dependence of the amplification of different emission components with respect to the viewing angle due to boosting. Solid lines represent inverse Compton emission from the spine, and dashed from the layer. In each part of the jet, there will be two sources of seed photons: SSC emitted in the same part of the jet, an EC coming from the other part of the jet. SSC component is given in black, and EC in red. We see that the SSC spine component is dominant at smaller angles, which is expected since in that case we would be facing it "down the barrel". We see that if the jet was inclined more than $\sim 20°$, it would imply a de-boosting of the spine emission. This means that the *intrinsic* luminosity of the spine would have to be higher to reproduce the observed radiation. This, in turn, would imply a higher power of the jet and, more importantly, a higher optical depth for VHE photons emitted by the layer, which would result in even softer VHE γ-ray spectrum.

3.5   Summary

We used MAGIC observations of M87 performed between 2005 and 2007 to characterise the VHE γ-ray emission. The particularity of our study is that all observations were performed during a quiescent state of the source. We investigated the accumulated number of excess events over time and found it to be quite linear, suggesting there were no significant changes of flux during our observations. This allowed us to investigate the quiescent state of the source. Our measurements are compatible with previously reported low states by VERITAS and H.E.S.S., which suggests that the observed low-emission level and spectral characteristics are stable over a long time period. We also find that the flux and spectral shape are consistent with a straight power-law extrapolation of the published *Fermi*-LAT spectrum at lower energies, even though the *Fermi*-LAT observations were performed after the MAGIC campaign was already finished.
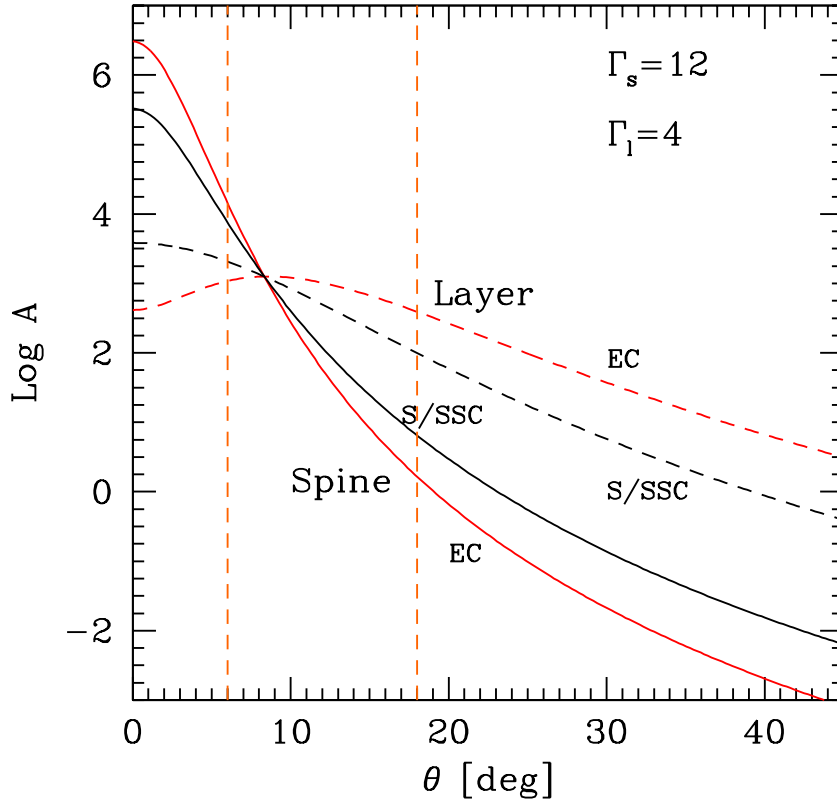
Figure 3.8 Amplification factors for the emission from different components of the jet, with respect to the viewing angle. Solid lines represent emission from the spine, and dashed from the layer. Black lines represent the SSC component, meaning the seed photons were emitted in the same part of the jet, while red represent the EC component, i.e. seed photons were emitted from the other part of the jet. The two vertical lines indicate 6° and 18°. Figure 2 of [17].

We were able to describe this emission with a structured jet model, which separates the jet into a spine and an outer layer. We assumed that the VHE γ-ray emission in the quiescent state originates from the radio core of the jet, as was previously inferred for the high-state emission. It should be noted, however, that the low-state emission alone cannot constrain the emission region due to the lack of variability of the measured signal and the softer VHE γ-ray spectrum. The parameters we adopted are consistent (even identical for the spine/layer dimensions and Doppler factors) with results from [17] for the high 2005 state. Because the present model includes GeV data from the *Fermi*-LAT, we were able to constrain the inverse Compton bump of the spine to a slightly lower luminosity compared to the assumptions in [17], which results in a stronger magnetic field for the spine. An interesting detail is the region in which the the emission from the spine rapidly decreases and the emission from the layer becomes dominant. The exact position depends on the chosen parameters (see Figure 3.6 and Table 3.1), but for our set of parameters this occurs between 40 and 100 GeV. Unfortunately, this energy range is exactly between parts of the spectrum covered by the *Fermi*-LAT and MAGIC. Currently, no measurements of M87 are available in this energy range. It is possible that future, deep observations of M87 and contemporaneous multiwavelength data will reveal a feature in the otherwise smooth power-law spectrum of M87, confirming or disproving the validity of the proposed scenario.

Chapter 4

PKS 1222+21

4.1 Introduction

Only three flat spectrum radio quasars (FSRQ) have been detected in the VHE γ-ray band so far. 3C 279 was discovered by MAGIC [166], and PKS 1510-089 by H.E.S.S. [167]. PKS 1222+21 (also known as 4C +21.35) is the third. It is located at a redshift of $z = 0.432$ [18]. At the time of discovery, it was the second most distant source of the VHE γ-radiation with well known redshift, after 3C 279[1]. Several knots with very large superluminal motion are visible in 2 cm VLBA images with apparent velocities up to 27 c [171]. It has a peculiar bent large-scale radio structure [172], which is brighter than the core [173, 174], so it is classified as a lobe-dominated quasar. The mass of the black hole in the centre of PKS 1222+21 was first estimated in 2004 to $\sim 1.5 \times 10^8 M_\odot$ [174]. However, that result is based on the relation between the H-β broad line and the continuum luminosity-BLR radius from [175], which in turn was obtained from reverberation mapping of a small number of AGN with a cosmology with a decelerating universe. Later Farina et al. estimated the mass, using broad emission line measurements from over 100 optical spectra from a variety of sources, to $M_{\mathrm{BH}} \sim 6 \times 10^8 \ M_\odot$ [176]. They

---

[1]The redshift measurement ($z = 0.444$) of the VHE BL Lac 3C 66A has large uncertainties [168]. In the meantime S3 0218+357 was discovered at $z = 0.944$ [169], and the redshift of PKS 1424+240 was estimated to be 0.6 [170].

also find that although the continuum emission in the optical band varies significantly, the broad line emission is virtually constant, and conclude that the BLR is not affected by the variations in the jet. The value that they found for M_{BH} agrees with the values found using SDSS spectrum by Shen et al. [177] and Shaw et al. [178].

PKS 1222+21 was observed by the Whipple telescope, which resulted in upper limits on the flux of $12 \times 10^{-12}\,\mathrm{cm^{-2}s^{-1}}$ for energies above $300\,\mathrm{GeV}$ [179]. It was first detected in the HE γ-ray band by the EGRET satellite [180]. The *Fermi*-LAT observed PKS 1222+21 since the beginning of the *Fermi Gamma-ray Space Telescope* science operations in 2008 August. It is listed in the *Fermi*-LAT first year catalogue [181] and in a catalogue of sources of γ-rays with $E > 100\,\mathrm{GeV}$ detected by the *Fermi*-LAT [182]. The source was in a quiescent state until 2009 September, when the flux started increasing gradually with occasional flares. The activity peaked in the first half of 2010, when it underwent two very strong outbursts in April and June composed of several major flares characterized by rise and decay time scales of the order of one day [183].

The MAGIC observations started on May 1, following an alert from the *Fermi*-LAT, reporting a strong flare on the night of April 24 [184]. The author of this thesis served as a MAGIC *flare advocate* in 2010 May. There are two flare advocates assigned to each observation period. Their task is to perform data analysis every day on the data collected the previous night for the sources showing enhanced activity in lower energy bands. The analysis is performed quickly and without detailed inspection of the data quality. The results are not meant for publication, but based on these results a decision is made whether to observe a given source on the following night and the duration of observation. Since we were aware of enhanced and variable emission of PKS 1222+21 as measured by the *Fermi*-LAT, we expected to detect a signal in the VHE γ-ray band. The first detection occurred on May 4. The statistical significance of the signal was on the level of $3 - 4\,\sigma$, which was not strong enough to claim a discovery of VHE γ-ray signal, however, it did motivate further observations. The campaign turned out to be rather frustrating, because the observations were first interrupted by a period of bad weather, followed by a full moon period, during which the MAGIC telescopes cannot
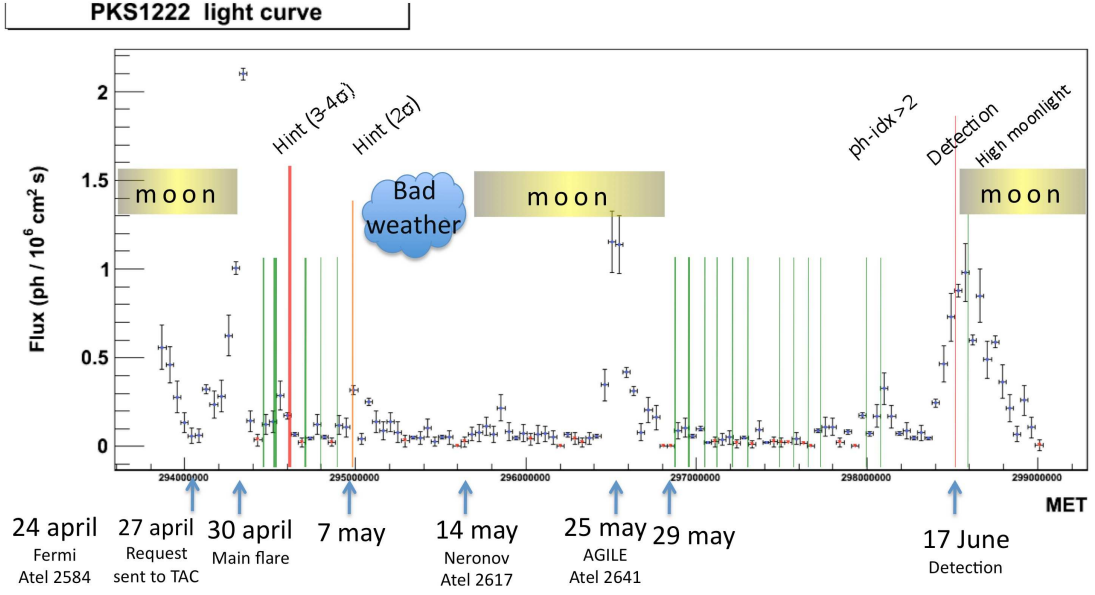
Figure 4.1 A schematic description of the MAGIC PKS 1222+21 campaign (vertical coloured lines) overimposed to the *Fermi*-LAT light curve. The integral flux above 1 GeV is marked by the blue circles, and by the red triangles when the flux is compatible with zero. The source was observed by MAGIC telescopes during a period of a month and a half. During that time it was very variable in HE γ-ray band, and probably active enough to be detected by the MAGIC telescopes before June 17. Unfortunately, MAGIC observations were interrupted by periods of strong moon and bad weather. The results of MAGIC data analysis is indicated for some dates above vertical lines. Below the graph, the most important dates are indicated. The Astronomer's telegrams mentioned are as follows: "Fermi Atel 2584" [184]; "Neronov Atel 2617" [186]; "AGILE Atel 2641" [185]. Image credit: A. Stamerra.

observe beacuse of the sky conditions and the corresponding technical limitations. The frustration got even worse when the γ-ray satellite AGILE[2] reported another flaring episode [185] during the full moon period. We resumed observations of PKS 1222+21 at the end of May, but by that time, the flare reported by AGILE seemed to have finished. Nevertheless, we extended observations of the source in June, and although another two flare advocates started their duty, former flare advocates kept daily data analysis. Finally, a clear detection with statistical significance over $5\,\sigma$ befell on June 17 during yet another flare. The source was observed for 30 minutes with moderate moon light,

---

[2]agile.rm.iasf.cnr.it

and just before the beginning of another full moon period. This was also the last chance to observe this source for another five months, since PKS 1222+21 is not observable from La Palma from July until November. The MAGIC campaign is schematically depicted in Figure 4.1.

The results of the observation performed on July 17 are particularly interesting because we measured the flux variability of the order of 10 minutes, which is the fastest time variation ever observed in a FSRQ[187], and among the shortest time scales measured for TeV emitters (see e.g. [188]). We report in details on those and other results of observations by the MAGIC telescopes in Section 4.2. There we also discuss the implications on the structure and emission mechanism from FSRQs. We present the data from observations in lower frequency bands during 2010 in Section 4.3, and discuss possible explanations for the observed emission in Section 4.3.6.

4.2 MAGIC observations and data analysis

MAGIC observed PKS 1222+21 between 2010 May 1 and June 19. In total, 16 hours of good quality data were collected. On May 3 (MJD 55319), MAGIC obtained an excess with respect to the background of ≈ 78 events in 2.2 hour of observation, which yielded a marginal detection with a signal significance of $4.4\,\sigma$ using the Eq. 17 of [123]. On June 17 (MJD 55364), MAGIC obtained a γ-ray excess of 190 events in a 30-min long observation, yielding a signal significance of $10.2\,\sigma$, implying the first significant detection of this source in VHE γ-rays [71].

None of the other nights showed a statistically significant excess of signal over the background. Upper limits at 95% confidence level (C.L.) were calculated above $150\,\mathrm{GeV}$ assuming a power-law with the same photon index measured on June 17 (i.e. $\Gamma = 3.75$) for the nights between May 5 and June 13. The rest of the nights were not included in the upper limit calculation due to strong moonlight constraints. The upper limits range between 1.4% Crab Nebula units (C.U., see Section 1.2.3) (on May 30; MJD 55346) and 12.7% C.U. (on June 12; MJD 55359), as reported in Table 4.1. Considering the period

Table 4.1 Daily upper limits estimated by MAGIC for E>150 GeV assuming a spectrum slope 3.7.

Date [UT]	Effective time [h]	Integral Limit [cm^{-2} s^{-1}] above 150 GeV	Integral Limit [in MAGIC C.U.]
2010-05-05	0.5	1.2e-11	3.7%
2010-05-06	0.7	1.1e-11	3.3%
2010-05-07	0.8	1.8e-11	5.5%
2010-05-08	1.4	1.7e-11	5.4%
2010-05-30	0.9	4.6e-12	1.4%
2010-05-31	1.0	2.6e-11	8.1%
2010-06-01	1.2	5.1e-12	1.6%
2010-06-02	0.9	1.0e-11	3.7%
2010-06-03	1.1	8.4e-12	2.6%
2010-06-04	1.2	8.0e-12	2.5%
2010-06-06	1.0	1.4e-11	4.3%
2010-06-07	0.6	2.1e-11	6.4%
2010-06-08	0.7	1.3e-11	4.0%
2010-06-09	0.9	2.4e-11	7.3%
2010-06-12	0.6	4.1e-11	12.7%
2010-06-13	0.6	2.5e-11	7.8%

from May 5 to June 13 (total time: 12.5 hrs) an upper limit of 1.6% C.U. was estimated.

Despite the short observation time on 2010 June 17, the strength of the signal allowed us to reconstruct the spectrum and perform a variability study of the measured integral fluxes above 100 GeV. The results are presented in the following two sections.

4.2.1 Light curve for 2010 June 17

The data from the 30 minute observation of PKS 1222+21 on 2010 June 17 was separated in five time bins, each lasting 6 minutes. The light curve in Figure 4.2 reveals clear flux variations. A fit with a constant resulted in $\chi^2/NDF = 28.3/4$, where NDF stands for the number of degrees of freedom. This is equivalent to probability of constant fit of $< 1.1 \times 10^{-5}$. There are no evidence of variations of the background (a fit with a constant yielded $\chi^2/NDF = 2.34/4$), so we can exclude a variation of the instrument performance
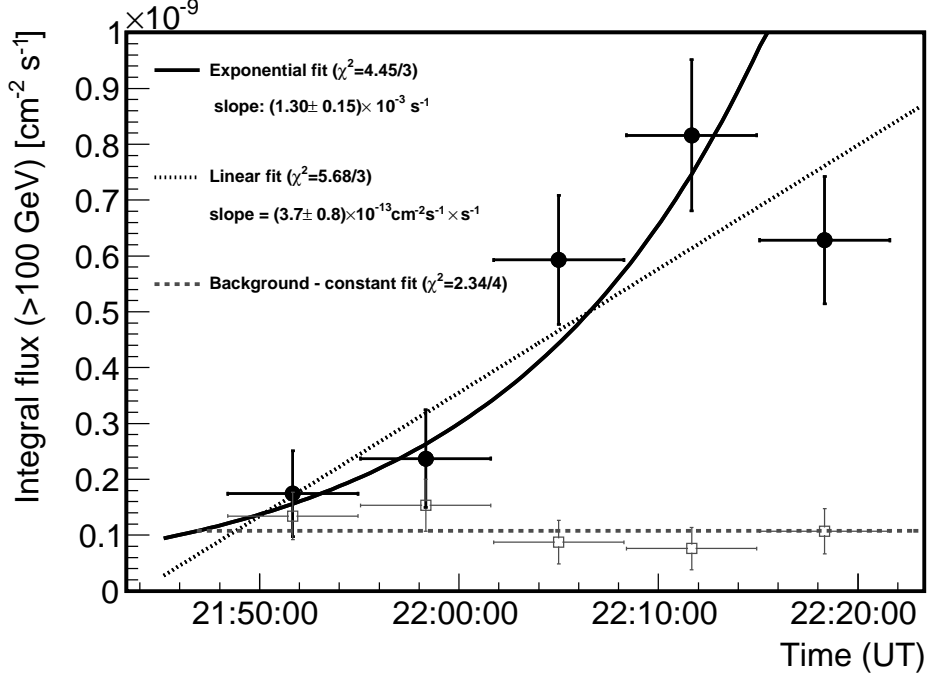
Figure 4.2 The light curve for PKS 1222+21 above 100 GeV (black filled circles), for 2010 June 17. The observation was carried out on MJD 55364. The flux was fitted with an exponential function (black solid line) and a linear function (black dotted line). The fluxes from the background events (grey open squares) are well fitted with a constant function (grey dashed line). Horizontal error bars represent width of time bins of 6 minutes.

as a cause of the observed signal variability. The signal points were also fitted with a linear and an exponential functions. Both fits are acceptable with $\chi^2/NDF = 5.68/3$ and $\chi^2/NDF = 4.45/3$ for the respective functions. However, only the exponential fit allows an unambiguous determination of the time scale. The doubling time of the flare is estimated as $8.6^{+1.1}_{-0.9}$ minutes, which is the fastest time variation ever observed in a FSRQ [187], and among the shortest time scales measured for TeV emitters (see e.g. [188]). The observed rapid variability suggests an extremely compact emission region (see expression 1.13), with size $R \leq ct_{\mathrm{var}}\delta/(1+z) \sim 10^{15} \, (\delta/80) \, (t_{\mathrm{var}}/10\,\mathrm{min})$ cm. If the emission region takes up the entire cross section of the jet, it implies that the emitting region is located at a distance $r \sim R/\theta_{\mathrm{open}} \sim 5.7 \times 10^{16}(\delta/80) \, (t_{\mathrm{var}}/10\,\mathrm{min}) \, (\theta_{\mathrm{open}}/1\,\mathrm{deg})^{-1}$ cm from the base of the jet, where θ_{open} is the half-opening angle of the jet. The radius of the BLR in PKS 1222+21 was estimated to $R_{BLR} \approx 2 \times 10^{17}$ cm [183]. Therefore, even for a highly

relativistic jet with $\delta \sim 100$, the location of the VHE γ-ray emission region should be well within the BLR.

4.2.2 VHE spectrum
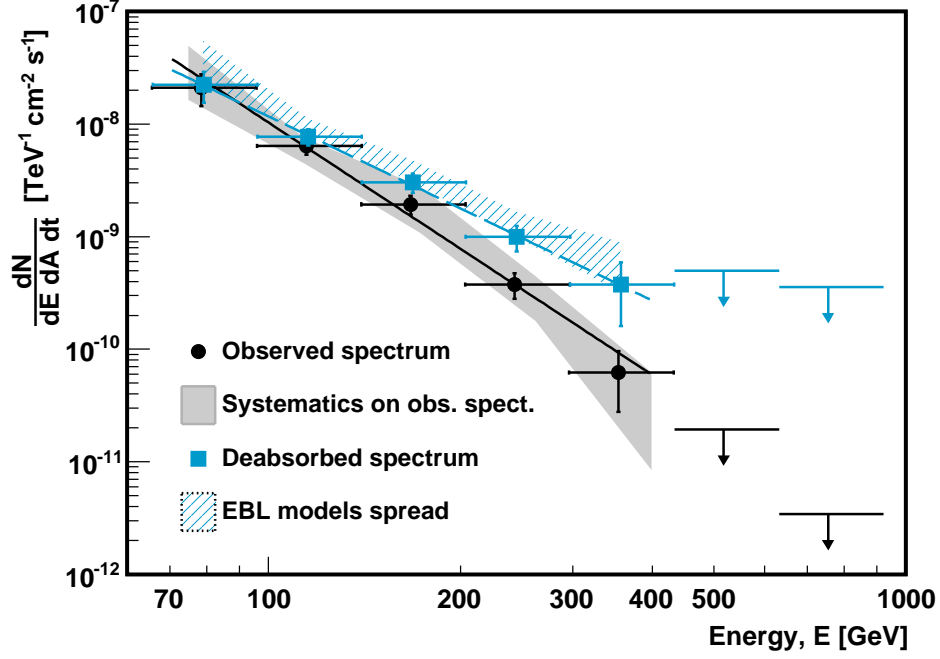
Figure 4.3 Observed and intrinsic differential energy spectrum of PKS 1222+21 as measured by MAGIC on 2010 June 17. Observed fluxes are shown as black points, with the best fit to a power-law shown with the black line. The analysis systematic uncertainties are indicated by the grey shaded area. The spectrum corrected for the attenuation by the EBL, using the EBL model by Domínguez et al. [108] is shown by the blue squares, with the best fit to a power-law shown by the dashed blue line. The uncertainties due to differences in the EBL models by [189, 190, 191, 166] are indicated by the blue-striped area. The upper limits at 95% C.L. for both spectra are indicated by arrows.

The observed differential energy spectrum was measured in the energy range from 70 GeV up to at least 400 GeV. It is shown in Figure 4.3. The spectrum was reconstructed using the "Tikhonov" unfolding algorithm as described in [127]. It can be

fitted with a single power-law

$$\frac{dN}{dE} = N_0 \left(\frac{E}{200\,\mathrm{GeV}} \right)^{-\Gamma} \tag{4.1}$$

with parameters $\Gamma = 3.75 \pm 0.27_{\mathrm{stat}} \pm 0.2_{\mathrm{syst}}$ and $N_0 = (7.8 \pm 1.2_{\mathrm{stat}} \pm 3.5_{\mathrm{syst}}) \times 10^{-10} \mathrm{TeV}^{-1} \mathrm{cm}^{-2} \mathrm{s}^{-1}$. This corresponds to an integral flux of $(9.0 \pm 3.6) \times 10^{-12}\,\mathrm{cm}^{-2}\mathrm{s}^{-1}$ (7% C.U.) above $300\,\mathrm{GeV}$, which is consistent with the upper limit set by the Whipple telescope (see Section 4.1). The spectrum corrected for the effect of EBL absorption using the EBL model from Domínguez et al. [108] can be also described by a single power-law with photon index $\Gamma = 2.72 \pm 0.34$ [71].

The *Fermi*-LAT data were separated in quiescent, intermediate and active state [183]. The active state between 2010 April 23 and 2010 June 24 (MJD $55309.00 - 55371.00$) includes two flares coincident with MAGIC detections, and the time interval between them. The spectral analysis for that entire period revealed a power-law shaped spectrum, with a break between 1 and $3\,\mathrm{GeV}$. The spectrum above the break extends up to $50\,\mathrm{GeV}$ with a slope between 2.4 and 2.8. This is consistent with the MAGIC measurement, and suggests that the spectrum in the $3 - 400\,\mathrm{GeV}$ interval can be described by a single power-law with photon index $\Gamma = 2.72 \pm 0.34$.

As we discussed in Section 1.1.4, VHE γ-rays produced within the BLR will annihilate with photons emitted from the gas clouds of the BLR. This manifests as a cut-off in the VHE band. Although a fit without a cut-off is compatible with the MAGIC measurements, a possibility of a cut-off in the MAGIC measured spectrum was investigated. The data were fitted with power-laws with different photon indeces and different values for the energy of the cut-off. For a spectral slope of 2.4, a possibility of a cut-off cannot be excluded above $130\,\mathrm{GeV}$, and for a spectral slope of 2.7, above $180\,\mathrm{GeV}$ [71]. These estimates were reached at the 95% C.L. using the χ^2 difference method (see e.g. [192]).

4.3 Multiwavelength observations

In order to investigate the properties of PKS 1222+21 and discuss possible explanations for emission, we collected data at wavelengths from centimetres to VHE γ-rays. Table 4.2 contains a list of the observatories used in this study.

Table 4.2 List of facilities used in this study and frequency bands in which the observations were performed.

Waveband	Observatory	Frequency/Band
Radio	SMA	230 GHz
	Metsähovi	37 GHz
	VLBA (MOJAVE)	15 GHz
	OVRO	15 GHz
	UMRAO	8.0, 14.5 GHz
	Medicina	5, 8 GHz
	F-GAMMA	2.6, 4.8, 8.4, 10.5, 14.6, 23.1, 32, 86.2, 142.3 GHz
Optical	Abastumani	R
	ATOM	R
	Crimean	R
	KVA	R
	St. Petersburg	R
	Swift-UVOT	v, b, u
UV	*Swift*-UVOT	$w1$, $m2$, $w2$
X-rays	*Swift*-XRT	0.3–10 keV
	Swift-BAT	15–50 keV
HE γ-rays	*Fermi*-LAT	0.1–300 GeV
VHE γ-rays	MAGIC	70 GeV – 5 TeV

4.3.1 *Fermi*-LAT observations

PKS 1222+21 is the most variable source in the first *Fermi*-LAT catalogue of sources above 10 GeV (1FHL; source name 1FHL J1224.8+2122) [193]. The *Fermi*-LAT observed PKS 1222+21 since the beginning of the *Fermi* science operations in 2008 August. The results of the *Fermi*-LAT observations since the beginning of the mission till 2010 August 4 are presented in [183]. The source was in a quiescent state until 2009 September, when

the flux started increasing gradually with occasional flares. Two very strong GeV flares were detected in 2010 April and June, with peaks on April 29 (MJD 55315) and June 17 (MJD 55365), respectively. The integral flux above $100 \, \text{MeV}$ during the active state changed between $\sim 0.2 \times 10^{-6} \, \text{cm}^{-2}\text{s}^{-1}$ and $\sim 14.2 \times 10^{-6} \, \text{cm}^{-2}\text{s}^{-1}$, while during the quiescent state on occasions it was as low as $\sim 0.04 \times 10^{-6} \, \text{cm}^{-2}\text{s}^{-1}$. The spectrum during the quiescent state between 2008 August and 2009 September was fitted by a single power-law with photon index $\Gamma = 2.57 \pm 0.07$, while the spectra during the active period is better described with a broken power-law, with the break around $1-3 \, \text{GeV}$ and photon indices around $1.8 - 2.3$ and $2.4 - 2.8$ below and above the break, respectively. Afterwards, the activity in γ-rays decreased, and by the mid-2011 the flux was back on the level it had before 2009 September[3].

4.3.2 *Swift* observations

The *Swift* satellite [194] is equipped with three detectors sensitive in optical through soft γ-ray bands. The Burst Alert Telescope (BAT) is sensitive in the $15 - 150 \, \text{keV}$ band [195]. With its wide FoV of, its main goal is to detect GRBs and determine their directions. It also performs an all-sky hard X-ray survey and serves as a hard X-ray transient monitor. The two other narrow FoV detectors are the X-ray Telescope (XRT), sensitive in the $0.2 - 10.0 \, \text{keV}$ band [196], and the UltraViolet Optical Telescope (UVOT), sensitive in the $170 - 600 \, \text{nm}$ band [197]). These two provide multiwavelength observations. The *Swift* satellite performed 28 observations of PKS 1222+21 in 2010 between February 12 and June 23, with all three on-board instruments.

The results of observations performed by the BAT between 2004 November and 2010 August are reported in the 70 month *Swift*-BAT catalogue [198]. The spectrum in the $14 - 195 \, \text{keV}$ range is compatible with a power-law with photon index of $1.76^{+0.25}_{-0.23}$ ($\chi^2 = 0.60$), and the unabsorbed flux in the same energy range is $(2.2 \pm 0.4) \times 10^{-11} \, \text{erg} \, \text{cm}^{-2} \, \text{s}^{-1}$. There is no indication of the flux variability on monthly base. The duration of each *Swift*

---

[3]fermi.gsfc.nasa.gov/FTP/glast/data/lat/catalogs/asp/current/lightcurves/PKSB1222+216_86400.png

pointing is around 20 minutes and the hard X-ray flux of PKS 1222+21 is below the sensitivity of the BAT instrument to be detected during a single snapshot, so no claims on the variability of the source on shorter time scales can be made.

The XRT and UVOT data analyses were described in [70]. The results of the observations with XRT, in the energy range of $0.3 - 10\,\mathrm{keV}$, during 2010 February – June are shown in Figure 4.6. The flux is varying in the range $(2.6 - 7.7) \times 10^{-12}\,\mathrm{erg\,cm^{-2}\,s^{-1}}$. In the same period, the photon index varied between 1.4 and 2.2, but it remained constant during the flares in γ-ray band. The UVOT measured following optical and UV magnitudes in the same period: $v = 15.67 - 15.21$, $b = 15.65 - 15.43$, $u = 14.67 - 14.34$, $w1 = 14.37 - 14.08$, $m2 = 14.25 - 13.90$ and $w2 = 14.16 - 13.90$. A typical error of the measurements is 0.06 mag. Both optical and UV fluxes show very little variability. However, the sampling is rather sparse, so a significant increase might have gone unnoticed. In addition, the UV contribution from the accretion disc might be dominant over the contribution from the jet, so any fluctuation in the jet emission in the UV band is less prominent.

4.3.3 Optical observations

Additional optical observations in R-band were performed using Abastumani, Crimean, St. Petersburg, ATOM and KVA telescopes. Details on the telescopes and their data analysis can be found in [70]. The KVA is also described in Section 5.3.3 of this thesis. A collection of data from several different observatories provides a well sampled light curve in the R-band, shown in Figure 4.6. The flux is clearly variable, but the two peaks are not nearly as prominent as the ones observed in the γ-ray band. These peaks occurring on April 20 (MJD 55306) and June 30 (MJD 55377), although close in time to γ-ray flares are not simultaneous to them. Additionally, the first peak in optical precedes the one in γ-rays, while the second comes after the γ-ray flare is already gone. Correlations between γ-ray and optical light curves were investigated in [70] comparing *Fermi*-LAT data to observations in R-band, and in [199] comparing *Fermi*-LAT light curve during

this epoch to the observations in *V*-band by the Steward Observatory. Neither of the analyses showed evidence of correlation.

4.3.4   Radio observations

The radio data are a collection of observations at frequencies between 5 and 230 GHz performed in the period from 2009 January 1 till 2011 February 28. The facilities that provided the data with their respective frequency of observation are listed in Table 4.2. A detailed description of these facilities and their data analysis can be found in [70] and references therein. The OVRO program is also described in Section 5.3.4 of this thesis. The behaviour of the source in radio and millimetre band can be seen in Figure 4.4. Although the flux density does show a steady increase since the late 2009, which is simultaneous to the increasing γ-ray activity observed by *Fermi*-LAT, the highest activity is reached in the beginning of 2011, by which time the γ-ray activity is already significantly lower than the highest period, and approaching the quiescent state. Some of these data for the shorter period around the MAGIC detected flares are shown in Figure 4.6. The highest flux density during high γ-ray activity was measured in the 23 GHz and 37 GHz bands on 2010 May 10 (MJD 55326) and June 18 (MJD 55365), respectively, which is close to γ-ray flares. However, the coverage is rather sparse and no firm conclusions can be drawn. The flux density increase is much lower than in the γ-ray band, but it might also be that due to the sparse coverage we missed the highest activity period. PKS 1222+21 is regularly observed by the Very Long Baseline Array (VLBA) at 15 GHz, as part of the Monitoring of Jets in Active Galactic Nuclei with VLBA Experiments (MOJAVE). From 1996 May till 2011 May, the MOJAVE tracked 14 different features in the jet of PKS 1222+21, some of them reaching apparent superluminal speeds of 27 *c* [171]. Figure 4.5 is a compilation of several images made by the VLABA between 2008 July and 2010 December. It shows the evolution of the jet, its radiation intensity at 15 GHz and linear polarization. The kinematic observations of the features of the jet suggest complex three dimensional trajectories, with possible helical
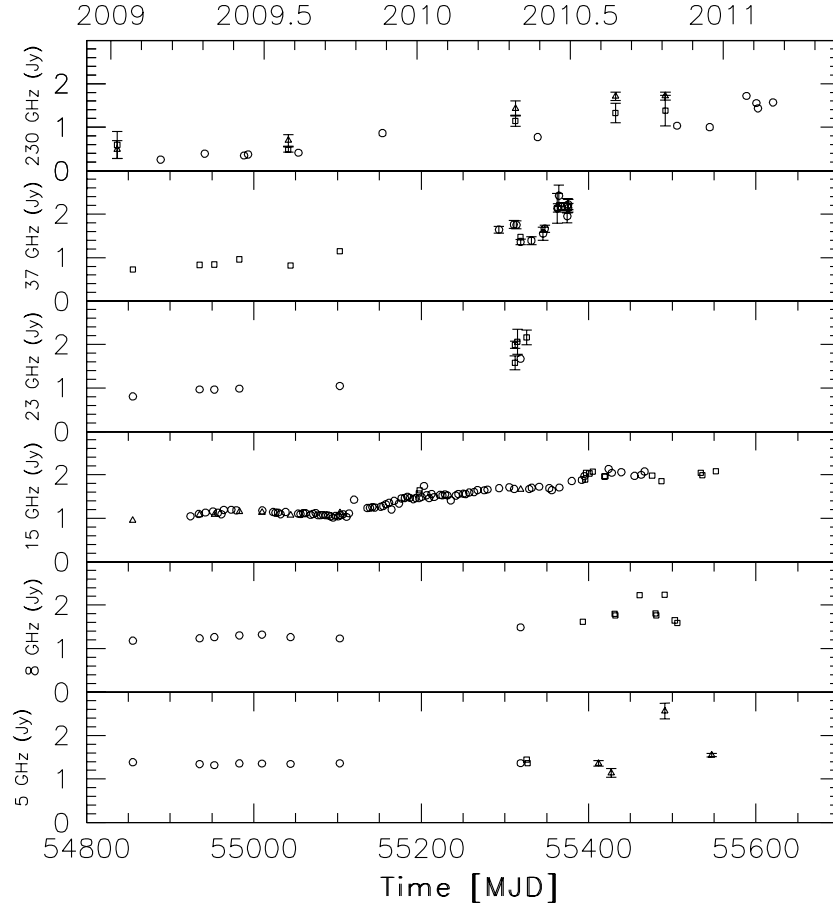
Figure 4.4 Radio and millimetre light curves of PKS 1222+21 for the period between 2009 January 1 (MJD 54837) and 2011 February 28 (MJD 55620) in units of Jy. The data are collected (from top to bottom panel) by SMA at 230 GHz (circles), IRAM at 142 GHz (squares) and 86 GHz (triangles); Metsähovi at 37 GHz (circles) and Effelsberg at 32 GHz (squares); Effelsberg at 23 GHz (circles) and Medicina a 22 GHz (squares); OVRO (circles), UMRAO (squares), Effelsberg (triangles) at 15 GHz; Effelsberg (circles) and UMRAO (squares) at 8 GHz; Effelsberg (circles), Medicina (squares), and UMRAO (triangles) at 5 GHz. For clarity errors are not shown when <5%.

form, but they are still being investigated in details by the MOJAVE collaboration.
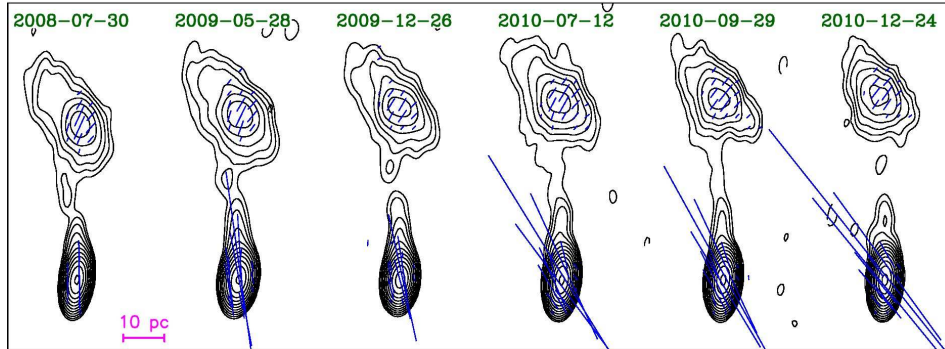
Figure 4.5 Total intensity and linear polarization images of PKS 1222+21 observed by VLBA at 15 GHz in different epochs as part of the MOJAVE program. Naturally-weighted total intensity images are shown by black contours, the contours are in successive powers of two times the base contour level of 0.2 mJy beam^{-1}. Electric polarization vectors direction is indicated by blue sticks, their length is proportional to the polarized intensity.

4.3.5 Multiwavelength light curve

The multiwavelength light curves of PKS 1222+21, from the data collected form the observatories listed in Table 4.2 in the period from 2010 April 9 (MJD 55295) till 2010 August 4 (MJD 55412) are shown in Figure 4.6. The top two panels show integral flux above 100 MeV, and the photon index as measured by the *Fermi*-LAT. The next two show the same for the $0.3 - 10$ keV band measured by the *Swift*-XRT. The UV flux measured by the *Swift*-UVOT with m2 filter ($\approx 200 - 250$ nm [200]) is shown in the fifth panel. The sixth panel contains results of the observations performed by *Swift*-UVOT with u filter ($\approx 307 - 386$ nm [200]), and *R*-band observations performed by Abastumani, ATOM, Crimean, KVA and St. Petersburg telescopes. In the last panel the radio light curve at 15, 23 and 37 GHz measured with Effelsberg, Medicina, Metsähovi, OVRO and UMRAO is presented. The times of the VHE γ-ray detections by MAGIC (May 3 and June 17) are indicated by the downward arrows in the first panel.

The detections by MAGIC on May 3 and June 17 are overlapping with the two γ-ray flares observed by the *Fermi*-LAT. As we saw in Section 4.1, the MAGIC observations
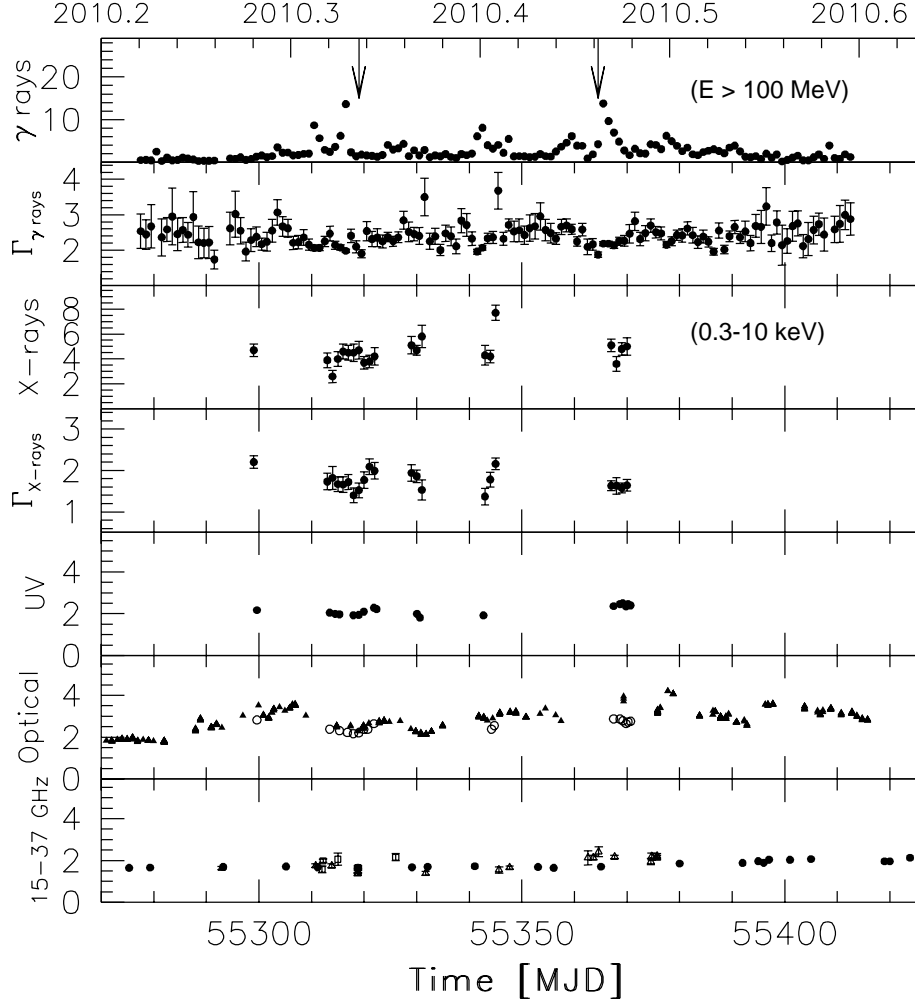
Figure 4.6 Multiwavelength light curves of PKS 1222+21 for the 2010 April 9 – August 4 (MJD 55295–55412) period. The top two panels show integral flux above 100 MeV in units of 10^{-6} photons cm^{-2} s^{-1}, and the photon index as measured by the *Fermi*-LAT taken from [183]. The *Swift*-XRT integral flux in the range 0.3–10 keV, in units of 10^{-12} erg cm^{-2} s^{-1}) and photon index are shown in the next two panels. The fifth panel shows UV data taken with *Swift*-UVOT with $m2$ filter in units of mJy. The sixth panel is optical light curve collected from following observatories: *Swift*-UVOT (u filter, open circles), Abastumani, ATOM, Crimean, KVA and St. Petersburg (R-band, filled triangles), all in units of mJy. The radio data for the 15 GHz (filled circles), 23 GHz (open squares) and the 37 GHz (open triangles) are shown in the last panel in units of Jy. They were obtained from Effelsberg, Medicina, Metsähovi, OVRO and UMRAO. The MAGIC detections are indicated by the downward arrows in the first panel. The errors in the $m2$, u, R and 15 GHz bands (typically 5% or less) and the γ-rays are omitted for clarity.

were restricted in time by periods of full moon. So although no firm claims can be made, it is quite possible that what MAGIC saw was the end of the first and the rising edge of the second γ-ray flare. This conclusion is especially appealing in the case of the second flare, where both the *Fermi*-LAT (Figure 4.6) and especially the MAGIC (Figure 4.2) light curves show very sudden change of flux. A connection between photon index and γ-ray flux was inspected in [183]. They find that the spectra during the active states are in general harder compared to the quiescent state, but claim no correlation on shorter time scales. We also see no correlation, but the spectral slopes during the flares are relatively flat (~ 2, Figure 4.6), which favours a higher flux in the 100 GeV energy region. Unfortunately, the flux of VHE γ-rays is below the sensitivity of the MAGIC telescopes, for order of an hour observations, except during the flares, so we are unable to perform such comparison in the VHE γ-ray band. However, the spectrum above 3 GeV, can be described by a single power-law. All this suggests that the emission observed by the MAGIC and the *Fermi*-LAT is a result of the same process in the source. The X-ray flux also shows variation, but on a much smaller scale than the γ-ray band.

4.3.6 The spectral energy distribution and plausible emission scenarios

As we have seen in Sections 4.2.1 and 4.2.2, the light curve and the spectrum measured by MAGIC give contradictory implications on the position of the VHE γ-ray emission region in PKS 1222+21. While a very rapid flux change suggests the emission region is very compact, and thus located inside the BLR, a lack of cut-off in the spectrum proves that there is no annihilation of VHE γ-rays on the soft photons from the BLR. So how do we fit together these two seemingly contradictory results? If the VHE γ-rays are produced inside the BLR, how are they transported without being annihilated? On the other hand, if the emission region is located outside of the BLR, what does it make so compact to produce such sudden variation of the flux? Here we discuss several emission scenarios that were suggested as a solution to this spectrum — light curve puzzle.

Probably the most exotic scenario brought to our attention is the one suggested by Tavecchio et al. [75]. They propose a standard external Compton model with a one-zone emission region as explained in Section 1.1.4. The problem of VHE γ-ray absorption in the BLR they solve by oscillations between γ-rays and axion-like particles (ALP). Axions are hypothetical scalar bosons first proposed in 1977 by Pecei and Quinn [201]. They used axions to explain why the CP-symmetry is conserved in strong interactions, although it should be broken according to Quantum Chromodynamics (QCD) theory, a puzzle known as the *strong CP problem*. Axions, if they exist, are also candidates for (at least a component of) dark matter. The existence of ALPs is predicted by several extensions of the Standard Model (SM). The photon-ALP oscillations are supposed to occur in the presence of magnetic fields. If this happened, the VHE γ-rays produced in PKS 1222+21 could convert to ALPs, which could pass through the BLR and convert back to the γ-rays. In this way, the VHE γ-ray flux would be significantly less attenuated. An obvious downside of this proposal is the fact that the ALPs are still only hypothetical particles; neither have they been experimentally detected, nor has any of the SM extensions that predict them been confirmed. If the ALP scenario was the only way to reconcile the lack of cut-off in the spectrum and the very short time scale of the flux variation, the detection of the VHE γ-ray flare in PKS 1222+21 would have another great importance as a strong argument for the existence of axions. However, we will see that there are other plausible scenarios that manage to explain the emission from PKS 1222+21.

An emission scenario based on a hadronic model was suggested by Dermer, Murase and Takami [74]. However, the "standard" hadronic models described in Section 1.1.4 face the same problem of VHE γ-ray annihilation as the leptonic models do. So they propose that the neutrons created in photo-pion reactions form a collimated outflow. Neutrons interact with IR photons from the dust torus to produce pairs of ultrarelativistic leptons, which radiate secondary γ-rays. Basically, the authors rely on neutral beams to circumvent the VHE γ-rays absorption in the BLR. This scenario implies that PKS 1222+21 is a source of ultra high energy cosmic rays and, inevitably, a strong source of neutrinos.

As such, it faces the same problem of all hadronic emission models, that a strong flux of neutrinos has not been detected from PKS 1222+21.

One-zone emission scenario

The scenario we propose is a simple one-zone leptonic external Compton (EC) scenario based on models by Finke, Dermer and Böttcher [59] and by Dermer et al. [60]. It was our intention to find a description that is capable of explaining the emission not only during the flaring state and solving the VHE spectrum — light curve puzzle, but that can also be applied to the quiescent state of the source. So the data that we collected, were separated in three quasi-simultaneous subsamples, two of which we consider to be part of the flaring states of 2010 April 29 (first flare) and 2010 June 17 (second flare), and the quiescent state prior to 2009 September 12. These periods were chosen according to the activity of the source observed with *Fermi*-LAT. When precisely simultaneous data for the flaring states were not available, we used observations nearest in time to the peaks in γ-ray flux measured by *Fermi*-LAT. So the MAGIC data from 2010 June 17 were included in the second flare, but for the first flare we used MAGIC data from 2010 May 3. We corrected the MAGIC data for the EBL absorption using the EBL model from Finke, Razzaque and Dermer [202]. The second flare data are the same ones reported in [71], except that the EBL model from Domínguez et al. [108] was used in that case, however, these two models are nearly identical in the given energy range. The *Fermi*-LAT spectrum for the second flare was obtained from the observation on 2010 June 17, while the spectrum for the first flare includes integrated data from the period of 2010 April 23 – May 2, and the quiescent state includes data from 2008 August 2008 till 2009 September 12, as already reported in Section 4.3.1. The quiescent state and the first flare spectra were taken from [183], and the second flare spectrum from [71]. The *Swift* spectra for the quiescent state were obtained from the observations performed on 2009 April 10 and 19, and for the first and the second flare from 2010 April 23 and 2010 June 20, respectively. The optical *R*-band and radio data were taken from 2010 April 28 and June 22, for the first and the second flare, respectively. In addition, we
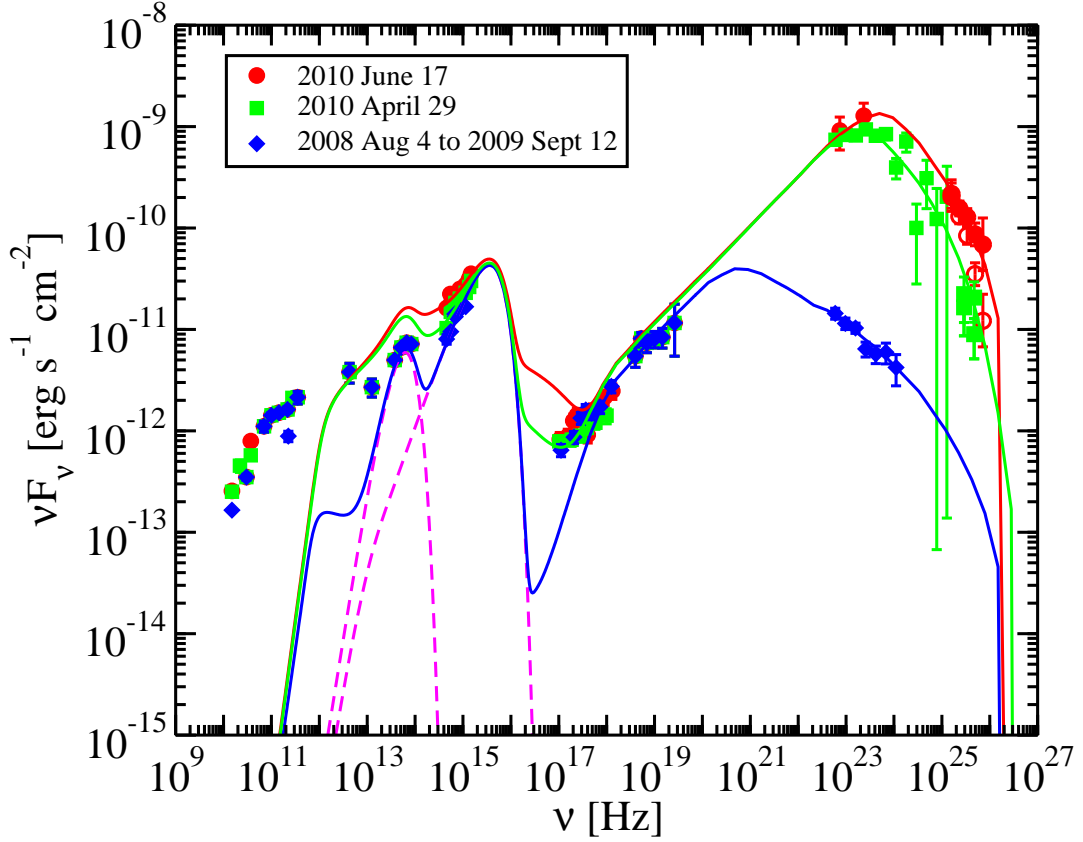
Figure 4.7 Spectral energy distribution of PKS 1222+21 during γ-ray flaring episodes of 2010 April 29 (green squares) and 2010 June 17 (red circles), and and a quiescent state between 2008 August 4 and 2009 September 12 (blue diamonds). The thermal emission component from the dust torus and the accretion disc is indicated by the dashed magenta lines. The MAGIC data are corrected for the EBL absorption using the model of [202]. Empty symbols are the observed data, while filled symbols indicate the EBL-corrected ones.

use the average *Swift*-BAT spectrum from the 70 month *Swift*-BAT catalogue [198], the microwave spectrum measured by the *Planck* satellite in 2009 December [203], and the IR data from the *Spitzer* satellite [204]. The data are shown in Figure 4.7. The quiescent state, first and second flare are represented with blue diamonds, green squares and red circles, respectively. The lines in the same colours represent the results of modelling for each respective period.

We propose that the γ-ray emission region is a single blob of ultrarelativistic electrons. Since PKS 1222+21 is a FSRQ, it is expected that the majority of emitted γ-rays are a

result of external Compton mechanism. That is, thermally emitted soft photons are up-scattered through inverse Compton scattering on ultrarelativistic electrons in the blob. Electrons also emit synchrotron radiation, and some part of it is also up-scattered, but this synchrotron self-Compton (SSC) contribution to the γ-ray flux is dominated by the EC contribution (see e.g. [205]). So we try to explain the radiation as a combination of synchrotron, SSC and EC emission. We assume the electrons in the blob to be distributed according to a broken power-law. We choose the variability time scale of 10 minutes, based on the MAGIC light curve of June 17, and use it to restrict the dimension of the blob to $R'_{\rm b} = 10^{15}$ cm, as explained in Section 4.2.1. From the VHE γ-ray spectrum (see Section 4.2.2), that is from the lack of a cut-off in the spectrum we know that the blob should be located outside of the BLR, which is on a distance of $R_{\rm BLR} \approx 2 \times 10^{17}$ cm from the black hole [183]. Considering the location of the blob, the expected source of seed photons is the dust torus, which we represent with a one-dimensional ring lying in the plain orthogonal to the jet, with radius $R_{\rm dust} = 1.8 \times 10^{19}$ cm, which is roughly consistent with the value of the dust sublimation radius calculated by Nenkova et al. [206]. In addition, the dust torus is characterised by the luminosity and temperature ($L_{\rm dust}$ and $T_{\rm dust}$). Our results for these two parameters are consistent with the ones found by Malmrose et al. [204]. There is an obvious additional source of thermal radiation and that is the accretion disc, contributing to the emission in the optical band. A blob of ultrarelativistic electrons, filled with magnetic field, is also a source of the synchrotron radiation. However, if the synchrotron contribution was dominant over thermal, the spectrum would appear much softer. Instead we clearly see a big blue bump in the SED. We represent the accretion disc with the Shakura-Sunyaev multi-temperature disc [207], whose emission is angle dependant on the orientation of the disc. For the mass of the black hole, we adopt the value from [176], $M_{\rm BH} \sim 6 \times 10^8\ M_\odot$. Since our γ-ray emission region is located outside of the BLR, only photons from the dust torus will serve as the target photons for the inverse Compton scattering, with a small contribution of the synchrotron photons from the blob. The radio emission of the source varies much more slowly than the γ-ray flux, so we are unable to identify the γ-ray emission region

with any of the several radio components. In fact, the slow variability suggests that the radio points in the SED are a superposition of radio emission from several self-absorbed components in the jet [208], rather than coming from a single emission region responsible for the rest of the radiation. Also, the size of the blob constrained by the causality requirements is much smaller than the region imaged by the VLBA (Figure 4.5). Therefore, we treat radio points in the SED as upper limits. The signal during the first flare and the quiescent state was too weak to calculate the VHE γ-ray spectrum, so we cannot perform the same analysis as for the first flare (see Section 4.2.2) to determine whether there is evidence of a cut-off in the spectrum. Also, the variability is not as pronounced as during the second flare. Nevertheless, we use the constraints on the dimension and the location of the blob from the second flare and impose them also for the first flare and the quiescent state. Is a single blob capable of emission observed both during two different flares and the quiescent state?

We find that the answer to this question is affirmative. The scenario we propose fits the observations in all three states with keeping most of the parameters the same. The parameters can be found in Table 4.3. We can see that the only difference between three different states is in the distribution of electrons. The break in the distribution for the first flare is at almost half the energy of the break for the second flare. This results in somewhat lower jet power during the first flare compared to the second one. The break during the quiescent state happens at much lower energies, and we change the normalization factor, but the rest of the parameters remain the same as for the flaring states. Our results do have some problems describing the X-ray data, with the proposed description of the flaring episodes overestimating the values, and the description of the quiescent state underestimating the soft X-ray values. However, the *Swift* observations were not strictly simultaneous to the MAGIC and *Fermi*-LAT observations during the flaring episodes; the *Swift* data used for the first flare were taken 6 days prior to the first and 3 days after the second flare. Therefore, the flux might have been somewhat different from what we have measured. The higher than predicted flux for the quiescent state could be the result of averaging over longer time period. It is also possible that

Table 4.3 Parameters for the SED shown in Figure 4.7.

Parameter	Symbol	2010 June 17	2010 April 29	Quiescent state
Redshift	z	0.432	0.432	0.432
Black Hole Mass	M_{BH}	$6 \times 10^8 \ M_\odot$	$6 \times 10^8 \ M_\odot$	$6 \times 10^8 \ M_\odot$
Gravitational Radius [cm]	R_{g}	8.8×10^{13}	8.8×10^{13}	8.8×10^{13}
Eddington Luminosity [erg s^{-1}]	L_{Edd}	7.8×10^{46}	7.8×10^{46}	7.8×10^{46}
Disc Eddington Ratio	$L_{\mathrm{disc}}/L_{\mathrm{Edd}}$	0.2	0.2	0.2
Disc Accretion Efficiency	η_{disc}	1/12	1/12	1/12
Inner Disc Radius [R_{g}]	R_{in}	3	3	3
Outer Disc Radius [R_{g}]	R_{out}	3×10^4	3×10^4	3×10^4
Bulk Lorentz Factor	Γ	40	40	40
Doppler Factor	δ_{D}	80	80	80
Magnetic Field [G]	B	0.7	0.7	0.7
Variability time scale [s]	t_{v}	6×10^2	6×10^2	6×10^2
Comoving Radius of the Blob [cm]	R'_{b}	1.0×10^{15}	1.0×10^{15}	1.0×10^{15}
Jet Height [cm]	r	8.8×10^{18}	8.8×10^{18}	8.8×10^{18}
Low-Energy Electron Spectral Index	p_1	2.0	2.0	2.0
High-Energy Electron Spectral Index	p_2	3.5	3.5	3.5
Minimum Electron Lorentz Factor	γ'_{min}	1.0	1.0	1.0
Break Electron Lorentz Factor	γ'_{brk}	1.0×10^3	6.0×10^2	26
Maximum Electron Lorentz Factor	γ'_{max}	4.0×10^4	2.0×10^4	4.0×10^4
Dust Torus luminosity [erg s^{-1}]	L_{dust}	5.5×10^{45}	5.5×10^{45}	5.5×10^{45}
Dust Torus temperature [K]	T_{dust}	1.1×10^3	1.1×10^3	1.1×10^3
Dust Torus radius [cm]	R_{dust}	1.8×10^{19}	1.8×10^{19}	1.8×10^{19}
Jet Power in Magnetic Field [erg s^{-1}]	$P_{\mathrm{j,B}}$	5.9×10^{42}	5.9×10^{42}	5.9×10^{42}
Jet Power in Electrons [erg s^{-1}]	$P_{\mathrm{j,e}}$	4.3×10^{44}	4.0×10^{44}	1.9×10^{44}

the X-ray emission region is somewhat larger than the γ-ray emission region, or that there is another source of X-rays, for example the corona of the accretion disc.

A similar scenario was proposed by Tavecchio et al. [63]. In addition to one-zone scenario, they propose two two-zone scenarios. They use another larger emission region to explain emission at lower energies. In that way they obtain a somewhat better fit to the X-ray part of the spectrum, which is produced in the larger emission region in the jet. They consider two possibilities for the location of the larger emission region: within the BLR, and above it. Although this scenario does fit the points in the soft X-ray region ($\sim 10^{17} - 10^{18}$ Hz; they do not use hard X-ray points $\sim 10^{19} - 10^{20}$ Hz) better than ours, the authors focus only on the second flare. Even if we assume that the same emission region configuration is responsible for both flaring episodes and that the two-zone scenario as proposed in [63] can be also applied to the first flare, it is not entirely

clear what happens with the compact blob during the quiescent state of the source. We demonstrated that our scenario is applicable to all three states. Admittedly, there is some degeneracy in the choice of the parameters, however, our goal was to inspect the possibility of explaining the emission with a simple one-zone scenario without invoking some exotic transport mechanisms mentioned in the beginning of this section. Moreover, we managed to find that the sets of parameters for different states of the source vary only in the distribution of electrons.

It remains to see how such compact emission region is able to form at parsec distance from the nucleus. First of all it should be pointed out that the γ-ray emission region probably constitutes only a small fraction of the jet. Considering the radius (R'_b) and the distance of the blob from the nucleus (r), and assuming that the blob covers the whole cross section of the jet, it would mean that the opening angle of the jet would be $\theta_{\text{open}} \sim R'_b/r \sim 10^{-4}\,\text{rad} \sim 0.007°$, which is highly unlikely, not to mention that the radio observations suggest a much wider jet (Figure 4.5). Several mechanisms through which a compact emission zone could form at parsec distance were discussed by Nalewajko et al. [209]. The authors favour the blob formation in magnetic reconnection events as proposed by Cerutti et al. [210]. Magnetic reconnection is a process of rearranging of the topology of a magnetic field. In highly conducting plasma this can lead to magnetic energy being converted to particle kinetic energy. However, Tavecchio et al. ([63]) argue that this scenario requires a magnetically dominated jet, while their as well as our own description suggests that the most of the jet's power is contained in particles (see Table 4.3). Another possibility is a hydrodynamic recollimation of the jet through interaction with the surrounding matter. A collision of a layer of the jet with an external medium results in a shock. If the shocked layer of the jet is efficiently cooled through radiation, the pressure after the shock is significantly reduced, and the jet can be focused through a very small cross sectional area, forming a compact emission region [157].

4.4 Summary

The FSRQ PKS 1222+21 was observed by the *Fermi*-LAT since the beginning of its mission in 2008 August. Even though the source was in a quiescent state until 2009 September, its later highly variable activity earned it the title of the most variable source in the first *Fermi*-LAT catalogue of sources above 10 GeV. High and variable flux detected by the *Fermi*-LAT in 2010 triggered observations by the MAGIC telescopes. MAGIC detected signal on two occasions contemporaneous with two flares detected by the *Fermi*-LAT. The rest of the MAGIC observations resulted in upper limits only, and on those nights the HE flux was significantly lower compared to the two flares. We have solid grounds (see Section 4.3.5) to assume that both HE and VHE γ-radiation is produced through the same mechanism in the same location. So we expect that enhanced activity in HE band implies also higher flux of VHE γ-rays. If this assumption is correct, it means that the VHE flux in the quiescent state is below the sensitivity of the MAGIC telescopes. During the second of the two flares, on the other hand, MAGIC measured one of the fastest time variation ($\sim$10 min) ever observed in a FSRQ and among the shortest time scales measured for TeV emitters. Combined with relatively hard spectrum in γ-ray band ($\Gamma = 2.7 \pm 0.3$) extending to at least 130 GeV without a cut-off, this detection presents quite a challenge to previously existing models of γ-ray production in AGN. We investigated a multiwavelength light curve for the 2010 February – June period in order to investigate any possible connection between activity in γ-ray band to other wavebands. We observed a moderate variability of the X-ray flux. The ratio of the highest to the lowest flux amplitude was around 3, with the photon index changing between 1.4 and 2.2. However, no correlation between the two was noticed. Some variability was also observed in the UV band, but on a much lower scale compared to the γ-ray band. The UV radiation is mostly contributed to the emission from the accretion disc, but the observed flux increase is to small to consider enhanced accretion to be the cause of the violent γ-ray activity. Two peaks in the optical band were spotted, but although close in time to the γ-ray flares, not simultaneous to them.

We suggested a simple one-zone external Compton scenario to explain the γ-ray emission. The size of the emission region was constrained to agree with the duration of the variability measured by MAGIC during the second flare. The location of the emission region is obviously outside the BLR, unless some exotic mechanism of the particle transport through the BLR is active. Otherwise, the VHE γ-ray spectrum would be cut off. We find that the scenario we propose fits both γ-ray flaring states as well as the quiescent state, and the difference is caused only by different distribution of electron in the emission region. This scenario is an elegant solution to the spectrum — light curve puzzle, differing from the standard one-zone EC models only by the location of the emission region at parsec distance from the nucleus. This should not pose a difficulty, since there are several mechanisms through which a compact region can be formed at such distances.

Still, we cannot exclude other possible scenarios, and we hope further observations will shed more light on this interesting problem. The MAGIC telescopes continue to monitor PKS 1222+21 as part of a Target of Opportunity (ToO) program during its flaring episodes. Given the fact that the VHE γ-ray flux from PKS 1222+21 in its quiescent state is below the sensitivity of the existing Cherenkov telescopes, we are looking forward to future observations with the CTA.

Chapter 5

H1722+119

5.1 Introduction

H1722+119 was first observed in the 1970's as part of the *Uhuru* X-ray sky survey and the *HEAO 1* Large Area Sky Survey (LASS). The resulting X-ray source catalogues (source name: 4U1722+11 in [211], and source name: 1H1720+117 in [212]) only state it as an X-ray source. Almost twenty years later, it was simultaneously and independently classified as a BL Lac object by Griffiths et al. [19] and Brissenden et al. [20]. Furthermore, the lower energy peak at $\nu_{\rm s} = 6.3 \times 10^{15}$ Hz was reported by Nieppola, Tornikoski and Valtaoja [52], classifying H1722+119 as an intermediate-energy-peaked BL Lac. A very high degree of linear polarization in optical region, reaching $17.6 \pm 1.0\%$ in *B*-band was reported in [20]. H1722+119 was later observed in radio band by the Owens Valley Radio Observatory (OVRO [213])[1]. It was also observed by the Very Long Baseline Array (VLBA) at 5 GHz as part of the study of radio properties of blazars detected by the *Fermi*-LAT [21] (source name: F17250+1151). There it was described as a compact source with a short jet. Infrared (IR) observations of H1722+119 were performed as part of Two Micron All-Sky Survey (2MASS [214]).

Although a featureless spectrum was reported by Brissenden et al. [20], Griffiths et al.

---

[1]www.astro.caltech.edu/ovroblazars

estimated redshift of the host galaxy based on an absorption feature to be 0.018 [19]. However, this result was not confirmed by other optical observations (e.g. [215, 216, 217]). In fact Sbarufatti et al. derived a lower limit of 0.17 [218]. Recently, Landoni et al. set the lower limit on the redshift, using the spectrograph X-Shooter at the European Southern Observatory Very Large Telescope, at 0.35 [219]. They detected no intrinsic or intervening spectral lines, ascribing it to an extreme optical beaming, setting the ratio of beamed and thermal emission to ≥ 400. Farina et al. (priv. comm.) observed H1722+119 with Nordic Optical Telescope in 2013 and were unable to detect the host galaxy. They set a lower limit on redshift at 0.4.

In this chapter we report on the discovery of the very high energy (VHE) γ-ray emission from H1722+119 by the MAGIC telescopes [22]. We use γ-ray spectra measured by MAGIC and *Fermi*-LAT to estimate the redshift, and study the multiwavelength characteristics of H1722+119.

5.2   MAGIC observations and data analysis

H1722+119 was listed as candidate TeV blazar by Costamante and Ghisellini [220] based on its X-ray and radio properties. It was first observed by MAGIC between 2005 and 2009 together with 20 other BL Lac candidates [221][2]. The stacked sample of observed blazars showed an average signal above $100\,\mathrm{GeV}$ with a significance of $4.9\,\sigma$, but the analysis of H1722+119 data alone resulted in $1.4\,\sigma$ after $32\,\mathrm{h}$ of observation, with an upper limit of flux above $140\,\mathrm{GeV}$ of $1.3 \times 10^{-11}\mathrm{cm}^{-2}\mathrm{s}^{-1}$.

The results used in the study presented here are based on the observations performed during six nights between 2013 May 17 and 22. The observations were triggered by the optical observations with the KVA (see Section 5.3.3). The author of this thesis analysed daily the data recorded the previous night. Based on his results, a decision was made whether to schedule observations for another night or not. Unlike the flare advocating,

---

[2]In that article the source is designated RX J1725.0+1152. It was selected based on its X-ray properties from [222].

described in Section 4.1, the author was now responsible for this source only, and only while this source was observed. The observation conditions during this campaign were ideal for the six consecutive nights the source was observed, and the observations were not interrupted by periods of the full moon.

Between the first and the second observation campaign the MAGIC system had undergone a series of major upgrades. During the first campaign, MAGIC operated only one 17 m telescope; it used a 576 pixel camera with two different sizes of pixels; trigger region was confined to the inner part of the camera (smaller pixels); and the data were recorded at a rate of 300 MHz, which was later upgraded to 2 GHz. The second MAGIC telescope was commissioned in the autumn of 2009, but not in time to join the campaign. The data presented here were taken in stereoscopic mode with two 17 m telescopes, both using cameras with 1039 equal sized pixels with extended trigger regions and electronics with 2 GHz readout rate. The current sensitivity of the instrument in 100–200 GeV energy range is roughly double the sensitivity of single MAGIC I telescope as it was operated in 2009. The ratio of the instrument sensitivities, with which the two campaigns were performed is even higher considering the instrument was upgraded during the first observation campaign. For details please refer to Table 2.1 and the corresponding chapter.

H1722+119 was observed in wobble mode with four false-source positions for a total of 12.5 h. After quality selection based on stability of event rates, the effective time amounted to 12 h. A total of 1 h of data was taken during twilight and were analysed together with the data taken during dark time [223]. Observations were performed at zenith angles between 16° and 37°. MAGIC obtained an excess of 337.5 events above 60 GeV with respect to the background, yielding a signal significance of 5.92 σ using Eq. 17 of [123]. The VHE γ-ray signal is shown in Figure 5.1.

The light curve of the integral VHE γ-ray flux above 150 GeV is shown in Figure 5.2. There is no evidence of variability of flux on a night-by-night basis. A fit with a constant flux of $(6.3 \pm 1.6) \times 10^{-12}\,\mathrm{cm^{-2}\,s^{-1}}$ resulted in $\chi^2/NDF = 3.5/5$, where NDF stands for the number of degrees of freedom. This is equivalent to $(2.0 \pm 0.5)\%$ Crab Nebula units
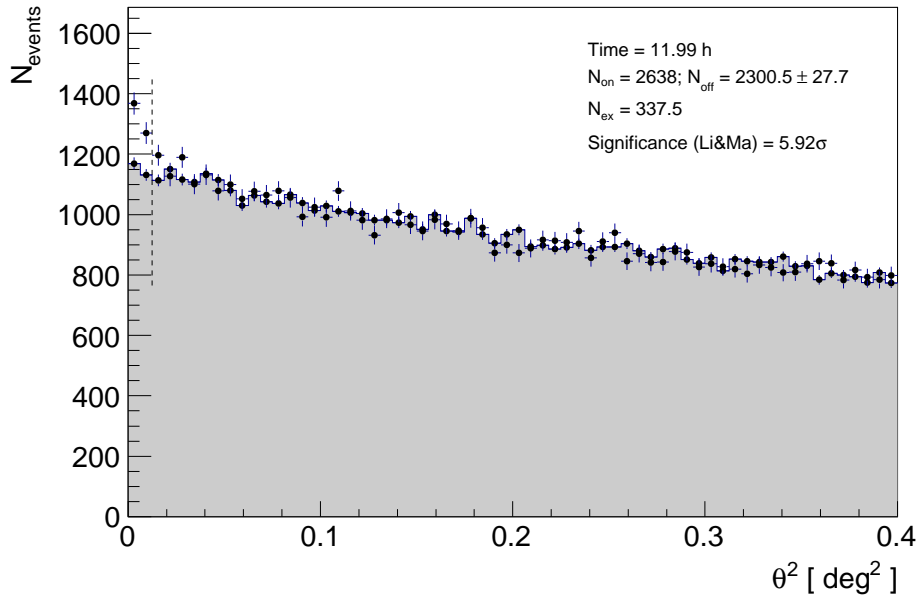
Figure 5.1 θ^2 distribution of ON-source (black points) and OFF-source (grey area) events. N_{on} is the number of all ON-source events with $\theta^2 < 0.0125\,\mathrm{deg}^2$ (vertical dashed line) with respect to the source position, and N_{off} the normalised number of all OFF-source events from the same region around OFF-source position.

(C.U., see Section 1.2.3). The measured flux is consistent with the upper limit set by the MAGIC observations of H1722+119 from the previous campaign [221].

The differential energy spectrum was reconstructed using the Forward Unfolding algorithm described in [127]. It can be described by a simple power-law function $dN/dE = N_0(E/200\,\mathrm{GeV})^{-\Gamma}$ with normalization $N_0 = (4.3 \pm 0.9) \times 10^{-11}\mathrm{TeV}^{-1}\,\mathrm{cm}^{-2}\,\mathrm{s}^{-1}$, and a photon index $\Gamma = 3.3 \pm 0.3$.

5.3 Multiwavelength observations

5.3.1 *Fermi*-LAT

The *Fermi*-LAT data used in this study were collected from 2013 January 1 (MJD 56293) to December 31 (MJD 56657). During this time, the *Fermi* observatory operated almost entirely in survey mode. Integrating over this period in the 0.1–100 GeV energy range,
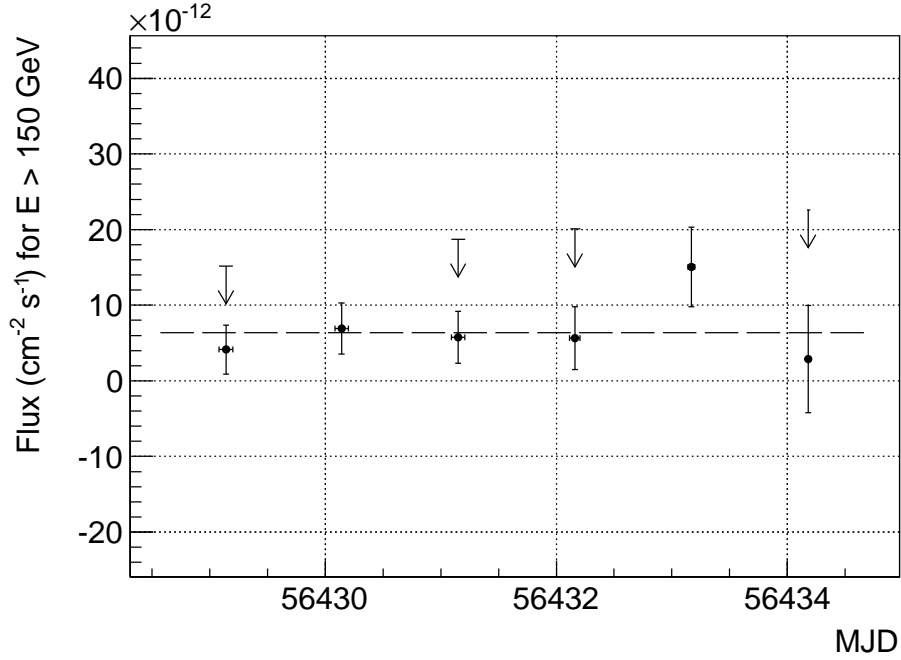
Figure 5.2 MAGIC light curve for energies above 150 GeV; one point per night. Horizontal error bars represent duration of each observation. Vertical arrows are upper limits for points whose relative error of the excess is > 0.5. Horizontal dashed line is a constant flux fit with parameters stated in the text.

and using a power-law model, the fit yielded a TS = 335, with *Fermi*-LAT measured an average flux of $(4.1 \pm 0.7) \times 10^{-8}\,\mathrm{cm^{-2}\,s^{-1}}$, and a photon index of $\Gamma = 1.99 \pm 0.08$. The *Fermi*-LAT light curve and the photon index evolution with 2-month time bins is shown in Figure 5.3. No significant increase of the γ-ray activity was observed by *Fermi*-LAT in 2013 May and June. Both the flux and the photon index can be fitted by a constant with the following parameters for the flux: $(3.43 \pm 0.56) \times 10^{-8}\,\mathrm{cm^{-2}\,s^{-1}}$ and $\chi^2/NDF = 3.87/5$, and the photon index: 1.96 ± 0.07 and $\chi^2/NDF = 1.68/5$. Leaving the photon index free to vary during 2013 May, we obtained a photon index of $\Gamma = 1.40 \pm 0.29$. This hardening of the HE γ-ray spectrum may be an indication of the shift of the inverse Compton peak at higher energies during the MAGIC detection. By considering only the period May 13–26, including the MAGIC observation period, and assuming $\Gamma = 1.40$, we obtained a flux of $(0.91 \pm 0.44) \times 10^{-8}\,\mathrm{cm^{-2}\,s^{-1}}$.

Table 5.1 Flux densities of H1722+119 in optical – UV bands measured by *Swift*-UVOT.

Filter	λ [Å] / ν [10^{14} Hz]	Flux density [mJy]		
		2008 May 31	2013 Jan 15	2013 May 20
v	5468 / 5.48	2.41 ± 0.11		4.10 ± 0.11
b	4392 / 6.83	1.68 ± 0.06	3.00 ± 0.07	3.46 ± 0.07
u	3465 / 8.65	1.43 ± 0.05	2.46 ± 0.07	2.72 ± 0.07
w1	2600 / 11.53	0.68 ± 0.03	1.34 ± 0.04	1.54 ± 0.04
m2	2246 / 13.35	0.64 ± 0.03	1.14 ± 0.04	1.30 ± 0.03
w2	1928 / 15.55	0.53 ± 0.02	1.06 ± 0.03	1.11 ± 0.03

5.3.2 *Swift*

The *Swift* satellite [194] performed three observations of H1722+119 on 2008 May 31, 2013 January 15 and May 20. The observations were carried out with all three on board instruments (the Burst Alert Telescope (BAT), the X-ray Telescope (XRT) and the UltraViolet Optical Telescope (UVOT), mentioned in Section 4.3.2). The hard X-ray flux of this source is below the sensitivity of the BAT instrument for the short exposure of these observations, therefore the data from this instrument are not used. Moreover, the source was not present in the *Swift* BAT 70-month hard X-ray catalogue [198]. The X-ray flux measured by XRT in 2008 May 31 was $(3.6 \pm 0.7) \times 10^{-12}\,\mathrm{erg\,cm^{-2}\,s^{-1}}$, and was a factor between 3 and 5 lower than the fluxes observed in 2013, i.e. $(1 - 2) \times 10^{-11}\,\mathrm{erg\,cm^{-2}\,s^{-1}}$. The UVOT flux densities are given in Table 5.1. We note that the flux densities observed in 2008 May 31 are a factor of 2 lower with respect to 2013 observations. The XRT and UVOT flux densities collected in 2013 are reported in Figure 5.3.

5.3.3 KVA data

The KVA (Kungliga Vetenskaps Akademientelescope) is located at the Observatorio del Roque de los Muchachos, La Palma (Canary Islands), and is operated by the Tuorla Observatory, Finland[3]. The telescope consists of a 0.6-m f/15 Cassegrain devoted to

---

[3]users.utu.fi/kani/1m

polarimetry, and a 0.35-m f/11 SCT auxiliary telescope for multicolour photometry. The telescope has been successfully operated remotely since autumn 2003. The KVA is used for optical support observations for MAGIC by making R-band (6400 Å, 4.68×10^{14} Hz) photometric observations, typically one measurement per night per source.

H1722+119 has been regularly monitored by the KVA since 2005. At the beginning of May 2013, after an extended optical high state, the source reached an R-band magnitude of 14.65, the brightest ever observed from this source. The high emission state triggered observations by MAGIC, but the MAGIC observations started during the decreasing part of the optical flaring activity. The KVA observed light curve for 2013 is shown in Figure 5.3 (one point per night). The flux varies quite a lot, the ratio between the highest and lowest point being 1.62, but we see no regularity in this variation. The data were reduced by the Tuorla Observatory Team as described in Nilsson et al. (2014, in prep.).

5.3.4 OVRO data

The OVRO is a 40-m radio telescope observing at 15 GHz band. In late 2007 it started blazar monitoring as a support of the *Fermi* telescope [213]. This monitoring program includes about 1800 known or likely γ-ray-loud blazars, including all candidate γ-ray blazar survey (CGRaBS) sources above declination $-20°$. The sources in this program are observed in total intensity twice per week with a 4 mJy (minimum) and 3% (typical) uncertainty on the flux density. Observations are performed with a dual-beam (each 2.5 arcmin full-width half-maximum) Dicke-switched system using cold sky in the off-source beam as the reference. Additionally, the source is switched between beams to reduce atmospheric variations. The absolute flux density scale is calibrated using observations of 3C 286, adopting the flux density (3.44 Jy) from [224]. This results in about a 5% absolute scale uncertainty, which is not reflected in the plotted errors.

The OVRO light curve for 2013 is shown in Figure 5.3 (one point per night). Although there is some indication of a short time variability, we fitted the whole sample with a

linear function ($F[\text{Jy}] = p_0 + p_1 \times t[\text{MJD}]$) to point out the general trend of increasing flux. The fit parameters are $p_0 = -5.98 \pm 0.58 \,\text{Jy}$, $p_1 = (1.07 \pm 0.10) \times 10^{-4} \,\text{Jy}$ and $\chi^2/NDF = 39.68/36$. We also considered a possibility of a constant flux, but that assumption was discarded with $\chi^2/NDF = 146.9/37$.

5.4 Multiwavelength properties

5.4.1 Redshift

VHE γ-rays are partially absorbed by the extragalactic background light through pair-production (see Section 1.2.6). The resulting flux attenuation is directly dependent on the redshift of the source and energy of γ-rays. A method developed by Prandini et al. [225] uses the fact that the VHE γ-ray flux is attenuated by the EBL to estimate the redshift of a given source. The method is based on the following assumptions: i) HE and VHE γ-rays are created by the same physical process in the same region, and ii) the intrinsic spectrum of the source in the VHE range cannot be harder than the spectrum in the HE range. The method uses contemporaneous MAGIC and *Fermi*-LAT measurements. It calculates the de-absorbed MAGIC spectra for various values of assumed redshift. The value for which the de-absorbed MAGIC spectral slope equals the *Fermi*-LAT spectral slope is marked by z^*. This method was tested on a set of TeV blazars with known redshifts, and it was determined that z^* is higher than true redshift values. However, Prandini et al. [225] managed to derive an empirical law, which describes the relation between the z^* and the true redshift, and allows them to estimate the true redshift of blazars of unknown distance. They used it to estimate the redshift of PKS 1424+240.

Applying this method to H1722+119, we estimate upper limit on redshift to be 0.95, with the most likely value $z = 0.34 \pm 0.15$. This result is in agreement with the latest results from [219] and Farina et al. For $z = 0.4$, and using the EBL model from [191], we find the parameters of the intrinsic (EBL-de-absorbed) VHE spectrum to be

$N_0 = (9.6 \pm 2.2) \times 10^{-11} \mathrm{TeV}^{-1} \mathrm{cm}^{-2} \mathrm{s}^{-1}$, and $\Gamma = 2.3 \pm 0.4$.

5.4.2 Light curve

As already mentioned in Section 5.3.3, MAGIC observations were triggered by an extended optical high state and the historical R-band maximum. The VHE γ-ray flux (Figure 5.2) appears to be constant and it is compatible with the previously established upper limit based on a combined data taken over several years. Therefore we conclude that the source was not flaring in the VHE γ-rays during MAGIC observations. Unfortunately, observations performed during six consecutive nights are not enough to study a longer term variability. However, we compared the HE γ-ray, optical and radio light curves for the entire year. The *Fermi*-LAT data were divided in 2-month time bins with the photon index left free to vary (Figure 5.3). There is no indication of any flux variability. OVRO data might indicate radio flux variability on a time scale of a few months. Additionally, comparison of fluxes on a time scale of the entire year reveals that the OVRO data show an obvious trend of increasing flux on a time scale of one year (dashed line in bottom panel of Figure 5.3), while the HE γ-ray flux appears to be constant.

5.4.3 Spectral energy distribution

We present the spectral energy distribution contemporaneous to MAGIC observations in Figure 5.4. In that period, one observation was performed by OVRO at 15 GHz (MJD 56434.29). Five observations were performed in R-band by the KVA. They were averaged to obtain a spectral point at 4.68×10^{14} Hz. The *Swift* data were obtained from the 2013 May 20 observation. The *Fermi*-LAT spectrum was calculated in the period 2013 May–June. MAGIC points were obtained with Schmelling's method as described in [127]. Based on the arguments discussed in Section 5.4.1, we adopt a value for redshift of 0.4, and EBL model from [191] to get the intrinsic VHE part of the spectrum.
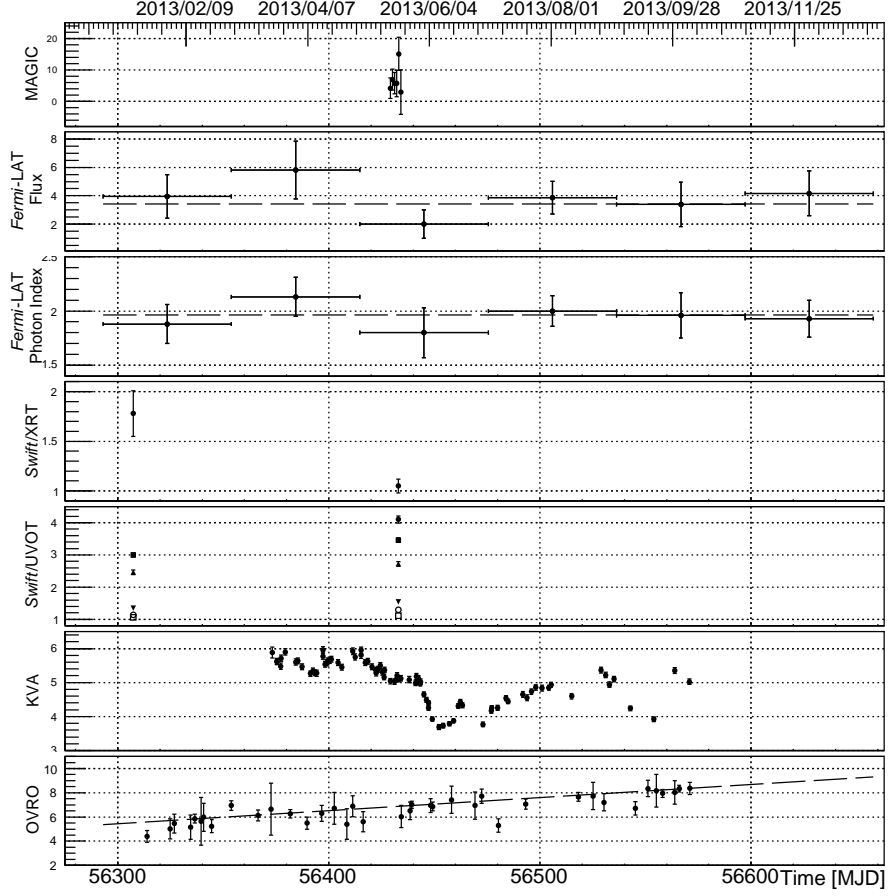
Figure 5.3 Combined light curve for year 2013. MAGIC points are the same as in Figure 5.2. Vertical arrows were omitted for clarity. For *Fermi*-LAT data we show evolution of the flux and the photon index with 2-month time bins. Horizontal dashed lines in both panels represent the fit with a constant. Dashed line in OVRO panel represents a linear function fit. All the fit parameters are given in the text. Flux units: MAGIC: $10^{-12}\mathrm{cm}^{-2}\,\mathrm{s}^{-1}$, *Fermi*-LAT: $10^{-8}\mathrm{cm}^{-2}\,\mathrm{s}^{-1}$, *Swift*-XRT: $10^{-11}\mathrm{erg}\,\mathrm{cm}^{-2}\,\mathrm{s}^{-1}$, *Swift*-UVOT: mJy, KVA: mJy, OVRO: Jy.

H1722+119 is a bona fide BL Lac type of source. None of the observations revealed anything about nature of the black hole environment, nor the host galaxy. There is no evidence in the SED of emission from the accretion disc, dust torus or BLR. There is, however, a surprising feature in the SED at a frequency of $\log\nu \sim 15$; an apparent discontinuity between points taken with filters v, b and u on one side, and $w1$, $m2$ and $w2$ on another. The R-band point measured with KVA is on the same level as the first three UVOT points. Taken as a whole, the spectrum in the optical–UV band appears curved,
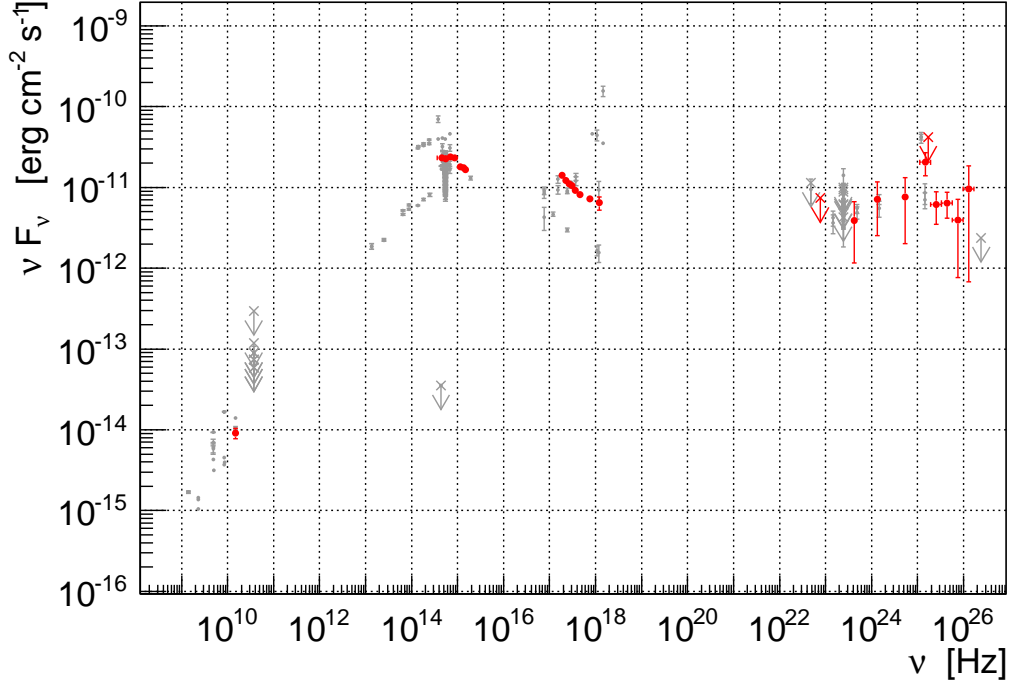
Figure 5.4 H1722+119 spectral energy distribution. The data contemporaneous with the MAGIC observations presented in this work, are marked by red dots. Crosses represent upper limits set by *Fermi*-LAT. Grey points (and crosses for upper limits) are archival measurements acquired from [226].

with a peak in the *b*-band and a steep slope in the UV. Emission models usually applied to BL Lac type of sources suggest that both optical–UV and X-ray parts of the SED are results of synchrotron radiation from the same region in the jet. However, that would manifest as a continuous and monotonic connection between these parts of the SED, which is obviously not compatible with our data. Ignoring the UV band, and focusing only on optical and X-ray bands, a monotonic connection becomes feasible again, so we assumed there was a problem affecting the data in the UV band. However, we were not able to find any indication of instrument malfunction, or error in the data analysis, that would have resulted in lower UV flux. Our next assumption was that the UV emission is partially absorbed, either within the source, or in the intergalactic space. If this was the case, a one-zone SSC model should be able to describe the observations. However, our efforts to find a well fitting one-zone emission scenario, did not bring a satisfactory

result. Although, our results were a good fit to the points in the X-ray band, they either underestimated the emission in optical band, or predicted an IC peak in $\sim 1 - 10\,\mathrm{GeV}$ region, when the data suggest an order of magnitude higher value for the position of the IC peak. Probably a more complex emission scenarios will have to be invoked in order to explain the observations. A two-zone SSC scenario would be more likely to produce a better fit, however it will still be difficult to explain a discontinuity in the optical–UV band as a difference in the contributions from different emission zones. Explaining the origin of the discontinuity might prove to be necessary for understanding the emission mechanism in H1722+119.

5.5   Summary

MAGIC detected VHE γ-radiation from BL Lac H1722+119 after observations were triggered by a historically high flux in R-band measured by the KVA. The MAGIC observations were performed during six consecutive nights and show no flux variability. No significant increase of the activity was observed at HE by *Fermi*-LAT in 2013 May, neither on short time-scales nor compared to the average 2013 flux. An indication of spectral hardening at HE might explain the VHE γ-ray flux high enough to be detected by the MAGIC telescopes. Changes in flux are quite obvious in optical and radio data. However, on a time scale of a year, radio flux seems to increase, while HE flux remains constant, so we cannot claim that the two components originate from the same physical region. Optical and radio fluxes can be compared on a shorter time scale, but again show no correlation. While radio flux is highest towards the end of the year, highest optical point is in April, followed by a quite sudden drop, which does not occur in radio data.

We used the method by Prandini et al. [225], and contemporaneous MAGIC and *Fermi*-LAT data to set the upper limit on the redshift of the source at 0.95, with the most likely value $z = 0.34 \pm 0.15$. Combined with the highest lower limit value obtained by Farina et al., we set redshift at 0.4.

Chapter 6

Conclusions and outlook

Active galactic nuclei are the most luminous persistent sources of electromagnetic radiation in the universe. They are compact regions in the centres of galaxies formed around supermassive black holes that actively accrete matter. Approximately 10% of AGN eject matter through relativistic jets. Objects whose jets are oriented close to the line of sight with the Earth are referred to as blazars. Jets are sources of electromagnetic radiation of all wavelengths from radio to γ-rays. They can extend to Mpc distances from the nucleus and can be brighter than the rest of the galaxy. Naturally they attract the attention of astronomers and astrophysicists. AGN were and still are extensively observed in all energy bands of electromagnetic spectrum from radio to X-rays. Although many interesting phenomena were discovered and explained based on those observations, an important piece of puzzle was missing until we were able to see the γ-ray part of the spectrum. γ-rays are produced through other physical processes than synchrotron and thermal radiation, which are mostly responsible for emission in energy bands below γ-rays. Therefore, observations in γ-rays do not only complete the global picture, but also reveal processes in AGN that we would otherwise be unaware of. Detecting VHE γ-radiation from AGN is a complex task. Apart from several technical difficulties, we also face two obstacles placed by the nature itself. First of all, VHE γ-rays are a rather rare phenomena. We saw in previous chapters that VHE γ-ray spectra of AGN usually follow a negative power-law (see Sections 3.3.1, 4.2.2 and 5.2). We saw from the example of PKS 1222+21 (see Section 4.2.1) that, what was considered a quite

violent flare, consisted in fact of 190 VHE γ-rays in 30 minutes. The second problem is that γ-rays traversing cosmological distances tend to be absorbed by the EBL. It is no wonder then that merely 58 AGN have been confirmed sources of VHE γ-rays so far [227]. Most of them (fifty to be exact) are classified as BL Lacs, what is expected, since radio galaxies are not blazars, and FSRQs are less common at redshifts below 0.5 (see Section 1.1.3). Only four radio galaxies are confirmed γ-ray emitters, and only three AGN are FSRQs. So each newly studied source greatly increases our knowledge and understanding of physics of AGN.

MAGIC collaboration detected 33 of those 58 AGN[1]. A list of all AGN detected so far by MAGIC, with their position, type, redshift and the references to MAGIC publications discussing particular sources is given in Table 6.1.

According to Aharonian [267] observations in HE and VHE γ-ray bands serve different and complementary purposes. Surveys performed by the *Fermi*-LAT and other satellite borne instruments detect a large number of sources and therefore establish a base for statistical studies of AGN. Present ground based observatories (H.E.S.S., MAGIC and VERITAS), on the other hand, do not have the ability to perform sky surveys. Instead, their observations are limited to dedicated observations of given objects. However, as we pointed out in Section 1.2.5, Cherenkov telescopes have much larger collection area than satellite borne detectors, so ground based γ-ray observatories detect higher number of γ-rays in the energy range of few tens to few hundreds of GeV compared to the satellite observatories, and in addition Cherenkov telescopes detect γ-rays of energies up to 10 TeV. So Aharonian [267] argues that satellite borne observations are better suited for studying populations of sources, while the ground based observatories have better use in studies of physical phenomena. Nevertheless, we decided to collect the results of AGN observations and studies performed by the MAGIC collaboration, to locate the sources we studied in this work (M87, PKS 1222+21 and H1722+119) in context of all detected AGN.

We show the redshift distribution of MAGIC detected AGN in Figure 6.1. As expected,

---

[1]The author of this thesis participated in first detections of two AGN.

Table 6.1 List of all AGN detected by MAGIC in the VHE γ-ray band. Asterisk next to the name of the source signifies it was first detected by MAGIC (20 in total). In AGN type column "Blazar" stands for unclassified type of blazar, and "RG" for radio galaxy. The quoted redshift is the one that was used for de-absorbing of the spectrum in MAGIC papers. The values marked with a † were obtained based on the attenuation of the VHE γ-ray flux by the EBL, as explained in Section 5.4.1. The coordinates are adopted from [227].

Name	RA	Dec	Type	Redshift	MAGIC Ref.
S3 0218+357*	02 21 05.5	+35 56 14	Blazar	0.944	[169]
NGC 1275*	03 19 48.1	+41 30 42	RG	0.017559	[228, 7]
IC 310*	03 16 43.0	+41 19 29	RG	0.0189	[8, 229]
M87	12 30 47.2	+12 23 51	RG	0.0042	[14, 15, 160, 230]
3C 279*	12 56 11.1	-05 47 22	FSRQ	0.5362	[166, 231]
PKS 1510-089	15 12 52.2	-09 06 21.6	FSRQ	0.361	[232]
PKS 1222+21*	12 24 54.4	+21 22 46	FSRQ	0.432	[71, 70]
BL Lacertae	22 02 43.3	+42 16 40	IBL	0.069	[233]
3C 66A	02 22 41.6	+43 02 35.5	IBL	0.444	[234]
MAGIC J2001+435*	20 01 13.5	+43 53 02.8	IBL	0.18	[235]
S5 0716+714*	07 21 53.4	+71 20 36	IBL	0.26; 0.31	[236, 237]
H1722+119*	17 25 04.3	11 52 15	IBL	0.4†	[22]
PG 1553+113	15 55 44.7	+11 11 41	HBL	0.4	[238, 239, 240]
Markarian 180*	11 36 26.4	+70 09 27	HBL	0.045	[241]
1ES 1011+496*	10 15 04.1	+49 26 01	HBL	0.212	[242]
1ES 0806+524	08 09 59	+52 19 00	HBL	0.138	[243]
PKS 1424+240	14 27 00	+23 47 40	HBL	0.6†	[170]
B3 2247+381*	22 50 06.6	+38 25 58	HBL	0.1187	[244]
1ES 1215+303*	12 17 48.5	+30 06 06	HBL	0.13	[245]
1ES 1741+196*	17 43 57.8	+19 35 09	HBL	0.083	[246]
1ES 0033+595*	00 35 52.63	+59 50 04.56	HBL	0.086	[247]
1ES 1727+502*	17 28 18.6	+50 13 10	HBL	0.055	[248]
RGB J0136+391*	01 36 32.5	+39 06 00	HBL		[249]
MS 1221.8+2452*	12 24 24.2	+24 36 24	HBL	0.218	[250]
RBS 0723*	08 47 12.9	+11 33 50	HBL	0.198	[251]
RX J1136.5+6737*	11 36 30.1	+67 37 04	HBL	0.1342	[252]
Markarian 421	11 04 19	+38 11 41	HBL	0.031	[253, 254, 255, 256, 51]
Markarian 501	16 53 52.2	+39 45 37	HBL	0.034	[257, 258, 259, 69]
1ES 2344+514	23 47 04.9	+51 42 17	HBL	0.044	[260, 261]
H1426+428	14 28 32.6	+42 40 21	HBL	0.129	[262]
1ES 1959+650	19 59 59.8	+65 08 55	HBL	0.048	[263, 264]
PKS 2155-304	21 58 52.7	-30 13 18	HBL	0.116	[265]
1ES 1218+304*	12 21 26.3	+30 11 29	HBL	0.182	[266]
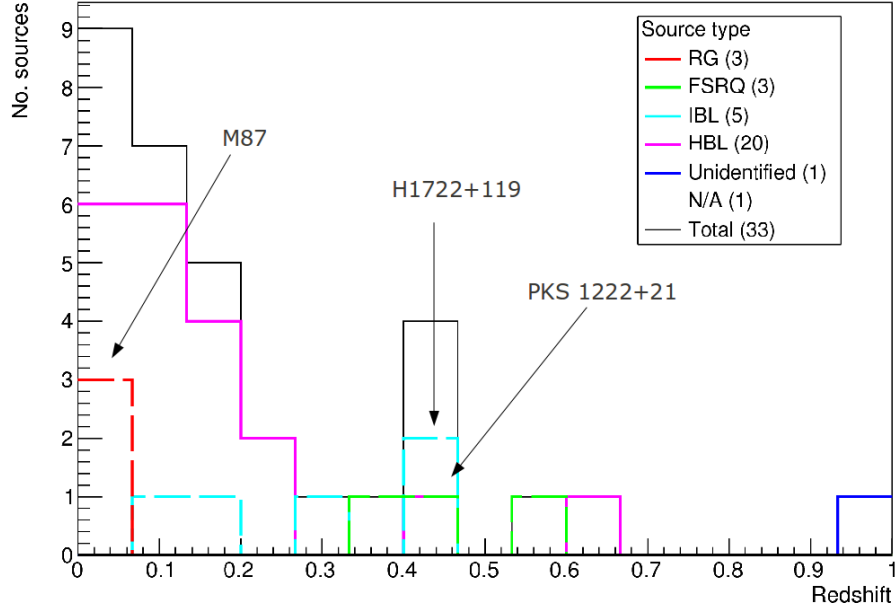
Figure 6.1 Distribution of MAGIC AGN according to redshift.

sources are more frequent at redshift below 0.2. Only two sources are at $z \gtrsim 0.5$. Unclassified blazar S3 0218+357 at $z = 0.944$ is a gravitationally lensed source. It is the first of that kind ever observed in VHE γ-rays [169]. The redshift is not determined for RGB J0136+391.

We also show intrinsic spectral slopes (photon indices) for AGN at different redshifts in Figures 6.2 and 6.3. In Figure 6.2, data are grouped according to the spectral shape. As we can see, spectra for most of them can be described by a simple power-law, given in equation (2.6). In few cases, however, the spectrum has a more complex shape; either power-law with an exponential cut-off, or log parabola, given in equations (6.1) and (6.2), respectively.

$$\frac{\mathrm{d}N}{\mathrm{d}E} = N_0 \left(\frac{E}{E_0} \right)^{-\Gamma} \exp \left(-\frac{E}{E_{\mathrm{co}}} \right) \tag{6.1}$$

$$\frac{\mathrm{d}N}{\mathrm{d}E} = N_0 \left(\frac{E}{E_0} \right)^{-\Gamma - \beta \log(E/E_0)} , \tag{6.2}$$
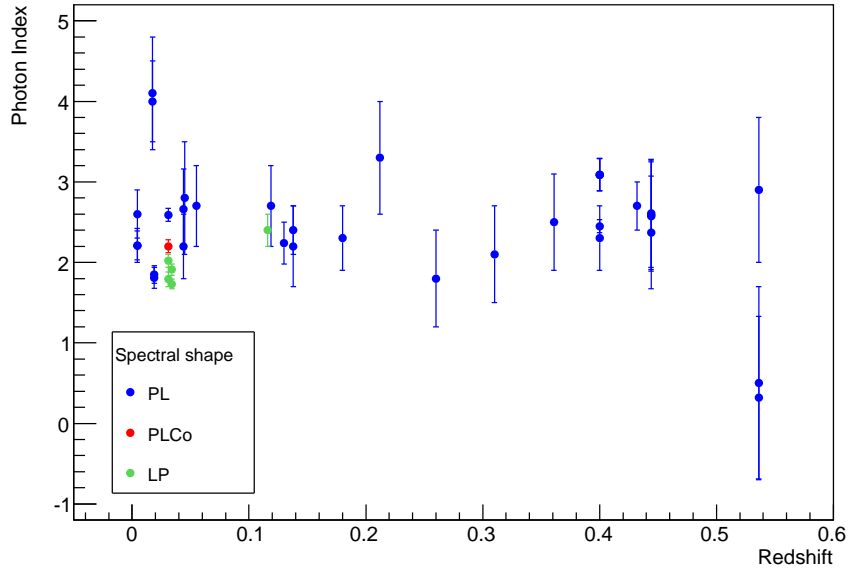
Figure 6.2 Intrinsic spectral slope of MAGIC AGN versus redshift. Different spectral shapes (PL – power-law, PLCo – power-law with cut-off, LP - log parabola) are grouped using different colours.

where N_0 is the normalisation, and it corresponds to the number of γ-rays of energy E_0, that hit the unit area in a unit of time. E_0 is a normalisation point arbitrarily chosen from the $0.1 - 1\,\mathrm{TeV}$ interval, and is usually referred to as the pivot energy. Data in Figure 6.3 were grouped as in Figure 6.1. We note that the correspondence between figures and Table 6.1 is not one-to-one. For some of the sources in Table 6.1, the spectrum was not de-absorbed, so they are not represented in Figures 6.2 and 6.3. Some other sources are represented more than once with several values. Different values for a given source are mostly results of using different EBL models for spectrum de-absorbing, or, as is the case with S5 0716+714, different methods of redshift determination resulting in different values for z, which in turn leads to different values for the intrinsic spectrum. In addition, for some sources, a fit to the spectral points was performed with more than one spectral shape (e.g. Markarian 421).

When studying distributions shown in Figures 6.2 and 6.3 the following issues should be considered. A precise EBL model and redshift of the source are necessary for determining

Figure 6.3 Intrinsic spectral slope of MAGIC AGN versus redshift. Different AGN classes are grouped using different colours (same convention as in Figure 6.1 applies).

the intrinsic spectrum of a source. But precise measurements of the observed spectra, together with precisely determined redshifts, are used to constrain the EBL models. Results used in this cenzus were collected from observations and resulting publications over almost a decade. During that time the theoretical models of EBL were significantly modified. Investigating references from Table 6.1, one can see how the precision of those models changed over time. For example in a study of a FSRQ 3C 279 from 2008 [166] models from [268] and [269] were used, referred to in [166] as "low" and "high" models, respectively, and obtained quite different results for the intrinsic spectrum (2.9 ± 0.9 vs. 0.5 ± 1.2). On the other hand, four different EBL models ([190, 108, 191, 189]) were used in the study of PKS 1222+21 from 2011 [71] (see Figure 4.3), and the uncertainties resulting from the differences between different models are smaller than the systematic uncertainties of the MAGIC data analysis. Therefore, in order to compare intrinsic spectral slopes of AGN, all of them should first be de-absorbed using a single EBL model; or several models, but then the resulting intrinsic spectra should be compared separately according to the model applied. This means that most of the spectra should

be de-absorbed anew. The proper procedure here would be to use the data analysis outputs from programs *fluxlc* or *flute* for mono, or stereo data, respectively (see Section 2.3.3). One might simply use points from the published studies and perform de-absorbing procedure on those. However, in the unfolding procedure the spectrum is calculated through a correlated fit procedure, which takes into account correlation between data points. Since the correlation information would be lost, if using published points, this might introduce significant systematic uncertainties. In any case, the spectral slopes taken as they are shown in Figures 6.2 and 6.3 should not be used for further comparison or analysis. Instead, the spectra should first be de-absorbed using the same EBL model for all the sources. Any of the suggested actions would require a significant amount of time. Therefore we believe a database of intermediate results of data analysis should be established, which could be reused in the future. Furthermore, there are only three sources whose spectra were consistent with shapes other than power-law. Those are Markarian 421, Markarian 501 and PKS 2155-304, all very bright sources. It is possible that spectra of other sources have more complex forms, but the sensitivity of the current instrument is too low to reveal spectral features inconsistent with power-law.

Still, we would like to discuss some questions that should be raised in case a similar study is performed in the future. To begin with, not all the spectra are determined in the same energy interval. One could simply compare spectral slopes regardless of the energy interval, and determine the interval and distribution of spectral slopes. However, it would be more interesting to determine the energy at which the spectral energy distribution in the γ-ray band is at its maximum, and study the spectral slope with respect to the position of the peak. A possible trend in such distribution could point to certain evolutionary characteristic of AGN. However, the peak often occurs in the HE γ-ray band, or VHE γ-ray band is too narrow to precisely determine the position of the peak, so this would require using data from satellite borne detectors, and observations should be performed simultaneously.

Another point concerns different emission states of the observed sources. The question is whether to consider a flaring state of a given source as a virtually different source.

Separating data to flaring and quiescent states is one possible solution. However, from our present knowledge of AGN, we do not see any fundamental difference between flaring and quiescent states. Furthermore, it is imaginable that an instrument of a significantly higher sensitivity would see what we consider a quiescent state to be in fact a series of "mini" flares. Therefore, there is no reason why different states of any single source should be separated from the entire sample. However, this does not mean that the total flux should not be considered. It would be very interesting to investigate whether the position of the peak in the SED, or the spectral slope depend on the integral flux of γ-rays. Comparing integral flux of different states for a single source is not a difficult task, however if we are to compare different sources, data should again be EBL corrected.

Finally we have to mention rather large uncertainties on the spectra. Over the course of years the MAGIC telescopes have evolved, and instrument upgrades (see Table 2.1) resulted in higher sensitivity. There is still much room for improvement, therefore we are looking forward to our participation in the upcoming instrument CTA, which is expected to lower the energy threshold for VHE γ-ray detection and have higher sensitivity than currently operational telescopes.

In this research characteristics of three individual sources were studied, all of them being members of a different class (radio galaxy: M87; IBL: H1722+119; and FSRQ: PKS 1222+21).

M87 was already known VHE γ-ray emitter. In the research presented here we focused on a quiescent emission state. Researchers are often focused on flaring states of sources, which is understandable given the sparsity of VHE γ-rays. Flares allow access to a large amount of data, while using little observation time. Still, in order to understand the physics of a given source, it is very important, if not necessary, to study the long term behaviour of the source paying special attention to its low emission state. A study of a three years long period gave us an insight into what we might call base line emission. The integral flux above $100\,\mathrm{GeV}$ is $(5.06 \pm 0.77) \times 10^{-12}\,\mathrm{cm^{-2}\,s^{-1}}$. The power-law spectrum shape with a spectral index of 2.21 ± 0.21 is consistent with values previously reported by other collaborations. It will be interesting to compare these values with future studies

and determine whether and how much the spectrum changes during and after flaring episodes, and whether the integral flux returns to the same level after flaring episodes. It would also be interesting to see the results of similar studies performed on other sources. If a constant base line emission is identified in other AGN, it might imply an existence of stable conditions within at least a part of the emission region. It would mean that variability of the flux originates in a separated part of the emission region, or from entirely different region. On the other hand, a variable emission could be produced in a single region, but a mechanism should be present that brings the emission at a certain base level. This further implies existence of an equilibrium state and conditions that provide it. Similar studies require a significant amount of observation time, which makes them more suited for the upcoming CTA. We used a somewhat exotic two-zone SSC "spine-layer" model to describe the emission. If this is the correct explanation, the relativistic jet is structured in two concentric layers. Each layer produces synchrotron and IC radiation on its own. In addition, synchrotron photons from each layer are also IC scattered in other layer. So the total emission is not obtained only by adding two independent zones, but an interplay of two connected layers. This scenario is appealing because it places the emission region in the vicinity of the nucleus, which agrees with the findings of a previous study.

PKS 1222+21 is only the third FSRQ detected so far in the VHE γ-ray band. With its hard spectrum in HE and VHE γ-ray band ($\Gamma = 2.7 \pm 0.3$) without apparent cut-off at energies below $130\,\mathrm{GeV}$ and an extremely fast variation of flux (flux doubled in $8.6^{+1.1}_{-0.9}$ minutes), observed on 2010 June 17, this detection poses a challenge to the existing models of VHE γ-radiation from FSRQ. Nevertheless, we managed to show that it is possible to produce the data by combining thermal emission from the dust torus and the accretion disc with a one-zone synchrotron emitting blob, with HE emission being a result of the combination of EC and SSC. We also show that it is possible to reproduce the emission during two flaring states and the quiescent state only by varying the distribution of electron in the source. Unfortunately, the quiescent emission from PKS 1222+21 in VHE γ-rays is too weak to be detected with the current instrument

sensitivity. Therefore, a study like the one we performed on M87 is another prospect for the CTA. We concluded that unless some exotic way of particle transportation is invoked, the γ-ray emission region has to be outside of the BLR. We hope and expect this result to be confirmed by future observations, and if this is the case, it remains to be determined whether this is a general rule in FSRQs, or an exception.

Our conclusion on the location of the emission region is obviously different from the one we reached in the case of M87. Locations of the emission regions in AGN might serve as an alternative classification criteria, which could better pronounce similarities and differences between sources. However, results on the γ-ray emission regions locations are in great respect model dependent, and there are other possible explanations for the observed emission that place emission regions in other locations than the ones we propose here. Therefore, the emission models should first be more strongly constrained by further observations, before the emission region locations can be used for AGN classification.

H1722+119 is an IBL type of source. Usually, emission from BL Lacs is modelled with a simple one-zone SSC emission model. However, in this case we were not able to find the set of parameters that would describe the emission in a satisfactory way. The SED shows a mysterious discontinuity between optical and UV data, suggesting the emission in the UV band was partially absorbed, but we were unable to determine the location nor the mechanism of attenuation. We found no evidence of γ-ray flux variability and, given our measured flux $(6.3\pm1.6)\times10^{-12}\text{cm}^{-2}\text{s}^{-1}$ is below previously determined upper limits, we are inclined to consider this the quiescent state. However, until some variation of the γ-ray flux are detected, we cannot make strong claims either way. At the same time, we find the fluxes in optical and radio band to be quite variable, with the radio flux rising throughout the year, thus finding no connection between radio and optical, and γ-ray emission. Previous optical observations detected no spectral lines and were unable to detect the host galaxy, so only a lower limit on the redshift of the source was set. Using contemporaneous measured HE and VHE γ-ray spectra, and EBL models we were able to estimate the redshift of the source. Combined with lower limits based on optical observations, we adopted a value of 0.4 for the redshift with the upper limit at

0.95. This enabled us to determine the intrinsic VHE γ-ray spectrum of the source.

It was our intention to compare emission from a FSRQ and a radio galaxy to a BL Lac, however our observations show a rather atypical shape of SED of H1722+119, featuring an abnormal discontinuity between optical and X-ray bands. For the other two models we managed to find an acceptable description for their emission. As expected the description for PKS 1222+21 includes a contribution from thermal emission, which is not present in the description of M87. Certainly the main question rising from these differences is whether these sources are fundamentally different. Is the fact that there are no visible lines in the optical spectrum of H1722+119 simply a consequence of large ratio of beamed and thermal emission? What would the emission from M87 look like if it was facing the Earth head on? Would we still need to invoke a complex model to explain the emission, or could a simple one-zone model be able to reproduce the emission that would be observed in that case? Perhaps thermal emission would be more pronounced then, and any applied model would have to account for that contribution. These and many other questions raised in this study remain to be answered by future studies.

Poglavlje 7

Prošireni sažetak: Svojstva visokoenergijskoga gama-zračenja iz aktivnih galaktičkih jezgri opažanih teleskopima MAGIC

7.1 Uvod

Astronomija γ-zraka vrlo visokih energija (en. *Very High Energy*, VHE, $100\,\mathrm{GeV}$ – $10\,\mathrm{TeV}$) je relativno novo područje istraživanja. Tehnologija potrebna za opažanje ovih najenergetskijih procesa u svemiru razvijena su tek u nekoliko proteklih desetljeća. γ-zrake samo djelomično prolaze kroz atmosferu, pri čemu stvaraju kaskade čestica ostavljajući svoju energiju u atmosferi. Zemaljski opservatoriji γ-zraka bilježe slabašne bljeskove svjetlosti poznate kao Čerenkovljevo zračenje, čime koriste atmosferu kao kalorimetar. Ova metodologija srodna je onoj koja se koristi u eksperimentima iz područja fizike elementarnih čestica i nuklearne fizike.

Aktivne galaktičke jezgre (en. *Active Galactic Nuclei*, AGN) najsjajniji su trajni izvori elektromagnetskog zračenja u svemiru. To su zbijena područja u središtima galaksija, koja zrače preko cijelog spektra elektromagnetskog zračenja. Smatramo da ih napajaju supermasivne crne rupe koje aktivno prikupljaju materiju akrecijom, a koje postoje u središtima svih masivnih galaksija. Neke od AGN stvaraju kolimirane mlazove kroz koje izbacuju dio prikupljene tvari ultrarelativističkim brzinama. Osim što su izvor elektromagnetskog zračenja, AGN se smatraju divovskim prirodnim ubrzivačima čestica[1].

Iz ova dva razloga proučavanje AGN u području γ-zraka smatra se križancem astrofizike i fizike elementarnih čestica te se naziva astročestičnom fizikom.

7.1.1 Aktivne galaktičke jezgre

Supermasivne crne rupe

Danas je prevladava mišljenje da se u središtu svake masivne galaksije nalazi super-masivna crna rupa (en. *Supermassive Black Hole*, SMBH). Crna rupa nastaje ako je materija mase M sadržana unutar Schwarzschildovog polumjera, definiranog sljedećim izrazom:

$$r_{\mathrm{S}} = \frac{2GM}{c^2},\tag{7.1}$$

gdje je G gravitacijska konstanta, c brzina svjetlosti u vakuumu. Najmanja poznata SMBH nalazi se u spiralnoj galaksiji bez središnjeg zadebljanja NGC 4178 [24], čija se masa procjenjuje na $M = 2.0^{+8.2}_{-1.6} \times 10^5 \, M_{\odot}$, s mogućim rasponom masa $\sim 10^4 - 10^5 \, M_{\odot}$. Pri tome $M_{\odot}$ označava masu Sunca, odnosno $(1.98855 \pm 0.00025) \times 10^{30} \, \mathrm{kg}$. Najveća do sada otkrivena SMBH je ona u divovskoj eliptičnoj galaksiji NGC 4889, čija je masa procijenjena na $(0.55 - 3.7) \times 10^{10} \, M_{\odot}$, s najvjerojatnijim iznosom od $2.1 \times 10^{10} \, M_{\odot}$ [25]. Koristeći izraz (7.1), možemo izračunati da Schwarzschildov polumjer ove SMBH iznosi $6.2 \times 10^{13} \, \mathrm{m}$, što je preko 400 astronomskih jedinica.

---

[1]Postoje indikacije o ubrzavanju protona i težih atomskih jezgri u mlazovima AGN do energija iznad $5 \times 10^{19} \, \mathrm{eV}$ (primjerice [1] i pripadne reference).

Aktivne galaktičke jezgre

Oko 1% SMBH aktivno prikuplja tvar akrecijom. Prema paradigmi AGN [2], najšire prihvaćenom opisu AGN, upravo su takve SMBH "motori" koji napajaju AGN. Masa koja pada prema njima obično tvori tanki akrecijski disk. Zbog velikog gravitacijskog gradijenta, između slojeva diska javlja se jako trenje, zbog čega se tvar u disku zagrijava na visoke temperature i ionizira. Akrecijski diskovi su izvori toplinskog zračenja. Vrh zračenja se u SED obično nalazi u optičkom, ili UV području, zbog čega se često naziva velika plava kvrga (en. *big blue bump*). Akrecijski disk je omotan koronom (en. *corona*), sfernom ljuskom elektrona visokih energija. Elektroni mogu raspršiti UV zračenje iz akrecijskog diska i inverznim Comptonovim raspršenjem stvoriti X-zrake. Jezgra je okružena sfernom raspodjelom oblaka plina, čiji atomi upijaju zračenje iz akrecijskog diska i zrače u optičkom i UV području. Zbog blizine crne rupe, moraju kružiti oko nje velikom brzinom, zbog čega su im emisijske linije jako raširene zbog Dopplerovog pomaka. Ovo se naziva područjem širokih linija (en. *Broad Line Region*, BLR). Oblaci plina koji se nalaze puno dalje od crne rupe moraju sporije rotirati te su emisijske linije manje proširenje pa se to naziva područjem uskih linija (en. *Narrow Line Region*, NLR). Crna rupa, akrecijski disk i BLR okruženi su velikim torusom plina i prašine, koji zaklanja jezgru ako se gleda pod velikim kutem. Proziran je samo za radiovalove, a sam je izvor toplinskog zračenja u IR području. Oko 10% AGN izbacuje tvar u obliku relativističkog mlaza.

Ono što opažač vidi uvelike ovisi o kutu pod kojim gleda AGN. Tako će i klasifikacija AGN ovisiti o nagibu u odnosu na smjer prema Zemlji. Struktura AGN je shematski prikazana na Slici 1.1, a klasifikacija na Slici 1.2.

Relativistički mlaz

Relativistički mlaz tvari je usko kolimiran i usmjeren duž osi AGN. Mlazovi su izvori elektromagnetskog zračenja svih valnih duljina od radiovalova do γ-zraka. Mlaz se stvara u blizini crne rupe, a može se protezati i stotinama kpc u svemir. U nekim mlazovima

opažena su svjetlija područja, takozvani čvorovi (en. *knots*). Tvar se niz mlaz kreće brzinama bliskima brzini svjetlosti, zbog čega čvorovi "love" svjetlost koju zrače. Ako je kut koji mlaz zatvara sa smjerom prema Zemlji mali, dva emitirana signala stići će do nas u kraćem vremenskom razmaku nego kad su odaslani, zbog čega će se stvoriti dojam da čvor, koji je odaslao signale putuje nadsvjetlosnom brzinom. Ovaj fenomen je uočljiv samo za male kutove otklona mlaza od smjera prema opažaču. Neki čvorovi završavaju dvostrukim elipsoidnim strukturama. Iako nije dokazano, smatra se je svaka AGN simetrična s obzirom na ravninu akrecijskog diska i da mlaz izlazi na obje strane. Još uvijek nije jasna fizika relativističkih mlazova, uključujući i sam nastanak. Najšire je prihvaćen Blandford-Znajek model [48], prema kojem je vakuum oko rotirajuće crne rupe nestabilan, zbog čega gotovo nestaju sile u elektromagnetskom polju u blizini horizonta događaja. Tada se energija i zakretni moment rotirajuće crne rupe mogu izvući čisto elektromagnetski. Prema Blandford-Payne modelu [49], zakretni moment može se magnetski izvući iz akrecijskog diska i prenijeti na mlaz. Čudi i to što mlazovi zadržavaju oblik i na ogromnim udaljenostima, što se objašnjava magnetski, ili kinetički dominiranim mlazovima. Prvi ostaju kolimirani zbog toroidalne sastavnice magnetskog polja, dok se u drugima tvar kreće balistički i ostat će na okupu dok ne naiđe na prepreku.

Elektromagnetsko zračenje iz AGN

Većina AGN opaženih u području VHE γ-zraka su *blazari* (Odjeljak 7.7), što znači na im je mlaz usmjeren prema Zemlji, ili oklonjen pod malim kutom. SED ovih izvora karakteriziraju dva vrha: vrh na nižoj energiji se nalazi između optičkog i područja X-zraka, dok se vrh na višoj energiji nalazi u području γ-zraka (Slika 1.3). Prema karakteristikama zračenja, blazari se mogu podijeliti u dvije skupine: radio kvazari ravnog spektra (en. *Flat Spectrum Radio Quasars*, FSRQ) i objekte tipa BL Lacertae (BL Lac). FSRQ imaju izražene široke i uske linije te jako kontinuirano zračenje u optičkom i području X-zraka. Često je uočljiv visok i širok vrh u optičkom-UV području, koji se povezuje s emisijom iz akrecijskog diska. Kod BL Lac izvora uske linije su jedva, ako uopće vidljive. Svojstvena im je jaka linijska polarizacija u radio i optičkom

području. Vrh na nižim energijama u SED kod FSRQ je zbroj doprinosa sinkrotronskog zračenja elektrona u mlazu i toplinskog zračenja iz diska i torusa. Kod BL Lac doprinosi samo sinkrotronsko zračenje. FSRQ aktivni u području γ-zraka se češće pojavljuju na udaljenostima koje odgovaraju crvenom pomaku 1 i više, dok su BL Lac grupirani oko $z = 0, 2$ (Slika 1.4). Detaljnija rasprava o sličnostima i razlikama između BL Lac i FSRQ ae može naći primjerice u [53, 54]. Prema položaju prvog vrha u SED, [52] dodatno dijele BL Lac na BL Lac s vrhom na niskim energijama (en. *Low-energy-peaked BL Lacs*, LBL, $\log \nu_s < 14.5$), BL Lac s vrhom na srednjim energijama (en. *Intermediate-energy-peaked BL Lacs*, IBL, $14.5 < \log \nu_s < 16.5$) i BL Lac s vrhom na visokim energijama (*High-energy-peaked BL Lacs*, HBL, $\log \nu_s > 16.5$).

Samo četiri AGN, koje nisu blazari, su do sada opažene u području VHE γ-zraka: M87 [5], Centaurus A [6], NGC 1275 [7] i IC 310 [8]. Klasificirane su kao radio galaksije (RG), vrste AGN vrlo sjajne u radio području, koje unose ogromnu energiju u međugalaktički prostor ($10^{60} - 10^{61}$ erg [56]). Osi su im otklonjene od smjera prema Zemlji, tako da su im često vidljivi mlazovi na obje strane.

Iako se znanstvenici slažu o izvoru zračenja koje čini vrh na nižim energijama, zračenje u vrhu na višim energijama pokušava se objasniti na dva fundamentalno različita načina: *leptonskim* i *hadronskim* modelima. Osnovno pitanje je mogu li se protoni u mlazu ubrzati do dovoljno visokih energija ($\gtrsim 10^{19}$ eV). Bez obzira na vrstu modela, područje zračenja opisuje se mjehurom čestica koji se ultrarelativistički giba niz mlaz s Lorentzovim faktorom $\Gamma = (1 - v^2/c^2)^{-1/2}$. Ako mlaz zatvara kut θ sa smjerom prema Zemlji, možemo definirati Dopplerov faktor

$$\delta = [\Gamma(1 - \beta \cos \theta)]^{-1}, \tag{7.2}$$

gdje je $\beta = v/c$. Zbog relativističkih efekata, mjereni tok zračenja bit će za faktor δ^4 veći, energije opaženih fotona bit će veće za faktor δ, a vremenske skale kraće za isti faktor. Spektralna raspodjela elektrona u mjehuru opisana je slomljenim zakonom

potencije

$$N(\gamma) = \begin{cases} n_0\gamma^{-p_1}, & \gamma < \gamma_{br} \\ n_0\gamma_{br}^{p_2-p_1}\gamma^{-p_2}, & \gamma > \gamma_{br}, \end{cases} \tag{7.3}$$

gdje je n_0 normalizacijski faktor gustoće elektrona, a γ_{br} Lorentzov faktor na kojem se raspodjela lomi. p_1 i p_2 su nagibi spektra na energijama ispod i iznad loma. Veličina mjehura se obično procjenjuje na $\sim 10^{16}$ cm, a može se ograničiti vremenskom skalom eventualne varijabilnosti izvora (t_{var})

$$R \leq ct_{\mathrm{var}}\frac{\delta}{1+z}. \tag{7.4}$$

U leptonskim modelima, fotoni koji čine prvi vrh u SED, raspršuju se inverznim Comptonovim raspršenjem na elektronima u mlazu te na taj način nastaju γ-zrake. Ti fotoni se nazivaju sjemenski fotoni. Ako su sjemenski fotoni nastali sinkrotronskim zračenjem elektrona u mlazu, govorimo o Synchrotron self Compton (SSC) modelima (primjerice [57, 59]), jer ista populacija elektrona stvara i sinkrotronske fotone i raspršuje ih. Ako su pak sjemenski fotoni došli iz akrecijskog diska ili torusa, govorimo o External Compton (EC) modelima (primjerice [60]).

Ukupna snaga mlaza u referentnom sustavu galaksije domaćina je

$$P_{\mathrm{j}} = 2\pi R^2\beta\Gamma^2 U_{\mathrm{tot}} = P_{\mathrm{j,par}} + P_{\mathrm{j,B}}, \tag{7.5}$$

gdje je U_{tot} ukupna gustoća energije u mlazu [61, 62, 59]. Ukupna snaga je zbroj doprinosa snage čestica ($P_{\mathrm{j,par}}$) i magnetskog polja ($P_{\mathrm{j,B}}$). Faktor 2 ulazi zbog pretpostavke o mlazu koji izlazi s obje strane crne rupe. Gustoća energije elektrona je

$$U_{\mathrm{e}} = \int_{\gamma_{\mathrm{min}}}^{\gamma_{\mathrm{max}}} \mathrm{d}\gamma\gamma N(\gamma), \tag{7.6}$$

pri čemu je $N(\gamma)$ dano izrazom (7.3), dok je gustoća energije dana magnetskog polja $U_{\mathrm{B}} = B^2/8\pi$. Ako se javlja samo sinkrotronsko zračenje, snaga mlaza će miti mini-

mizirana pod pretpostavkom ekviparticije energije u mlazu, $P_{\text{j,par}} \approx P_{\text{j,B}}$, ali ovi doprinosi se mogu razlikovati da bi se objasnilo zračenje putem inverznog Comptonovog raspršenja [60].

Hadronski modeli pretpostavljaju da se protoni u mlazu ubrzavaju dovoljno da uzrokuju foto-pionsku produkciju kroz reakcije $\gamma + p \rightarrow n + \pi^+$, ili $\gamma + p \rightarrow p + \pi^0$. Prvi vrh u SED je prema hadronskim modelima sinkrotronsko zračenje elektrona u mlazu, dok je drugi vrh zbroj nekoliko doprinosa. Protoni na energijama od $\gtrsim 10^{19}$ eV sinkrotronski zrače γ-zrake, neutralni pioni se raspadaju na par γ-zraka, a dolazi i do inverznog Comptonovog raspršenja na sekundarnim nabijenim česticama ($\pi^{\pm}$, $\mu^{\pm}$). U raspadu nabijenih piona nastajat će neutrini ($\pi^+ \rightarrow \nu_{\mu} + \mu^+ \rightarrow \nu_{\mu} + \nu_{\mu} + \nu_{\text{e}} + \text{e}^+$).

Detaljniji pregled modela zračenja može se naći u [67] i pripadnim referencama.

Hadronski modeli zahtjevaju snažna magnetska polja, koja bi ultrarelativističke protone zadržala u području zračenja (u mjehuru). Uz to, predviđaju visok tok neutrina. Za očekivati je da će se pojačani tok neutrina vidjeti istovremeno s opaženim pojačanim tokom γ-zraka, ali to do sada nije opaženo. Leptonski modeli se ne suočavaju s ovim problemima i za sada se pokazuju uspješnijima u modeliranju opaženog zračenja.

7.1.2 γ-astronomija

γ-zračenje je elektromagnetsko zračenje najviših energija. U astrofizici, elektromagnetsko zračenje energije veće od 100 keV ($\nu > 10^{19}$ Hz) smatra se γ-zračenjem. Opisat ćemo nekoliko osnovnih načina nastanka γ-zraka.

Inverzno Comptonovo raspršenje

Comptonovo raspršenje je dobro poznati čestični proces, kojeg je 1923. godine opisao Arthur H. Compton [76]. To je neelastično raspršenje fotona na nabijenoj čestici prikazano na Slici 1.5. Promjena frekvencije fotona pri Comptonovom raspršenju dana je sljedećim

izrazom:

$$\nu' = \frac{\nu}{1 + \frac{h\nu}{m_e c^2}(1 - \cos\theta)}, \tag{7.7}$$

pri čemu su ν i ν' frekvencije fotona prije i nakon raspršenja, m_e je masa elektrona, θ kut raspršenja fotona u odnosu na početni zalet, h Planckova konstanta, a c je brzina svjetlosti u vakuumu. Comptonov rezultat je relativističko poopćenje Thomsonovog raspršenja, što je elastični proces. Udarni presjek za Tomsonovo raspršenje izvodimo iz klasične elektrodinamike

$$\frac{d\sigma_T}{d\cos\theta} = \frac{3}{16\pi}\sigma_T\left(1 + \cos^2\theta\right), \quad \sigma_T = \frac{8\pi}{3}\left(\frac{e^2}{m_e c^2}\right)^2, \tag{7.8}$$

gdje je e naboj elektrona. Da bismo izračunali udarni presjek Comptonovog raspršenja, moramo se poslužiti kvantnom elektrodinamikom. Feynmanovi dijagrami koji doprinose udarnom presjeku prikazani su na Slici 1.6. Klein-Nishinova (KN) formula, nazvana prema njezinim autorima, izvedena 1929. godine [77], kaže:

$$\frac{d\sigma_{KN}}{d\cos\theta} = \frac{3}{16\pi}\sigma_T\left(\frac{\nu'}{\nu}\right)^2\left[\frac{\nu'}{\nu} + \frac{\nu}{\nu'} - \sin^2\theta\right]. \tag{7.9}$$

U slučaju da je frekvencija raspršenog fotona jednaka frekvenciji dolaznog, ovaj izvod svodi se na Thomsonovu formulu.

Uključimo li izraz (7.7) u (7.9) te integriramo po kutu θ, dobit ćemo izraz za ukupni udarni presjek kod Comptonovog raspršenja

$$\sigma_{KN} = \sigma_T\frac{3}{4}\left\{\frac{1+x}{x^3}\left[\frac{2x(1+x)}{1+2x} - \ln(1+2x)\right] + \frac{1}{2x}\ln(1+2x) - \frac{1+3x}{(1+2x)^2}\right\}, \tag{7.10}$$

pri čemu smo upotrijebili pokratu $x = h\nu/m_e c^2$ (omjer energije dolaznog fotona i energije mirovanja elektrona). U nerelativističkom ($x \ll 1$) i ultrarelativističkom ($x \gg 1$)

približenju ovaj izraz poprima sljedeće oblike:

$$\sigma \simeq \begin{cases} \sigma_{\mathrm{T}} \left(1 - 2x + \frac{26x^2}{5} + \cdots\right) & \text{za } x \ll 1 \text{ (Thomsonov režim)}, \\ \frac{3}{8}\sigma_{\mathrm{T}}x^{-1} \left(\ln 2x + \frac{1}{2}\right) & \text{za } x \gg 1 \text{ (Klein-Nishinov režim)}. \end{cases} \tag{7.11}$$

Ovaj izraz može se poopćiti za raspršenje fotona na bilo kojoj nabijenoj čestici. Važno je primijetiti da se udarni presjek u prvom približenju ne mijenja s energijom ulaznog fotona sve dok smo u Thomsonovom režimu. U Klein-Nishinovom režimu udarni presjek opada s porastom energije ulaznog fotona.

Compton je izveo svoj rezultat za elektron koji u početnom trenutku miruje te prema tome može samo primiti energiju od fotona. Međutim, ako je kinetička energija elektrona velika u usporedbi s energijom fotona, elektron može predati dio svoje kinetičke energije fotonu. Ovo se naziva inverznim Comptonovim raspršenjem i smatra se jednim od najvažnijih kanala za nastanak γ-zraka u astrofizičkim izvorima.

Prosječna prenesena snaga pri raspršenju izotropno raspodijeljenih fotona na elektronu je

$$P = \frac{4}{3}\sigma_{\mathrm{T}}c\beta^2\gamma^2 U_{\mathrm{ph}}, \tag{7.12}$$

gdje je γ Lorentzov faktor ($\gamma = (1 - \beta^2)^{-1/2}$, $\beta = v/c$), a U_{ph} gustoća energije dolaznih fotona. Spektralna emisivnost, odnosno ukupna snaga emitirana iz jediničnog volumena u jedinični prostorni kut po jedinici frekvencije, pri inverznom Comptonovom raspršenju izotropnog monokromatskog fotonskog polja na populaciji elektronima, čije energije su raspodijeljene prema potencijskom zakonu ($N(\gamma) = n_0\gamma^{-p}$), je

$$J(\nu) = \frac{1}{4\pi}\frac{(4/3)^{(p-1)/2}}{2}\sigma_{\mathrm{T}}cn_0\frac{U_{\mathrm{ph}}}{\nu_0}\left(\frac{\nu}{\nu_0}\right)^{-(p-1)/2}, \tag{7.13}$$

gdje je ν_0 frekvencija dolaznih fotona, a $N(\nu_0)$ njihova gustoća. Za detaljne izračune spektra inverznog Comptonovog raspršenja, čitatelj se upućuje na primjerice [78, 79].

γ-zraka može nastati i u nuklearnim reakcijama, poništenjem para čestica-antičestica (primjerice $e^- + e^+ \to \gamma + \gamma$), ili raspadom nestabilne čestice (primjerice $\pi^0 \to \gamma + \gamma$).

γ-zrake nikada ne nastaju pri toplinskom zračenju.

Sinkrotronsko zračenje

Sinkrotronsko zračenje je važna pojava za astrofiziku. Nabijena čestica koja se giba u magnetskom polju međudjelovat će s magnetskim poljem, a putanja će mu imati oblik zavojnice duž silnica magnetskog polja. Žiroskopska frekvencija i polumjer dani su izrazima

$$\omega_{\mathrm{B}} = \frac{qB}{\gamma mc}, \tag{7.14}$$

$$r_{\mathrm{g}} = \frac{c\beta \sin \alpha}{\omega_{\mathrm{B}}}, \tag{7.15}$$

pri čemu su B: magnetska indukcija, a γ, m i q Lorentzov faktor, masa i naboj čestice. α je kut između brzine čestice i magnetskog polja. Nerelativistička čestica emitirat će zračenje frekvencije koja će biti jednaka žiroskopskoj frekvenciji. To se naziva ciklotronsko zračenje. Zračenje čestice koja se kreće relativističkom brzinom u magnetskom polju bit će relativistički usmjereno, te će svo zračenje biti odaslano unutar malog kuta $\theta = 1/\gamma$, kao što je prikazano na Slici 1.7.

Spektar sinkrotronskog zračenja je složen (Slika 1.8). Većina energije će se izračiti fotonima kutne frekvencije niže od kritične ω_{C}

$$\omega_{\mathrm{C}} = \frac{3\gamma^2 qB \sin \alpha}{2mc} = \frac{3}{2}\gamma^3 \omega_{\mathrm{B}} \sin \alpha \tag{7.16}$$

Snaga zračenja dana je Larmorovom formulom:

$$P = \frac{2q^2}{3c^3}\gamma^4 \left(\frac{v_\perp}{\omega_{\mathrm{B}}}\right)^2, \tag{7.17}$$

gdje $v_\perp$ označava komponentu brzine čestice okomitu na magnetsko polje. Snagu zračenja izotropne raspodjele elektrona dobit ćemo usrednjavanjem po α

$$P = \frac{4}{3}\sigma_\mathrm{T} c \beta^2 \gamma^2 U_\mathrm{B}. \tag{7.18}$$

U_B je gustoća energije magnetskog polja ($U_\mathrm{B} = B^2/8\pi$), a σ_T Thomsonov udarni presjek (jednadžba 7.8). Usporedimo li ovaj rezultat sa snagom zračenja inverznog Comptonovog raspršenja (jednadžba 7.12) dobijemo

$$\frac{P_\mathrm{IC}}{P_\mathrm{synch}} = \frac{U_\mathrm{ph}}{U_\mathrm{B}}. \tag{7.19}$$

Spektar sinkrotronskog zračenja opisan je sljedećim izrazom:

$$P(\omega) = \frac{\sqrt{3}q^3 B \sin\alpha}{2\pi m c^2} F(\omega/\omega_\mathrm{C}), \quad F(x) \equiv x \int_x^\infty K_{5/3}(\xi)\mathrm{d}\xi, \tag{7.20}$$

pri čemu je $K_\alpha(x)$ je modificirana Besselova funkcija druge vrste. Asimptotski oblici $F(x)$ su

$$F(x) \simeq \begin{cases} \frac{4\pi}{\sqrt{3}\Gamma(1/3)} \left(\frac{x}{2}\right)^{1/3} & \text{za } x \ll 1, \\ \left(\frac{\pi}{2}\right)^{1/2} \mathrm{e}^{-x} x^{1/2} & \text{za } x \gg 1, \end{cases} \tag{7.21}$$

gdje je $\Gamma(t)$ gama funkcija.

Pretpostavimo li raspodjelu čestica prema zakonu potencije ($N(\gamma) = n_0 \gamma^{-p}$), ukupna izračena snaga u jediničnom volumenu i po jediničnoj frekvenciji, također će imati oblik zakona potencije

$$P(\omega) = \frac{\sqrt{3}q^3 n_0 B \sin\alpha}{2\pi m c^2 (p+1)} \Gamma\left(\frac{p}{4} + \frac{19}{12}\right) \Gamma\left(\frac{p}{4} - \frac{1}{12}\right) \left(\frac{mc\omega}{3qB\sin\alpha}\right)^{-(p-1)/2}. \tag{7.22}$$

Sinkrotronsko zračenje jedne čestice bit će eliptično polarizirano, međutim, za skup čestica koje glatko raspodijeljene u odnosu na kut α, eliptična sastavnica polarizacije će se poništiti pa će ukupno zračenje biti djelomično linearno polarizirano. Stupanj

polarizacije ukupnog zračenja čestica raspodjeljenih prema zakonu potencije, kakve smo pretpostavili gore, bit će

$$\Pi = \frac{p+1}{p+7/3}. \tag{7.23}$$

Vjerojatnost da elektron sinkrotronski izrači γ-zraku je zanemarivo mala, ali elektronsko sinkrotronsko zračenje ima drugu važnu ulogu. Proton ($m_\mathrm{p} \approx 2000 m_\mathrm{e}$), s druge strane, će puno manje energije gubiti sinkrotronskim zračenjem (u odnosu na elektron jednake energije) pa je sasvim moguće da će u astrofizičkim ubrzivačima čestica doseći dovoljno visoke energije da sinkrotronski izrači γ-zrake.

Astrofizički izvori γ-zraka

Astrofizički izvori γ-zraka (Slika 1.9) mogu se, prema tome nalaze li se u Mliječnoj stazi ili ne, podijeliti na galaktičke i izvangalaktičke izvore. Ukratko ćemo opisati vrste izvora, osim AGN, koje smo opisali u Odjeljku 7.1.1.

Dvojni sustavi su sustavi koje čine kompaktni objekt (neutronska zvijezda, ili crna rupa) i prateća zvijezda. Ukoliko je prateća zvijezda dovoljno velika (primjerice crveni div), njezin materijal padat će na kompaktni objekt i oblikovati akrecijski disk. Dio materije bit će izbačen u obliku relativističkog mlaza.

Ostaci supernova (en. *Supernova Remnants*, **SNR)** su brzo rastuće strukture materijala izbačenog pri eksplozijama supernova. Fronta širenja je udarni val.

Pulsari su brzorotirajuće neutronske zvijezde sa snažnim magnetskim poljima na površini. Elektroni se u magnetosferi pulsara ubrzavaju do relativističkih brzina. Pulsari zrače u cijelom elekromagnetskom spektru, uključujući i γ-zrake. Također energijom napajaju maglice pulsarskog vjetra (en. *Pulsar Wind Nebula*, PWN).

Maglice pulsarskog vjetra su posebne vrste SNR, u kojima se nalazi pulsar. Za astronomiju VHE γ-zraka vrlo je važna Rakova maglica (en. *Crab Nebula*). To je snažan i relativno stabilan izvor VHE γ-zraka, zbog čega se koristi kao standardna svijeća za zemaljske teleskope γ-zraka. Često se ukupni tok VHE γ-zračenja izražava u jedinicama Rakove maglice (C.U.).

Zvjezdorodne galaksije su nepravilne galaksije, u kojima je se stvaranje novih zvijezda i eksplozija supernova odvija češće nego u običnim galaksijama. U njima se nalazi više SNR, koje same za sebe nisu dovoljno sjajne da bi bile vidljive iz druge galaksije. Međutim ukupni sjaj se može uočiti. Do sada su VHE γ-zrake opažene iz samo dvije zvjezdorodne galaksije: M82 [83] i NGC 253 [84].

Provale γ-zraka (en. *Gamma-ray Bursts*, **GRB)** su najeksplozivniji događaji u svemiru od velikog praska. To su kratkotrajne provale γ-zraka, koje mogu trajati od nekoliko milisekundi do nekoliko minuta. Mogu se podijeliti u dvije skupine: kratko trajne GRB traju kraće od dvije sekunde i dugotrajne GRB, koje traju duže od dvije sekunde. Kratkotrajne se povezuju sa spajanjem kompaktnih objekata (neutronske zvijezde, ili crne rupe) [85, 86, 87], dok su dugotrajne posljedica urušavanja velikih supernova na kozmološkim udaljenostima [88].

Tamna materija (en. *Dark Matter*, **DM)** je materija koja čini gotovo 27% ukupnog sadržaja mase i energije u svemiru[2] [89]. DM ne zrači pa je nije lako uočiti. Priroda joj još nije razjašnjena, ali najčešće se objašnjava nakupinama slabo međudjelujućih masivnih čestica (WIMP), pri čijem bi raspadu mogle nastajati γ-zrake. Iako je postojanje tamne materije dokazano utjecajem na vidljivu materiju (primjerice [90]), još uvijek nedostaje neposredna detekcija čestica tamne materije ili produkata njihovog raspada.

7.1.3   Opažanje γ-zraka

Atmosfera nije prozirna za γ-zrake. Da bismo opažali γ-zrake iz astrofizičkih izvora, moramo izbjeći atmosferu. To možemo učiniti na dva načina: slanjem detektora van atmosfere na umjetnim satelitima, ili koristeći atmosferu kao dio detektora.

---

[2]Oko 68% otpada na zagonetnu tamnu energiju, dok vidljiva materija čini manje od 5% [89].

Opažanja satelitima

Opažanja γ-zraka postala su moguća 1960-ih godina razvojem svemirskih programa i umjetnih satelita. Prvi teleskop γ-zraka postavljen je na satelit Explorer XI, koji je NASA poslala u Zemljinu orbitu 1961. godine. Bio je namijenjen opažanju γ-zraka energije veće od 50 MeV. Tijekom 23 dana, prikupio je 9 sati podataka u načinu rada "pointing into space". 22 snimljena događaja su klasificirani kao γ-zrake, dok je 22000 događaja pripisano nabijenim kozmičkim zrakama. Ovo se smatra početkom astronomije u području γ-zraka. Više o misiji se može naći u [91], dok su rezultati objavljeni u [92] i [93].

Fermi Gamma-ray Space Telescope

Mnogi teleskopi su postavljeni u Zemljinu orbitu od Explorera XI. Najnoviji i najosjetljiviji je *Fermi Gamma-ray Space Telescope* (nadalje *Fermi*) prikazan na Slici 1.10. Budući da se naše istraživanje u velikoj mjeri temelji na podacima s *Fermija*, reći ćemo nešto više o njemu.

Fermi je međunarodna i međuinstitucijska svemirska misija pokrenuta 2008. Satelit nosi dva detektora γ-zraka: Gamma-ray Burst Monitor (GBM) i Large Area Telescope (LAT). Osnovna namjena GBM-a jest rano otkrivanje provala γ-zračenja. Sastoji se od dvije vrste scintilacijskih detektora. 12 detektora od natrijevog jodida (NaI) i 2 od bizmutovog germanata (BGO) smješteni su na bočnim stranama satelita, tako da zajedno s LAT detektorom pokrivaju gotovo cijelo nebo. NaI detektori su osjetljivi u području energija od nekoliko keV do oko 1 MeV. U slučaju otkrivanja GRB, određuju položaj i okidaju promatranja. BGO detektori pokrivaju raspon energija od 150 keV do 30 Mev. *Fermi*-LAT, kako ćemo ga nadalje oslovljavati, glavni je detektor na satelitu. Koristi tehnologiju sličnu onoj koja se koristi u detektorima čestica. *Fermi*-LAT ima oblik kocke, duljine stranice 1,8 m, a sastoji se od nekoliko sastavnica. Kada γ-zraka udari u detektor, prvo pogađa slojeve volframa, kroz interakcijom s atomskim jezgrama stvara elektron-pozitron par. Između slojeva volframa nalaze se detektori od silicijskih vrpci.

Elektroni i pozitroni ioniziraju silicij, koji pri tome odašilja električne impulse. Koristeći računalne algoritme, iz tih se signala rekonstruiraju smjer i vrijeme dolaska primarne γ-zrake. Posljednja sastavnica detektora je slikovni kalorimetar od cezij jodida, koji služi za mjerenje energije γ-zrake. *Fermi*-LAT je osjetljiv u području energija od $20\,\mathrm{MeV}$ do $300\,\mathrm{GeV}$. Kutna razlučivost je promjenjiva od $\sim 3°$ pri $100\,\mathrm{MeV}$ do $\sim 0,1°$ pri $300\,\mathrm{GeV}$. Vidno polje detektora je $2,4\,\mathrm{sr}$. Radi u dva načina opažanja. Pregled neba (en. *all-sky-survey*) je primarni način rada, u kojem se prvo pregledava jedna nebeska polutka tijekom jedne orbite, nakon čega se njiše da bi pregledao drugu polutku u sljedećoj orbiti. Na taj način pokrije cijelo nebo za 3 sata, pri čemu se svaka točka na nebu kontinuirano opaža 30 minuta. Usmjerena opažanja su drugi način rada, ali svi podaci koje koristimo u ovom istraživanju prikupljeni su načinom pregleda neba. Detaljan opis *Fermi*-LAT-a se može naći u [94], a više podataka o radnim značajkama detektora u [95].

Čerenkovljevi atmosferski teleskopi

Svi teleskopi nošeni satelitima su ograničeni veličinom instrumenta. Povećanjem veličine i mase uređaja značajno rastu složenost i cijena eksperimenta. Ovaj problem savršeno ilustrira činjenica da akronim LAT znači Large Area Telescope (hr. teleskop velike površine), iako je iskoristiva površina detektora manja od $1\,\mathrm{m}^2$. Kao što smo vidjeli u Odjeljku 7.1.2, spektralna raspodjela γ-zraka iz astrofizičkih izvora prati negativni zakon potencije. Prema tome, prikupna površina detektora je od iznimne važnosti. Dodatni nedostatak satelitskih detektora je njihova nedostupnost. U slučaju kvara, popravci su složeni i skupi i neizvedivi u kratkom roku.

Zemaljski teleskopi mogu imati znatno veću površinu od satelitskih, a da im pri tome cijena ne bude previsoka. Međutim, atmosfera nije prozirna za γ-zrake. Čerenkovljevi atmosferski teleskopi (en. *Imaging atmospheric Cherenkov telescopes*, IACT) oslanjaju se na tu činjenicu te koriste atmosferu kao dio detektora.

γ-zraka u atmosferi elektromagnetski međudjeluje s atomskim jezgrama u zraku te se pri tome pretvara u elektron-pozitron par. Svaki od njih zakočnim zračenjem (*bremsstrahlung*)

zrači fotone vrlo visokih energija, koji se ponovo pretvaraju u elektron-pozitron par. Na taj način nastaje takozvani atmosferski pljusak čestica (en. *Extensive Air Shower*, EAS). Budući da elektroni, pozitroni i γ-zrake međudjeluju samo elektromagnetski, ova vrsta pljuska se naziva elektromagnetski pljusak (Slika 1.11). Pljusak ima oblik stošca s frontom u obliku diska. Razvija se sve dok je prosječna energija novonastalih elektrona i pozitrona veća od kritične E_C. Ispod te energije uglavnom gube energiju ioniziranjem okolnog medija. U tom trenutku razvoj pljuska prestaje. Vrijednost E_C ovisi o svojstvima medija. U Zemljinoj atmosferi iznosi približno 86 MeV. Broj nastalih čestica približno je jednak omjeru energije primarne γ-zrake i E_C. Visina na kojoj pljusak doseže svoj maksimum također ovisi o mediju, a u našoj atmosferi je to na oko 10 km n.m.v. Teoriju elektromagnetskih pljuskova su 1937. godine predložili Bhabha and Heitler [97] te Carlson i Oppenheimer [98], ali detalji su godinu kasnije razradili Landau i Rumer [99].

Kozmička zraka visoke energije će također izazvati atmosferski pljusak čestica, ali u ovom slučaju pljusak se razvija ne samo pod djelovanjem elektromagnetske, nego i jake i slabe nuklearne sile. Hadron, za razliku od γ-zrake, se neće apsorbirati u prvoj reakciji, nego će se nastaviti raspršivati predajući svoju energiju. Produkti raspršenja su uglavnom nestabilni mezoni (π^0, $\pi^\pm$, K$^\pm$ itd.). E_C za hadrone je oko 1 GeV po nukleonu, što je prag za tvorbu piona. Razlike u razvoju pljuskova ostavit će trag u njihovom izgledu. Pljuskovi koje su uzrokovale γ-zrake su vrlo homogeni, dok hadronski pljuskovi često sadrže nekoliko razdvojenih potpljuskova. Razlika je prikazana na Slici 1.12.

Nabijena čestica koja prolazi kroz dielektrični medij polarizira okolne električne dipole. Nakon što čestica prođe, dipoli se vraćaju u svoj ravnotežni položaj, pri čemu zrače slabu svjetlost u plavom do ultraljubičastom području. Ako je brzina čestice veća od fazne brzine svjetlosti u tom mediju, poremećaj će se zadržati u tragu čestice, a dipoli će se koherentno vratiti u ravnotežni položaj. Fotoni izračeni iz različitih točaka duž putanje čestice bit će odaslani u fazi u smjeru brzine čestice i stvoriti uski impuls svjetlosti. Ovaj oblik zračenja se naziva Čerenkovljevo, prema Pavelu Aleksejeviču Čerenkovu, koji ga je eksperimentalno otkrio 1934. 1958. je za to otkriće podijelio Nobelovu nagradu za

fiziku s Iljom Mihajlovičem Frankom i Igorom Jevgenijevičem Tammom, koji su ponudili teorijski opis zračenja.

Da bi elektron uzrokovao Čerenkovljevo zračenje u zraku na razini mora, mora imati energiju $\gtrsim 21\,\text{MeV}$. Odnos kuta pod kojim će bljesak biti odaslan (θ) i energije dan je relacijom

$$\cos\theta = \frac{1}{n\beta}, \tag{7.24}$$

gdje je n je indeks loma svjetlosti. Za zrak na razini mora iznosi $n \approx 1.0003$ pa će kut zračenja Čerenkovljevog bljeska u odnosu na brzinu čestice biti mali, $\theta \approx 0,1°$. Svaki elektron u pljusku čestica pri tlu izrači oko 45 Čerenkovljevih fotona za svaki prijeđeni metar. Čestični pljusak primarne γ-zrake energije 1 TeV će rezultirati s oko 100 Čerenkovljevih fotona po m^2 površine na tlu. Relativna razlika brzine čestica u pljusku i brzine svjetlosti u zraku iznosi oko 10^{-4}, tako da će Čerenkovljev bljesak pljuska trajati samo nekoliko nanosekundi. Samo mali udio energije primarne čestice (10^{-4}) će se pretvoriti u Čerenkovljevo zračenje. Elektromagnetski pljusak i Čerenkovljevo zračenje koje uzroku je prikazano na Slici 1.13.

S tla se γ-zrake opažaju pomoću Čerenkovljevih atmosferskih teleskopa, koji snimaju Čerenkovljevo zračenje u atmosferi uzrokovano čestičnim pljuskovima. Strogo uzevši, IACT su optički teleskopi, budući da im se kamere sastoje od fotomultiplikatorskih cijevi (en. *Photomultiplier Tubes*, PMT). FACT (First G-APD Cherenkov Telescope) je prvi IACT koji koristi Gaigerove lavinske fotodiode (G-APD) te mu je jedan od ciljeva pokazati prednosti korištenja G-ADP pred PMT u Čerenkovljevim teleskopima. Eksperiment je započeo 2011. godine i još traje. Svaki od ovih elemenata kamere naziva se piksel. Osjetljivi su na svjetlost valnih duljina između 300 i 700 nm, jer je ozon snažno apsorbira fotone valnih duljina kraćih od 300 nm, dok u području preko 700 nm dominira pozadinska svjetlost noćnog neba. Ipak, IACT koriste atmosferu kao dio detektora, prema tome atmosfera je kalorimetar, a IACT brojač. S tog stanovišta tehnika zemaljskog opažanja γ-zraka je istovjetna onoj koja se koristi u čestičnim i nuklearnim eksperimentima.

Prvi IACT je bio 10 metarski Whipple teleskop, koji je sa radom počeo 1968. godine. Pomoću njega otkriveno je VHE γ-zračenje iz Rakove maglice 1989. [104], a iz Markarjana 421 1992., čime je to postala prva AGN otkrivena u području VHE γ-zraka [10]. Opažanja pomoću više teleskopa uvela je kolaboracija HEGRA (High Energy Gamma-Ray Astronomy), čiji su teleskopi opažali u razdoblju od 1987. do 2002. godine. Među postignuća kolaboracije HEGRA ubraja se i otkriće VHE γ-zraka iz M87 [5]. Trenutačno u svijetu postoje tri znanstvene kolaboracije, koje koriste IACT za opažanje VHE γ-zraka: H.E.S.S.[3] (High Energy Stereoscopic System), MAGIC[4] (Major Atmospheric Gamma Imaging Cherenkov) i VERITAS[5] (Very Energetic Radiation Imaging Telescope Array System). Kolaboracije H.E.S.S. i MAGIC su nastale iz kolaboracije HEGRA. MAGIC je izgradila svoje teleskope na mjestu gdje su stajali teleskopi HEGRA, u Observatorio del Roque de los Muchachos, na kanarskom otoku La Palma u Španjolskoj, dok je H.E.S.S. izgradila teleskope u Namibiji. VERITAS je naslijednik kolaboracije Whipple.

CTA[6] (Cherenkov Telescope Array) je projekt na svjetskoj razini, koji je trenutačno u razvojnoj fazi. Početak izgradnje planiran je za kraj 2015. godine, dok se početak opažanja očekuje 2020. CTA bi trebao biti smješten na dvije lokacije i to jednoj na sjevernoj i jednoj na južnoj polutki. Sjeverni CTA trebao bi se sastojati od 19, a južni od 99 teleskopa. Očekuje se da će biti osjetljiv na γ-zrake od nekoliko desetaka GeV do preko 100 TeV [105, 106].

Čerenkovljevi teleskopi MAGIC detaljnije su opisani u Odjeljku 7.3.

7.1.4   Izvangalaktička pozadinska svjetlost

Svemir je ispunjen difuznim elektromagnetskim zračenjem svih valnih duljina. Zračenje u područjima od infracrvenog do ultraljubičastog (0,1–1000 μm) se naziva izvangalaktička

---

[3]www.mpi-hd.mpg.de/hfm/HESS/HESS.shtml

[4]wwwmagic.mpp.mpg.de

[5]veritas.sao.arizona.edu

[6]portal.cta-observatory.org

pozadinska svjetlost (en. *Extragalactic Background Light*, EBL, Slika 1.14). Smatra se da potječe od svjetlosti zvijezda i prašinom prerađene svjetlosti zvijezda, te svjetlosti koja potječe iz aktivnih galaktičkih jezgri. VHE γ-zrake međudjeluju s fotonima EBL-a pri čemu se pretvaraju u elektron-pozitron par te je zbog toga njihov tok na putu do Zemlje prigušen. Prigušenje ovisi o energiji γ-zrake i crvenom pomaku izvora (z). Veza između mjerenog i intrinzičnog spektra izvora dana je relacijom

$$\left.\frac{\mathrm{d}N(E)}{\mathrm{d}E}\right|_{obs} = \left.\frac{\mathrm{d}N(E)}{\mathrm{d}E}\right|_{int} \mathrm{e}^{-\tau(E,z)}, \tag{7.25}$$

pri čemu je τ optička dubina dana s

$$\tau(E,z) = \int_0^z \mathrm{d}z' \frac{\mathrm{d}l(z')}{\mathrm{d}z'} \frac{1}{2} \int_{-1}^{+1} \mathrm{d}\mu(1-\mu) \int_{\epsilon_{th}}^{\infty} \mathrm{d}\epsilon' n_{\mathrm{EBL}}(\epsilon', z') \sigma_{\gamma\gamma}(E(1+z'), \epsilon', \mu). \tag{7.26}$$

Prvi integral uzima u obzir udaljenost koju je γ-zraka prešla, u drugom integriramo po kutu raspršenja pri čemu vrijedi pokrata $\mu \equiv \cos\theta$, a treći uračunava vjerojatnost raspršenja. n_{EBL} je gustoća fotona EBL-a u referentnom sustavu, a $\sigma_{\gamma\gamma}$ udarni presjek za nastanak elektron-pozitron para. ϵ_{th} je energijski prag reakcije, koji ovisi o energiji γ-zrake i kutu μ. Dobro poznavanje spektralne distribucije energije (en. *Spectral Energy Distribution*, SED) EBL-a, uz pretpostavku točno određenog crvenog pomaka izvora, omogućava nam rekonstrukciju intrinzičnog spektra. Taj proces nazivamo deapsorpcija. S druge strane, precizni mjerenjem spektra, uz točno određeni crveni pomak, možemo postaviti granice na EBL.

7.2 Kozmičke zrake

Signal γ-zraka iz astrofizičkih izvora (Odjeljak 7.1.2) prikriven je pozadinom koju čine kozmičke zrake. To su nabijene čestice ogromnih energija, nastale uglavnom izvan Sunčevog sustava. Čine ih većinom protoni (90%) i α-čestice (oko 9%). Ostalo su elektroni i teže atomske jezgre. Zbog toga se često nazivaju hadronima. SNR su izvori

velikog udjela kozmičkih zraka [109, 110]. Vjeruje se da su i AGN izvori kozmičkih zraka, iako to nije dokazano. Budući da su nabijene, kozmičke zrake podložne su utjecaju Zemljinog i Sunčevog magnetskog polja, i magnetskog polja galaksije i međugalaktičkog prostora, te je time izgubljena informacija o izvoru iz kojeg dolaze. Opservatoriji γ-zraka proučavaju kozmičke zrake opažanjem područja u kojima se očekuje povećana gustoća kozmičkih zraka. Međutim, pri ulasku kozmičkih zraka u atmosferu, ostavljaju trag sličan onome kojeg ostavljaju γ-zrake te zbog toga predstavljaju pozadinu. Spektar kozmičkih zraka iznad energije od 10 TeV/nukleon (Slika 1.16) se može opisati zakonom potencije

$$\frac{\mathrm{d}N}{\mathrm{d}E} \propto E^{-\alpha}, \tag{7.27}$$

pri čemu je

$$\alpha = \begin{cases} 2.7, & E < 10^{16}\,\mathrm{eV}, \\ 3.0, & 10^{16} < E < 10^{18}\,\mathrm{eV}. \end{cases} \tag{7.28}$$

Nagib spektra smanjuje se na energijama iznad 10^{19} eV. Dva prijeloma u spektru, na 10^{16} eV i 10^{19} eV nazivaju se "koljeno" i "gležanj", a upućuju na moguće granice energija različitih kozmičkih ubrzivača čestica.

7.3   Teleskopi MAGIC

Teleskopi MAGIC (Major Atmospheric Gamma Imaging Cherenkov) Floriana Goebela[7] (Slika 2.1) su dva 17 m IACT smješteno u Observatorio del Roque de los Muchachos na kanarskom otoku Palma u Španjolskoj (28°45′ sjeverne geografske širine, 18°54′ zapadne geografske dužine), na 2200 m nadmorske visine. Teleskopi su optimizirani za opažanje γ-zraka energija iznad 50 GeV. Iako mogu opažati samostalno, obično se opaža stereoskopski.

---

[7]Florian Goebel je bio istaknuti član kolaboracije MAGIC. Dao je vrijedan doprinos, a posebno radom na teleskopu MAGIC-II. Izgubio je život u tragičnoj nesreći radeći na izgradnji teleskopa MAGIC-II 10. rujna 2008. U njegovu čast, teleskopi MAGIC su preimenovani u teleskopi MAGIC Floriana Goebela. Od onda, sva opažanja teleskopima MAGIC se obustavljaju 10. rujna

Teleskopima upravlja međunarodna znanstvena kolaboracija, koju čine znanstvenici s 24 institucije iz 10 zemalja. Skupina znanstvenika iz Hrvatske, okupljenih u Hrvatski konzorcij MAGIC (en. *Croatian MAGIC Consortium*), pridružila se kolaboraciji MAGIC 2008. godine, a godinu dana kasnije primljena je u punopravno članstvo.

7.3.1 Opis teleskopa

Izgradnja teleskopa MAGIC-I dovršena je 2003. godine, a od sljedeće godine teleskop je opažao punim kapacitetom. Drugi teleskop, MAGIC-II dovršen je 2009.

Reflektor svakog teleskopa ima promjer od 17 m. Zbog lagane konstrukcije (Slika 2.2), koja koristi cijevi od karbonskih vlakana, teleskopi teže oko 64 t, pri čemu na dio koji se može micati u smjeru zenita (uključujući zrcala i kameru) otpada 20 t. Ovo omogućava brzo okretanje teleskopa, što je važno kod opažanja GRB. Ukupna površina reflektora je 236 m^2. I promjer reflektora i žarišna duljina iznose 17 m. Reflektori su sastavljeni od dijelova dimenzije 1×1 m. Zrcala MAGIC-I su aluminijska (Slika 2.3), dok je dio zrcala MAGIC-II od aluminija, a dio od stakla s naparenim aluminijem. Zrcala se mogu pomicati te tako kompenzirati iskrivljavanje oblika pod težinom kamere.

Kamere (Slika 2.4) se sastoje od 1039 piksela. Svaki piksel je PMT s vidnim poljem od $0,1°$. Svaki piksel je osjetljiv na pojedinačne fotone, s kvantnom učinkovitošću od $\approx 32\%$. Vidno polje kamere iznosi $3,6°$. Kamera teleskopa MAGIC-I u početku se sastojala od 577 piksela u dvije veličine (Slika 2.5). Zamijenjena je 2012. godine.

Okidanje se obavlja na tri razine. LT0 je okidač pojedinačnih piksela, LT1 je topološki okidač, koji radi prema logici najbližih susjeda (en. *Nearest-Neighbour*, NN), a LT3 je koincidentni okidač, koji osigurava da su oba teleskopa okinuta u određenom vremenskom prozoru.

Signal teleskopa se digitalizira pomoću Domino Ring Sampler (DRS) čipa. Frekvencija uzorkovanja je 2×10^9 uzoraka po sekundi.

7.3.2 Opažanja teleskopima MAGIC

Opažanja obavlja posada teleskopa, koja se sastoji od 4–5 članova kolaboracije. Jedna opažačka smjena traje 3–4 tjedna, ovisno o djelatnosti koju članovi posade obavljaju. Zbog osjetljivosti PMT na Mjesečevu svjetlost, teleskopima se ne može opažati tijekom 3–4 noći oko punog Mjeseca.

Opažanja se mogu vršiti na dva načina: ON-OFF i wobble. U ON-OFF načinu opažanja, teleskopi su usmjereni prema izvoru (tako da se izvor nalazi u središtu kamere), a za procjenu pozadine potrebna su dodatna opažanja područja neba na kojem nema izvora VHE γ-zraka. Pri wobble načinu opažanja [119] kamera je otklonjena od izvora za $0{,}4°$, tako da se ta opažanja mogu koristiti i za procjenu pozadine.

Teleskopima se može opažati pojedinačno, ali obično se koriste u stereoskopskom načinu opažanja.

Stanje različitih podsustava se tijekom opažanja prati pomoću programa iScream (Interactive Surveillance system for Checking the Report files and Exposing Alerts in MAGIC, Slika 2.6), kojeg je razvio autor ovog rada. iScream upozorava posadu teleskopa ukoliko parametri podsustava nisu unutar sigurnih granica. Time se osigurava kvaliteta podataka te štiti sigurnost posade i teleskopa.

7.3.3 Analiza podataka teleskopa MAGIC

Podaci s teleskopa MAGIC analiziraju se skupom računalnih programa MARS (MAGIC Analysis and Reconstruction Software) [120], napisanih u jeziku C++ u okruženju ROOT[8] [121].

Analiza se može podijeliti na nisku, srednju i visoku razinu (Slika 2.8). Niska razina analize podataka uključuje kalibraciju podataka te čišćenje i parametrizaciju slike. Obavlja se automatski nakon opažanja. Parametrizacijom slike računaju se parametri koji karakteriziraju sliku atmosferskog pljuska u kameri. Na osnovu tih parametara odvaja se slika pljuskova izazvanih γ-zrakama od onih izazvanih hadronima te određivanje njihovog sm-

---

[8]ROOT is maintained in CERN. root.cern.ch/drupal

jera i procjena energije. Srednju i visoku razinu analize podataka vrše analizatori. U srednjoj razini odabiru kvalitetne podatke te spajaju podatke oba teleskopa, a u visokoj se određuje signal (Slika 2.11) i izračunava njegova statistička signifikantnost prema jednadžbi 17 iz [123] te računaju spektar (Slika 2.12) i svjetlosna krivulja (Slika 2.13).

7.4 Messier 87

Messier 87 (M87) je divovska eliptična radio galaksija u zviježđu Djevice. Od nas je udaljena $16,4 \pm 0,5$ Mpc [12][9]. Crveni pomak M87 iznosi $z = (4,238 \pm 0,017) \times 10^{-3}$ [129]. Masa vidljive tvari u M87 iznosi $(4-5) \times 10^{11} M_\odot$ [135], ali prema [28], omjer mase i sjaja iznosi $6,3 \pm 0,8$ pa je stvarna masa galaksije puno veća. Zbog svoje veličine, M87 je središte našeg lokalnog svemira. Masa crne rupe u središtu galaksije iznosi $(6,4 \pm 0,5) \times 10^9 M_\odot$ [28]. AGN stvara relativistički mlaz tvari koji se proteže preko $20''$ [138], što odgovara udaljenosti od 2 kpc od jezgre. Mlaz je otkrio H. D. Curtis [9] 1918. godine. Mlaz je otklonjen od smjera prema Zemlji između $10°$ [139] i $45°$ [140].

7.4.1 Studija niskog stanja emisije u razdoblju 2005.–2007. godine

U razdoblju od 2005. do 2007. godine teleskop MAGIC-I je opažao M87 ukupno 154,1 sat. Od toga je 128,6 sati podataka zadržano nakon provjere kakvoće. Namjera nam je bila ispitati svojstva VHE γ-zračenja iz M87 u niskom stanju emisije. Emisija VHE γ-zraka potvrđena je sa statističkom značajnošću od $7\,\sigma$. Da bismo se uvjerili da je AGN bila u stanju niske emisije tijekom opažanja, prikazali smo kumulativni broj događaja u vremenu (Slika 3.2). Svjetlosna krivulja podataka razvrstanih po mjesecima prikazana je na Slici 3.3. Ukupni tok zračenja u području VHE γ-zraka smo usporedili s konstantnim iznosa $(5,06 \pm 0,77) \times 10^{-12}\,\mathrm{s^{-1}cm^{-2}}$, što je rezultiralo reduciranim χ^2 od 0.51. Spektar

---

[9]Novije istraživanje [128] određuje udaljenost M87 na $16,4 \pm 0,5$ Mpc, ali u našem istraživanju koristili smo vrijednost iz [12]. Oba rezultata su unutar statističke pogreške.

se može dobro opisati zakonom potencije: $dN/dE = N_0\,(\mathrm{E}/300\,\mathrm{GeV})^{-\Gamma}$ sa spektralnim indeksom $\Gamma = 2,21 \pm 0,21$ i normalizacijom toka $N_0 = (7,7 \pm 1.3) \times 10^{-8}\,\mathrm{TeV^{-1}s^{-1}m^{-2}}$. Spektar je prikazan plavim kružićima na Slici 3.4. Budući da nije bilo istovremenih opažanja u području HE γ-zraka, upotrijebili smo podatke *Fermi*-LAT teleskopa (crveni kvadrati na Slici 3.4) dobivenih u prvih 10 mjeseci opažanja (4. kolovoza 2008. – 31. svibnja 2009., [158]). Zajednički spektar MAGIC i *Fermi*-LAT podataka je zakon potencije s parametrima $\Gamma = 2.17 \pm 0,03$ i $N_0 = (7,1 \pm 1.0) \times 10^{-8}\,\mathrm{TeV^{-1}s^{-1}m^{-2}}$.

Modeliranje zračenja

Zračenje smo pokušali opisati takozvanim kičma-plašt (en. *spine-layer*) modelom. To je dvozonski leptonski SSC model u kojem se ultrarelativistički elektroni gibaju kroz mlaz u dva sloja. Unutarnji, brži sloj se naziva kičma, a vanjski plašt. Elektroni u oba sloja sinkrotronski zrače fotone, koji se kasnije raspršuju na tim istim elektronima te zbog inverznog Comptonovog raspršenja nastaju γ-zrake. Model je skiciran na Slici 3.7. Rezultat modeliranja prikazan je na Slici 3.6, a parametri modela su dani u Tablici 3.1.

7.5 PKS 1222+21

PKS 1222+21 (alternativna oznaka 4C +21.35) je FSRQ s crvenim pomakom $z = 0,432$ [18]. Opažan je teleskopima MAGIC u razdoblju od 3. svibnja do 19. lipnja 2010. Zračenje u području VHE γ-zraka otkriveno je teleskopima MAGIC 17. lipnja 2010. Tu noć, opažen je snažan bljesak izvora te je u samo 30 minuta opažanja, detektirano 190 γ-zraka. Tok zračenja se je udvostručio u $8,6^{+1,1}_{-0,9}$ minuta (Slika 4.2) [71]. Izmjereni spektar se može opisati zakonom potencije sa spektralnim indeksom $3,75 \pm 0,27$. Da bi se dobio intrinzični spektar izvora, treba uzeti u obzir prigušenje toka zbog međudjelovanja s EBL. Korišten je model EBL iz [108] te je za nagib intrinzičnog spektra dobivena vrijednost $2,72 \pm 0,34$ (Slika 4.3) [71]. Postojanje granice u spektru (en. *cut-off*) je isključeno do energije od 130 GeV. Ovaj rezultat upućuje na to da se područje zračenja

mora nalaziti van BLR. U protivnom bi se γ-zrake poništile s optičkim fotonima koji nastaju u BRL. U isto vrijeme, brza promjena toka zračenja upućuje na relativno malo područje zračenja. Signal je opažen već 3. svibnja, također u vrijeme bljeska izvora, ali s manjom značajnošću ($4,4\sigma$). Za opažanja između 5. i 13. svibnja postavljene su gornje granice na tok zračenja. Rezultati su dani u Tablici 4.1. Gornje granice nisu računate za ostale dane zbog velikog utjecaja Mjeseca.

7.5.1 Zračenje na različitim valnim duljinama

Uređaji korišteni u ovom istraživanju su navedeni u Tablici 4.2.

Svjetlosna krivulja na više valnih duljina (Slika 4.3.5) prikazuje podatke teleskopa *Fermi*-LAT, *Swift* (XRT; UVOT, filtri u i $m2$), optički R-pojas (Abastumani, ATOM, Crimean, KVA, St. Petersburg) te radio između 15 i 37 GHz (Effelsberg, Medicina, Metsähovi, OVRO, UMRAO) prikupljenih u razdoblju 9. travnja – 4 kolovoza 2010. (MJD 55295–55412). Uz to, u drugom i četvrtom odjeljku su prikazani nagibi spektara γ-zraka i X-zraka opaženih teleskopima *Fermi*-LAT i *Swift*-XRT. Vremena u kojima su teleskopi MAGIC uočili bljeskove zračenja, označena su strelicama na vrhu svjetlosne krivulje. Svjetlosna krivulja teleskopa *Fermi*-LAT light pokazuje dva izražena bljeska i to vremenski bliska detekcijama pomoću teleskopa MAGIC (29. travnja (MJD 55315) i 18. lipnja (MJD 55365)), što upućuje da je isti mehanizam zračenja odgovoran za zračenje u oba energijska područja. Zanimljivo je primijetiti i da je u to doba nagib spektra mjeren pomoću *Fermi*-LAT manje strm ($\Gamma_\gamma \sim 2$), što pogoduje zračenju i do nekoliko stotina GeV. Opažanja na nižim energijama također pokazuju promjenljiv tok zračenja, ali u puno manjoj mjeri te s vremenskim pomakom u odnosu na područje γ-zraka.

Modeliranje zračenja

Prikupljene podatke smo podijelili u tri skupine i od njih sastavili tri SED, prikazane na Slici 4.7). Crveni kružići predstavljaju podatke za koje smatramo da su vezani uz bljesak

od 17. lipnja, dok su zelenim kvadratićima prikazani podaci iz bljeska 29. travnja. Ostali podaci, prikupljeni u razdoblju od 4. kolovoza 2008. do 12. rujna 2009., su svrstani u treću skupinu i smatraju se zračenjem u mirnom stanju izvora. Na slici su prikazanim plavim rombima. Podaci s teleskopa MAGIC od 3. svibnja 2010. su svrstani u zelenu, a od 17. lipnja u crvenu skupinu. Korekcija na EBL je napravljena koristeći model iz [108]. Za masu crne rupe koristimo vrijednost iz [176], gdje je procijenjena na $M_{BH} \sim 6 \times 10^8$ $M_\odot$, koristeći mjerenja širokih emisijskih linija iz preko 100 optičkih spektara iz različitih izvora.

Sva tri razdoblja smo modelirali jednozonskim leptonskim modelom. Zračenje u IR području pripisujemo toplinskom zračenju iz torusa, dok ono u optičkom pripisujemo toplinskom zračenju iz akrecijskog diska. Rezultati modeliranja zračenja iz torusa, slični su rezultatima u [204]. Zračenje u području γ-zraka modeliramo kombinacijom EC i SSC modela, pri čemu je EC doprinos dominantan. Rezultati modeliranja prikazani su na Slici 4.7, a parametri sva tri modela su dani u Tablici 4.3. Ističemo kako se modeli za različita razdoblja razlikuju samo u raspodjeli relativističkih elektrona.

7.6   H1722+119

H1722+119 je izvor tipa BL Lac s vrhom na srednjim energijama ($\nu_s = 6,3 \times 10^{15}$ Hz [52]). Iako je u [19] crveni pomak procijenjen na $0,018$, taj rezultat kasnije nije potvrđen (primjerice [215, 216, 217]). Naprotiv, postavljene su donje granice na crveni pomak i to $0,17$ [218], $0,35$ [219] i $0,4$ Farina et al.(priv. comm.). Zadnji izvor navodi i da nisu uspjeli detektirati galaksiju domaćina. Teleskopi MAGIC-I je opažao H1722+119 u razdoblju od 2005. do 2009. godine, ali nije otkriven signal [221]. Postavljena je gornja granica na tok VHE γ-zračenja energija većih od 140 GeV na $1,3 \times 10^{-11}$cm^{-2}s^{-1}.

Početkom svibnja 2013. optički teleskop KVA zabilježio je najvišu magnitudu u povijesti za ovaj izvor u R-pojasu od 14,65. To je potaklo opažanja teleskopima MAGIC, koji su opažali tijekom šest uzastopnih noći od 17. do 22. svibnja. Prikupljeno je

12,5 sati podataka, od čega 12 sati dobre kakvoće. Signal je otkriven sa statističkom značajnošću od $5,92\,\sigma$ (Slika 5.1). Svjetlosna krivulja područja VHE γ-zraka (Slika 5.2) prikazuje podatke grupirane po danima. Ukupni tok zračenja energija većih od $150\,\text{GeV}$ je konstantan i iznosi $(6,3 \pm 1,6) \times 10^{-12}\text{cm}^{-2}\text{s}^{-1}$ ($\chi^2/\text{ss} = 3,5/5$), što je konzistentno s prethodno postavljenom gornjom granicom [221]. Spektar se može opisati jednostavnim zakonom potencije $\mathrm{dN/dE} = \mathrm{N}_0(\mathrm{E}/200\,\text{GeV})^{-\Gamma}$, pri čemu je $\mathrm{N}_0 = (4,3 \pm 0,9) \times 10^{-11}\text{cm}^{-2}\text{s}^{-1}\text{TeV}^{-1}$, a spetralni indeks $\Gamma = 3,3 \pm 0,3$.

7.6.1 Zračenje na različitim valnim duljinama

Da bismo što bolje razumjeli što se događa u izvoru, iskoristili smo opažanja na nižim energijama i to teleskopima *Fermi*-LAT, sva tri detektora na satelitu *Swift* (BAT, XRT i UVOT) [194], KVA i OVRO. Skupna svjetlosna krivulja prikazana je na Slici 5.3. Tok zračenja mjeren teleskopom *Fermi*-LAT izgleda konstantan $(3,43 \pm 0,56) \times 10^{-8}$ ph cm^{-2} s^{-1} ($\chi^2/\text{ss} = 3,87/5$). Na istoj slici smo prikazali i evoluciju spektralnog nagiba. Također smo dobili dobro slaganjem s konstantnim nagibom od $1,96 \pm 0,07$ ($\chi^2/\text{ss} = 1,68/5$). Ipak ako se odredi nagib spektra za kratko razdoblje oko opažanja teleskopima MAGIC, od 13. do 26. svibnja, spektralni indeks ima nešto manji nagib, $1,40\pm0,29$, što bi moglo upućivati na pomak inverznog Comptonovog vrha prema višim energijama. Za razliku od toka zračenja u području γ-zraka, tok zračenja u optičkom i radio području nije konstantan. Tok u radio području smo usporedili s pretpostavkom stalnog porasta kroz godinu i dobili dobro slaganje s rezultatom $\chi^2/\text{ss} = 39,68/36$.

Budući da crveni pomak izvora nije bio precizno određen, upotrijebili smo podatke iz područja HE i VHE γ-zraka. Kao što smo vidjeli u Odjeljku 7.1.4, tok VHE γ-zraka se prigušuje međudjelovanjem s EBL, zbog čega će mjereni spektar biti strmiji od intrinzičnog spektra izvora. Iz istog razloga, spektar u HE području nikada nije strmiji od spektra u VHE području. Metoda [225] koristi tu činjenicu da procijeni crveni pomak izvora i postavi gornju granicu. Dobili smo vrijednost $z = 0,34 \pm 0,15$ uz gornju granicu od 0,95.

H1722+119 je izvor tipa BL Lac. SED takvih izvora se obično modelira jednozonskim SSC modelom. Mjerenja istovremena s teleskopima MAGIC prikazana su na Slici 5.4 crvenim točkama. Crveni križići predstavljaju gornje granice određene opažanjima teleskopa *Fermi*-LAT. Sive točke su arhivska mjerenja preuzeta iz [226]. Na žalost, nismo uspjeli naći skup parametara jednozonskog SSC modela koji dobro opisuju zračenje izvora. Uz to u optičkom-UV području javlja se neuobičajen skok između točaka. Nismo utvrdili nikakve probleme s uređajem ili analizom podataka, koji bi mogli biti uzrok tome, međutim nije jasno ni je li skok posljedica procesa u samom izvoru, ili u međugalaktičkom prostoru. Za bolje opisivanje podataka u SED, vjerojatno će biti potrebni složeniji modeli emisije, ali prije toga bi trebalo razumjeti uzrok spomenutog skoka.

7.7 AGN opažene teleskopima MAGIC

Detekcija γ-zraka vrlo visokih energija nije trivijalan zadatak. γ-zrake su rijetki događaji. Na primjeru izvora, koje smo proučavali, vidjeli smo da spektar u području γ-zraka obično prati zakon potencije. Uz to, γ-zrake, koje prelaze kozmološke udaljenosti mogu se apsorbirati u međudjelovanju s izvangalaktičkim pozadinskim zračenjem. Stoga ne čudi da ih je do sada u području VHE γ-zraka otkriveno tek 58. Većina njih spadaju u razred BL Lac, što je očekivano, budući da radio galaksije nisu blazari, a izvori iz razreda FSRQ se rjeđe pojavljuju na crvenim pomacima ispod 0,5 (vidi primjerice [55]).

Kolaboracija MAGIC izmjerila je VHE γ-zračenje iz 33 AGN do sada. Njihov popis s koordinatama, razredom, crvenim pomakom i referencama na odgovarajuće publikacije kolaboracije MAGIC, dan je u Tablici 6.1. Raspodjela ovih izvora prema razredu i crvenom pomaku prikazana je na Slici 6.1. U skladu s očekivanjima, većina izvora ima crvene pomake manje od 0,2, a za samo dva izvora $z \gtrsim 0,5$. Blazar nepoznatog razreda S3 0218+357 na $z = 0,944$ je prvi opaženi u području VHE γ-zraka čija je emisija pojačana gravitacijskom lećom. To je vrlo vjerojatno i razlog zbog kojeg je izvor toliko udaljen vidljiv u području VHE γ-zraka. Izvoru RGB J0136+391 nije određen crveni

pomak.

Prikazali smo i nagib intrinzičnog spektra za AGN na različitim crvenim pomacima na Slikama 6.2 i 6.3. Veza između slika i Tablice 6.1 nije jedan na jedan, jer za neke izvore nije određen intrinzični spektar, dok je za neke određen više puta. Pri tome su različite vrijednost posljedica korištenja različitih modela EBL ili određivanje crvenog pomaka različitim metodama (S5 0716+714). Na Slici 6.2 podaci su grupirani prema obliku spektra. Za većinu njih spektar se može opisati zakonom potencije 7.29, dok je u nekoliko slučajeva upotrebljen složeniji oblik i to zakon potencije s granicom (7.30), ili logaritamska parabola (7.31).

$$\frac{\mathrm{d}N}{\mathrm{d}E} = N_0 \left(\frac{E}{E_0} \right)^{-\Gamma} \tag{7.29}$$

$$\frac{\mathrm{d}N}{\mathrm{d}E} = N_0 \left(\frac{E}{E_0} \right)^{-\Gamma} \exp\left(-\frac{E}{E_{\mathrm{co}}} \right) \tag{7.30}$$

$$\frac{\mathrm{d}N}{\mathrm{d}E} = N_0 \left(\frac{E}{E_0} \right)^{-\Gamma - \beta \log(E/E_0)}, \tag{7.31}$$

pri čemu je N_0 normalizacijski faktor, koji odgovara broju γ-zraka energije E_0 koji padnu na jediničnu površinu u jedinici vremena. E_0 je normalizacijska točka proizvoljno uzeta iz intervala $0.1 - 1\,\mathrm{TeV}$. Spektar nekih izvora (primjerice Markarjan 421) je opisan s više od jednog oblika. Podaci na Slici 6.3 su grupirani po istom ključu kao na Slici 6.1.

Podaci prikazani u Tablici 6.1 i Slikama 6.1, 6.2 i 6.3 rezultati su studija provođenih tijekom gotovo deset godina. Tijekom tog razdoblja, naše poznavanje spektralne raspodjele energije pozadinskog zračenja se povećalo. U skladu s time, mnoge podatke bi trebalo ponovo analizirati kako bi se mogli međusobno uspoređivati, što bi bio iznimno dugotrajan posao. Uz to nepouzdanosti pri određivanju spektra su velike i postoji puno mjesta za poboljšanje. Zbog toga s nestrpljenjem očekujemo naš rad u nadolazećem Cherenkov Telescope Array (CTA), od kojeg se očekuje snižavanje energijskog praga osjetljivosti za detekciju VHE γ-zraka i veća osjetljivost u odnosu na postojeće Čerenkovljeve teleskope. Ova studija je važan korak u pripremi ključnih znanstvenih opažačkih programa AGN pomoću CTA.

7.8   Zaključak

Aktivne galaktičke jezgre su najsjajniji trajni izvori elektromagnetskog zračenja u svemiru. To su kompaktna područja u središtima galaksija formirana oko supermasivnih crnih rupa, koje aktivno prikupljaju tvar akrecijom. Oko 10% AGN izbacuju tvar u obliku relativističkih mlazova. AGN čiji su mlazovi usmjereni približno prema Zemlji nazivamo blazarima. Mlazovi su izvori elektromagnetskog zračenja svih valnih duljina od radiovalova do γ-zraka. Neki se protežu i do udaljenosti od Mpc od jezgre, a sjajem mogu nadmašiti cijelu galaksiju u kojoj se nalaze. AGN se već dugo i pomno promatraju u svim područjima electromagnetskog spektra od radiovalova do X-zraka, što je polučilo mnoge zanimljive rezultate i objašnjenja pojava u AGN. Međutim, važan dio slagalice je nedostajao dok nismo imali priliku promatrati AGN u području γ-zraka. Ne samo da su ta opažanja upotpunila sliku, nego su otkrila fizikalne pojave kojih do tada nismo bili svjesni. Ipak smo još uvijek bliže početku nego kraju istraživanja AGN. Do dovršetka ovog rada, samo 58 AGN su potvrđene kao izvori γ-zraka vrlo visokih energija [227]. Većina njih (pedeset) su klasificirane kao BL Lac i to uglavnom kao HBL. Samo sedam ih je klasificirano kao IBL. Samo četiri radio galaksije su potvrđeni izvori VHE γ-zraka, a samo tri su FSRQ. Zbog toga otkriće i proučavanje svakog novog izvora uvelike pridonosi našem poznavanju i razumijevanju fizike AGN. U ovom istraživanju proučavana su svojstva tri AGN, pri čemu svaka od njih spada u drugi rijetki razred (radio galaksija: M87, IBL: H1722+119 i FSRQ: PKS 1222+21).

M87 je otprije poznati izvor VHE γ-zraka. U ovom istraživanju smo se usredotočili na mirno stanje zračenja (en. *quiescent emission state*). Često je naša pažnja usmjerena na bljeskove (en. *flare*) iz AGN, što je razumljivo kada se u obzir uzme mala učestalost γ-zraka. Bljeskovi omogućuju prikupljanje velikog broja podataka za kratko vrijeme opažanja. Ipak, da bismo razumjeli što se događa u pojedinom izvoru, vrlo je važno, ako ne i neophodno, proučavati dugoročno ponašanje izvora s posebnom pažnjom usmjerenom na mirno stanje emisije. Proučavanjem podataka prikupljenih tijekom tri godine omogućilo nam je uvid u ono što bismo mogli nazvati osnovnom razinom zračenja, a to

je ukupni tok zračenja od $(5, 06 \pm 0, 77) \times 10^{-12} \, \text{s}^{-1} \text{cm}^{-2}$. Spektar koji prati zakon potencije s nagibom od $2, 21 \pm 0, 21$ slaže se s vrijednostima, koje su prethodno objavili drugi istraživači. S velikim zanimanjem iščekujemo rezultate budućih studija i usporedbu s našim rezultatima, da bismo utvrdili mijenja li se spektar tijekom i nakon bljeskova zračenja i u kojoj mjeri. Model koji smo upotrijebili za opis zračenja je neuobičajeni dvozonski SSC "kičma-plašt" model, prema kojem se relativistički mlaz sastoji od dva koncentrična sloja, svaki od njih je izvor zračenja, a zračenje koje opažamo je kombinacija njihovih doprinosa.

PKS 1222+21 je tek treći do sada otkriveni FSRQ u području VHE γ-zraka. Tijekom bljeska opaženog 17. lipnja 2010. izmjerena je izrazito brza promjena toka zračenja (tok se udvostručio za $8, 6^{+1,1}_{-0,9}$ minuta). Pri tome je spektar u području γ-zraka relativno tvrd ($\Gamma = 2, 7 \pm 0, 3$) bez uočljive granice do $130 \, \text{GeV}$. S ovim svojstvima PKS 1222+21 predstavlja izazov za postojeće modele VHE γ-zračenja iz FSRQ. Usprkos tome, ponudili smo model koji objašnjava opažanja i to zbrajanjem doprinosa toplinskog zračenja iz torusa prašine i akrecijskog diska sa jednozonskim sinkrotronskim zračenjem iz mlaza. Zračenje u području γ-zraka je ponovo zbroj EC i SSC doprinosa. Modelirali smo zračenje tijekom dva bljeska te mirnog stanja s promjenom samo jednog parametra i to raspodjele elektrona u izvoru. Nažalost, zračenje VHE γ-zraka tijekom mirnog stanja je preslabo da bi se moglo detektirati trenutačno dostupnim uređajima. Zaključili smo da područje zračenja γ-zraka mora biti izvan BLR, osim ako na djelu nije neki egzotični način prijenosa γ-zraka. Nadamo se i očekujemo da će ovaj rezultat biti potvrđen budućim opažanjima. Ukoliko bude, ostaje za pokazati vrijedi li to općenito za FSRQ, ili se radi o iznimci. Također smo otkrili naznake progradno brzorotirajuće crne rupe.

H1722+119 spada u klasu IBL. Obično se zračenje iz BL Lac izvora modelira jednozonskim SSC modelom, međutim nismo uspjeli naći zadovoljavajući skup parametara koji opisuju zračenje iz ovog izvora. Budući da nema naznake promjenjivosti toka zračenja u području γ-zraka, a ukupni tok zračenja $(6, 3 \pm 1, 6) \times 10^{-12} \text{cm}^{-2}\text{s}^{-1}$ je niži od gornje granice postavljene u prethodnoj studiji, vjerujemo da je izvor bio u mirnom stanju tijekom opažanja. Ipak, to može biti potvrđeno tek nakon što se opazi promjenjivost

toka γ-zračenja. Uspoređujući rezultate u području γ-zraka s mjerenjima u optičkom i radio području, uočljiva je promjena toka zračenja na tim frekvencijama, pri čemu tok u radio području raste kroz cijelu godinu. Prema tome ne vidimo nikakvu povezanost zračenja u ova tri područja. Iskoristili smo spektar u HE i VHE području γ-zraka da procijenimo crveni pomak izvora. U kombinaciji s donjom granicom postavljenom na osnovu opažanja u optičkom području, odredili smo da crveni pomak iznosi 0,4 s gornjom granicom na 0,95.

Sva tri izvora pripadaju različitim razredima AGN, te smo morali koristiti različite modele zračenja da bismo opisali izvore. Najzanimljivije pitanje u ovom slučaju je jesu li ovi izvori fundamentalno različiti. Je li činjenica što nema uočljivih linija u optičkom dijelu spektra H1722+119 posljedica samo velikog omjera relativistički usmjerenog zračenja u odnosu na toplinsko? Kako bi izgledalo zračenje iz M87 kada bi mlaz bio usmjeren prema Zemlji? Bi li i u tom slučaju bili potrebni složeni modeli da opišu zračenje, ili bi jednozonski model bio dovoljan? Ova ali i mnoga druga pitanja ostaju otvorena za buduća istraživanja.

Sastavili smo popis AGN koje su opažene teleskopima MAGIC, kao korak prema planiranju istraživanja sustavom CTA.

Bibliography

[1] I. DUȚAN, L. I. CARAMETE. Ultra-high-energy cosmic rays from low-luminosity active galactic nuclei. *Astroparticle Physics*, **62**[0]:206 – 216, 2015.

[2] M. URRY. The AGN Paradigm for Radio-Loud Objects. In S. COLLIN, F. COMBES, I. SHLOSMAN, editors, *Active Galactic Nuclei: from Central Engine to Host Galaxy, ASP Conference Series*, **290**, 2003.

[3] B. M. PETERSON. The broad-line region in active galactic nuclei. In D. ALLOIN, R. JOHNSON, P. LIRA, editors, *Physics of Active Galactic Nuclei at all Scales*, **693** of *Lecture Notes in Physics*, pages 77–100. Springer, Berlin Heidelberg, 2006.

[4] J. S. DUNLOP ET AL. Quasars, their host galaxies and their central black holes. *Monthly Notices of the Royal Astronomical Society*, **340**[4]:1095–1135, 2003.

[5] F. AHARONIAN ET AL. Is the giant radio galaxy M87 a TeV gamma-ray emitter? *Astronomy and Astrophysics*, **403**[1]:L1–L5, 2003.

[6] F. AHARONIAN ET AL. Discovery of very high energy γ-ray emission from Centaurus a with H.E.S.S. *The Astrophysical Journal Letters*, **695**[1]:L40, 2009.

[7] J. ALEKSIĆ ET AL. Detection of very-high energy γ-ray emission from NGC 1275 by the MAGIC telescopes. *Astronomy and Astrophysics*, **539**:L2, 2012.

[8] J. ALEKSIĆ ET AL. Detection of very high energy γ-ray emission from the Perseus Cluster head-tail galaxy IC 310 by the MAGIC telescopes. *The Astrophysical Journal Letters*, **723**[2]:L207, 2010.

[9] H. D. CURTIS. Descriptions of 762 nebulae and clusters photographed with the Crossley reflector. *Publications of Lick Observatory*, **13**:9–42, 1918.

[10] M. PUNCH ET AL. Detection of TeV photons from the active galaxy Markarian 421. *Nature*, **358**:477–478, 1992.

[11] F. AHARONIAN ET AL. Fast variability of tera-electron volt γ rays from the radio galaxy M87. *Science*, **314**[5804]:1424–1427, 2006.

[12] S. Mei et al. The ACS Virgo Cluster survey. XIII. SBF distance catalog and the three-dimensional structure of the Virgo Cluster. *The Astrophysical Journal*, **655**[1]:144, 2007.

[13] V. A. Acciari et al. Observation of gamma-ray emission from the galaxy M87 above 250 GeV with VERITAS. *The Astrophysical Journal*, **679**[1]:397, 2008.

[14] The VERITAS Collaboration et al. Radio imaging of the very-high-energy γ-ray emission region in the central engine of a radio galaxy. *Science*, **325**[5939]:444–448, 2009.

[15] J. Albert et al. Very High Energy Gamma-Ray Observations of Strong Flaring Activity in M87 in 2008 February. *The Astrophysical Journal Letters*, **685**[1]:L23, 2008.

[16] V. A. Acciari et al. Veritas 2008–2009 monitoring of the variable gamma-ray source M87. *The Astrophysical Journal*, **716**[1]:819, 2010.

[17] F. Tavecchio, G. Ghisellini. Spine–sheath layer radiative interplay in subparsec-scale jets and the TeV emission from M87. *Monthly Notices of the Royal Astronomical Society: Letters*, **385**[1]:L98–L102, 2008.

[18] D. E. Osterbrock, R. W. Pogge. Optical spectra of narrow emission line Palomar-Green galaxies. *Astrophysical Journal*, **323**:108, 1987.

[19] R. E. Griffiths et al. 4U1722+11 - The discovery of an X-ray selected BL Lac object. *Monthly Notices of the Royal Astronomical Society*, **240**:33–39, September 1989.

[20] R. J. V. Brissenden et al. H1722+119 – a highly polarized X-ray-selected BL Lacertae object. *The Astrophysical Journal*, **350**:578–584, February 1990.

[21] J. D. Linford et al. Contemporaneous VLBA 5 GHz observations of Large Area Telescope detected blazars. *The Astrophysical Journal*, **744**:177, January 2012.

[22] J. Cortina, the MAGIC collaboration. Discovery of very high energy gamma-ray emission from BL Lac object H1722+119 by the MAGIC telescopes. *ATel*, **5080**, May 2013.

[23] K. Schwarzschild. On the Gravitational Field of a Mass Point According to Einstein's Theory. *Sitzungsberichte der Königlich Preussischen Akademie der Wissenschaften*, pages 189–196, 1916.

[24] N. J. Secrest et al. The *Chandra* view of NGC 4178: The lowest mass black hole in a bulgeless disk galaxy? *The Astrophysical Journal*, **753**:38, 2012.

[25] N. J. McConnell et al. Two ten-billion-solar-mass black holes at the centres of giant elliptical galaxies. *Nature*, **480**:215–218, 2011.

[26] C. Rodriguez et al. A compact supermassive binary black hole system. *The Astrophysical Journal*, **646**:49–60, 2006.

[27] S. Gillessen et al. Monitoring stellar orbits around the massive black hole in the galactic center. *The Astrophysical Journal*, **692**:1075–1109, 2009.

[28] K. Gebhardt, J. Thomas. The black hole mass, stellar mass-to-light ratio, and dark halo in M87. *The Astrophysical Journal*, **700**:1690–1701, 2009.

[29] K. Gültekin et al. The M-σ and M-L relations in galactic bulges and determinations of their intrinsic scatter. *The Astrophysical Journal*, **698**:198–221, 2009.

[30] N. Häring, H.-W. Rix. On the black hole mass-bulge mass relation. *The Astrophysical Journal*, **604**:L89–L92, 2004.

[31] E. Sani et al. The Spitzer/IRAC view of black hole-bulge scaling relations. *Monthly Notices of the Royal Astronomical Society*, **413**:1479–1494, 2011.

[32] D. J. Croton et al. The many lives of active galactic nuclei: cooling flows, black holes and the luminosities and colours of galaxies. *Monthly Notices of the Royal Astronomical Society*, **365**:11–28, 2006.

[33] R. S. Somerville et al. A semi-analytic model for the co-evolution of galaxies, black holes and active galactic nuclei. *Monthly Notices of the Royal Astronomical Society*, **391**:481–506, 2008.

[34] R. C. E. van den Bosch et al. An over-massive black hole in the compact lenticular galaxy NGC 1277. *Nature*, **491**:729–731, 2012.

[35] A. E. Reines et al. An actively accreting massive black hole in the dwarf starburst galaxy Henize 2-10. *Nature*, **470**:66–68, 2011.

[36] J.-P. De Villiers et al. Magnetically driven accretion in the Kerr metric. III. Unbound outflows. *The Astrophysical Journal*, **620**[2]:878, 2005.

[37] R. Kerr. Gravitational field of a spinning mass as an example of algebraically special metrics. *Phys. Rev. Lett.*, **11**:237–238, Sep 1963.

[38] R. H. Boyer, R. W. Lindquist. Maximal analytic extension of the Kerr metric. *Journal of Mathematical Physics*, **8**[2]:265–281, 1967.

[39] Sheperd S. Doeleman et al. Jet-launching structure resolved near the supermassive black hole in M87. *Science*, **338**[6105]:355–358, 2012.

[40] H. Netzer. Active galactic nuclei: Basic physics and main components. In D. Alloin, R. Johnson, P. Lira, editors, *Physics of Active Galactic Nuclei at all Scales*, **693** of *Lecture Notes in Physics*, pages 1–38. Springer, Berlin Heidelberg, 2006.

[41] F. Haardt, L. Maraschi. A two-phase model for the X-ray emission from Seyfert galaxies. *Astrophysical Journal*, **380**:L51–L54, 1991.

[42] S. Bianchi, R. Maiolino. AGN obscuration and the Unified Model. *Advances in Astronomy*, **2012**, 2012.

[43] P. L. Biermann et al. Single and binary black holes and their active environment. In N. Sanchez, H. de Vega, editors, *Proceedings of the 7eme Colloquium Cosmologie "High Energy Astrophysics from and for Space"*, 2002.

[44] J. K. Becker. High-energy neutrinos in the context of multimessenger astrophysics. *Physics Reports*, **458**[4-5]:173 – 246, 2008.

[45] J. Bagchi et al. Megaparsec relativistic jets launched from an accreting supermassive black hole in an extreme spiral galaxy. *The Astrophysical Journal*, **788**[2]:174, 2014.

[46] Y. Uchiyama et al. Shedding new light on the 3C 273 jet with the Spitzer Space Telescope. *The Astrophysical Journal*, **648**[2]:910, 2006.

[47] F. N. Owen, J. A. Eilek, N. E. Kassim. M87 at 90 centimeters: A different picture. *The Astrophysical Journal*, **543**[2]:611, 2000.

[48] R. D. Blandford, R. L. Znajek. Electromagnetic extraction of energy from Kerr black holes. *Monthly Notices of the Royal Astronomical Society*, **179**:433, 1977.

[49] R. D. Blandford, D. G. Payne. Hydromagnetic flows from accretion discs and the production of radio jets. *Monthly Notices of the Royal Astronomical Society*, **199**:883, 1982.

[50] M. Sikora et al. Are quasar jets dominated by Poynting flux? *The Astrophysical Journal*, **625**[1]:72, 2005.

[51] A. A. Abdo et al. Fermi Large Area Telescope observations of Markarian 421: The missing piece of its spectral energy distribution. *The Astrophysical Journal*, **736**[2]:131, 2011.

[52] E. Nieppola, M. Tornikoski, E Valtaoja. Spectral energy distributions of a large sample of BL Lacertae objects. *Astronomy and Astrophysics*, **445**:441–450, January 2006.

[53] J. H. FAN. Relation between BL Lacertae objects and flat-spectrum radio quasars. *The Astrophysical Journal Letters*, **585**[1]:L23, 2003.

[54] G. GHISELLINI ET AL. The transition between BL Lac objects and flat spectrum radio quasars. *Monthly Notices of the Royal Astronomical Society*, **414**[3]:2674–2689, 2011.

[55] M. ACKERMANN ET AL. The second catalog of active galactic nuclei detected by the Fermi Large Area Telescope. *The Astrophysical Journal*, **743**[2]:171, 2011.

[56] P. P. KRONBERG ET AL. Magnetic energy of the intergalactic medium from galactic black holes. *The Astrophysical Journal*, **560**[1]:178, 2001.

[57] F. TAVECCHIO, L. MARASCHI, G. GHISELLINI. Constraints on the physical parameters of TeV blazars. *The Astrophysical Journal*, **509**[2]:608, 1998.

[58] M. URRY, P. PADOVANI. Unified schemes for radio-loud active galactic nuclei. *Publications of the Astronomical Society of the Pacific*, **107**[715]:803–845, 1995.

[59] J. D. FINKE, C. D. DERMER, M. BÖTTCHER. Synchrotron self-Compton analysis of TeV X-ray-selected BL Lacertae objects. *The Astrophysical Journal*, **686**[1]:181, 2008.

[60] C. D. DERMER ET AL. Gamma-ray studies of blazars: Synchro-Compton analysis of flat spectrum radio quasars. *The Astrophysical Journal*, **692**[1]:32, 2009.

[61] A. CELOTTI, A. C. FABIAN. The kinetic power and luminosity of parsec-scale radio jets – an argument for heavy jets. *Monthly Notices of the Royal Astronomical Society*, **264**[1]:228–236, 1993.

[62] A. CELOTTI, G. GHISELLINI, A. C. FABIAN. Bulk comptonization spectra in blazars. *Monthly Notices of the Royal Astronomical Society*, **375**[2]:417–424, 2007.

[63] F. TAVECCHIO ET AL. On the origin of the γ-ray emission from the flaring blazar PKS 1222+216. *Astronomy and Astrophysics*, **534**:A86, 2011.

[64] G. GHISELLINI, F. TAVECCHIO, M. CHIABERGE. Structured jets in TeV BL Lac objects and radiogalaxies. *Astronomy and Astrophysics*, **432**[2]:401–410, 2005.

[65] J.-P. LENAIN ET AL. A synchrotron self-Compton scenario for the very high energy γ-ray emission of the radiogalaxy M87. *Astronomy and Astrophysics*, **478**[1]:111–120, 2008.

[66] M. GEORGANOPOULOS, E. S. PERLMAN, D. KAZANAS. Is the core of M87 the source of its TeV emission? Implications for unified schemes. *The Astrophysical Journal Letters*, **634**[1]:L33, 2005.

[67] M. BÖTTCHER ET AL. Leptonic and hadronic modeling of Fermi-detected blazars. *The Astrophysical Journal*, **768**[1]:54, 2013.

[68] H. TAKAMI. γ-rays as a diagnostic of the origin of core radiation in low-luminosity active galactic nuclei. *Monthly Notices of the Royal Astronomical Society*, **413**[3]:1845–1851, 2011.

[69] A. A. ABDO ET AL. Insights into the high-energy γ-ray emission of Markarian 501 from extensive multifrequency observations in the Fermi era. *The Astrophysical Journal*, **727**[2]:129, 2011.

[70] M. ACKERMANN ET AL. Multifrequency studies of the peculiar quasar 4C +21.35 during the 2010 flaring activity. *The Astrophysical Journal*, **786**[2]:157, 2014.

[71] J. ALEKSIĆ ET AL. MAGIC discovery of very high energy emission from the FSRQ PKS 1222+21. *The Astrophysical Journal Letters*, **730**[1]:L8, 2011.

[72] N. MANKUZHIYIL ET AL. The environment and distribution of emitting electrons as a function of source activity in Markarian 421. *The Astrophysical Journal*, **733**[1]:14, 2011.

[73] S. CUTINI ET AL. Radio–gamma-ray connection and spectral evolution in 4C +49.22 (S4 1150+49): the Fermi, Swift and Planck view. *Monthly Notices of the Royal Astronomical Society*, **445**[4]:4316–4334, 2014.

[74] C. D. DERMER, K. MURASE, H. TAKAMI. Variable gamma-ray emission induced by ultra-high energy neutral beams: Application to 4C +21.35. *The Astrophysical Journal*, **755**[2]:147, 2012.

[75] F. TAVECCHIO ET AL. Evidence for an axion-like particle from PKS 1222+216? *Phys. Rev. D*, **86**:085036, Oct 2012.

[76] A. H. COMPTON. A quantum theory of the scattering of X-rays by light elements. *Phys. Rev.*, **21**:483–502, May 1923.

[77] O. KLEIN, Y. NISHINA. Über die Streuung von Strahlung durch freie Elektronen nach der neuen relativistischen Quantendynamik von Dirac. *Zeitschrift für Physik*, **52**[11-12]:853–868, 1929.

[78] F. C. JONES. Calculated spectrum of inverse-Compton-scattered photons. *Phys. Rev.*, **167**:1159–1169, Mar 1968.

[79] G. R. BLUMENTHAL, R. J. GOULD. Bremsstrahlung, synchrotron radiation, and Compton scattering of high-energy electrons traversing dilute gases. *Rev. Mod. Phys.*, **42**:237–270, Apr 1970.

[80] G. B. RYBICKI, A. P. LIGHTMAN. *Radiative processes in astrophysics*. Wiley New York, 1979.

[81] R. WAGNER. VHE γ-ray sky map and source catalog. https://www.mppmu.mpg.de/~rwagner/sources/, November 2011.

[82] J. ALEKSIĆ ET AL. The major upgrade of the MAGIC telescopes, Part II: The achieved physics performance using the Crab Nebula observations. *eprint arXiv:1409.5594*, 2014.

[83] V. A. ACCIARI ET AL. A connection between star formation activity and cosmic rays in the starburst galaxy M82. *Nature*, **462**:770–772, 2009.

[84] F. ACERO ET AL. Detection of gamma rays from a starburst galaxy. *Science*, **326**[5956]:1080–1082, 2009.

[85] D. B. FOX ET AL. The afterglow of GRB 050709 and the nature of the short-hard γ-ray bursts. *Nature*, **437**:845–850, 2005.

[86] L. PIRO. Astrophysics: Short-burst sources. *Nature*, **437**:822–823, 2005.

[87] G. SCHILLING. Short gamma ray bursts: Mystery solved. *Science*, **310**[5745]:37, 2005.

[88] J. VAN PARADIJS ET AL. Transient optical emission from the error box of the γ-ray burst of 28 February 1997. *Nature*, **386**:686–689, 1997.

[89] PLANCK COLLABORATION ET AL. Planck 2013 results. XVI. Cosmological parameters. *Astronomy and Astrophysics*, **571**:A16, 2014.

[90] D. CLOWE ET AL. A direct empirical proof of the existence of dark matter. *The Astrophysical Journal Letters*, **648**[2]:L109, 2006.

[91] W. L. KRAUSHAAR, G. W. CLARK. Gamma Ray Astronomy. *Scientific American*, **206**:52–61, 1962.

[92] W. L. KRAUSHAAR, G. W. CLARK. Search for primary cosmic gamma rays with the satellite Explorer XI. *Phys. Rev. Lett.*, **8**:106–109, Feb 1962.

[93] W. KRAUSHAAR ET AL. Explorer XI experiment on cosmic gamma rays. *Astrophysical Journal*, **141**:845, 1965.

[94] W. B. ATWOOD ET AL. The Large Area Telescope on the Fermi Gamma-Ray Space Telescope mission. *The Astrophysical Journal*, **697**[2]:1071, 2009.

[95] R. RANDO ET AL. Fermi LAT performance. http://www.slac.stanford.edu/exp/glast/groups/canda/lat_Performance.htm, November 2013.

[96] J. MATTHEWS. A Heitler model of extensive air showers. *Astroparticle Physics*, **22**[5-6]:387 – 397, 2005.

[97] H. J. BHABHA, W. HEITLER. The passage of fast electrons and the theory of cosmic showers. *Proceedings of the Royal Society of London. Series A, Mathematical and Physical Sciences*, **159**[898]:pp. 432–458, 1937.

[98] J. F. Carlson, J. R. Oppenheimer. On multiplicative showers. *Phys. Rev.*, **51**:220–231, Feb 1937.

[99] L. Landau, G. Rumer. The cascade theory of electronic showers. *Proceedings of the Royal Society of London. Series A, Mathematical and Physical Sciences*, **166**[925]:pp. 213–228, 1938.

[100] T. Matano et al. Transverse momentum of hadrons and subcores of extensive air showers. In *Proceedings of the 14th International Cosmic Ray Conference, Muenchen, Germany*, **12**, page 4364, 1975.

[101] D. Hrupec. *Extragalactic sources of rapidly variable high energy gamma radiation.* PhD thesis, University of Zagreb, Croatia, 2008.

[102] H. Anderhub et al. Design and operation of FACT — the first G-APD Cherenkov telescope. *Journal of Instrumentation*, **8**[06]:P06008, 2013.

[103] R. Mirzoyan, the HEGRA Collaboration. Cherenkov light observations with the HEGRA detector at the Roque de los Muchachos observatory. *New Astronomy Reviews*, **42**[6–8]:547 – 551, 1998.

[104] T. C. Weekes et al. Observation of TeV gamma rays from the Crab Nebula using the atmospheric Cerenkov imaging technique. *The Astrophysical Journal*, **342**[2]:379–395, 1989.

[105] J. Hinton et al. A new era in gamma-ray astronomy with the Cherenkov Telescope Array. *Astroparticle Physics*, **43**[0]:1 – 2, 2013. Seeing the high-energy universe with the Cherenkov Telescope Array – The science explored with the CTA.

[106] B.S. Acharya et al. Introducing the CTA concept. *Astroparticle Physics*, **43**[0]:3 – 18, 2013. Seeing the high-energy universe with the Cherenkov Telescope Array – The science explored with the CTA.

[107] H. Dole et al. The cosmic infrared background resolved by Spitzer. *Astronomy and Astrophysics*, **451**[2]:417–429, 2006.

[108] A. Domínguez et al. Extragalactic background light inferred from AEGIS galaxy-SED-type fractions. *Monthly Notices of the Royal Astronomical Society*, **410**[4]:2556–2578, 2011.

[109] M. Ackermann et al. Detection of the characteristic pion-decay signature in supernova remnants. *Science*, **339**[6121]:807–811, 2013.

[110] J. Aleksić et al. Morphological and spectral properties of the W51 region measured with the MAGIC telescopes. *Astronomy and Astrophysics*, **541**:A13, 2012.

[111] W. F. HANLON. Updated cosmic ray spectrum. `http://www.physics.utah.edu/~whanlon/spectrum.html`, September 2014.

[112] S. RITT. The DRS chip: Cheap waveform digitizing in the GHz range. *Nuclear Instruments and Methods in Physics Research Section A: Accelerators, Spectrometers, Detectors and Associated Equipment*, **518**[1-2]:470 – 471, 2004. Frontier Detectors for Frontier Physics: Proceedin.

[113] J. CORTINA ET AL. Technical performance of the MAGIC telescope. In B. SRIPATHI ACHARYA ET AL., editors, *Proceedings of the 29th International Cosmic Ray Conference, Pune, India*, **3**, page 359, Mumbai, India, 2005. Tata Institute of Fundamental Research.

[114] J. ALBERT ET AL. FADC signal reconstruction for the MAGIC telescope. *Nuclear Instruments and Methods in Physics Research Section A: Accelerators, Spectrometers, Detectors and Associated Equipment*, **594**[3]:407 – 419, 2008.

[115] F. GOEBEL ET AL. Upgrade of the MAGIC telescope with a multiplexed fiberoptic 2 GSamples/s FADC data acquisition system. In ROGELIO CABALLERO ET AL., editors, *Proceedings of the 30th International Cosmic Ray Conference, Merida, Mexico*, **3**, pages 1481–1484, Mexico City, Mexico, 2008. Universidad Nacional Autónoma de México.

[116] J. ALEKSIĆ ET AL. Performance of the MAGIC stereo system obtained with Crab Nebula data. *Astroparticle Physics*, **35**[7]:435 – 448, 2012.

[117] J. SITAREK ET AL. Analysis techniques and performance of the Domino Ring Sampler version 4 based readout for the MAGIC telescopes. *Nuclear Instruments and Methods in Physics Research Section A: Accelerators, Spectrometers, Detectors and Associated Equipment*, **723**[0]:109 – 120, 2013.

[118] J. ALEKSIĆ ET AL. The major upgrade of the MAGIC telescopes, Part I: The hardware improvements and the commissioning of the system. *eprint arXiv:1409.6073*, 2014.

[119] V. P. FOMIN ET AL. New methods of atmospheric Cherenkov imaging for gamma-ray astronomy. I. The false source method. *Astroparticle Physics*, **2**:137–150, 1994.

[120] R. ZANIN ET AL. Mars, the MAGIC analysis and reconstruction software. *Proceedings of 33rd ICRC*, 2013.

[121] R. BRUN, F. RADEMAKERS. ROOT – An object oriented data analysis framework. *Nuclear Instruments and Methods in Physics Research Section A: Accelerators, Spectrometers, Detectors and Associated Equipment*, **389**[1-2]:81 – 86, 1997. New Computing Techniques in Physics Research V.

[122] A. M. HILLAS. Cerenkov light images of EAS produced by primary gamma. *Proceedings of 19th ICRC*, **3**:445–448, 1985.

[123] T.-P. Li, Y.-Q. Ma. Analysis methods for results in gamma-ray astronomy. *The Astrophysical Journal*, **272**:317, 1983.

[124] M. Bertero. Linear inverse and ill-posed problems. **75** of *Advances in Electronics and Electron Physics*, pages 1 – 120. Academic Press, 1989.

[125] M. Schmelling. The method of reduced cross-entropy a general approach to unfold probability distributions. *Nuclear Instruments and Methods in Physics Research Section A: Accelerators, Spectrometers, Detectors and Associated Equipment*, **340**[2]:400 – 412, 1994.

[126] A. Tikhonov, V. Arsenin. *Solutions of ill-posed problems*. Scripta Series in Mathematics. V. H. Winston & sons, 1977.

[127] J. Albert et al. Unfolding of differential energy spectra in the MAGIC experiment. *Nuclear Instruments and Methods in Physics Research Section A: Accelerators, Spectrometers, Detectors and Associated Equipment*, **583**[2-3]:494 – 506, 2007.

[128] S. Bird et al. The inner halo of M87: A first direct view of the red-giant population. *Astronomy and Astrophysics*, **524**:A71, Dec 2010.

[129] M. Cappellari et al. The ATLAS³ᴰ project – I. A volume-limited sample of 260 nearby early-type galaxies: science goals and selection criteria. *Monthly Notices of the Royal Astronomical Society*, **413**[2]:813–836, 2011.

[130] M. Baes et al. The Herschel Virgo Cluster survey. *Astronomy and Astrophysics*, **518**:L53, 2010.

[131] W. Dehnen. M87 as a galaxy. In Hermann-Josef Röser, Klaus Meisenheimer, editors, *The Radio Galaxy Messier 87*, **530** of *Lecture Notes in Physics*, pages 31–42. Springer Berlin Heidelberg, 1999.

[132] K.-S. Park, M.-S. Chun. Dynamical structure of NGC 4486. *Journal of Astronomy and Space Science*, **4**[1]:35–45, Jun 1987.

[133] E. Emsellem, D. Krajnović, M. Sarzi. A kinematically distinct core and minor-axis rotation: the MUSE perspective on M87. *[arxiv:1408.6844]*, 2014.

[134] M. Doherty et al. The edge of the M87 halo and the kinematics of the diffuse light in the Virgo Cluster core. *Astronomy and Astrophysics*, **502**[3]:771–786, 2009.

[135] M. Cappellari et al. The SAURON project – IV. The mass-to-light ratio, the virial mass estimator and the fundamental plane of elliptical and lenticular galaxies. *Monthly Notices of the Royal Astronomical Society*, **366**[4]:1126–1150, 2006.

[136] P. E. J. Nulsen, H. Böhringer. A ROSAT determination of the mass of the central Virgo Cluster. *Monthly Notices of the Royal Astronomical Society*, **274**[4]:1093–1106, 1995.

[137] N. Tamura et al. A Subaru/Suprime-Cam wide-field survey of globular cluster populations around M87 – I. Observation, data analysis and luminosity function. *Monthly Notices of the Royal Astronomical Society*, **373**[2]:588–600, 2006.

[138] H. L. Marshall et al. A high-resolution X-ray image of the jet in M87. *The Astrophysical Journal*, **564**[2]:683, 2002.

[139] J. A. Biretta, W. B. Sparks, F. Macchetto. Hubble space telescope observations of superluminal motion in the M87 jet. *The Astrophysical Journal*, **520**[2]:621, 1999.

[140] C. Ly, R. C. Walker, W. Junor. High-frequency VLBI imaging of the jet base of M87. *The Astrophysical Journal*, **660**[1]:200, 2007.

[141] J. A. Biretta, F. Zhou, F. N. Owen. Detection of proper motions in the M87 jet. *The Astrophysical Journal*, **447**:582, 1995.

[142] C. C. Cheung, D. E. Harris, Ł. Stawarz. Superluminal radio features in the M87 jet and the site of flaring TeV gamma-ray emission. *The Astrophysical Journal Letters*, **663**[2]:L65, 2007.

[143] E. S. Perlman et al. Month-timescale optical variability in the M87 jet. *The Astrophysical Journal Letters*, **599**[2]:L65, 2003.

[144] D. E. Harris et al. Variability timescales in the M87 jet: Signatures of E^2 losses, discovery of a quasi period in HST-1, and the site of TeV flaring. *The Astrophysical Journal*, **699**[1]:305, 2009.

[145] K. Hada et al. An origin of the radio jet in M87 at the location of the central black hole. *Nature*, **477**:185–187, 2011.

[146] A. S. Wilson, Y. Yang. Chandra X-ray imaging and spectroscopy of the M87 jet and nucleus. *The Astrophysical Journal*, **568**[1]:133, 2002.

[147] Ł. Stawarz, M. Sikora, M. Ostrowski. High-energy gamma rays from FR I jets. *The Astrophysical Journal*, **597**[1]:186, 2003.

[148] A. Neronov, F. A. Aharonian. Production of TeV gamma radiation in the vicinity of the supermassive black hole in the giant radio galaxy M87. *The Astrophysical Journal*, **671**[1]:85, 2007.

[149] F. M. Rieger, F. A. Aharonian. Variable VHE gamma-ray emission from non-blazar AGNs. *Astronomy and Astrophysics*, **479**[1]:L5–L8, 2008.

[150] A. LEVINSON, F. RIEGER. Variable TeV emission as a manifestation of jet formation in M87? *The Astrophysical Journal*, **730**[2]:123, 2011.

[151] D. GIANNIOS, D. A. UZDENSKY, M. C. BEGELMAN. Fast TeV variability from misaligned minijets in the jet of M87. *Monthly Notices of the Royal Astronomical Society*, **402**[3]:1649–1656, 2010.

[152] M. V. BARKOV, F. A. AHARONIAN, V. BOSCH-RAMON. Gamma-ray flares from red giant/jet interactions in active galactic nuclei. *The Astrophysical Journal*, **724**[2]:1517, 2010.

[153] M. C. BEGELMAN, M. SIKORA. Inverse Compton scattering of ambient radiation by a cold relativistic jet — A source of beamed, polarized continuum in blazars? *The Astrophysical Journal*, **322**:650, 1987.

[154] J. SITAREK, W. BEDNAREK. Time-dependent gamma-ray production in the anisotropic inverse compton $e^{\pm}$ pair cascade initiated by electrons in active galaxies. *Monthly Notices of the Royal Astronomical Society*, **409**[2]:662–678, 2010.

[155] P. ROUSTAZADEH, M. BÖTTCHER. Very high energy gamma-ray-induced pair cascades in blazars and radio galaxies: Application to NGC 1275. *The Astrophysical Journal*, **717**[1]:468, 2010.

[156] Ł STAWARZ ET AL. Dynamics and high-energy emission of the flaring HST-1 knot in the M87 jet. *Monthly Notices of the Royal Astronomical Society*, **370**[2]:981–992, 2006.

[157] O. BROMBERG, A. LEVINSON. Recollimation and radiative focusing of relativistic jets: Applications to blazars and M87. *The Astrophysical Journal*, **699**[2]:1274, 2009.

[158] A. A. ABDO ET AL. Fermi Large Area Telescope gamma-ray detection of the radio galaxy M87. *The Astrophysical Journal*, **707**[1]:55, 2009.

[159] J. ALEKSIĆ ET AL. Observations of the blazar 3C 66A with the MAGIC telescopes in stereoscopic mode. *The Astrophysical Journal*, **726**[2]:58, 2011.

[160] J. ALEKSIĆ ET AL. MAGIC observations of the giant radio galaxy M87 in a low-emission state between 2005 and 2007. *Astronomy and Astrophysics*, **544**:A96, 2012.

[161] B. BALMAVERDE, A. CAPETTI, P. GRANDI. The Chandra view of the 3C/FR I sample of low luminosity radio-galaxies. *Astronomy and Astrophysics*, **451**[1]:35–44, 2006.

[162] D. GIANNIOS, D. A. UZDENSKY, M. C. BEGELMAN. Fast TeV variability in blazars: Jets in a jet. *Monthly Notices of the Royal Astronomical Society: Letters*, **395**[1]:L29–L33, 2009.

[163] Y.-R. LI ET AL. Spins of supermassive black holes in M87. II. Fully general relativistic calculations. *The Astrophysical Journal*, **699**[1]:513, 2009.

[164] E. S. PERLMAN ET AL. Deep 10 micron imaging of M87. *The Astrophysical Journal Letters*, **561**[1]:L51, 2001.

[165] B. BALMAVERDE, R. D. BALDI, A. CAPETTI. The accretion mechanism in low-power radio galaxies. *Astronomy and Astrophysics*, **486**[1]:119–130, 2008.

[166] THE MAGIC COLLABORATION ET AL. Very-high-energy gamma rays from a distant quasar: How transparent is the universe? *Science*, **320**[5884]:1752–1754, 2008.

[167] S. J. WAGNER, H.E.S.S. COLLABORATION. Detection of VHE gamma-ray emission from a type 1 quasar. *American Astronomical Society, HEAD meeting #11, #27.06*, 2010.

[168] D. A. BRAMEL ET AL. Observations of the BL Lacertae object 3C 66A with STACEE. *The Astrophysical Journal*, **629**[1]:108, 2005.

[169] R. MIRZOYAN, THE MAGIC COLLABORATION. Discovery of very high energy gamma-ray emission from gravitationally lensed blazar S3 0218+357 with the MAGIC telescopes. *ATel*, **6349**, July 2014.

[170] J. ALEKSIĆ ET AL. MAGIC long-term study of the distant TeV blazar PKS 1424+240 in a multiwavelength context. *Astronomy and Astrophysics*, **567**:A135, 2014.

[171] M. L. LISTER ET AL. Mojave. X. Parsec-scale jet orientation variations and superluminal motion in active galactic nuclei. *The Astronomical Journal*, **146**[5]:120, 2013.

[172] D. J. SAIKIA, P. J. WIITA, T. W. B. MUXLOW. 1222+216 – a wide-angle-tailed quasar? *Astronomical Journal*, **105**:1658, 1993.

[173] P. KHARB, P. SHASTRI. Optical nuclei of radio-loud AGN and the Fanaroff-Riley divide. *Astronomy and Astrophysics*, **425**[3]:825–836, 2004.

[174] J.-M. WANG, B. LUO, L. C. HO. The connection between jets, accretion disks, and black hole mass in blazars. *The Astrophysical Journal Letters*, **615**[1]:L9, 2004.

[175] S. KASPI ET AL. Reverberation measurements for 17 quasars and the size-mass-luminosity relations in active galactic nuclei. *The Astrophysical Journal*, **533**[2]:631, 2000.

[176] E. P. FARINA ET AL. The optical spectrum of PKS 1222+216 and its black hole mass. *Monthly Notices of the Royal Astronomical Society*, **424**[1]:393–398, 2012.

[177] Y. Shen et al. A catalog of quasar properties from Sloan Digital Sky Survey Data Release 7. *The Astrophysical Journal Supplement Series*, **194**[2]:45, 2011.

[178] M. S. Shaw et al. Spectroscopy of broad-line blazars from 1LAC. *The Astrophysical Journal*, **748**[1]:49, 2012.

[179] A. D. Kerrick et al. Upper limits on TeV gamma-ray emission from active galactic nuclei. *The Astrophysical Journal*, **452**:588, 1995.

[180] R. C. Hartman et al. The Third EGRET Catalog of high-energy gamma-ray sources. *The Astrophysical Journal Supplement Series*, **123**[1]:79, 1999.

[181] A. A. Abdo et al. Fermi Large Area Telescope First Source Catalog. *The Astrophysical Journal Supplement Series*, **188**[2]:405, 2010.

[182] A. Neronov, D. Semikoz, Ie. Vovk. High Galactic latitude Fermi sources of γ-rays with energies above 100 GeV. *Astronomy and Astrophysics*, **529**:A59, 2011.

[183] Y. T. Tanaka et al. Fermi Large Area Telescope detection of bright γ-ray outbursts from the peculiar quasar 4C +21.35. *The Astrophysical Journal*, **733**[1]:19, 2011.

[184] D. Donato, the Fermi Large Area Telescope Collaboration. Fermi LAT observed another strong GeV flare from 4C 21.35 (PKS 1222+21). *ATel*, **2584**, April 2010.

[185] A. Bulgarelli et al. AGILE detection of gamma-ray emission from 4C+21.35 (PKS 1222+21). *ATel*, **2641**, May 2010.

[186] A. Neronov, D. Semikoz, Ie. Vovk. Discovery of VHE gamma-ray emission from 4C +21.35 with Fermi. *ATel*, **2617**, May 2010.

[187] L. Foschini et al. Search for the shortest variability at gamma rays in flat-spectrum radio quasars. *Astronomy and Astrophysics*, **530**:A77, 2011.

[188] HESS Collaboration et al. VHE γ-ray emission of PKS 2155-304: Spectral and temporal variability. *Astronomy and Astrophysics*, **520**:A83, 2010.

[189] T. M. Kneiske, H. Dole. A lower-limit flux for the extragalactic background light. *Astronomy and Astrophysics*, **515**:A19, 2010.

[190] R. C. Gilmore et al. GeV gamma-ray attenuation and the high-redshift UV background. *Monthly Notices of the Royal Astronomical Society*, **399**[4]:1694–1708, 2009.

[191] A. Franceschini, G. Rodighiero, M. Vaccari. Extragalactic optical-infrared background radiation, its time evolution and the cosmic photon-photon opacity. *Astronomy and Astrophysics*, **487**[3]:837–852, 2008.

[192] M. Lampton, B. Margon, S. Bowyer. Parameter estimation in X-ray astronomy. *Astrophysical Journal*, **208**:177, 1976.

[193] M. Ackermann et al. The first Fermi-LAT catalog of sources above 10 GeV. *The Astrophysical Journal Supplement Series*, **209**[2]:34, 2013.

[194] N. Gehrels et al. The Swift gamma-ray burst mission. *The Astrophysical Journal*, **611**[2]:1005, 2004.

[195] S. D. Barthelmy et al. The Burst Alert Telescope (BAT) on the SWIFT Midex mission. *Space Science Reviews*, **120**[3-4]:143–164, 2005.

[196] D. N. Burrows et al. The Swift X-ray telescope. *Space Science Reviews*, **120**[3-4]:165–195, 2005.

[197] P. W. A. Roming et al. The Swift ultra-violet/optical telescope. *Space Science Reviews*, **120**[3-4]:95–142, 2005.

[198] W. H. Baumgartner et al. The 70 month Swift-BAT all-sky hard X-ray survey. *The Astrophysical Journal Supplement Series*, **207**[2]:19, 2013.

[199] P. S. Smith, G. D. Schmidt, B. T. Jannuzi. The optical properties of PKS 1222+216 during the Fermi mission. *2011 Fermi Symposium proceedings - eConf C110509*, 2011.

[200] T. S. Poole et al. Photometric calibration of the Swift ultraviolet/optical telescope. *Monthly Notices of the Royal Astronomical Society*, **383**[2]:627–645, 2008.

[201] R. D. Peccei, H. R. Quinn. CP conservation in the presence of pseudoparticles. *Phys. Rev. Lett.*, **38**:1440–1443, Jun 1977.

[202] J. D. Finke, S. Razzaque, C. D. Dermer. Modeling the extragalactic background light from stars and dust. *The Astrophysical Journal*, **712**[1]:238, 2010.

[203] Planck Collaboration et al. Planck 2013 results. XXVIII. The Planck Catalogue of Compact Sources. *Astronomy and Astrophysics*, **571**:A28, 2014.

[204] M. P. Malmrose et al. Emission from hot dust in the infrared spectra of gamma-ray bright blazars. *The Astrophysical Journal*, **732**[2]:116, 2011.

[205] G. Ghisellini et al. A theoretical unifying scheme for gamma-ray bright blazars. *Monthly Notices of the Royal Astronomical Society*, **301**:451, 1998.

[206] M. Nenkova et al. AGN dusty tori. II. Observational implications of clumpiness. *The Astrophysical Journal*, **685**[1]:160, 2008.

[207] N. I. Shakura, R. A. Sunyaev. Black holes in binary systems. Observational appearance. *Astronomy and Astrophysics*, **24**:337, 1973.

[208] A. KONIGL. Relativistic jets as X-ray and gamma-ray sources. *The Astrophysical Journal*, **243**:700, 1981.

[209] K. NALEWAJKO ET AL. Energetic constraints on a rapid gamma-ray flare in PKS 1222+216. *Monthly Notices of the Royal Astronomical Society*, **425**[4]:2519–2529, 2012.

[210] B. CERUTTI ET AL. Beaming and rapid variability of high-energy radiation from relativistic pair plasma reconnection. *The Astrophysical Journal Letters*, **754**[2]:L33, 2012.

[211] W. FORMAN ET AL. The fourth Uhuru catalog of X-ray sources. *The Astrophysical Journal*, **38**:357–412, December 1978.

[212] K. S. WOOD ET AL. The HEAO A-1 X-ray source catalog. *The Astrophysical Journal*, **56**:507–649, December 1984.

[213] J. L. RICHARDS ET AL. Blazars in the Fermi era: The OVRO 40 m telescope monitoring program. *The Astrophysical Journal Supplement*, **194**:29, June 2011.

[214] L. S. MAO. 2MASS observation of BL Lac objects II. *New Astronomy*, **16**:503–529, December 2011.

[215] M.-P. VÉRON-CETTY, P. VÉRON. Spectroscopic observations of sixteen BL Lacertae candidates. *Astronomy and Astrophysics Supplement Series*, **100**:521–529, September 1993.

[216] R. FALOMO ET AL. The optical to near-infrared emission of BL Lac objects — simultaneous observations. *Astronomical Journal*, **106**:11–27, July 1993.

[217] R. FALOMO, R. SCARPA, M. BERSANELLI. Optical spectrophotometry of blazars. *The Astrophysical Journal Supplement*, **93**:125–143, July 1994.

[218] B. SBARUFATTI ET AL. ESO very large telescope optical spectroscopy of BL Lacertae objects. II. New redshifts, featureless objects, and classification assessments. *Astronomical Journal*, **132**:1–19, July 2006.

[219] M. LANDONI ET AL. Spectroscopy of BL Lac objects of extraordinary luminosity. *Astronomy and Astrophysics, in press*, 2014.

[220] L. COSTAMANTE, G. GHISELLINI. TeV candidate BL Lac objects. *Astronomy and Astrophysics*, **384**:56–71, March 2002.

[221] J. ALEKSIĆ ET AL. Gamma-ray excess from a stacked sample of high- and intermediate-frequency peaked blazars observed with the MAGIC telescope. *The Astrophysical Journal*, **729**[2]:115, 2011.

[222] D. DONATO ET AL. Hard X-ray properties of blazars. *Astronomy and Astrophysics*, **375**:739–751, September 2001.

[223] D. Britzger et al. Studies of the influence of moonlight on observations with the MAGIC telescope. *Proceedings of* 31st *ICRC*, 2009.

[224] J. W. M. Baars et al. The absolute spectrum of CAS A – an accurate flux density scale and a set of secondary calibrators. *Astronomy and Astrophysics*, **61**[1]:99–106, 1977.

[225] E. Prandini et al. Constraining blazar distances with combined Fermi and TeV data: An empirical approach. *Monthly Notices of the Royal Astronomical Society: Letters*, **405**[1]:L76–L80, 2010.

[226] ASI Science Data Center. ASDC SED Builder. http://tools.asdc.asi.it/SED/, September 2014.

[227] S. Wakely, D. Horan. TeVCat online γ-ray catalog. http://tevcat.uchicago.edu/, September 2014.

[228] J. Aleksić et al. Contemporaneous observations of the radio galaxy NGC 1275 from radio to very high energy γ-rays. *Astronomy and Astrophysics*, **564**:A5, 2014.

[229] J. Aleksić et al. Rapid and multiband variability of the TeV bright active nucleus of the galaxy IC 310. *Astronomy and Astrophysics*, **563**:A91, 2014.

[230] A. Abramowski et al. The 2010 very high energy γ-ray flare and 10 years of multi-wavelength observations of M87. *The Astrophysical Journal*, **746**[2]:151, 2012.

[231] J. Aleksić et al. MAGIC observations and multiwavelength properties of the quasar 3C 279 in 2007 and 2009. *Astronomy and Astrophysics*, **530**:A4, 2011.

[232] J. Aleksić et al. MAGIC gamma-ray and multifrequency observations of flat spectrum radio quasar PKS 1510-089 in early 2012. *Astronomy and Astrophysics, in press*, 2014.

[233] J. Albert et al. Discovery of very high energy γ-ray emission from the low-frequency-peaked BL Lacertae object BL Lacertae. *The Astrophysical Journal Letters*, **666**[1]:L17, 2007.

[234] J. Aleksić et al. Observations of the blazar 3C 66A with the MAGIC telescopes in stereoscopic mode. *The Astrophysical Journal*, **726**[2]:58, 2011.

[235] M. Mariotti, the MAGIC collaboration. Discovery of Very High Energy gamma-ray emission from 1FGL J2001.1+4351 by MAGIC. *ATel*, **2753**, July 2010.

[236] H. Anderhub et al. Discovery of very high energy γ-rays from the blazar S5 0716+714. *The Astrophysical Journal Letters*, **704**[2]:L129, 2009.

[237] D. MAZIN ET AL. Discovery of very high energy gamma-rays from the blazar S5 0716+714. *Proceedings of 31st ICRC*, 2009.

[238] J. ALBERT ET AL. Detection of very high energy radiation from the BL Lacertae object PG 1553+113 with the MAGIC telescope. *The Astrophysical Journal Letters*, **654**[2]:L119, 2007.

[239] J. ALEKSIĆ ET AL. PG 1553+113: Five years of observations with MAGIC. *The Astrophysical Journal*, **748**[1]:46, 2012.

[240] J. ALEKSIĆ ET AL. Probing the very-high-energy gamma-ray spectral curvature in the blazar PG 1553+113 with the MAGIC telescopes. *eprint arXiv:1408.1975*, 2014.

[241] J. ALBERT ET AL. Discovery of very high energy γ-rays from Markarian 180 triggered by an optical outburst. *The Astrophysical Journal Letters*, **648**[2]:L105, 2006.

[242] J. ALBERT ET AL. Discovery of very high energy γ-rays from 1ES 1011+496 at z = 0.212. *The Astrophysical Journal Letters*, **667**[1]:L21, 2007.

[243] K. BERGER ET AL. Studying flux variability of the BL Lac object 1ES0806+524 with MAGIC in a multi-wavelength context. *Proceedings of 33rd ICRC*, 2013.

[244] J. ALEKSIĆ ET AL. Discovery of VHE γ-ray emission from the BL Lacertae object B3 2247+381 with the MAGIC telescopes. *Astronomy and Astrophysics*, **539**:A118, 2012.

[245] J. ALEKSIĆ ET AL. Discovery of vhe γ-rays from the blazar 1ES 1215+303 with the MAGIC telescopes and simultaneous multi-wavelength observations. *Astronomy and Astrophysics*, **544**:A142, 2012.

[246] K. BERGER, THE MAGIC COLLABORATION. Overview of the results from extragalactic observations with the MAGIC telescopes. *Proceedings of 32nd ICRC*, 2011.

[247] M. MARIOTTI, THE MAGIC COLLABORATION. VHE detection of the blazar 1ES 0033+595 by MAGIC. *ATel*, **3719**, October 2011.

[248] J. ALEKSIĆ ET AL. Discovery of very high energy gamma-ray emission from the blazar 1ES 1727+502 with the MAGIC telescopes. *Astronomy and Astrophysics*, **563**:A90, 2014.

[249] D. MAZIN, MAGIC COLLABORATION. Highlights from the MAGIC telescopes. *AIP Conference Proceedings*, **1505**[1]:186–193, 2012.

[250] J. CORTINA, THE MAGIC COLLABORATION. Discovery of very high energy gamma-ray emission from MS1221.8+2452 with the MAGIC telescopes. *ATel*, **5038**, May 2013.

[251] R. Mirzoyan, the MAGIC collaboration. Discovery of very high energy gamma-ray emission from RBS 0723 with the MAGIC telescopes. *ATel*, **5768**, January 2014.

[252] R. Mirzoyan, the MAGIC collaboration. Discovery of very high energy gamma-ray emission from BL Lac object RX j1136.5+6737 by the MAGIC telescopes. *ATel*, **6062**, April 2014.

[253] J. Albert et al. Observations of Markarian 421 with the MAGIC telescope. *The Astrophysical Journal*, **663**[1]:125, 2007.

[254] I. Donnarumma et al. The june 2008 flare of Markarian 421 from optical to TeV energies. *The Astrophysical Journal Letters*, **691**[1]:L13, 2009.

[255] J. Aleksić et al. MAGIC TeV gamma-ray observations of Markarian 421 during multiwavelength campaigns in 2006. *Astronomy and Astrophysics*, **519**:A32, 2010.

[256] J. Aleksić et al. Mrk 421 active state in 2008: The MAGIC view, simultaneous multi-wavelength observations and SSC model constrained. *Astronomy and Astrophysics*, **542**:A100, 2012.

[257] J. Albert et al. Variable very high energy γ-ray emission from Markarian 501. *The Astrophysical Journal*, **669**[2]:862, 2007.

[258] H. Anderhub et al. Simultaneous multiwavelength observation of Mkn 501 in a low state in 2006. *The Astrophysical Journal*, **705**[2]:1624, 2009.

[259] V. A. Acciari et al. Spectral energy distribution of Markarian 501: Quiescent state versus extreme outburst. *The Astrophysical Journal*, **729**[1]:2, 2011.

[260] J. Albert et al. Observation of very high energy γ-rays from the AGN 1ES 2344+514 in a low emission state with the MAGIC telescope. *The Astrophysical Journal*, **662**[2]:892, 2007.

[261] J. Aleksić et al. The simultaneous low state spectral energy distribution of 1ES 2344+514 from radio to very high energies. *Astronomy and Astrophysics*, **556**:A67, 2013.

[262] E. Leonardo et al. Multiwavelength observation of the blazar 1ES1426+428 in May-June 2008. *Proceedings of 31st ICRC*, 2009.

[263] J. Albert et al. Observation of very high energy gamma-ray emission from the active galactic nucleus 1ES 1959+650 using the MAGIC telescope. *The Astrophysical Journal*, **639**[2]:761, 2006.

[264] G. Tagliaferri et al. Simultaneous multiwavelength observations of the blazar 1ES 1959+650 at a low TeV flux. *The Astrophysical Journal*, **679**[2]:1029, 2008.

[265] D. HADASCH ET AL. High zenith angle observations of PKS 2155-304 with the MAGIC telescope. *Proceedings of* 31st *ICRC*, 2009.

[266] J. ALBERT ET AL. Discovery of very high energy gamma rays from 1ES 1218+30.4. *The Astrophysical Journal Letters*, **642**[2]:L119, 2006.

[267] F. AHARONIAN. Gamma rays from active galactic nuclei. `http://lapth.cnrs.fr/pg-nomin/chardon/IRAP_PhD/Felix%20_Aharonian.pdf`, September 2012.

[268] J. R. PRIMACK, J. S. BULLOCK, R. S. SOMERVILLE. Observational gamma-ray cosmology. *AIP Conference Proceedings*, **745**[1]:23–33, 2005.

[269] F. W. STECKER, M. A. MALKAN, S. T. SCULLY. Intergalactic photon spectra from the far-IR to the UV Lyman limit for $0 < z < 6$ and the optical depth of the universe to high-energy gamma rays. *The Astrophysical Journal*, **648**[2]:774, 2006.

Acronyms and abreviations

1FHL   First *Fermi* Hard source List

ADC   Analogue-to-Digital Converter

AGN   Active Galactic Nucleus

ALP   Axion-like Particle

AMC   Active Mirror Control

BAT   Burst Alert Telescope

BGO   Bismuth Germanate ($Bi_4Ge_3O_{12}$)

BH   Black Hole

BL Lac   BL Lacertae Object

BLR   Broad Line Region

CH   Counting House

CIB   Cosmic Infrared Background

C.L.   Confidence Level

CMB   Cosmic Microwave Background

COB   Cosmic Optical Background

CTA   Cherenkov Telescope Array

C.U.   Crab Nebula Units

DB   Database

DM   Dark Matter

DRS   Domino Ring Sampler

DT	Discriminator Threshold
EAS	Extensive Air Shower
EBL	Extragalactic Background Light
EC	External Compton
FACT	First G-APD Cherenkov Telescope
FADC	Flash Analogue-to-Digital Converter
FoV	Field of View
FSRQ	Flat Spectrum Radio Quasar
G-APD	Geiger-mode Avalanche Photodiodes
GBM	Gamma-ray Burst Monitor
GRB	Gamma-ray Burst
HBL	High-energy-peaked BL Lac
HEGRA	High Energy Gamma-Ray Astronomy
H.E.S.S.	High Energy Stereoscopic System
IACT	Imaging Atmospheric Cherenkov Telescope
IBL	Intermediate-energy-peaked BL Lac
IPR	Individual Pixel Rate
IR	Infrared
iScream	Interactive Surveillance System for Checking the Report Files and Exposing Alerts in MAGIC
KN	Klein-Nishina
LAT	Large Area Telescope
LBL	Low-energy-peaked BL Lac
LP	Log Parabola
LT0	Level Zero Trigger
LT1	Level One Trigger
LT3	Level Three Trigger

LUT	Lookup Tables
MAGIC	Major Atmospheric Gamma Imaging Cherenkov
MARS	MAGIC Analysis and Reconstruction Software
MC	Monte Carlo
MOJAVE	Monitoring of Jets in Active Galactic Nuclei with VLBA Experiments
MUX	Custom made multiplex system used for MAGIC-I readout
NaI	Sodium Iodide
NLR	Narrow Line Region
NN	Nearest Neighbour
NSB	Night Sky Background
OSA	On Site Analysis
phe	Photoelectron
PIC	Port d'Informació
PL	Pover Law
PLCo	Power Law with Cut-off
PMT	Photomultiplier Tube
QCD	Quantum Chromodynamics
RF	Random Forest
RG	Radio Galaxy
RRD	Round-Robin Database
SED	Spectral Energy Distribution
SM	Standard Model
SMBH	Supermassive Black Hole
SNR	Supernova Remnant
SSC	Synchrotron Self-Compton
TAC	Time Allocation Committee

ToO	Target of Opportunity
UV	Ultraviolet
VERITAS	Very Energetic Radiation Imaging Telescope Array System
VHE	Very High Energy
VLBA	Very Long Baseline Array
VLBI	Very-long-baseline Interferometry
WIMP	Weakly Interacting Massive Particle

Author's contributions

Chapter 2: The MAGIC Telescopes

The author wrote two computer codes presented in this chapter: *iScream* and *significance.C*. *iScream* is a program that monitors the state of the MAGIC subsystems during the observations, and alerts the telescope operators in case some of the parameters are outside of the optimal range. In such way, operators are able to prevent data loss and possible damage or injuries. *significance.C* is a ROOT macro used for optimisation of cuts in the data analysis.

Chapter 3: Messier 87

The results presented in this chapter were published in article "MAGIC observations of the giant radio galaxy M87 in a low-emission state between 2005 and 2007" [160]. The author is a corresponding author for that publication. He performed the data analysis, participated in the interpretation of the results, prepared the spectrum plot (Figure 3.4 in this work) and wrote parts of the text. To the author's knowledge these results were not presented in any other doctoral thesis.

Chapter 4: PKS 1222+21

This chapter includes results from two articles: "MAGIC discovery of VHE Emission from the FSRQ PKS 1222+21" [71] and "Multifrequency Studies of the Peculiar Quasar

4C +21.35 during the 2010 Flaring Activity" [70], and a conference contribution "Very high energy γ-radiation from the radio quasar 4C 21.35" (Proceedings of the International Astronomical Union; Tuffs, R. J.; Popescu, C. C. (ed.); Cambridge; Cambridge University Press, 2012).

The author participad in the discovery of the VHE γ-radiation from PKS 1222+21 by performing the data analysis. Although he is not listed as a corresponding author in paper [71], he presented that work with a poster conference contribution and wrote the proceeding paper as the leading author. He contributed to [70] by the MAGIC telescope data analysis, discussion, and writing text regarding the MAGIC telescope data analysis and results, and is a corresponding author. The results presented in [71] were already used in a doctoral thesis of Josefa Becerra González "Study of Very High Energy Gamma Ray Sources: Discovery of the Blazars PKS 1222+21 and 1ES 1215+303" (University of La Laguna, Spain, 2011). While Becerra González focuses on the results of observations from 2010 June 17, our study spans over longer time period, and includes contemporaneous observations in lower frequencies. All data were separated in three epochs in order to study different emission states of the source. The results from [71] are an important part of the whole, and as such were presented here. In addition, those results are important for setting constraints on the proposed emission model. Becerra González proposes a different emission model in her thesis.

Chapter 5: H1722+119

This chapter reports on the discovery of the VHE γ-radiation from the blazar H1722+119 and a multiwavelength study of the contemporaneous observations. The author of this thesis is the leading author of the corresponding article that is currently being prepared for publication. He performed the MAGIC telescopes data analysis, led the discussion on the results, prepared plots, and wrote most of the text.

Curriculum vitae

The author was born in Rijeka, Croatia in 1978, where he finished primary and secondary school.

In 2007, he graduated from the Faculty of Science, University of Zagreb with the thesis titled "*T-dualnost u teoriji struna*" ("T-duality in string theory") under the supervision of prof. dr. sc. Predrag Dominis Prester.

After the graduation, he worked for four months as a physics teacher in primary schools "Škurinje" in Rijeka, and "Čavle" in Čavle, Croatia. In 2008, the author started working at the University of Rijeka - Department of Physics as a teaching assistant. At the same time he joined the MAGIC collaboration as a member of Croatian MAGIC Consortium and started his research of very high energy γ-radiation from active galactic nuclei, using MAGIC telescopes. In 2009 he spent three months in the Max Planck Institute for Physics (Werner-Heisenberg-Institut) in Munich, Germany. In the same year, he became a full member of the MAGIC collaboration. In 2009 he was enrolled in the doctoral programme at the Faculty of Science, University of Zagreb. He is the author of 48 scientific articles, and attended 3 scientific conferences and 4 schools.

The author actively promotes science. He participates in the organisation of "*Riječka škola fizike*" ("Rijeka School of Physics") at the Department of Physics, University of Rijeka, performs public talks and scientific shows.

List of publications

Refereed published articles

1. Ackermann, M.; ...; Babić, Ana; ...; Dominis Prester, Dijana; ...; Ferenc, Daniel; ...; Godinović, Nikola; ...; Hrupec, Dario; ...; Lelas, Damir; ...; Puljak, Ivica; ...; Surić, Tihomir; ...; Šnidarić, Iva; ...; Terzić, Tomislav; ... (The Fermi-LAT collaboration, The MAGIC collaboration). **Multifrequency Studies of the Peculiar Quasar 4C +21.35 During the 2010 Flaring Activity.** The Astrophysical journal. **786** (2014), 157; 1-46

2. Aleksić, Jelena; ...; Babić, Ana; ...; Dominis Prester, Dijana; ...; Ferenc, Daniel; ...; Godinović, Nikola; ...; Hrupec, Dario; ...; Lelas, Damir; ...; Puljak, Ivica; ...; Surić, Tihomir; ...; Šnidarić, Iva; ...; Terzić, Tomislav. **Contemporaneous observations of the radio galaxy NGC 1275 from radio to very high energy gamma-rays.** Astronomy and astrophysics. **564** (2014), A5; 1-13.

3. Aleksić, Jelena; ...; Babić, Ana; ...; Dominis Prester, Dijana; ...; Ferenc, Daniel; ...; Godinović, Nikola; ...; Hrupec, Dario; ...; Lelas, Damir; ...; Puljak, Ivica; ...; Surić, Tihomir; ...; Šnidarić, Iva; ...; Terzić, Tomislav. **MAGIC upper limits on the GRB 090102 afterglow.** Monthly notices of the Royal Astronomical Society. **437** (2014), 3103-3111.

4. Aleksić, Jelena; ...; Babić, Ana; ...; Dominis Prester, Dijana; ...; Ferenc, Daniel; ...; Godinović, Nikola; ...; Hrupec, Dario; ...; Lelas, Damir; ...; Puljak, Ivica; ...; Surić, Tihomir; ...; Šnidarić, Iva; ...; Terzić, Tomislav. **MAGIC observations and multifrequency properties of the flat spectrum radio quasar 3C 279 in 2011.** Astronomy and astrophysics. **567** (2014), A41; 1-14.

5. Aleksić, Jelena; ...; Babić, Ana; ...; Dominis Prester, Dijana; ...; Ferenc, Daniel; ...; Godinović, Nikola; ...; Hrupec, Dario; ...; Lelas, Damir; ...; Puljak, Ivica; ...; Surić, Tihomir; ...; Šnidarić, Iva; ...; Terzić, Tomislav. **MAGIC long-term study of the distant TeV blazar PKS 1424+240 in a multiwavelength context.** Astronomy and astrophysics. **567** (2014), A135; 1-15.

6. Aleksić, Jelena; ...; Babić, Ana; ...; Dominis Prester, Dijana; ...; Ferenc, Daniel; ...; Godinović, Nikola; ...; Hrupec, Dario; ...; Lelas, Damir; ...; Puljak, Ivica;

...; Surić, Tihomir; ...; Šnidarić, Iva; ...; Terzić, Tomislav. **Optimized dark matter searches in deep observations of Segue 1 with MAGIC.** Journal of cosmology and astroparticle physics. **02** (2014), 008; 1-35.

7. Aleksić, Jelena; ...; Babić, Ana; ...; Dominis Prester, Dijana; ...; Ferenc, Daniel; ...; Godinović, Nikola; ...; Hrupec, Dario; ...; Lelas, Damir; ...; Puljak, Ivica; ...; Surić, Tihomir; ...; Šnidarić, Iva; ...; Terzić, Tomislav. **Search for Very-High-Energy Gamma Rays from the z = 0.896 Quasar 4C +55.17 with the MAGIC telescopes.** Monthly notices of the Royal Astronomical Society. **440** (2014), 1; 530-535.

8. Aleksić, Jelena; ...; Babić, Ana; ...; Dominis Prester, Dijana; ...; Ferenc, Daniel; ...; Godinović, Nikola; ...; Hrupec, Dario; ...; Lelas, Damir; ...; Puljak, Ivica; ...; Surić, Tihomir; ...; Šnidarić, Iva; ...; Terzić, Tomislav. **MAGIC gamma-ray and multifrequency observations of flat spectrum radio quasar PKS 1510-089 in early 2012.** Astronomy and astrophysics. **569** (2014), A46; 1-21.

9. Aleksić, Jelena; ...; Babić, Ana; ...; Dominis Prester, Dijana; ...; Ferenc, Daniel; ...; Godinović, Nikola; ...; Hrupec, Dario; ...; Lelas, Damir; ...; Puljak, Ivica; ...; Surić, Tihomir; ...; Šnidarić, Iva; ...; Terzić, Tomislav. **Detection of bridge emission above 50 GeV from the Crab pulsar with the MAGIC telescopes.** Astronomy and astrophysics. **565** (2014), L12-L16.

10. Aleksić, Jelena; ...; Babić, Ana; ...; Dominis Prester, Dijana; ...; Ferenc, Daniel; ...; Godinović, Nikola; ...; Hrupec, Dario; ...; Lelas, Damir; ...; Puljak, Ivica; ...; Surić, Tihomir; ...; Šnidarić, Iva; ...; Terzić, Tomislav. **MAGIC search for VHE gamma-ray emission from AE Aquarii in a multiwavelength context.** Astronomy and astrophysics. **568** (2014), A109; 1-8.

11. Aleksić, Jelena; ...; Babić, Ana; ...; Dominis Prester, Dijana; ...; Ferenc, Daniel; ...; Godinović, Nikola; ...; Hrupec, Dario; ...; Lelas, Damir; ...; Puljak, Ivica; ...; Surić, Tihomir; ...; Šnidarić, Iva; ...; Terzić, Tomislav; ...; ...; Wilms, J. **Rapid and multi-band variability of the TeV-bright active nucleus of the galaxy IC 310.** Astronomy and astrophysics. **563** (2014), A91-1-A91-9.

12. Aleksić, Jelena; ...; Babić, Ana; ...; Dominis Prester, Dijana; ...; Godinović, Nikola; ...; Hrupec, Dario; ...; Lelas, Damir; ...; Puljak, Ivica; ...; Surić, Tihomir; ...; Šnidarić, Iva; ...; Terzić, Tomislav. **Discovery of TeV gamma-ray emission from the pulsar wind nebula 3C 58 by MAGIC.** Astronomy and astrophysics. **567** (2014), L8; 1-5.

13. Aleksić, Jelena; ...; Dominis Prester, Dijana; ...; Ferenc, Daniel; ...; Godinović, Nikola; ...; Hrupec, Dario; ...; Lelas, Damir; ...; Puljak, Ivica; ...; Surić, Tihomir; ...; Šnidarić, Iva; ...; Terzić, Tomislav. **Discovery of very high energy gamma-ray emission from the blazar 1ES 1727+502 with the MAGIC Telescopes.** Astronomy and astrophysics. **563** (2014), A90; 1-6.

14. Aleksić, Jelena; ...; Dominis Prester, Dijana; ...; Ferenc, Daniel; ...; Godinović, Nikola; ...; Hrupec, Dario; ...; Lelas, Damir; ...; Puljak, Ivica; ...; Surić, Tihomir; ...; Šnidarić, Iva; ...; Terzić, Tomislav; ...; Zanin, R. **The Simultaneous Low State Spectral Energy Distribution of 1ES 2344+514 from Radio to Very High Energies.** Astronomy and astrophysics. **556** (2013), A67-1-A67-28.

15. Aleksić, Jelena; ...; Dominis Prester, Dijana; ...; Ferenc, Daniel; ...; Godinović, Nikola; ...; Hrupec, Dario; ...; Lelas, Damir; ...; Puljak, Ivica; ...; Surić, Tihomir; ...; Šnidarić, Iva; ...; Terzić, Tomislav; ...; Zanin, R. **Very high energy gamma-ray observation of the peculiar transient event Swift J1644+57 with the MAGIC telescopes and AGILE.** Astronomy & Astrophysics. **552** (2013), A112-1-A112-6.

16. Aleksić, Jelena; ...; Dominis Prester, Dijana; ...; Ferenc, Daniel; ...; Godinović, Nikola; ...; Hrupec, Dario; ...; Lelas, Damir; ...; ...; Puljak, Ivica; ...; Šnidarić, Iva; ...; Surić, Tihomir; ...; Terzić, Tomislav; Backes, M. **Observations of the magnetars 4U 0142+61 and 1E 2259+586 with the MAGIC telescopes.** Astronomy & astrophysics. **549** (2013), A23-1-A23-4.

17. A. Abramowski; ...; Dominis Prester, Dijana; ...; Ferenc, Daniel; ...; Godinović, Nikola; ...; Hrupec, Dario; ...; Lelas, Damir; ...; Puljak, Ivica; ...; Surić, Tihomir; ...; Terzić, Tomislav; ...; Wood, D.L. **The 2010 very high energy gamma-ray flare and 10 years of multi-wavelength observations of M 87.** The Astrophysical journal. **746** (2012), 151; 1-19.

18. Aleksić, Jelena; ...; Dominis Prester, Dijana; ...; Ferenc, Daniel; ...; Godinović, Nikola; ...; Hrupec, Dario; ...; Lelas, Damir; ...; Puljak, Ivica; ...; Surić, Tihomir; ...; Šnidarić, Iva; ...; Terzić, Tomislav. **Constraining Cosmic Rays and Magnetic Fields in the Perseus Galaxy Cluster with TeV observations by the MAGIC telescopes.** Astronomy & Astrophysics. **541** (2012), A99-1-A99-12.

19. Aleksić, Jelena; Dominis Prester, Dijana; Ferenc, Daniel; Godinović, Nikola; Hrupec, Dario; ...; Lelas, Damir; ...; Puljak, Ivica; ...; Surić, Tihomir; Šnidarić, Iva; Terzić, Tomislav. **High zenith angle observations of PKS 2155-304 with the MAGIC-I telescope.** Astronomy & Astrophysics. **544** (2012), A75-1-A75-9.

20. Aleksić, Jelena; ...; Dominis Prester, Dijana; ...; Ferenc, Daniel; ...; Godinović, Nikola; ...; Hrupec, Dario; ...; Lelas, Damir; ...; Puljak, Ivica; ...; Surić, Tihomir; ...; Šnidarić, Iva; ...; Terzić, Tomislav; ...; Buson, S. **Discovery of VHE gamma-ray emission from the BL Lac object B3 2247+381 with the MAGIC telescopes.** Astronomy & Astrophysics. **539** (2012), A118-1-A118-6.

21. Aleksić, Jelena; ...; Dominis Prester, Dijana; ...; Ferenc, Daniel; ...; Godinović, Nikola; ...; Hrupec, Dario; ...; Lelas, Damir; ...; Puljak, Ivica; ...; Surić, Tihomir; ...; Šnidarić, Iva; ...; Terzić, Tomislav; ...; Ghisellini, G. **MAGIC observations**

of the giant radio galaxy M 87 in a low-emission state between 2005 and 2007. Astronomy and astrophysics. **544** (2012), A96-1-A96-8.

22. Aleksić, Jelena; ...; Dominis Prester, Dijana; ...; Ferenc, Daniel; ...; Godinović, Nikola; ...; Hrupec, Dario; ...; Lelas, Damir; ...; Puljak, Ivica; ...; Surić, Tihomir; ...; Šnidarić, Iva; ...; Terzić, Tomislav; ...; Tammi, J. **Discovery of VHE gamma-rays from the blazar 1ES 1215+303 with the MAGIC Telescopes and simultaneous multi-wavelength observations.** Astronomy & Astrophysics. **544** (2012), A142-1-A142-10.

23. Aleksić, Jelena; ...; Dominis Prester, Dijana; ...; Ferenc, Daniel; ...; Godinović, Nikola; ...; Hrupec, Dario; ...; Lelas, Damir; ...; Puljak, Ivica; ...; Surić, Tihomir; ...; Šnidarić, Iva; ...; Terzić, Tomislav; ...; Zanin, R. **Performance of the MAGIC stereo system obtained with Crab Nebula data.** Astroparticle physics. **35** (2012), 7; 435-448.

24. Aleksić, Jelena; ...; Dominis Prester, Dijana; ...; Ferenc, Daniel; ...; Godinović, Nikola; ...; Hrupec, Dario; ...; Lelas, Damir; ...; Puljak, Ivica; ...; Surić, Tihomir; ...; Šnidarić, Iva; ...; Terzić, Tomislav; ...; Zanin, R. **Detection of VHE gamma-rays from HESS J0632+057 during the 2011 February X-ray outburst with the MAGIC telescopes.** The Astrophysical journal. **754** (2012), 1; L10-1-L10-5.

25. Aleksić, Jelena; Dominis Prester, Dijana; Ferenc, Daniel; Godinović, Nikola; Hrupec, Dario; Lelas, Damir; Puljak, Ivica; Surić, Tihomir; Terzić, Tomislav. **Mrk 421 active state in 2008: the MAGIC view, simultaneous multi-wavelength observations and SSC model constrained.** Astronomy and astrophysics. **542** (2012), A100-1-A100-11.

26. Aleksić, Jelena; Dominis Prester, Dijana; Ferenc, Daniel; Godinović, Nikola; Hrupec, Dario; Lelas, Damir; Puljak, Ivica; Surić, Tihomir; Terzić, Tomislav. **Detection of very high energy gamma-ray emission from NGC 1275 by the MAGIC telescopes.** Astronomy & Astrophysics. **539** (2012), L2-1-L2-4.

27. Aleksić, Jelena; ...; Dominis Prester, Dijana; ...; Ferenc, Daniel; ...; Godinović, Nikola; ...; Hrupec, Dario; ...; Lelas, Damir; ...; Puljak, Ivica; ...; Surić, Tihomir; ...; Terzić, Tomislav; ...; D'Ammando, F. **PG 1553+113: five years of observations with MAGIC.** The Astrophysical journal. **748** (2012), 46; 1-11.

28. Aleksić, Jelena; ...; Dominis Prester, Dijana; ...; Ferenc, Daniel; ...; Godinović, Nikola; ...; Hrupec, Dario; ...; Lelas, Damir; ...; Puljak, Ivica; ...; Surić, Tihomir; ...; Terzić, Tomislav; ...; Zanin, R. **Detection of the gamma-ray binary LS I +61 303 in a low flux state at Very High Energy gamma-rays with the MAGIC Telesopes in 2009.** The Astrophysical journal. **746** (2012), 80; 1-6.

29. Aleksić, Jelena; ...; Dominis Prester, Dijana; ...; Ferenc, Daniel; ...; Godinović, Nikola; ...; Hrupec, Dario; ...; Lelas, Damir; ...; Puljak, Ivica; ...; Šnidarić, Iva; ...;

Surić, Tihomir; ...; Terzić, Tomislav; ...; Zanin, R. **Morphological and spectral properties of the W51 region measured with the MAGIC telescopes.** Astronomy & astrophysics. **541** (2012), A13-1-A13-11.

30. Abdo, A. A.; ...; Dominis Prester, Dijana; ...; Ferenc, Daniel; ...; Godinović, Nikola; ...; Hrupec, Dario; ...; Puljak, Ivica; ...; Surić, Tihomir; ...; Terzić, Tomislav; ... (Fermi-LAT collaboration, MAGIC collaboration, VERITAS collaboration, GASP-WEBT consortium). **Insights into the High-energy gamma-ray Emission of Markarian 501 from Extensive Multifrequency Observations in the Fermi Era.** The Astrophysical journal. 727 (2011), 129; 129-1-129-25.

31. Abdo, A. A.; ...; Dominis Prester, Dijana; ...; Ferenc, Daniel; ...; Godinović, Nikola; ...; Hrupec, Dario; ...; Puljak, Ivica; ...; Surić, Tihomir; ...; Terzić, Tomislav; ...; Zook, A. **Fermi-LAT Observations of Markarian 421: the Missing Piece of its Spectral Energy Distribution.** The Astrophysical journal. **736** (2011), 131; 1-61.

32. Acciari, V.A.; ...; Dominis Prester, Dijana; ...; Ferenc, Daniel; ...; Godinović, Nikola; ...; Hrupec, Dario; ...; Puljak, Ivica; ...; Surić, Tihomir; ...; Terzić, Tomislav; ...; Hayashida, M. **Spectral Energy Distribution of Markarian 501 : Quiescent State vs. Extreme Outburst.** The Astrophysical journal. **729** (2011), 1; 2-25.

33. Aleksić, Jelena; ...; Dominis Prester, Dijana; ...; Ferenc, Daniel; ...; Godinović, Nikola; ...; Hrupec, Dario; ...; Lelas, Damir; ...; Puljak, Ivica; ...; Surić, Tihomir; ...; Šnidarić, Iva; ...; Terzić, Tomislav. **Phase-resolved energy spectra of the Crab Pulsar in the range of 50-400 GeV measured with the MAGIC Telescopes.** Astronomy and astrophysics. **540** (2011), A69; A69-1-A69-6.

34. Aleksić, Jelena; ...; Dominis Prester, Dijana; ...; Ferenc, Daniel; ...; Godinović, Nikola; ...; Hrupec, Dario; ...; Lelas, Damir; ...; Puljak, Ivica; ...; Surić, Tihomir; ...; Šnidarić, Iva; ...; Terzić, Tomislav; ...; Hirotani, K. **Observations of the Crab pulsar between 25 and 100 GeV with the MAGIC I telescope.** The Astrophysical journal. **742** (2011), 43-1-43-14.

35. Aleksić, Jelena; ...; Dominis Prester, Dijana; ...; Ferenc, Daniel; ...; Godinović, Nikola; ...; Hrupec, Dario; ...; Lelas, Damir; ...; Puljak, Ivica; ...; Surić, Tihomir; ...; Terzić, Tomislav. **MAGIC observations and multiwavelength properties of the quasar 3C279 in 2007 and 2009.** Astronomy and astrophysics. **530** (2011), A4-1-A4-11.

36. Aleksić, Jelena; ...; Dominis Prester, Dijana; ...; Ferenc, Daniel; ...; Godinović, Nikola; ...; Hrupec, Dario; ...; Lelas, Damir; ...; Puljak, Ivica; ...; Surić, Tihomir; ...; Terzić, Tomislav; ...; Buson, S. **MAGIC discovery of VHE Emission from the FSRQ PKS 1222+21.** The Astrophysical journal. **730** (2011), L8; 1-6.

37. Aleksić, Jelena; ...; Dominis Prester, Dijana; ...; Ferenc, Daniel; ...; Godinović, Nikola; ...; Hrupec, Dario; ...; Lelas, Damir; ...; Puljak, Ivica; ...; Surić, Tihomir; ...; Terzić, Tomislav; ...; Strigari, L.E. **Searches for Dark Matter annihilation signatures in the Segue 1 satellite galaxy with the MAGIC-I telescope.** Journal of cosmology and astroparticle physics. **9** (2011), 035-1-035-26.

38. Aleksić, Jelena; ...; Dominis Prester, Dijana; ...; Ferenc, Daniel; ...; Godinović, Nikola; ...; Hrupec, Dario; ...; Lelas, Damir; ...; Puljak, Ivica; ...; Surić, Tihomir; ...; Terzić, Tomislav; ... Zanin, R. **A search for Very High Energy gamma-ray emission from Sco X-1 with the MAGIC telescopes.** The Astrophysical journal. Supplement series. **735** (2011), L5-1-L5-5.

39. Aleksić, Jelena; ...; Dominis Prester, Dijana; ...; Ferenc, Daniel; ...; Godinović, Nikola; ...; Hrupec, Dario; ...; Puljak, Ivica; ...; Surić, Tihomir; ...; Terzić, Tomislav. **Gamma-ray Excess from a Stacked Sample of High- and Intermediate-Frequency Peaked Blazars Observed with the MAGIC Telescope.** The Astrophysical journal. **729** (2011), 115; 1-14.

40. Aleksić, Jelena; ...; Dominis Prester, Dijana; ...; Ferenc, Daniel; ...; Godinović, Nikola; ...; Hrupec, Dario; ...; Puljak, Ivica; ...; Surić, Tihomir; ...; Terzić, Tomislav. **Observations of the Blazar 3C 66A with the MAGIC Telescopes in Stereoscopic Mode.** The Astrophysical journal. **726** (2011), 58-1-58-10.

41. Aleksić, Jelena; ...; Dominis Prester, Dijana; ...; Ferenc, Daniel; ...; Godinović, Nikola; ...; Hrupec, Dario; ...; Puljak, Ivica; ...; Surić, Tihomir; ...; Terzić, Tomislav. **Magic gamma-ray telescope observation of the perseus cluster of galaxies: Implications for cosmic rays, dark matter, and NGC 1275.** The Astrophysical journal. **710** (2010), 1; 634-647.

42. Aleksić, Jelena; ...; Dominis Prester, Dijana; ...; Ferenc, Daniel; ...; Godinović, Nikola; ...; Hrupec, Dario; ...; Puljak, Ivica; ...; Surić, Tihomir; ...; Terzić, Tomislav. **Search for an extended VHE gamma-ray emission from Mrk 421 and Mrk 501 with the MAGIC Telescope.** Astronomy and astrophysics. **524** (2010), A77-1-A77-8.

43. Aleksić, Jelena; ...; Dominis Prester, Dijana; ...; Ferenc, Daniel; ...; Godinović, Nikola; ...; Hrupec, Dario; ...; Puljak, Ivica; ...; Surić, Tihomir; ...; Terzić, Tomislav. **MAGIC constraints on Gamma-ray emission from Cygnus X-3.** The Astrophysical journal. **721** (2010), 1; 843-855.

44. Aleksić, Jelena; ...; Dominis Prester, Dijana; ...; Ferenc, Daniel; ...; Godinović, Nikola; ...; Hrupec, Dario; ...; Puljak, Ivica; ...; Surić, Tihomir; ...; Terzić, Tomislav. **MAGIC Upper Limits for two Milagro-detected, Bright Fermi Sources in the Region of SNR G65.1+0.6.** The Astrophysical journal. **725** (2010), 2; 1629-1632.

45. Aleksić, Jelena; ...; Dominis Prester, Dijana; ...; Ferenc, Daniel; ...; Godinović, Nikola; ...; Hrupec, Dario; ...; Puljak, Ivica; ...; Surić, Tihomir; ...; Terzić, Tomislav; ... Semikoz, D.V. **Detection of very high energy gamma-ray emission from the Perseus cluster head-tail galaxy IC 310 by the MAGIC telescopes.** The Astrophysical journal. **723** (2010), L207-L212.

46. Dominis Prester, Predrag; Terzić, Tomislav. **alpha'-exact entropies for BPS and non-BPS extremal dyonic black holes in heterotic string theory from ten-dimensional supersymmetry.** Journal of High Energy Physics. **12** (2008), 12; 088-1-088-27.

Refereed articles accepted for publication

1. Aleksić, Jelena; ...; Babić, Ana; ...; Dominis Prester, Dijana; ...; Ferenc, Daniel; ...; Godinović, Nikola; ...; Hrupec, Dario; ...; Lelas, Damir; ...; Puljak, Ivica; ...; Surić, Tihomir; ...; Šnidarić, Iva; ...; Terzić, Tomislav. **MAGIC reveals a complex morphology within the unidentified gamma-ray source HESS J1857+026.** Astronomy and astrophysics. (2014)

2. Aleksić, Jelena; ...; Babić, Ana; ...; Dominis Prester, Dijana; ...; Ferenc, Daniel; ...; Godinović, Nikola; ...; Hrupec, Dario; ...; Lelas, Damir; ...; Puljak, Ivica; ...; Surić, Tihomir; ...; Šnidarić, Iva; ...; Terzić, Tomislav. **First broadband characterization and redshift determination of the VHE blazar MAGIC J2001+439.** Astronomy and astrophysics. (2014)

Articles in preparation

1. Aleksić, Jelena; ...; Babić, Ana; ...; Dominis Prester, Dijana; ...; Ferenc, Daniel; ...; Godinović, Nikola; ...; Hrupec, Dario; ...; Lelas, Damir; ...; Puljak, Ivica; ...; Surić, Tihomir; ...; Šnidarić, Iva; ...; Terzić, Tomislav. **Discovery of very high energy γ-ray emission from the blasar H1722+119 by the MAGIC telescopes and its multifrequency characteristics.** MNRAS

Conference contributions

1. Terzić, Tomislav. **MAGIC Status and Results.** LHC Days in Split, 2012. (invited talk).

2. Terzić, Tomislav; Becerra González, Josefa; Maraschi, Laura; Mazin, Daniel; Prandini, Elisa; Saito, Koji; Sitarek, Julian; Stamerra, Antonio; Tavecchio, Fabrizio; Treves, Aldo. **Very high energy γ-radiation from the radio quasar 4C 21.35.** Proceedings of the International Astronomical Union / Tuffs, Richard J. ; Popescu, Cristina C. (ed.). Cambridge : Cambridge University Press, 2012. 414-416 (poster, publication).

3. Terzić, Tomislav; Dominis Prester, Dijana; Ferenc, Daniel; Godinović, Nikola; Hrupec, Dario; Lelas, Damir; Puljak, Ivica; Surić, Tihomir; Šnidarić, Iva. **Visokoenergijsko γ-zračenje iz kvazara PKS 1222+216.** Knjiga sažetaka / Gajović, Andreja ; Tokić, Vedrana ; Zorić, Maja ; Maruščak, Tomislav (ed.). Zagreb : Hrvatsko fizikalno društvo, 2011. 74-74 (talk, abstract).

4. Antunović, Željko; Dominis Prester, Dijana; Ferenc, Daniel; Godinović, Nikola; Hrupec, Dario; Puljak, Ivica; Surić, Tihomir; Terzić, Tomislav. **Visokoenergijska γ-astronomija teleskopima MAGIC.** Knjiga sažetaka / Buljan, Hrvoje ; Horvatić, Davor (ed.). Zagreb : Hrvatsko fizikalno društvo, 2009. 44 (talk, abstract).

5. Terzić, Tomislav; Antunović, Željko; Dominis Prester, Dijana; Ferenc, Daniel; Godinović, Nikola; Hrupec, Dario; Puljak, Ivica; Surić, Tihomir. **Opažanje galaksije M87 MAGIC teleskopom.** Knjiga sažetaka / Buljan, Hrvoje ; Horvatić, Davor (ed.). Zagreb : Hrvatsko fizikalno društvo, 2009. 166 (poster, abstract).

Other publications

1. Aleksić, Jelena; ...; Babić, Ana; ...; Dominis Prester, Dijana; ...; Ferenc, Daniel; ...; Godinović, Nikola; ...; Hrupec, Dario; ...; Lelas, Damir; ...; Puljak, Ivica; ...; Surić, Tihomir; ...; Šnidarić, Iva; ...; Terzić, Tomislav. **Discovery of very high energy gamma-ray emission from RBS 0723 with the MAGIC telescopes**, 2014. (discovery).

2. Aleksić, Jelena; ...; Babić, Ana; ...; Dominis Prester, Dijana; ...; Ferenc, Daniel; ...; Godinović, Nikola; ...; Hrupec, Dario; ...; Lelas, Damir; ...; Puljak, Ivica; ...; Surić, Tihomir; ...; Šnidarić, Iva; ...; Terzić, Tomislav. **Upper Limits on the VHE Gamma-Ray Flux of SN2014J in M82 From Observations by MAGIC**, 2014. (discovery).

3. Aleksić, Jelena; ...; Babić, Ana; ...; Dominis Prester, Dijana; ...; Ferenc, Daniel; ...; Godinović, Nikola; ...; Hrupec, Dario; ...; Lelas, Damir; ...; Puljak, Ivica; ...; Surić, Tihomir; ...; Šnidarić, Iva; ...; Terzić, Tomislav. **Exceptionally high ¿100 GeV flux state of 1ES 1011+496**, 2014. (discovery).

4. Aleksić, Jelena; ...; Babić, Ana; ...; Dominis Prester, Dijana; ...; Ferenc, Daniel; ...; Godinović, Nikola; ...; Hrupec, Dario; ...; Lelas, Damir; ...; Puljak, Ivica; ...; Surić, Tihomir; ...; Šnidarić, Iva; ...; Terzić, Tomislav. **Discovery of Very High Energy Gamma-Ray Emission from BL Lac object RX J1136.5+6737 by the MAGIC Telescopes**, 2014. (discovery).

5. Aleksić, Jelena; ...; Babić, Ana; ...; Dominis Prester, Dijana; ...; Godinović, Nikola; ...; Hrupec, Dario; ...; Lelas, Damir; ...; Puljak, Ivica; ...; Surić, Tihomir; ...;

Šnidarić, Iva; ...; Terzić, Tomislav. **Discovery of Very High Energy Gamma-Ray Emission From Gravitationally Lensed Blazar S3 0218+357 with the MAGIC Telescopes**, 2014. (discovery).

6. Aleksić, Jelena; ...; Dominis Prester, Dijana; ...; Ferenc, Daniel; ...; Godinović, Nikola; ...; Hrupec, Dario; ...; Lelas, Damir; ...; Puljak, Ivica; ...; Surić, Tihomir; ...; Šnidarić, Iva; ...; Terzić, Tomislav. **Discovery of Very High Energy Gamma-Ray Emission from BL Lac object H1722+119 by the MAGIC Telescopes**, 2013. (discovery).

7. Aleksić, Jelena; ...; Dominis Prester, Dijana; ...; Ferenc, Daniel; ...; Godinović, Nikola; ...; Hrupec, Dario; ...; Lelas, Damir; ...; Puljak, Ivica; ...; Surić, Tihomir; ...; Šnidarić, Iva; ...; Terzić, Tomislav. **Discovery of Very High Energy Gamma-Ray Emission from MS1221.8+2452 with the MAGIC telescopes**, 2013. (discovery).

8. Aleksić, Jelena; ...; Dominis Prester, Dijana; ...; Ferenc, Daniel; ...; Godinović, Nikola; ...; Hrupec, Dario; ...; Lelas, Damir; ...; Puljak, Ivica; ...; Surić, Tihomir; ...; Šnidarić, Iva; ...; Terzić, Tomislav. **MAGIC and VERITAS detect an unprecedented flaring activity from Mrk 421 in very high energy gamma-rays**, 2013. (detection).

9. Aleksić, Jelena; ...; Dominis Prester, Dijana; ...; Ferenc, Daniel; ...; Godinović, Nikola; ...; Hrupec, Dario; ...; Lelas, Damir; ...; Puljak, Ivica; ...; Surić, Tihomir; ...; Šnidarić, Iva; ...; Terzić, Tomislav. **MAGIC discovers VHE gamma-ray emission from the blazar 1ES 1727+502**, 2012. (discovery).

10. Aleksić, Jelena; ...; Dominis Prester, Dijana; ...; Ferenc, Daniel; ...; Godinović, Nikola; ...; Hrupec, Dario; ...; Lelas, Damir; ...; Puljak, Ivica; ...; Surić, Tihomir; ...; Šnidarić, Iva; ...; Terzić, Tomislav. **MAGIC detection of renewed activity from the radio galaxy IC 310**, 2012. (detection).

11. Aleksić, Jelena; ...; Dominis Prester, Dijana; ...; Ferenc, Daniel; ...; Godinović, Nikola; ...; Hrupec, Dario; ...; Lelas, Damir; ...; Puljak, Ivica; ...; Surić, Tihomir; ...; Šnidarić, Iva; ...; Terzić, Tomislav. **MAGIC detects an unprecedented high VHE gamma-ray emission from the blazar PG 1553+113**, 2012. (detection).

12. Aleksić, Jelena; ...; Dominis Prester, Dijana; ...; Ferenc, Daniel; ...; Godinović, Nikola; ...; Hrupec, Dario; ...; Lelas, Damir; ...; Puljak, Ivica; ...; Surić, Tihomir; ...; Šnidarić, Iva; ...; Terzić, Tomislav. **MAGIC and Swift detection of renewed activity from the blazar PG1553+113 during a MWL campaign**, 2012. (detection).

13. Aleksić, Jelena; ...; Dominis Prester, Dijana; ...; Ferenc, Daniel; ...; Godinović, Nikola; ...; Hrupec, Dario; ...; Lelas, Damir; ...; Puljak, Ivica; ...; Surić, Tihomir;

...; Šnidarić, Iva; ...; Terzić, Tomislav. **MAGIC detects very high energy gamma-ray emission from the FSRQ PKS 1510-089**, 2012. (detection).

14. Aleksić, Jelena; ...; Dominis Prester, Dijana; ...; Ferenc, Daniel; ...; Godinović, Nikola; ...; Hrupec, Dario; ...; Lelas, Damir; ...; Puljak, Ivica; ...; Surić, Tihomir; ...; Šnidarić, Iva; ...; Terzić, Tomislav. **VHE detection of the blazar 1ES 0033+595 by MAGIC**, 2011. (detection).

15. Aleksić, Jelena; ...; Dominis Prester, Dijana; ...; Ferenc, Daniel; ...; Godinović, Nikola; ...; Hrupec, Dario; ...; Puljak, Ivica; ...; Surić, Tihomir; ...; Terzić, Tomislav. **Discovery of Very High Energy Gamma-Ray Emission from 1ES 1215+303 by MAGIC**, 2011. (discovery).

16. Aleksić, Jelena; ...; Dominis Prester, Dijana; ...; Ferenc, Daniel; ...; Godinović, Nikola; ...; Hrupec, Dario; ...; Puljak, Ivica; ...; Surić, Tihomir; ...; Terzić, Tomislav. **MAGIC confirms VHE gamma-ray emission from HESS J0632+057 between 7-9 Feb 2011**, 2011. (discovery).

17. Aleksić, Jelena; ...; Dominis Prester, Dijana; ...; Ferenc, Daniel; ...; Godinović, Nikola; ...; Hrupec, Dario; ...; Puljak, Ivica; ...; Surić, Tihomir; ...; Terzić, Tomislav. **MAGIC observes a very high energy gamma-ray flare from 1ES0806+524**, 2011. (discovery).

18. Aleksić, Jelena; ...; Dominis Prester, Dijana; ...; Ferenc, Daniel; ...; Godinović, Nikola; ...; Hrupec, Dario; ...; Lelas, Damir; ...; Puljak, Ivica; ...; Surić, Tihomir; ...; Šnidarić, Iva; ...; Terzić, Tomislav. **VERITAS and MAGIC Report Flaring in Very High Energy Gamma Rays from M87**, 2010. (detection).

19. Aleksić, Jelena; ...; Dominis Prester, Dijana; ...; Ferenc, Daniel; ...; Godinović, Nikola; ...; Hrupec, Dario; ...; Lelas, Damir; ...; Puljak, Ivica; ...; Surić, Tihomir; ...; Šnidarić, Iva; ...; Terzić, Tomislav. **MAGIC detects VHE gamma-ray emission from IC 310**, 2010. (detection).

20. Aleksić, Jelena; ...; Dominis Prester, Dijana; ...; Ferenc, Daniel; ...; Godinović, Nikola; ...; Hrupec, Dario; ...; Puljak, Ivica; ...; Surić, Tihomir; ...; Terzić, Tomislav. **No significant enhancement in the VHE gamma-ray flux of the Crab Nebula measured by MAGIC in September 2010**, 2010. (discovery).

21. Aleksić, Jelena; ...; Dominis Prester, Dijana; ...; Ferenc, Daniel; ...; Godinović, Nikola; ...; Hrupec, Dario; ...; Puljak, Ivica; ...; Surić, Tihomir; ...; Terzić, Tomislav. **Discovery of Very High Energy Gamma-Ray Emission from NGC1275 by MAGIC**, 2010. (discovery).

22. Aleksić, Jelena; ...; Dominis Prester, Dijana; ...; Ferenc, Daniel; ...; Godinović, Nikola; ...; Hrupec, Dario; ...; Puljak, Ivica; ...; Surić, Tihomir; ...; Terzić, Tomislav. **Discovery of Very High Energy Gamma-Ray Emission from B3 2247+381 by MAGIC**, 2010. (discovery).

23. Aleksić, Jelena; ...; Dominis Prester, Dijana; ...; Ferenc, Daniel; ...; Godinović, Nikola; ...; Hrupec, Dario; ...; Puljak, Ivica; ...; Surić, Tihomir; ...; Terzić, Tomislav. **Discovery of Very High Energy gamma-ray emission from 1FGL J2001.1+4351 by MAGIC**, 2010. (discovery).

24. Aleksić, Jelena; ...; Dominis Prester, Dijana; ...; Ferenc, Daniel; ...; Godinović, Nikola; ...; Hrupec, Dario; ...; Puljak, Ivica; ...; Surić, Tihomir; ...; Terzić, Tomislav. **MAGIC detects a VHE flare from 4C +21.35 (PKS 1222+21)**, 2010. (discovery).

25. Aleksić, Jelena; ...; Dominis Prester, Dijana; ...; Ferenc, Daniel; ...; Godinović, Nikola; ...; Hrupec, Dario; ...; Puljak, Ivica; ...; Surić, Tihomir; ...; Terzić, Tomislav. **MAGIC observes increased VHE gamma ray flux from M87**, 2010. (discovery).